Technische Universität München
TUM School of Engineering and Design

Aerodynamic Evaluation of Camber Morphed Helicopter Rotor Blades

Amine Abdelmoula

Vollständiger Abdruck der von der TUM School of Engineering and Design der Technischen Universität München zur Erlangung eines

Doktors der Ingenieurwissenschaften (Dr.-Ing.)

genehmigten Dissertation.

Vorsitz: Prof. Dr. Ilkay Yavrucuk

Prüfende der Dissertation:

1. Prof. Dr.-Ing. Manfred Hajek
2. Prof. Dr. Jürgen Rauleder

Die Dissertation wurde am 21.10.2024 bei der Technischen Universität München eingereicht und durch die TUM School of Engineering and Design am 03.02.2025 angenommen.

Zusammenfassung

Diese Dissertation präsentiert eine umfassende Analyse der aerodynamischen Effekte eines aktiven Wölbungsmechanismus an Hubschrauberrotorblättern, wobei der Schwerpunkt auf Wölbungkonzepten liegt, die dem Fishbone Active Camber (FishBAC) ähneln. Unter Verwendung einer Kombination aus zweidimensionalen (2D) stationären und instationären Strömungssimulationen (CFD) sowie high-fidelity Kopplungssimulationen von CFD und Strukturdynamik-Solvern (CSD) umfasst diese Arbeit drei Untersuchungen, die analysieren, wie die Verformung der Wölbung von 75% der Profilsehne bis zur Hinterkante die aerodynamischen Lasten und das gesamte Rotorströmungsfeld beeinflusst.

Die erste Untersuchung schließt eine Lücke in der Literatur, indem sie aerodynamische Daten für Tragflächenprofile mit Wölbungsmechanismus generiert, die für die Modellierung von Hubschrauberrotorblättern mit low-fidelity Lösern benötigt werden. Hierbei werden stationäre 2D CFD Simulationen inm Strömungslöser DLR-TAU verwendet, um die aerodynamischen Koeffizienten von verformten Tragflächenprofilen mit Wölbungsmechanismus zu evaluieren. Im Vergleich zum Basisprofil NACA23012 zeigen die Tragflächenprofile mit Wölbungsmechanismus, bei einer Verformung der Wölbung von bis zu 10 Grad nach unten, signifikante Steigerungen des maximalen Auftriebskoeffizienten sowie eine Erweiterung des Auftriebs. Diese Ergebnisse deuten darauf hin, dass der Wölbungsmechanismus die Auftriebs-zu-Widerstands-Verhältnisse verbessern kann, während gleichzeitig hohe Auftriebswerte beibehalten werden. Dies ist insbesondere von Bedeutung für den Schwebeflug und den Langsamflug.

Die zweite Untersuchung konzentriert sich auf instationäre aerodynamische Effekte, die durch die kombinierte Anwendung von Nickbewegung und aktiver Wölbungsverformung entstehen. Instationäre CFD-Simulationen, durchgeführt mit TAU, werden mit stationären Ergebnissen aus CAMRAD II verglichen. Diese Untersuchung zeigt, dass dynamische Wölbungsverformungen eine Phasenverschiebung in den aerodynamischen Lasten verursachen, insbesondere bei Auftrieb und Nickmoment. Zudem konnten stationäre Modelle den Widerstand nicht präzise erfassen. Diese Erkenntnisse verdeutlichen die Limitationen stationärer Modelle und die Notwendigkeit fortschrittlicher Methoden zur Berücksichtigung der Fluidträgheit bei dynamischen Bewegungen.

In der dritten Untersuchung wurde eine high-fidelity CFD/CSD-Kopplung entwickelt, um dreidimensionale instationäre Effekte auf einen vierblättrigen Rotor zu analysieren. Dieser high-fidelity Ansatz zeigt, dass die aktive Verformung der Wölbung die aerodynamischen Lasten erheblich umverteilt, den Rotornachlauf beeinflusst und die Stärke der Blattspitzenwirbel verringert. Diese Effekte konnten von numerische Ansätzen geringerer Genauigkeit nicht erfasst werden, was die Bedeutung von high-fidelity Simulationen zur Vorhersage komplexer aerodynamischer Verhaltensweisen bei Rotorblättern mit aktivem Wölbungsmechanismus unterstreicht.

Abstract

This thesis presents a comprehensive analysis of the aerodynamic effects of active camber morphing on helicopter rotor blades, focusing on concepts similar to the Fishbone Active Camber (FishBAC). Using a combination of two-dimensional (2D) steady and unsteady Computational Fluid Dynamics (CFD) simulations, along with high-fidelity CFD/CSD (Computational Structural Dynamics) coupling simulations, this work comprises three investigations which examine how camber morphing from the 75% chord to the trailing edge affects aerodynamic loads and the overall rotor flow field.

The first investigation addresses the lack of published airfoil data for camber morphed blade sections, using 2D steady CFD simulations in TAU to evaluate the aerodynamic coefficients of camber-deflected airfoils. Compared to the baseline NACA23012 airfoil, camber deflections of up to 10 degrees downward demonstrated significant increases in maximum lift coefficient and a broader lift envelope. These results suggest that camber morphing can improve lift-to-drag ratios whilst maintaining high lift values. This can be particularly beneficial for high-lift operations such as hover and low-speed flight.

The second investigation focuses on the unsteady aerodynamic effects of combined pitching and camber morphing. Unsteady CFD simulations, computed with TAU, were compared to steady-state results from CAMRAD II. This investigation reveals that dynamic camber morphing causes significant phase shifts in aerodynamic loads, especially in lift and pitching moments. Furthermore, the steady models failed to accurately capture drag. These findings highlight the limitations of steady-state models and the need for advanced methods to capture fluid inertia during dynamic airfoil motions.

In the third investigation, a high-fidelity CFD/CSD coupling framework was developed to analyze three-dimensional unsteady effects on a four-bladed rotor. This high-fidelity approach showed that camber morphing significantly redistributed aerodynamic loads, reshaped the rotor wake, and reduced tip vortex strength. These effects were not captured by lower-fidelity models, underscoring the importance of using high-fidelity simulations to predict complex aerodynamic behavior in rotorcraft with camber morphing.

Acknowledgments

I am deeply grateful to my doctoral supervisor, Professor Manfred Hajek for his trust in me and his unwavering support and encouragement throughout my PhD journey. From the very beginning, his confidence in my abilities and his insightful guidance have been truly invaluable. I am especially thankful for his understanding and helpful advice during difficult moments, as well as for his patience and calm approach in every interaction.

I would also like to express my sincere gratitude to my mentor, Professor Jürgen Rauleder, for his guidance throughout the SABRE project. His encouraging to step outside my comfort zone and our insightful discussions have been invaluable sources of inspiration and motivation throughout my work. Furthermore. I would like to thank Professor Ilkay Yavrucuk for his invaluable support and engaging discussions during the final stages of my PhD journey.

I am deeply thankful to my colleagues Dominik, Sumeet Kumar, Muhammed Kürsat Yurt, and Stefan Platzer for their invaluable support. Their insightful discussions, constant encouragement during challenging times, and the collaborative, positive working environment they fostered were pivotal to my research journey. I am especially grateful for the constructive feedback, professional exchanges, and the friendly conversations they always made time for. I would like also to express my gratitude to my friend Maximilian Ehrle for our valuable CFD discussions and exchange. I also want to thank my colleagues Victor Z., Lukas M., Jonas J., Jonas K., Moritz L., Tobias P., Markus R., Willem R., Florian B., Jakob. B, Bastian H., Lukas G., and all the other colleagues for contributing to the positive atmosphere with their good humor, uplifting energy, and engaging conversations. Thanks also to Martina Thieme, for being such a positive force for our institute. Her constant encouragement and positive attitude was a blessing during my PhD journey.

I would like to sincerely thank the team at Leibniz Supercomputing Centre, the TAU developers at Deutsches Zentrum für Luft- und Raumfahrt, and the preCiCE community. Special thanks to Qunsheng Huang, Gerasimos Chourdakis, and Benjamin Uekermann for their friendly, and invaluable support in developing the CFD/CSD coupling. Their assistance were essential to the success of this work and always greatly appreciated.

A special thank you to my dear friend Jonathan Wright. Your mentorship, kindness, and constant presence, especially when I needed someone to talk to, have meant the world to me. I'm truly grateful for your generosity and for always being there with encouragement and understanding.

Finally, I would like to express my deepest gratitude to my family and friends for their unwavering support throughout this journey. I am especially thankful to my parents and sisters for their love and patience, which have been invaluable in helping me overcome the challenges along the way.

Contents

Abbreviations and Symbols V

List of Figures XI

List of Tables XVII

1. Introduction 1
- 1.1. Motivation . . . 1
- 1.2. State of the Art . . . 2
  - 1.2.1. Individual Blade Control . . . 2
  - 1.2.2. Active Twist . . . 4
  - 1.2.3. Trailing Edge Flaps . . . 6
  - 1.2.4. Multi-Morphing Mechanisms . . . 8
- 1.3. Objectives of the thesis . . . 10

2. Methodology 13
- 2.1. Theoretical Principles . . . 13
  - 2.1.1. Methods and Capabilities of the CFD Solver TAU . . . 13
    - 2.1.1.1. Turbulence Modeling . . . 14
    - 2.1.1.2. Spatial and Temporal Discretization . . . 15
    - 2.1.1.3. RBF Method for Grid Deformation . . . 16
  - 2.1.2. Methods and Capabilities of the CSD Solver CAMRAD II . . . 18
- 2.2. Modeling 2D Steady Aerodynamics of Camber Morphed Airfoils . . . 19
  - 2.2.1. Workflow of TAU Steady Simulations . . . 19
  - 2.2.2. Definition of Camber Morphing . . . 19
  - 2.2.3. Grid Topology and Quality for 2D Airfoils . . . 23
- 2.3. Modeling Unsteady Aerodynamics of Camber Morphed Airfoils . . . 26
  - 2.3.1. Work flow of TAU Unsteady Simulations . . . 26
    - 2.3.1.1. Grid Deformation Applied for the 2D Airfoil . . . 26
  - 2.3.2. CAMRAD Model for Unsteady Aerodynamic Test Case . . . 29
- 2.4. Modeling of the Active and Passive Rotors using CFD/CSD Coupling . . . 31
  - 2.4.1. Workflow of the Loose CFD/CSD Coupling . . . 31
  - 2.4.2. Grid Generation for the Rotor Blades in CFD Domain . . . 34
  - 2.4.3. Modeling of the Blade Motion in CFD Solver . . . 43
  - 2.4.4. Grid Deformation for the Active Blade Sections . . . 44
  - 2.4.5. Modeling of the Rotor in the CSD Solver . . . 47

3. Results and Discussion **51**
3.1. Evaluation of Steady Aerodynamics for 2D Steady Camber-Morphed Airfoils 51
3.1.1. Aim of the Study 51
3.1.2. Numerical Setup 54
3.1.3. Verification Case 54
3.1.4. Effect of Camber Morphing on Lift Coefficient 57
3.1.5. Effect of Camber Morphing on Drag Coefficient 58
3.1.6. Effect of Camber Morphing on Aerodynamic Efficiency 59
3.1.7. Effect of Camber Morphing on Moment Coefficient 62
3.1.8. Effect of Camber Morphing on Center of Pressure 63
3.1.9. Effect of Camber Morphing on Pressure Distribution 64
3.1.10. Summary and Conclusions 67
3.2. Evaluation of Unsteady Aerodynamics for 2D Camber-Morphed Airfoils 69
3.2.1. Aim of the Study 69
3.2.2. Numerical Setup 71
3.2.3. Verification Case 73
3.2.4. Evaluation of the Lift, Drag and Moment Coefficient 77
3.2.5. Comparison of the Pressure Distribution and Velocity Profiles 90
3.2.6. Summary and Conclusions 93
3.3. Evaluation of aerodynamic Characteristics for passive and active rotors using CFD/CSD coupling 95
3.3.1. Aim of the Study 95
3.3.2. Numerical Setup 96
3.3.3. Verification of the CSD Model 98
3.3.4. Convergence of the CFD/CSD Coupling 101
3.3.5. Evaluation of the Blade Motion for the Passive and Active Blades 104
3.3.6. Evaluation of the Sectional Blade Thrust for the Passive and Active Rotor . . . 104
3.3.7. Evaluation of the Sectional Drag Variation for the Passive and Active Blades . 109
3.3.8. Evaluation of the Pressure Variation for the Passive and Active Blades 111
3.3.9. Evaluation of the Wake for the Passive and Active Blades 115
3.3.10. Evaluation of the Trailing Vortices 117
3.3.11. Evaluation of the Vorticity at the Retreating and Advancing Blades 119
3.3.12. Comparison of Computed Thrust and Drag using CFD/CSD Coupling Against Free Wake and Linear Inflow 124
3.3.13. Summary and Conclusions 131

4. Summary and Conclusion **133**

A. List of Publications by the Author Relating to the Dissertation **137**

B. Appendix related to the subsection 3.1 Evaluation of Steady Aerodynamics for 2D Steady Camber-Morphed Airfoils **139**

C. Appendix related to the subsection 3.2 Evaluation of Unsteady Aerodynamics for 2D Camber-Morphed Airfoils **141**
C.0.1. Evaluation of global difference 141

D. Appendix related to the subsection 3.3 Evaluation of aerodynamic Characteristics for passive and active rotors using CFD/CSD coupling **145**
D.0.1. Convergence of the grid deformation 145
D.0.2. Convergence of the CFD/CSD coupling 146

Bibliography **149**

Abbreviations and Symbols

List of symbols

Greek

Symbol	Description	Unit
α	Angle of Attack	deg
α_0	Zero-lift Angle of Attack	deg
α_s	Rotor shaft tilt (pos. aft)	deg
β	flap angle	deg.
δ	camber morphing deflection	deg
$\Delta\alpha$	increment of the angle of attack	deg
$\Delta\alpha_{b_n}$	translation of the control base	m
$\Delta\delta$	increment of the camber deflection	deg
$\Delta\theta_0$	variation in collective pitch angle	deg
$\Delta\theta_{1c}$	variation in lateral pitch angle	deg
$\Delta\theta_{1s}$	variation in longitudinal pitch angle	deg
ΔL_i	Difference between computed sectional forces computed using CFD between successive coupling step	N
ΔM_i	Difference between computed sectional moments computed using CFD between successive coupling step	Nm
ΔM	increment of Mach number	-
Δs	cell length	m
Δt	time step	s
Δx	translation in x direction relative to the x coordinate of the reference point	m
Δy	translation in y direction relative to the y coordinate of the reference point	m
Δz	translation in z direction relative to the z coordinate of the reference point	m

Symbol	Description	Unit
ΔC_d	difference between C_d in CAMRAD II and TAU unsteady	%
ΔC_l	difference between C_l in CAMRAD II and TAU unsteady	%
ΔC_m	difference between C_m in CAMRAD II and TAU unsteady	%
Δ	Difference	%
ϵ_i	Slope angle of the obtained morphed camber line	$m^2\,s^{-3}$
ζ	lead-lag angle	deg
Θ	Pitch angle	deg
θ_0	Blade collective pitch angle	deg
θ_{1c}	Blade longitudinal cyclic pitch angle	deg
θ_{1s}	Blade lateral cyclic pitch angle	deg
θ_{twist}	Blade twist	deg.
κ	Cell orthogonality	-
λ	Relaxation factor	-
λ_2	vortex core line detection criterion	-
μ	advance ratio	$kg\,m^{-1}\,s^{-1}$
μ_t	Eddy viscosity	-
ν	Kinematic viscosity	$m^2\,s^{-1}$
ν_t	Eddy viscosity	$m^2\,s^{-1}$
ξ	Azimuthal angle of plane of data extraction	deg.
$\tilde{\nu}$	Spalart–Allmaras viscosity	$m^2\,s^{-1}$
ρ	Air density	$kg\,m^{-3}$
σ	Rotor solidity	-
σ	Standard deviation	m
τ_w	Wall shear stress	
ϕ	Rotor index angle	deg
ψ	Rotor blade azimuth angle	deg
ω	Turbulence frequency / rate of dissipation per unit turbulent kinetic energy	s^{-1}
ω	Vorticity	s^{-1}
Ω	Rotational frequency of the rotor	Hz
Ω	Rotation rate tensor	s^{-1}

Roman

Symbol	Description	Unit
a	Speed of sound	$\mathrm{m\,s^{-1}}$
AR	cells growth rate	-
c	Rotor blade chord length	m
C_l	2D pitching lift coefficient	-
C_d	2D pitching drag coefficient	-
C_m	2D pitching moment coefficient	-
C_nM^2	Section thrust force coefficient	-
C_xM^2	Section chordwise force coefficient	-
c_{my}	Airfoil pitching moment coefficient	-
c_p	2D Pressure coefficient	-
c_pM^2	sectional blade pressure coefficient	-
d	Absolute difference	
dC_d	Absolute difference in C_d	
dC_l	Absolute difference in C_l	
dC_m	Absolute difference in C_m	
$\vec{d}_b$	Control point translation vector	-
F_x	Force along x axis	N
F_y	Force along y axis	N
F_z	Force along z axis (shaft axis)	N
f_δ	morphing frequency	s^{-1}
f_θ	pitching frequency	s^{-1}
k	Turbulent kinetic energy	$\frac{m^2}{s^{-2}}$
k	Coefficient of third-order polynomial z_{m_i} along the morphing section	-
k	Reduced frequency	-
k_β	Flapping spring constant	Nm/rad
k_ζ	Lagging spring constant	Nm/rad
k	Turbulent kinetic energy	$\mathrm{m^2\,s^{-2}}$
L	Section lift per unit span	$\mathrm{N\,m^{-1}}$
M	Mach number	-
m_t	slope along the morphing interval	-
N	Number of points	-
N	Number of revolutions	-
N_b	Number of rotor blades	-
p	Pressure	$\mathrm{N\,m^{-2}}$
P	Point in data set	
P	Power	W

Symbol	Description	Unit
P_b	Matrix of control points	-
r	Radial coordinate in cylindrical coordinates	-
r	Radial distance from rotational axis	m
R	Rotor radius	m
Re	Reynolds number	-
S	Strain rate tensor	s^{-1}
s	Spanwise fully camber morphing section	m
t	Time	s
t	Spanwise linear transition morphing section	m
t_{end}	Physical time of CFD simulation	s
T	Rotor thrust at time step t	N
T_{total}	Rotor thrust for one rotor revolution	N
T_∞	Air temperature	°C
T_θ	Pitching time period	s
U_{tip}	Rotor tip velocity	$m\,s^{-1}$
U_∞	Incoming flow velocity	$m\,s^{-1}$
U_T	Rotational velocity	$m\,s^{-1}$
U	Velocity vector	$m\,s^{-1}$
v_i	Induced velocity	$m\,s^{-1}$
x,y,z	Distance in Cartesian coordinate system	m
X,Y,Z	Cartesian coordinate system	-
x_{cp}	Center of pressure	-
$\vec{x}_{bj}$	Point from the grid surface	-
y	Wall normal coordinate	m
y_a	Begin aerodynamic section	m
y^+	Dimensionless wall distance	-
z	Unit vector normal to plane	-

Subscripts

Symbol	Description
eff	Effective
exp	Experiment
p	pressure
pp	Peak-to-peak
i,j,k	Direction in computational space

Symbol	Description
i	inertial
l	Lower rotor
mag	Magnitude
max	Maximum
r	Radial direction
ref	Reference
T	Turbulent
tip	Blade tip
TE	Trailing edge
tot	Total
u	Upper rotor
x,y,z	Coordinate directions

Superscripts

Symbol	Description
–	Average
$'$	Fluctuating part

Abbreviations

Symbol	Description
2D	2-Dimensional
3D	3-Dimensional
CFD	Computational Fluid Dynamics
CFL	Courant–Friedrichs–Lewy Number
CSD	Computational Structure Dynamics
EXP	Experimental
LES	Large Eddy Simulation
RANS	Reynolds-Averaged Navier–Stokes equations
RBF	Radial Basis Functions
SA	Spalart-Allmaras turbulence model
SST	Shear stress transport turbulence model
TE	Trailing Edge
URANS	Unsteady Reynolds-Averaged Navier–Stokes equations

List of Figures

1.1. BO105 and UH-60A rotor system installed with IBC actuators on the large rotor test apparatus in the NASA Ames Research Center 40-by 80-Foot wind tunnel. 4
1.2. Active twist systems used for the ATR and STAR research programs. 5
1.3. Active trailing-edge flap used for the Boeing SMART rotor and BK117 helicopter. . . 8
1.4. Illustration of the SABRE project's multi-morphing rotor vision and the investigated active camber morphing concept. 10

2.1. Summary of the relevant steps to generate the morphed airfoils[5]. 20
2.2. Morphing of camber line based on the FishBAC concept. This figure is inspired from [5] and[40]. 21
2.3. Generation of the upper and lower surfaces of a camber morphed airfoil [5]. 22
2.4. The applied O-grid topology for the computational domain of camber airfoil with deflection $\delta = 10$ deg. 23
2.5. Comparison of the CFD mesh growth rate and cell orthogonality κ around the basline and camber morphing airfoil with δ=10 deg. 25
2.6. Workflow of the 2D unsteady simulation in TAU. 27
2.7. Comparison between the deformed grid surface shapes (black lines) and target camber morphed airfoils (red symbols) at different conditions. 28
2.8. Comparison of cell orthogonality κ between the primary and deformed grids with pitch angle $\theta = 8$ deg and morphing deflection $\delta = 4$ deg. 28
2.9. Illustration of the key parameter of the one bladed CAMRAD II model. 29
2.10. Time line of the explicit loose coupling[4]. 32
2.11. Coupling workflow based on the delta loads method[4]. 33
2.12. Mapping strategies for aerodynamic loads and blade motion[4]. 34
2.13. Discretization of the computational domain using overlapping grids. 35
2.14. Illustration of the modeled BO105 surface blade in the CFD domain. 36
2.15. Illustration of the grid resolution along the chord length. 37
2.16. Slice through the blade block along its span, illustrating the block's spanwise dimensions. 38
2.17. Illustration of the dimensions of the transfer block and outer chimera boundary in yellow. The close-up of the grid section along a constant z value shows the overlapping region with a blade block. 39
2.18. Illustration of the relevant boundary needed for the Chimera interpolations between the transfer block and blade blocks. 41
2.19. Illustration of the shape of the background grid and relevant boundary conditions. The close-up view shows the Chimera boundary needed to exchange data with the rotating transfer block. 42

2.20. Illustration of the dimensions of the background grid and the interpolation region. The interpolation zone between the background and the transfer block is highlighted turquoise. 42
2.21. Hierarchy of motion applied to grid blocks. 43
2.22. Definition of the active camber section and the actuation profile. 45
2.23. Distribution of the scattered data which defines the target blade deformation. 46
2.24. Illustration of the camber morphing section and the schedule applied over the azimuth ψ to morph the camber of the blades. 46
2.25. Comparison of cell orthogonality κ at $r/R = 0.75$ between the passive and active blade at pitch angle $\theta = 8$ deg and morphing deflection $\delta = 4$ deg. The shape of the active blade is obtained by means of grid deformation. 47
2.26. Representation of the flap and lead-lag hinge locations in a CFD/CSD coupling model and a simplified BO105 equivalent model. 48
2.27. Representation of the relative blade properties in CAMRAD II along the blade span. 49

3.1. Variation of Mach number over the rotor azimuth ψ for $U_{tip} = 218$ m/s. 52
3.2. Illustration of the investigated camber morphed airfoil and definition of angle of attack and camber morphing deflection. 53
3.3. Validation of the computed lift coefficient C_l with the experimental data from [22] for different Mach numbers. 55
3.4. Validation of the computed drag coefficient C_d with the experimental data from [22] for different Mach numbers. 55
3.5. Validation of the computed moment coefficient C_m with the experimental data from [22] for different Mach numbers. 55
3.6. Comparison of aerodynamic coefficients computed by TAU against the coefficient obtained by SU2 at Mach 0.4 for the baseline airfoil. 56
3.7. Comparison of aerodynamic coefficients computed by TAU against the coefficient obtained by SU2 at Mach 0.4 for the camber morphed airfoil with the deflection $\delta = 4$ deg. 56
3.8. Comparison of aerodynamic coefficients computed by TAU against the coefficient obtained by SU2 at Mach 0.4 for the camber morphed airfoil with the deflection $\delta = 8$ deg. 57
3.9. Variation of the lift coefficient C_l of the morphed airfoils over the angle of attack α for the Mach numbers $M = 0.4$ and $M = 0.6$. 58
3.10. Variation of the drag coefficient C_d of the morphed airfoils over the lift coefficient C_l for the Mach numbers $M = 0.4$ and $M = 0.6$. 59
3.11. Variation of C_l/C_d of the morphed airfoils over the lift coefficient C_l for the Mach number $M = 0.4$ and $M = 0.6$. 61
3.12. Variation of $(C_l/C_d)_{max}$ of the morphed airfoils over $C_{l,max}$ for the Mach numbers $M = 0.4$ and $M = 0.6$. 61
3.13. Variation of the moment coefficient C_m of the morphed airfoils over the lift coefficient C_l for the Mach numbers $M = 0.4$ and $M = 0.6$. 62
3.14. Variation of the center of pressure of the morphed airfoils over the lift coefficient C_l for the Mach numbers $M = 0.4$ and $M = 0.6$ 64
3.15. Comparison of the pressure distribution c_p along the chord length at $M = 0.4$. 65

3.16. Comparison of pressure contours for constant lift coefficient($C_l = 1.225$) of different morphed airfoils at $M = 0.4$. 66
3.17. Illustration of prescribed pitching motion combined with camber morphing actuation cycle of the insvetigated cases, Baseline, 1P and 2P listed in Table 3.1. 72
3.18. Illustration of the dimensions of the investigated NACA0012 airfoil with trailing edge flap and the applied oscillation motion for main airfoil and the trailing edge. The experimental data are extracted from [69] 74
3.19. Wind Tunnel boundary condition in the CFD simulation 75
3.20. Illustration of the grid used to validate the numerical setup for the unsteady investigation. 75
3.21. Illustration of the grid used to validate the numerical setup for the unsteady investigation. 76
3.22. Validation of grid and numerical setup of NACA0012 with trailing-edge flap by means of different wind tunnel measurements for $M = 0.5$, experimental data extracted from [69]. 76
3.23. Validation of the numerical setup for unsteady investigations using NACA0012 with trailing-edge: Exp IoA data extracted from [69], CFD Overflow data extracted from [75], CFD++ data extracted from [78]. 78
3.24. Variation of C_l over pitching period for the baseline case at $M = 0.4$, with $f_\theta = 7$ Hz and $f_\delta = 0$ Hz. 80
3.25. Variation of C_l over pitching period for the 1P case at $M = 0.4$, with $f_\theta = 7$ Hz and $f_\delta = 7$ Hz. 80
3.26. Variation of C_l over pitching period for the 2P case at $M = 0.4$, with $f_\theta = 7$ Hz and $f_\delta = 14$ Hz. 80
3.27. Variation of C_m over pitching period for the baseline case at $M = 0.4$, with $f_\theta = 7$ Hz and $f_\delta = 0$ Hz. 86
3.28. Variation of C_m over pitching period for the 1P case at $M = 0.4$, with $f_\theta = 7$ Hz and $f_\delta = 7$ Hz. 86
3.29. Variation of C_m over pitching period for the 2P case at $M = 0.4$, with $f_\theta = 7$ Hz and $f_\delta = 14$ Hz. 86
3.30. Variation of C_d over pitching period for the baseline case at $M = 0.4$, with $f_\theta = 7$ Hz and $f_\delta = 0$ Hz. 89
3.31. Variation of C_d over pitching period for the 1P case at $M = 0.4$, with $f_\theta = 7$ Hz and $f_\delta = 7$ Hz. 89
3.32. Variation of C_d over pitching period for the 2P case at $M = 0.4$, with $f_\theta = 7$ Hz and $f_\delta = 14$ Hz. 89
3.33. Velocity profile extraction locations on the airfoil surface: Upper surface probe locations A and B were positioned at $x/c = 0.1$ and $x/c = 0.25$, respectively. Lower surface probe locations C and D were positioned at $x/c = 0.1$ and $x/c = 0.25$, respectively. . . 91
3.34. Comparison of the pressure distribution c_p and velocity profiles over the airfoil surface during the unsteady downstroke and upstroke, as well as in the steady state at $\theta_0 = 4$ deg, for the baseline case for the reduced frequency $k = 0.045$ and Mach number $M = 0.4$. 92

3.35. Comparison of the pressure distribution c_p along the airfoil surface and velocity profiles during the unsteady downstroke and upstroke, as well as in the steady state at $\theta_0 = 4$ deg, when camber morphing with the frequency $f_\delta = 7$ Hz was synchronized with the pitch motion (1P case) for the reduced frequency $k = 0.045$ and Mach number $M = 0.4$. 92
3.36. Comparison of the pressure distribution c_p along the airfoil surface and velocity profiles during the unsteady downstroke and upstroke, as well as in the steady state at $\theta_0 = 4$ deg, when camber morphing with the frequency $f_\delta = 14$ Hz was applied simultaneous to the pitch motion (2P case)for the reduced frequency $k = 0.045$ and Mach number $M = 0.4$. 93
3.37. Comparison of blade displacement computed by the rotor CFD/CSD coupling and the equivalent BO105 model rotor models using CAMRAD II at an advancing ratio of $\mu = 0.15$. 100
3.38. Comparison between the thrust distribution computed by the rotor CFD/CSD coupling and the equivalent BO105 model rotor models using CAMRAD II at an advancing ratio of $\mu = 0.15$. 100
3.39. Comparison of target trim thrust against the CFD total rotor thrust T_{total} over simulated rotor revolutions for both passive and active rotors across coupling iterations at an advancing ratio of $\mu = 0.15$. 101
3.40. Variation in the absolute differences of collective pitch θ_0, lateral pitch θ_{1c}, and longitudinal pitch θ_{1s} for passive and active rotors across coupling iterations. 102
3.41. Comparison of rotor thrust T (integrated thrust F_z variation) at time step for passive and active blades across rotor revolutions, with each color representing a different CFD/CSD coupling iteration at an advancing ratio of $\mu = 0.15$. 102
3.42. Comparison of the section force $C_n M^2$ between the CFD/CSD coupling steps for the passive and active rotor at $\psi = 90$ deg at an advancing ratio of $\mu = 0.15$, with the green curve (Coupling 4) obscured by the red curve (Coupling 5). 103
3.43. Comparison of blade motion between the passive and active rotors across the rotor azimuth ψ at an advancing ratio of $\mu = 0.15$. 105
3.44. Distribution of the blade sectional thrust coefficient $C_n M^2$ over the passive and active rotor disk at an advancing ratio of $\mu = 0.15$. 107
3.45. Comparison of the sectional thrust coefficient $C_n M^2$ along azimuth ψ at $r/R = 0.5$ and $r/R = 0.75$. 107
3.46. Variation sectional thrust coefficient $C_n M^2$ over the blade radius for passive and active rotor at different azimuth angles ψ. 108
3.47. Distribution of the blade sectional drag coefficient $C_x M^2$ over the passive and active rotor disk at an advancing ratio of $\mu = 0.15$. 110
3.48. Variation of the chordwise force coefficient $C_x M^2$ along azimuth ψ at the radial station $r/R = 0.5$ and $r/R = 0.75$. 110
3.49. Comparison of the distribution of $c_p M^2$ over the upper surface for passive and active blades at different azimuth angles $\psi = 0, 90, 180$, and 270 deg. 113
3.50. Comparison of the sectional pressure distribution $c_p M^2$ along the blade span at $r/R = 0.75$ for passive and active rotors at azimuth angles $\psi = 0, 90, 180$ deg and 270 deg. 114
3.51. Comparison of the sectional pressure distribution $c_p M^2$ along the blade span at $r/R = 0.9$ for passive and active rotors at azimuth angles $\psi = 90$ and 180 deg. 114

3.52. Comparison of the vortex structures near to the passive and active rotors by means of the λ_2 criteria. . . . 116
3.53. Comparison of active and passive rotor wake structures using the vorticity isosurfaces with $\omega = 80$ 1/s. . . . 117
3.54. Comparison of vorticity distribution between passive and active rotors at slice A, extracted at $r/R = 0.5$. . . . 118
3.55. Comparison of vorticity distribution between passive and active rotors at slice B, extracted at $r/R = 0.9$. . . . 118
3.56. Comparison of the vortex structures passing near the vicinity of the advancing blade at $\psi = 90$ deg for the passive and active rotors by means of the magnitude of the vorticity. . . . 122
3.57. Comparison of the vortex structures passing near the vicinity of the retreating blade at $\psi = 270$ deg for the passive and active rotors by means of the magnitude of the vorticity. . . . 123
3.58. Comparison of the blade sectional thrust coefficient C_nM^2 distribution over the passive rotor disk, obtained using linear inflow, free wake, and CFD/CSD methods at an advancing ratio of $\mu = 0.15$. . . . 126
3.59. Comparison of the blade sectional thrust coefficient C_nM^2 distribution over the active rotor disk, obtained using linear inflow, free wake, and CFD/CSD methods at an advancing ratio of $\mu = 0.15$. . . . 126
3.60. Comparison of the blade sectional thrust coefficient C_nM^2 distribution at the blade section $r/R = 0.75$ over the rotor azimuth ψ, obtained using linear inflow, free wake, and CFD/CSD methods at an advancing ratio of $\mu = 0.15$. . . . 127
3.61. Comparison of the blade sectional drag coefficient C_xM^2 distribution over the passive rotor disk, obtained using linear inflow, free wake, and CFD/CSD methods at an advancing ratio of $\mu = 0.15$. . . . 127
3.62. Comparison of the blade sectional drag coefficient C_xM^2 distribution over the active rotor disk, obtained using linear inflow, free wake, and CFD/CSD methods at an advancing ratio of $\mu = 0.15$. . . . 128
3.63. Comparison of the blade sectional drag coefficient C_xM^2 distribution at the blade section $r/R = 0.75$ over the rotor azimuth ψ, obtained using linear inflow, free wake, and CFD/CSD methods at an advancing ratio of $\mu = 0.15$. . . . 128

B.1. Grid convergence study for the baseline airfoil and camber morphed airfoil with $\delta =$ 4 deg, basedon the grid resolutions listed in B.1 140
B.2. Comparison of pressure patterns for constant lift coefficient($C_l = 1.225$) of different morphed airfoils. . . . 140
B.3. Pressure patterns for different angle of attack of the morphed airfoil $\delta = 8°$. . . . 140

C.1. Evaluation of global deviations between unsteady CFD and CAMRAD II results with and without ONERA Edlin corrections of the case listed in Table 3.1. Dark colors show the integrated deviation of raw steady results from unsteady results, while light colors show the deviation of ONERA Edlin-corrected steady results from unsteady results. . . . 141
C.2. Comparison of the velocity contours for the baseline case at $M = 0.4$ and θ_{mean}. . . . 143
C.3. Comparison of the velocity contours for 1P case at $M = 0.4$ and θ_{mean}. . . . 143

C.4. Comparison of the velocity contours for 2P case at $M = 0.4$ and θ_{mean}. 143

D.1. Influence of RBF Base Points on Blade Deformation 146
D.2. Comparison of the lift, drag, and density residuals over the number of the revolutions for passive and active rotor. 147
D.3. Comparison of the $C_n M^2$, $C_x M^2$, and $C_y M^2$ between the CFD/CSD coupling steps for the passive and active rotor at $\psi = 90$ deg. 148

List of Tables

2.1. Input parameter for the one bladed CAMRAD II model. 29
2.2. Grid resolution and cell types used for the different blocks of the computational domain. 35
2.3. Actuation inputs used to determine the camber morphing deflection over the azimuth ψ for the active blades. 45
2.4. Rotor geometry and test conditions for the CFD/CSD and the BO105 equivalent models. 50

3.1. Overview of the investigated cases. 70
3.2. Input flight condition in the TAU CFD and CAMRAD II CSD simulations. 97
3.3. Trim conditions in CAMRAD II for the model used in CFD/CSD and the BO105 equivalent model. 98
3.4. Comparison of both aerodynamic forces and moments obtained by means of the trimmed DLR equivalent BO105 rotor and the CAMRAD II rotor model used for the CFD/CSD coupling. 99
3.5. Comparison of the passive and active blade motions: mean values and first harmonics of pitch, flap and lead-lag angles. 104
3.6. Comparison of the total required power for passive versus active rotors, obtained using linear inflow, free wake, and CFD/CSD methods at an advancing ratio of $\mu = 0.15$. 127

B.1. Grid resolution used for the convergence study. 139

1. Introduction

1.1. Motivation

The global commercial helicopter industry has experienced significant growth, tripling in size over the past decade. Notably, European manufacturers have increased their market share to 60% [82]. Despite recent economic challenges and volatility in the oil and gas sector, the helicopter market is projected to achieve sustained medium-to-long-term growth [82]. In order to retain Europe's leadership in the civil helicopter market, intensified focus on improving fuel efficiency and reducing greenhouse gas emissions in helicopter design is essential, aligning with the ACARE 'Flightpath 2050' strategy's goals for substantial reductions in human-caused climate impact and the growing consumer demand for efficiency [123].

Present helicopter rotor system designs face considerable limitations due to the wide range of operating conditions they must accommodate, leading to inevitable compromises in blade geometry and resulting in less than optimal efficiency across different flight conditions. Additionally, blades undergo a variety of operating conditions within a single rotation around the rotor shaft, ranging from high velocities and low angles of attack on the advancing side to lower speeds and high angles of attack on the retreating side. Ideally, the airfoil and blade shapes for these conditions should be different. However, engineers are currently forced to select a single blade geometry that represents a compromise between these conditions, thus constraining aerodynamic efficiency. This compromise leads to increased power requirements and fuel consumption for any given flight condition, contributing to higher emissions and environmental impact.

Optimizing helicopter blade performance across a wide range of demanding operational conditions presents a significant engineering challenge. This complexity is driven by the need to balance blade geometry for optimal performance in both hover and forward flight. The compromise inherent in current designs leads to inefficiencies, manifesting as increased power requirements, higher fuel consumption, and greater emissions. The development of morphing rotor systems represents a significant advancement in this area, offering the potential to dynamically adjust blade shapes in response to the specific aerodynamic demands of varying flight conditions, thus mitigating the need for compromise. The pursuit of enhanced rotor performance across a broad spectrum of operational scenarios is at the forefront of helicopter technology research. The rotor's aerodynamic environment is notably complex due to its unsteady and three-dimensional nature. Blade sections on conventional single main rotors are subject to diverse flow conditions, influenced by both the flight regime and their instantaneous position relative to incoming airflow. During hover, for example, inflow velocity increases towards the blade tips. In Contrast, in forward flight, blade sections on the advancing side of the rotor disk experience higher velocities than those on the

retreating side, necessitating cyclic adjustments in pitch angle by the pilot to maintain lift equilibrium. In high-speed forward flight, particularly, rotor blades on the advancing side can encounter Mach numbers exceeding 0.8, where compressibility effects introduce significant aerodynamic challenges, including wave-drag penalties, shock-induced flow separation, and increased vibratory loads [16, 53]. The primary objective under these conditions is to delay the onset of drag divergence to higher Mach numbers [16]. On the retreating side, with Mach numbers below 0.4, maintaining lift in the face of stall conditions becomes critical [16, 56]. The occurrence of dynamic stall, characterized by a leading-edge vortex sweeping across the blade surface, results in torsional stresses and significant power inefficiencies [56]. As a result, rotor systems optimized for specific local flow conditions tend to perform suboptimally in other conditions [74]. Traditional rotor designs, featuring passive blades that retain a fixed shape across different flight conditions, are limited to static modifications for optimization. In contrast, the active control of blade geometry, which involves dynamically altering blade shape during operation, has shown promise in enhancing performance and reducing vibrations.

1.2. State of the Art

To address the limitations imposed by conventional helicopter rotor designs, researchers have explored various active rotor concepts as potential solutions to the challenges posed by demanding and diverse flight conditions. These systems introduce the ability to dynamically adjust blade characteristics in response to changing conditions. This eliminates the need for compromises and enables significant improvements in power consumption, vibration reduction, and aeroacoustics. Among the concepts investigated to explore the potential of active rotor technology are individual blade control, active twist, trailing edge flaps, and combined morphing mechanisms. The following section will present the most relevant previous research focused on these promising systems.

1.2.1. Individual Blade Control

Conventional helicopters rely on swashplates for first-order harmonic pitch control throughout the rotor revolution. The advancements in actuator technology have revolutionized this approach, enabling independent pitch control for each blade at any point in its rotation. This allows for precise control of blade pitch to achieve specific aerodynamic loads and dynamic blade responses, fulfilling diverse design objectives. In the following are the most relevant studies that explored the application of IBCs for helicopter rotors. A comprehensive wind tunnel investigation was conducted at the NASA Ames Research Center's 40-by-80-Foot wind tunnel, as shown in Fig. 1.1a, to explore the influence of individual blade control (IBC) systems on the aerodynamics and aeroacoustics of a BO105 four-bladed hingeless rotor system. The testing procedure and measurement test data have been documented in [98, 51, 49, 50, 111]. This research was undertaken through a collaborative consortium involving various organizations including NASA Ames Research Center, ZF Luftfahrttechnik GmbH, the U.S. Army , DLR, and Eurocopter Deutschland GmbH. The key findings of the investigations conducted, were recently published in the NASA reports [47, 48].

The studies demonstrated a considerable potential of IBC in diminishing both Blade-Vortex Interaction (BVI) noise and hub vibration. Remarkably, in descent flight scenarios, the integration of 2/rev IBC with additional harmonic inputs resulted in reductions of BVI noise by 12 dB (equivalent to an 85% decrease) at relevant microphone locations. Simultaneously, this input achieved 75% reduction in the dominant 4/rev vibratory hub loads. Furthermore, the implementation of 2/rev IBC in high-speed forward flight conditions led to performance enhancements of up to 7%. Encouraged by the promising test results of the BO105 rotor with IBC, similar investigations were conducted also in the NASA Ames wind tunnel using the UH60 rotor [46, 84, 85]. Several actuation frequencies and schedules were used, as explained in [63] and shown in Fig. 1.1b. This research was a collaborative effort involving NASA, the US Army, Sikorsky, and ZFL. The investigations [46, 84] revealed that at an advance ratio of $\mu = 0.1$, the hub vibration was significantly reduced by up to 70% by applying 3/rev and 4/rev IBC input signals with specific amplitudes and phase shifts. Furthermore, a BVI noise reduction of 6 to 8 dB was obtained on the advancing side and a 10 dB reduction on the retreating side at an advance ratio of $\mu = 0.16$ by applying a specific 2/rev IBC input signal [85]. At higher speeds ($\mu = 0.41$), the application of an optimized 2/rev IBC input signal resulted in a maximum rotor power reduction of 5.1%, which corresponds to an 8.6% enhancement in the lift-to-effective drag ratio L/D [85]. Further flight tests [62, 11, 34, 10] investigated the potential benefits and challenges of applying IBC systems on real-world applications, using the CH-53G production helicopter. The studies demonstrated a 3 dB decrease in BVI noise during descent, a 6-7% reduction in power requirements at 130 knots, and a 30% reduction in pitch link loads at the same speed [62, 11]. Furthermore, applying 1/rev harmonic inputs with three vibration signals in the cosinus function yielded a 60% reduction in vibrations. Using 2/rev inputs yielded an even greater 84% vibration reduction, highlighting the potential of IBC for improving cockpit comfort [34].

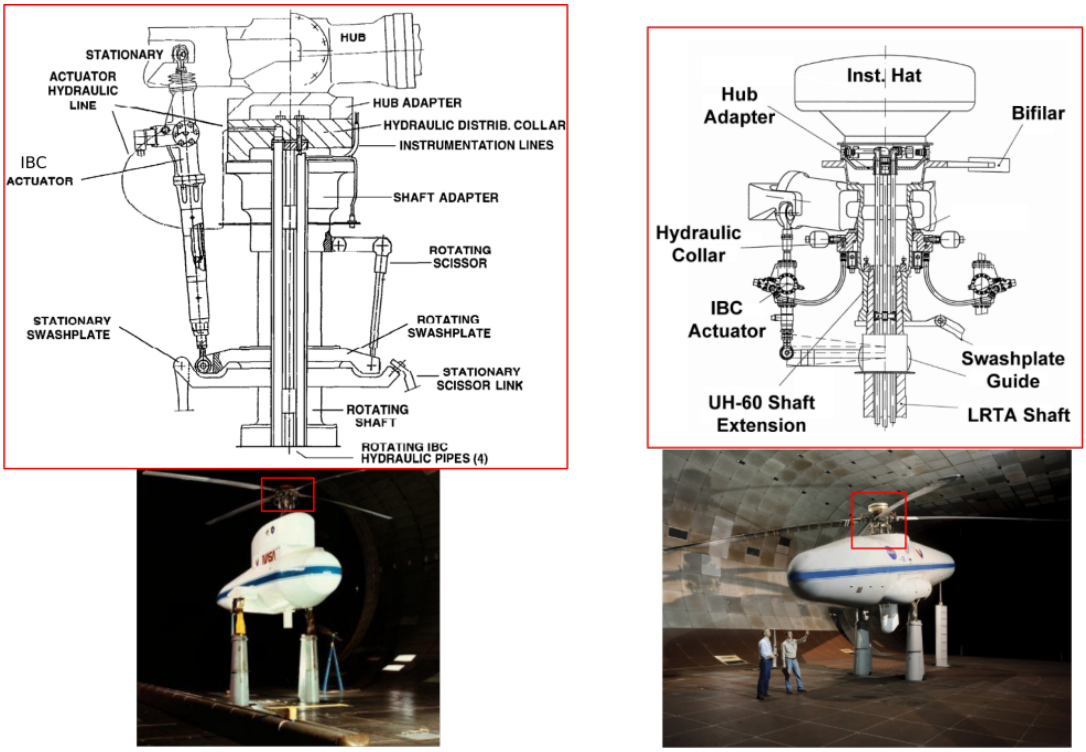

(a) Detail of the BO105 hub area showing IBC actuators[47].

(b) Detail of the UH60A hub area showing IBC actuators[85].

Figure 1.1.: BO105 and UH-60A rotor system installed with IBC actuators on the large rotor test apparatus in the NASA Ames Research Center 40-by 80-Foot wind tunnel.

1.2.2. Active Twist

Most helicopter rotor blades have a built-in twist, resulting in a varying angle of attack along the span. This twist remains constant for a given flight condition. Active twist technology, in contrast, dynamically adjusts the blade's twist profile for each rotor blade during flight, offering significant advantages in optimizing aerodynamic efficiency and reducing vibrations. The NASA/Army/MIT Active Twist Rotor (ATR) project provided valuable insights into the potential and challenges of active twist technology for helicopter vibration reduction through various studies [118, 20, 116, 117, 105]. Both wind tunnel tests (see Fig. 1.2a) and comprehensive numerical analyses using CAMRAD II demonstrated that active twist control significantly impacted all system loads [118]. Notably, it offered reductions in fixed-system loads ranging from 60% to 95%, depending on the flight condition and applied twist schedule [118, 116]. Closed-loop tests of the ATR rotor further confirmed the effectiveness of active twist, achieving a substantial reduction of vibrations across various flight conditions [105]. For instance, the normal shear component of vibrations caused by imperfect blade tracking was reduced by 70% with a 1/rev[1] controller. Additionally, simultaneous reductions in 1/rev and 4/rev normal force vibrations were achieved by using collective twist actuation

[1] The controller applies a signal with a period of one revolution (1/rev).

for the 1/rev component and a combination of longitudinal and lateral cyclic actuation for the 4/rev component [105]. A high-frequency active twist system for a full-scale UH-60A rotor was investigated in [53] using coupled Computational Fluid Dynamics (CFD)/Computational Structural Dynamics (CSD) analysis and lifting line theory. This study explored different input frequencies and schedules and demonstrated that performance improvements can be achieved by increasing lift generation on the advancing side, particularly in regions experiencing negative tip loading, without incurring additional drag penalties. The coupled CFD/CSD approach yielded higher than predicted improvements in lift-to-drag ratio (L/D) and power consumption when compared with the lifting line theory. For example, a 2/rev active twist schedule with a 2-degree amplitude and 180-degree phase shift resulted in a 4.7% increase in L/D and a 2.3% reduction in power consumption according to CFD simulations. In contrast, the lifting line theory predicted a smaller gain of 3.1% in L/D and a less significant power consumption reduction of 1.5% when compared with to the baseline rotor configuration. Furthermore, the study explored an advancing-side-only active twist strategy with a 6 degrees pitch-up actuation. This configuration displayed a remarkable increase in L/D of up to 8.6%, highlighting the potential for further performance enhancements.

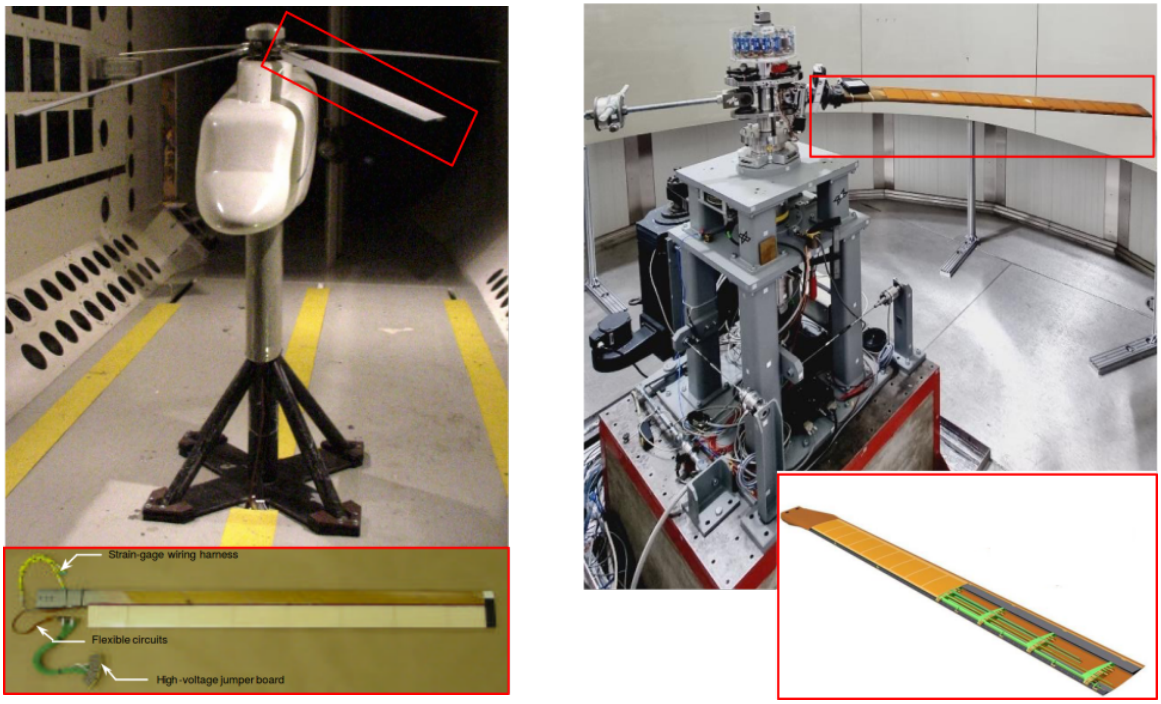

(a) ATR blade in the whirl tower from [117] with detailed rotor blade design[20].

(b) STAR blade in the whirl tower with detailed rotor blade design[27].

Figure 1.2.: Active twist systems used for the ATR and STAR research programs.

Within the STAR program, an international collaboration involving DLR, US Army, NASA, ONERA, KARI, Konkuk University, JAXA, Glasgow University, and DNW investigated the potential of active twist technology using a Mach-scaled rotor as depicted in Fig. 1.2b, resembling the BO105 model. This study employed various numerical approaches, including comprehensive analysis tools like CAMRAD II and S4, high-fidelity CFD/CSD simulations, and wind tunnel tests. Preliminary inves-

tigations explored different harmonic inputs for active twist control. The findings of these investigations, summarized in [27], demonstrated that during high-speed flight, power gains achieved with active twist were comparable to those obtained through the IBC system. This suggests that there is a potential to reduce either power requirements or vibration levels, although noticeable discrepancies exist in predictions across different methods. The maximum power reduction observed was 2.9%. Currently, the STAR2 program is building upon these findings to explore optimal input signals for active twist to minimize vibration, power consumption, and noise across diverse flight speed conditions.

1.2.3. Trailing Edge Flaps

Helicopter rotor blades can be equipped with active flaps along the trailing edge. These adjustable flaps dynamically vary their angle throughout the blade's rotation (azimuth) during flight, in order to optimize the aerodynamic characteristics of the blades and rotor vibration across varying conditions. In the FRIENDCOPTER project, a consortium of 34 research institutes and universities investigated the benefits of using trailing edge flaps to enhance cabin vibration reduction, noise mitigation, and power consumption efficiency. The project implemented piezoelectric active patches to avoid the use of discrete trailing edge flaps. These investigations were conducted using a variety of numerical tools for theoretical studies and were further validated through actual test flights. The results of the studies summarized in the final technical report [64], showed remarkable outcomes, including the possibility of achieving of up to 90% reduction in cabin vibrations and of up to 50% reduction in noise levels as predicted by simulations, which were confirmed by flight tests with EC130 and EC135 helicopters. Furthermore, the project highlighted a potential 6% decrease in power requirements during high-speed forward flight under optimal conditions for a highly loaded isolated rotor. The Boeing Smart Material Actuated Rotor Technology (SMART) program, a collaborative effort between DARPA, NASA, the Army, and Boeing, aimed to demonstrate significant reductions in noise, rotor-induced vibration and aerodynamic performance for a full-scale five-bladed bearingless MD900 helicopter rotor using piezoelectric actuators and shape memory alloys, as depicted Fig. 1.3a, to actively adjust the shape of a trailing edge flap in real-time. This adaptability allowed the rotors to be optimized for various flight conditions, including hovering, forward flight, and takeoff/landing. The investigations were conducted experimentally in the 40- by 80-Foot Wind Tunnel at NASA Ames [41] and also by means of several numerical studies [92]. In these investigations, Piezoelectric actuators, controlling a trailing edge flap at 75% chord ($0.75c$), were integrated along the rotor blade span from 74% to 92% rotor radius ($0.74R$ to $0.92R$). Different actuation signals ranging from 1/rev to 5/rev were tested. Results of these studies showed reductions of up to 6 dB from blade vortex interactions and in plane noise [109, 92] and reductions in vibratory hub loads of about 80%, with minor reduction in required power [72, 109]. Within the project ADASYS (Adaptive Dynamic Systems) the capability of piezoelectric materials to actuate the trailing edge flap was explored for a four-bladed hingeless rotor of the BK117/EC145 helicopter, as shown in Fig. 1.3b. The project was a joint effort between Eurocopter, European Airbus Defense & Space (EADS), and DLR [32, 33]. The flap system consisted of three identical trailing edge flaps with a chord of $0.15c$, placed adjacent to each other between the radual position $0.67R$ and $0.83R$. The flaps were driven by piezoelectric actuators [33, 100]. The achieved improvements ranged from 50% to 90% in the reduction of vibrations across various flight speeds, highlighting

the potential of active trailing edge flaps for helicopter vibration control [100]. Several research efforts [96, 52, 54] explored the application of trailing edge flaps to enhance L/D and vibration characteristics of the UH-60A rotor. For instance, a comprehensive analysis from University of Maryland [96] using the UMARC code assumed that the trailing edge flap was located between $0.65R$ and $0.75R$, starting from $0.85c$ up to the trailing edge. These inputs effectively reduced the negative loading on the advancing blade, thereby alleviating the load on both the front and rear portions of the rotor disk. The study showed that power reductions in the order of 2% at a flight advance ratio of $\mu = 0.3$ and between 4% and 5% at $\mu = 0.4$ were achieved with half peak-to-peak (HPP) actuation amplitudes ranging from 5 to 10 degrees. Additionally, it was demonstrated that employing a combination of 1, 2, 3, 4, and 5/rev actuation inputs could lead to a power reduction of 1.5% and a substantial decrease in in-plane vibratory loads of over 50%. A further study [52] investigated the impact of varying trailing edge flap width and length on high-speed forward flight with $\mu = 0.368$ using different actuation schedules. Three radial positions were examined: inner section ($0.625R$ - $0.775R$), middle section ($0.675R$- $0.825R$), and outer section ($0.725R$ - $0.875R$). The effect of trailing edge flap chord width was studied using three variations: 10%, 15%, and 20% of the chord. To study the effect of trailing edge flap chord width, UH-60A helicopter blades with the considered flap configurations were analyzed using CFD/CSD coupling under actuation schedules of 1/rev, 2/rev, and non-harmonic. Here, the code WIND-US-HELI was used as the high-fidelity CFD solver and RCAS as CSD solver. The results of the study showed that while the 1/rev actuation signal was applied, the highest increase in L/D was 7.3% with a 3.3% reduction in rotor power, and a 41% decrease in hub vibration. This was achieved when the trailing edge flap was located between $0.65R$ and $0.75R$, and having a length of 10% chord width. For the 2/rev actuation signal, the same L/D was achieved with 2.3% reduction in power, and of up to 30% reduction in hub vibratory loads, as the trailing edge was placed between $0.625R$ and $0.775R$ and with length of $0.10c$ along the trailing section. While applying the nonharmonic deployment (advancing side 2.67 degrees and retreating side 6.67 degrees), the same improvement in L/D was achieved using a trailing edge flap located between $0.50R$ and $0.90R$, starting from $0.85c$ until the trailing edge. The improvement of L/D was observed alongside a 3.3% reduction in power, and of up to 54% decrease in hub vibratory loads [52]. Building upon their previous work, the authors of [54] used the same CFD/CSD coupling framework to further explore the impact of a gap between the UH60-A blade planform when a trailing edge flap was integrated. Their study separated and analyzed the effects of span and chord gaps on rotor lift to drag ratio L/D in comparison to the baseline configuration. Notably, span gaps exhibited less impact on enhancing L/D than chord gap. Furthermore, the findings were compared to an investigation featuring a fully integrated trailing edge in the UH60 blade. This comparison demonstrated that a fully integrated trailing edge significantly enhanced the lift-to-drag ratio (L/D) when compared to blades with span gaps, chord gaps, and the baseline configuration.

(a) Boeing SMART rotor with active trailing-edge flaps in the NASA Ames wind tunnel [41].

(b) First flight of the BK117 helicopter with active trailing edge flaps [100].

Figure 1.3.: Active trailing-edge flap used for the Boeing SMART rotor and BK117 helicopter.

The potential of active trailing edge flaps to reduce power consumption, vibration, and noise in helicopters remains an active area of research. Recently as part of the European Clean Sky program, Leonardo developed a full-scale demonstrator featuring an active trailing edge flap system powered by piezoelectric actuation. This demonstrator, presented in [108], aimed to assess the capabilities and limitations of two active flap configurations on the AW139 rotor blade, positioned along the span section $0.525R - 0.675R$ and the section $0.833R - 0.90R$ respectively. Preliminary results indicated that the active blade could achieve a maximum thrust increase of up to 7% and a maximum L/D enhancement of 2-9% depending on flight conditions. These preliminary findings serve as a valuable foundation for future flight tests, where various actuation input signals (4, 5, and 6/rev) will be employed to conduct frequency sweeps for blade mode identification and vibration loads and L/D [108].

1.2.4. Multi-Morphing Mechanisms

To overcome the limitations of fixed-shape blades in diverse and demanding flight conditions, helicopters can integrate various morphing structures.

This allows to apply different active mechanisms to adjust the blade shape to achieve specific design target, e.g. reduction of required power or vibration. This enables exploring of the potential of both individual morphing mechanisms and their combined effects across a range of scenarios. Recently, six partners across Europe – University of Bristol, Centro Italiano Ricerche Aerospaziali, German Aerospace Center, Delft University of Technology, Technical University of Munich and Swansea University collaborated under the Horizon 2020 program to tackle the challenging task of morphing helicopter blades within the SABRE (Shape Adaptive Blades for Rotorcraft Efficiency) project. The objective of this project was to push the boundaries of current state of the art by combining expertise from diverse disciplines and exploring six distinct research concepts: SMA twist, inertial twist, FishBAC, TRIC, linear chord extension, and active tendons, as shown in Fig.

1.4a. The morphing mechanism was subjected to a wide range of frequencies, including 1/rev, 2/rev, and various harmonic input combinations. The aim of these investigations was to assess the mechanism's potential for reducing power consumption, NOx, and CO2 emissions while simultaneously exploring its impact on vibration and noise generation. For this purpose, multiple-fidelity numerical tool chains were developed and employed to explore the design space of each morphing concept and gain preliminary understanding of the resulting rotor dynamics. Subsequently, wind tunnel and whirl tower tests were conducted on selected mechanisms to validate their structural response under applied aerodynamic forces and moments. The Technical University of Munich (TUM) investigated the capabilities of the FishBAC concept (shown in Fig. 1.4b) as an active camber mechanism developed by the University of Bristol and Swansea University. The morphed camber was applied continuously from the $0.75c$ until the trailing edge of the blade. As demonstrated in [5], applying FishBAC morphing also from $0.75c$ to NACA23012 and SC1094R8 rotor airfoils achieved higher maximum lift coefficient ($C_{l,max}$) at $M = 0.4$ compared to a trailing edge flap. Furthermore, the FishBAC approach yielded a superior overall lift-to-drag ratio (C_l/C_d). Within the SABRE project, various camber morphing frequencies and schedules were explored, including quasi-static, 1/rev, 2/rev, and combined harmonic input approaches. Additionally, the impact of varying the active section size across the blade span was evaluated, with different morphing schedules being optimized for diverse scenarios. In these studies, the isolated rotor of a BO105 helicopter was considered as a baseline to evaluate the impact of different active camber schedules on the required power, vibration, and noise emissions at various flight speeds. The benefits of active camber morphing on various flight conditions were investigated using the CAMRAD II and a free wake inflow model in [68]. The width of the active camber section, actuation frequency, and schedules were varied for hovering to high-speed flight ($\mu = 0.35$), with results compared to a baseline rotor. In the hovering condition, the best reduction in required power, 8% less than baseline, was achieved with quasi-static camber deflection $\delta = 5.4$ deg applied along the blade span from $0.22R$ to $0.90R$ of the blade radius. Similarly, a gain of 7.9% in required power was achieved in high-speed forward flight at $\mu = 0.35$ using the same active camber section and by means of the combination of 1/rev and 2/rev actuation input signal. Additionally, at high forward speeds, a 25% reduction in peak-to-peak pitch link loads was achieved in combination with the power reduction. The same CAMRAD II models of the active rotor used in [67] were coupled with PWS-WOWOP [70] to evaluate aeroacoustic noise and vibration alongside power at various flight speeds between $\mu = 0.05$ and $\mu = 0.35$. This investigation revealed that active camber morphing can achieve a combined reduction in rotor noise, power, and hub vibration, but only at low advance ratios of $\mu = 0.10$ and $\mu = 0.15$. Moreover, active camber cases that led to reduced required power also resulted in noise reduction for all advance ratios between $\mu = 0.05$ and $\mu = 0.35$.

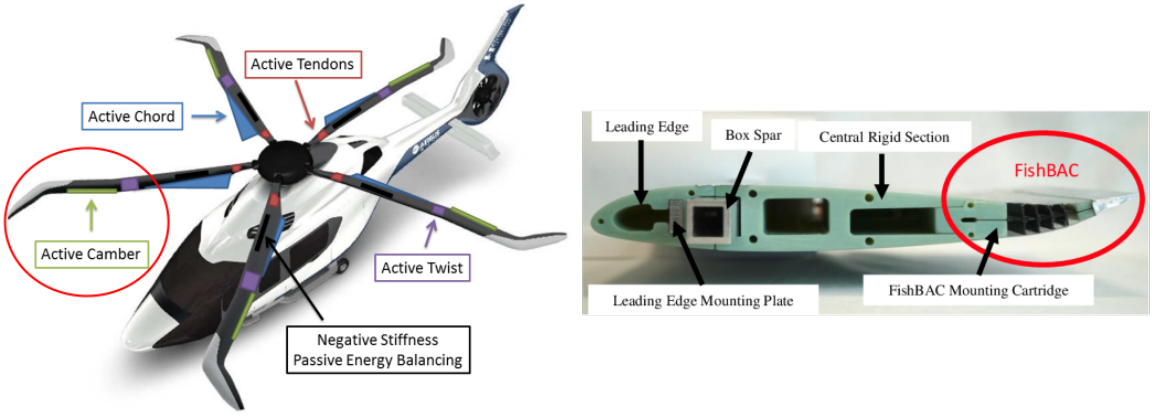

(a) Multi-morphing rotor concept presented within the SABRE project[95].

(b) Active camber morphing based on the FishBAC concept[99].

Figure 1.4.: Illustration of the SABRE project's multi-morphing rotor vision and the investigated active camber morphing concept.

1.3. Objectives of the thesis

A key aspect of the SABRE project's comprehensive analysis is to accurately model the aerodynamics of the active camber morphing rotor. Existing analysis tools such as CAMRAD II and Dymore rely on airfoil tables containing aerodynamic coefficients C_l, C_d, and C_m for the different blade sections, modeled as panels, at various Mach numbers and angles of attack. These coefficients are obtained through steady CFD solvers. Prior to the SABRE project, the FishBAC concept had not been explored as a camber morphing mechanism for helicopter blades. Consequently, no published airfoil tables existed for the specific camber-morphed blade sections relevant to this project. To address this gap, airfoil tables were generated for morphed sections with deflections ranging from -2 deg to 12 deg for Mach number ranging from 0.2 to 0.9. At each Mach number, the angle of attack was varied from -10 deg to the static stall angle for each prescribed airfoil shape. Within the scope of this thesis, steady CFD simulations were conducted to evaluate the impact of camber morphing on the aerodynamic characteristics of a baseline airfoil. The SABRE project also investigated 2D unsteady effects not captured by the static tables, in order to gain a deeper understanding of the FishBAC concept's aerodynamic behavior. This analysis quantified discrepancies between steady and unsteady performance, and uncertainties introduced when using static airfoil data. The SABRE project took computational analysis a step further by developing a high-fidelity coupled CFD/CSD framework within the project. This framework was achieved by coupling the structural dynamics capabilities of CAMRAD II with the 3D compressible Navier-Stokes finite volume CFD solver TAU. This enabled the investigation of previously unresolved three-dimensional, unsteady, and non-linear aerodynamic effects, such as those arising from dynamic actuation camber morphing. Thus, the framework provided insights, for example, into how rotor wake structures vary over the azimuth due to this morphing and allowed for accurate prediction of blade-vortex in-

teractions (BVI), which are inherently three-dimensional and transient phenomena. Furthermore, the three-dimensional aerodynamic loads from the CFD/CSD coupling can be used to replace the aerodynamics models within the comprehensive analysis tools. This high-fidelity approach unlocks further investigations, enabling accurate analysis of vibration, aeroacoustics, and even approximations of NOx and CO2 emissions. In line with the SABRE project's objectives, this thesis tackles the central question of how active camber morphing using the FishBAC concept impacts the aerodynamics of helicopter blades. This main objective was addressed through three different scientific questions, which were investigated using a variety of fidelity levels, starting with 2D steady CFD analysis for prescribed camber morphed airfoils and progressing to high fidelity coupled CFD/CSD simulations of isolated rotors featuring active camber morphing blades. To address the central scientific question of this thesis, the results chapter explores the following key questions that serve as the core of each section:

- **How do the 2D steady-state aerodynamic coefficients used in comprehensive analysis tools like CAMRAD II or Dymore change when the blade section undergoes camber morphing?** The first section explores the impact of camber morphing on airfoil aerodynamics using 2D steady-state CFD simulations in TAU. Starting with the NACA23012 airfoil with a tab as the baseline, various prescribed morphed camber airfoil shapes were analyzed at Mach numbers 0.4 and 0.6 across a broad range of rotor-relevant angles of attack. The aerodynamic characteristics of these morphed airfoils, including lift coefficient C_l, drag coefficient C_d, pitching moment coefficient C_m, pressure coefficient c_p, and center of pressure x_{cp} were compared to the baseline to assess the effectiveness of camber morphing for aerodynamic performance improvement, expressed as C_l/C_d.

- **Do 2D steady-state aerodynamic coefficients provide sufficient accuracy when approximating the aerodynamic loads on a camber-morphing blade section undergoing simultaneous pitching?** The second section investigates the discrepancies between steady and unsteady aerodynamic effects during combined camber morphing and pitching. It directly compares steady aerodynamic coefficients extracted from CAMRAD II's airfoil tables at Mach 0.4 with unsteady coefficients computed for a 2D airfoil undergoing synchronized pitching and dynamic camber morphing at each time step within an unsteady TAU solver. Notably, the ONERA-Edlin model is integrated into the comprehensive analysis to adjust steady-state coefficients and account for unsteadiness. This comprehensive approach aims to identify potential shortcomings and discrepancies that arise when unsteady effects are modeled within conventional rotor aeromechanics analysis codes. For this purpose, the BO105 helicopter main rotor airfoil NACA23012 was used as the baseline. It was pitched at 7 Hz, and the dynamic camber morphing was applied at two distinct frequencies: 7 Hz and 14 Hz. The analysis evaluated airfoil coefficients, pressure distribution, and velocity profiles perpendicular to both the lower and upper surfaces, providing a detailed understanding of the aerodynamic interactions under these conditions.

- **How does dynamic actuation of the camber morphing affect the flow field of an isolated four-bladed rotor?** The third section presents a high-fidelity and extensible CFD/CSD loose coupling approach developed for passive and active rotor blades. The capability of this CFD/CSD coupling approach was demonstrated by means of a passive and an active four-bladed isolated rotor. The camber morphing section was integrated between 35% and 85%

of the rotor radius, incorporating a linear transition region between the passive and fully active sections of the blades. For the active rotor, a non-harmonic actuation schedule was applied, previously shown to reduce rotor power requirements in comprehensive analysis studies [65, 66, 67]. At every time step, the camber of the active rotor blades was morphed in addition to the rigid blade motion – pitch, lead-lag, and flap. This analysis focuses on high-fidelity aerodynamic aspects not captured by traditional comprehensive analysis tools. Specifically, it investigates the variations in thrust and drag distribution, blade surface pressure, blade-vortex interaction, and wake structure resulting from dynamic camber morphing. Additionally, the results obtained with the CFD/CSD coupling approach for both active and passive rotor were compared with standalone comprehensive analysis results (CAMRAD II) using free wake and linear inflow models to highlight the differences in fidelity level between these investigation approaches.

Previous investigations of Fishbone Active Camber (FishBAC) technology have primarily relied on either low-fidelity methods such as comprehensive analysis tools (e.g., CAMRAD II) or simpler 2D steady-state aerodynamic methods to explore similar scientific questions. This study aims to broaden the understanding of FishBAC's impact on active helicopter rotor aerodynamics by employing a different level computational modeling strategy that utilizes both low and high-fidelity methods. This approach allows for a more detailed analysis compared to previous studies with limitations. In this thesis, the influence of FishBAC is investigated on both isolated airfoils (2D) and complete rotor configurations (3D), incorporating trimmed rotor dynamics. Additionally, unlike prior investigations, this work expands the scope of analysis to encompass the structure of the rotor wake, the interactions between blade vortices, and the distribution of pressure across the blade surface as FishBAC morphing is activated. By comparing the aerodynamic characteristics of a FishBAC-equipped active rotor to a passive rotor under identical conditions, this research seeks to unlock valuable insights regarding the potential benefits of FishBAC technology. This knowledge will ultimately contribute to future rotorcraft design.

2. Methodology

2.1. Theoretical Principles

This chapter presents the key aspects of the numerical simulations conducted to address the scientific questions explored in this thesis. The chapter focuses on the numerical solvers and the specific numerical discretization techniques applied and highlights the assumptions and mathematical models used within the numerical solvers. A comprehensive explanation of the grid strategies used for both 2D grids and full-resolution blades is presented, along with the grid deformation methods implemented for 2D and 3D grids. Additionally, the workflow of the developed CFD/CSD coupling for rotor trim in CFD simulations and the simplifications made for the rotor model in the CSD part are presented.

2.1.1. Methods and Capabilities of the CFD Solver TAU

The TAU software developed by the German Aerospace Center (DLR) was used to solve the fluid dynamics problems addressed in this dissertation. The selection of TAU was driven by multiple studies that explored dynamic stall on pitching airfoils [97, 35, 60, 61] and other successful investigations for helicopter simulations [93, 103, 73, 110].

TAU is a comprehensive finite volume Computational Fluid Dynamics (CFD) code, designed to solve the compressible Navier-Stokes (NS) equations operating on a single core or in parallel. In this thesis, the CFD simulations were conducted with the TAU-2020.1.0 version and the choice of TAU solver was also motivated by its adaptable operational capabilities. It offers different utilities, including pre-processing, solving, overset grid method (Chimera), grid deformation, and adaptation. These utilities can be either used as a stand-alone executable code or controlled using a Python scripting environment. This enables the software to model diverse physical problems and enhances the capacity to automate and command simulation procedures. Moreover, TAU supports a wide range of methodologies to solve the compressible Navier–Stokes. This includes advanced approaches like large-eddy simulation (LES) and detached-eddy simulation (DES), alongside established methods like unsteady and steady Reynolds-Averaged Navier-Stokes (URANS/RANS). Further flexibility comes from a diverse set of turbulence models. Additionally, TAU's overset grid functionality, also known as Chimera grids, allows for modeling periodic rigid motion of a computational domain relative to specific references. This feature is particularly useful for simulating the movement of physical components, such as rotorcraft blades, where overlapping grids enable relative motions between different parts of the mesh. For non-periodic motion, TAU uses a grid

deformation technique. The prescribed grid deformation, applied relative to the primary grid, is saved as scattered data. This data is then used to deform the grid using Radial Basis Function (RBF) interpolation.

The present work adopted the Unsteady Reynolds-Averaged Navier-Stokes (URANS) approach to numerically solve the Navier–Stokes equations. This mean that, when the solution is assumed to be time independent, the time derivatives are zero, and the equations simplify to the steady-state Reynolds-Averaged NavierStokes (RANS) equations. In the URANS and RANS equations, the instantaneous fluid velocity and pressure are decomposed into a mean (time-averaged) component and a fluctuating component. The process of time-averaging the non-linear terms in the Navier-Stokes equations introduces the Reynolds stress term which represents how turbulence affects the overall flow. The URANS equations for compressible flow, as addressed in TAU [37], are formulated as follows:
Mean continuity equation:

$$\frac{\partial \overline{\rho}}{\partial t} + \frac{\partial}{\partial x_j}(\overline{\rho}\,\overline{u_j}) = 0 \tag{2.1}$$

Mean momentum equation:

$$\frac{\partial}{\partial t}(\overline{\rho}\,\overline{u_i}) + \frac{\partial}{\partial x_j}(\overline{\rho}\,\overline{u_i}\,\overline{u_j}) = -\frac{\partial \overline{p}}{\partial x_i} + \frac{\partial \tau_{ij}}{\partial x_j} - \frac{\partial \overline{\rho u_i' u_j'}}{\partial x_j} \tag{2.2}$$

In these equations, $\overline{\rho}$, $\overline{u_i}$, and $\overline{p}$ represent the time-averaged density, velocity, and pressure. The Reynolds stress tensor, represented by the term $\overline{\rho u_i' u_j'}$, cannot be directly solved from the available information and needs to be approximated. The challenge of approximating the Reynolds stress tensor in compressible flows is known as the closure problem. To address this and approximate the terms $\overline{\rho u_i' u_j'}$, the Boussinesq hypothesis, adapted for compressible flows, is applied. It aims to linearly correlate the Reynolds stresses with the mean rate of strain, incorporating adjustments for density variations:

$$\overline{\rho u_i' u_j'} = -\overline{\rho}\,\nu_t \left(\frac{\partial \overline{u_i}}{\partial x_j} + \frac{\partial \overline{u_j}}{\partial x_i} - \frac{2}{3}\delta_{ij}\frac{\partial \overline{u_k}}{\partial x_k} \right) + \frac{2}{3}\overline{\rho}\,k\delta_{ij} \tag{2.3}$$

Here, ν_t denotes the turbulent viscosity and k the turbulent kinetic energy which can be solved using turbulence models to close the system of equations.

2.1.1.1. Turbulence Modeling

In this thesis, the Spalart-Allmaras SA-neg turbulence model is used due to its demonstrated robustness and efficiency across diverse aerodynamic applications, as referenced in [102]. Notably, the model has proven particularly suitable for simulations of isolated helicopter blades when using the TAU code. Studies like [101], exploring dynamic stall on a rotating blade, have shown that

while both SA and $k-\omega$ SST capture overall trends in sectional forces and moments, slight differences between the two models were obtained near the extreme values of forces and moments. Additionally, study [89] demonstrates the ability of the SA-neg model to accurately predict tip vortex trajectories, size, and strength in both ground-effect and coaxial counter-rotating hover scenarios, comparable to experimental data and other models such as SST-SAS, SSG/LRR-ω.

The SA-neg model solves a only single transport equation for the turbulent viscosity ν_t. This model does not solve a transport equation for the turbulent kinetic energy k, unlike other eddy-viscosity turbulence models. In regions with positive turbulent viscosity ($\nu_t > 0$), the SA-neg model produces results identical to the SA-Standard model. However, when ν_t becomes negative, the model uses alternative expressions for the production, destruction, and diffusion terms compared to the SA-Standard model. These modifications enable the model to handle negative ν_t values without compromising numerical stability [28]. Moreover, the turbulent layer is fully resolved over the entire viscous surfaces without using any wall functions. A detailed description of the implemented SA-neg model in TAU can be found in [28].

2.1.1.2. Spatial and Temporal Discretization

All investigations presented in this thesis were computed using the second-order central scheme for spatial discretization and the implicit second-order backward Euler scheme for temporal discretization. This choice is motivated by the reliable results achieved with these schemes in previous studies of isolated rotor blades using the TAU code [39, 101, 89].

Spatial discretization:

In the following, the settings for the second order central scheme used in this study are presented. The convective mean flow flux is calculated using the "Flux of Average" method, while the convective flux for the turbulent term is computed using the second-order Roe scheme `Roe2nd`. Matrix dissipation is chosen as the preferred dissipation scheme. For three-dimensional investigations involving rigid body motion of the blade, the parameter `Compute exact whirl flux` is activated, to include an additional flux term which is integrated over the control volume surface. More details about the implementation of these schemes are provided in [28].

Temporal discretization:

The implicit second-order backward Euler scheme offers the advantage of allowing larger time steps compared to explicit methods. This translates to a significant reduction in the number of time steps required for unsteady simulations, leading to faster computation time. Moreover, a dual-time-stepping is used for all unsteady simulations. This approach transforms each physical time step into a pseudo-stationary problem, and unlocks the power of acceleration techniques typically used for steady-state problems, such as local time stepping. As a result, the backward Euler scheme not only allows a substantial computational cost saving but also delivers numerical stability. More insights into dual time stepping and the implementation of the backward Euler scheme are found in [28].

2.1.1.3. RBF Method for Grid Deformation

When modeling motion involving complex shape transformations which cannot be modeled as rigid body motion, such as active camber concepts, the computational grid has to be adjusted during the simulation. In the TAU solver, the Radial Basis Function (RBF) approach is used for this purpose. The RBF method is used in hybrid-unstructured grids to ensure efficient mesh deformation. This technique ensures that the deformed meshes maintain high quality, in particular orthogonality near their boundaries [115]. Moreover, connectivity data are not required for this method. This allows the modelling of flexible and arbitrary motions. For further information are detailed in [7].

The RBF method involves polynomial interpolation of a displacement vector field, which is used to determine each deformed node within a certain volume mesh related to specific defined boundaries, defined as `RBF radius zero weight` in TAU. To enable independent grid deformation for specific groups of surfaces and volumes, TAU offers the ability to define separate displacement fields through `RBF groups`. This allows, for example, for applying unique grid deformations to individual helicopter rotor blades within the same simulation. For every `RBF group`, the displacement field is defined through coordinates of the control points x,y, and z from the undeformed corresponding grid surface and their respective relative displacement vectors Δx, Δy, and Δz needed to obtained the deformed grid. These have to be defined in a scattered-data file for each `RBF groups` and do not have to include all the grid surface points. The format of these data files is as follows:

```
 7927 #Number of control points
 #       x             y             z          Δ x           Δ y           Δ z
2.021465e-01 3.743552e+00 2.451333e-03 1.818464e-05 0.000000e+00 -1.582787e-03
2.022088e-01 3.743552e+00 2.337788e-03 1.075224e-05 0.000000e+00 -1.586560e-03
2.022357e-01 3.743552e+00 1.597565e-03 -3.691536e-05 0.000000e+00 -1.586758e-03
2.022401e-01 3.743552e+00 1.927372e-03 -1.571099e-05 0.000000e+00 -1.587725e-03
1.024735e-01 3.779339e+00 1.483054e-02 2.063816e-04 0.000000e+00 -7.260407e-07
1.237581e-01 3.779339e+00 1.258943e-02 1.717117e-04 0.000000e+00 -6.081233e-07
 .
 .
 .
```

The deformation routine in TAU is divided into three steps:

- **Calculation of wall distances:**
  For each RBF group, the nearest wall distance is calculated for all points within the associated volume mesh and saved to a separate file, such as "Blade1Distance.nc". The computed nearest wall distances are used to determine the magnitude of the deformation depending on the `RBF radius full weight` and `RBF radius zero weight` defined for each of the `RBF groups`. In case, the primanry mesh(undormed mesh) and its boundary markers do not change, the wall distance file can be reused for the further grid deformation, as explained in [42]

- **Determination of RBF equation systems:**
  The theoretical foundation of this method rests on the following interpolation function, as explained in [26]:

$$s(\vec{x}) = \sum_{j=1}^{n_b} \alpha_j \phi(||\vec{x} - \vec{x}_{bj}||) + p(\vec{x}), \tag{2.4}$$

  where $\vec{x}_{bj}$ represents a point from the grid surface and $p(\vec{x})$ represents a linear polynomial of the form $p(\vec{x}) = \beta_1 + \beta_2 x + \beta_3 y + \beta_4 z$. Additionally, ϕ represents the used radial basis function (RBF), with its argument being the Euclidean norm of $\vec{x} - \vec{x}_{bj}$. The coefficients α_j and β_j can be determined by solving the following system of equations:

$$\begin{bmatrix} \vec{d}_b \\ 0 \end{bmatrix} = \begin{bmatrix} M_{b,b} & P_b \\ P_b^T & 0 \end{bmatrix} \begin{bmatrix} \vec{\alpha} \\ \vec{\beta} \end{bmatrix}, \tag{2.5}$$

  where $\vec{d}_b = [\Delta\alpha_{b_1} \ ... \ \Delta\alpha_{b_n}]^T$ is the vector that defines the translation of the control base points. $M_{b,b}$ is an $n_b \times n_b$ matrix which is populated with the RBF values $\phi_{b_i b_j} = \phi(||\vec{x}_{bi} - \vec{x}_{bj}||)$, with n_b being the number of base points. The P_b is an $n_b \times 4$ matrix which contains the control base points in the following form $[1 \ x_{b_j} \ y_{b_j} \ z_{b_j}]$. The solution of the system of equations 2.5 can be obtained by inverting the matrix $M_{b,b}$. Further details on this can be found in [26, 42].

- **Calculation of point displacements:**
  After solving of the system of equations, the interpolation function 2.4 can be applied at any mesh point in the RBF group.

Moreover, the following input parameters affects the grid deformation:

```
RBF radius full weight: 0.0
RBF radius zero weight: 0.3
RBF markers specifying group: 9,12,13
RBF maximum number of base points used: 8000
RBF name: volume-spline
```

The parameter `RBF radius full weight` defines the wall distance where the interpolation function $s(x)$ is fully applied. The influence of $s(x)$ on a mesh point gradually decreases beyond this radius, reaching zero at the `RBF radius zero` weight distance. This transition zone is determined based on the mesh surfaces specified through the parameter `RBF markers specifying group`. The `RBF maximum number of base points` parameter in TAU allows you to control the number of base points within an `RBF group`. This number significantly impacts the time required to solve the associated system of equations. While increasing the base points generally leads to a more accurate grid deformation, it also comes at the cost of higher computational time. Several radial basis functions (RBFs) can be used for deformation, including the `Thin Plate`, `Spline` and

`Volume Spline` functions, which are also implemented in TAU. In this study, the `Volume Spline` function is chosen due to its demonstrated superior accuracy and lower computational cost compared to other RBF options, as demonstrated in [40] for dynamically BO105 morphed blades using the FishBAC concept.

2.1.2. Methods and Capabilities of the CSD Solver CAMRAD II

CAMRAD II, developed by Johnson Aeronautics [58], is as a software package for comprehensive rotor aeromechanical analysis. It combines modeling approaches like multi-body dynamics, flexible beam elements, and airloads calculations with lifting line method and free wake, enabling the assesment of rotorcraft performance, stress, vibration and stability analyses. In this study, CAMRAD II was chosen to trim the 3D CFD simulation of the active and passive blades. This choice was mainly driven by the reliable results for CFD/CSD coupling, as demonstrated in different studies [77, 14, 6, 59, 17].

CAMRAD II enables simulations of wide range of operating conditions for rotorcraft, including forward flight, hover, and transition phases in both wind tunnel setup and free flight scenarios. Each major rotorcraft component, such as the main rotor, tail rotor, and fuselage, can be defined independently within CAMRAD II. This study modeled an isolated rotor configuration with four blades. The blade geometry is defined by the radius, chord, and twist profiles, with flaps whose deflection angle that can vary along the blade span. Structural characteristics of the elastic blades, such as mass distribution and stiffness properties such as flap bending stiffness (EI_x), lag bending stiffness (EI_z), torsional stiffness (GJ), axial stiffness (EA), and blade mass (m_b) can be provided along the blade span. However, the structural blade response can still be computed using either elastic or rigid beam analysis. In CAMRAD II, the calculation of induced velocity can be performed using various inflow models, including uniform inflow, linear inflow, or a free wake approach.

The blade aerodynamic forces and moments are computed using lifting line theory. This method relies on aerodynamic coefficients listed in a C81 table, also referred to airfoil table or lookup table. These coefficients define the lift, drag , and moment coefficients (C_l,C_d, and C_m respectively) of the airfoil as functions of angle of attack and Mach number. Two-dimensional lifting line models offer faster simulations compared to three-dimensional models, but this comes at the cost of reduced accuracy. To address this trade-off, CAMRAD II allows the incorporation of external aerodynamic loads, including unsteady three-dimensional CFD simulations, to improve the overall accuracy of its predictions. The differences between the lifting line forces and moments computed in CAMRAD II and the external forces and moments are stored in a delta table. CAMRAD II offers the capability to precisely adjust a rotor's state through its trim capability. This allows the model to be fine-tuned based on combinations of forces, moments generated by the rotor. The pitch, flap and lead-lag of the individual blades is determined based on the trimmed solution. Moreover, CAMRAD II addresses the lim itations of steady aerodynamic coefficients from the airfoil tables by incorporating various models to account for unsteady effects. These models provide correction functions that account for the influence of wake vortices and "added/apparent mass" effects on the aerodynamic forces acting on an oscillating airfoil sections. These effects, related to the inertia of the air and the acceleration related to the motion of airfoil [74]. Since the steady

airfoil tables are obtained using static airfoil simulations, the aerodynamic coefficients in the airfoil tables should be corrected. These models, such as ONERA EDLIN and Leishman-Beddoes, are based on the incompressible thin-airfoil theory incorporate separate formulations for modeling attached flow and separated flow cases [58]. They contain a number of empirical parameters to model the aerodynamic loads when the flow becomes seperated. The separated flow scenarios are usually used to model dynamic stall phenomenon . Additionally, CAMRAD II offers a suite of dynamic stall models, including those developed by Johnson, Boeing, and ONERA, to capture the non-linear and unsteady forces and moments generated by the leading-edge vortex.

2.2. Modeling 2D Steady Aerodynamics of Camber Morphed Airfoils

This section presents the methods used to evaluate the impact of camber morphing on the steady aerodynamic characteristics of a 2D airfoil in the result section 3.1. The workflow of the 2D steady-state simulations conducted within the TAU software suite is explained. The process of applying camber morphing, the generation of the grid, and the criteria used to assess grid quality during the simulations are all described.

2.2.1. Workflow of TAU Steady Simulations

The TAU steady RANS solver is used to compute aerodynamic coefficients of the baseline and camber morphed airfoils, discussed in the results section 3.1. A second-order backward Euler scheme and a central scheme are used for time and spatial discretizations, respectively. The flow is assumed to be fully turbulent throughout the analysis, with the Spalart-Allmaras (SA) one-equation model used for turbulence modeling. The steady simulations for prescribed camber morphed shapes cover a wide range of angles of attack, from -10 deg to the stall angle (α_{stall}), with an increment of $\Delta\alpha = 0.5$ deg. In the vicinity of the stall region, the step size is refined to $\Delta\alpha = 0.25$ deg for improved resolution. For every prescribed camber morphed case and baseline, the closest previous simulation was used as the starting point to ensure numerical stability. The angle of attack sweep is performed at various Mach numbers ranging from 0.2 to 0.9. Furthermore, the same workflow, numerical setup, and grid topology is used in the baseline and camber-morphed airfoil simulations in order to ensure consistency and minimize errors arising from numerical discrepancies. Methods:steadySetup , with an increment of $\Delta\alpha = 0.5$ deg

2.2.2. Definition of Camber Morphing

Figure 2.1 summarizes the relevant steps executed to generate the shape of the camber morphed airfoil. In the following, the steps involve in generating a 2D surface suitable for CFD simulations are explained. The process includes morphing the camber line and both upper and lower surfaces of the baseline airfoil. In the first part of step 1, the discretization of both the upper and lower surfaces is performed using Bezier splines. This is necessary because the baseline airfoil shape

is typically defined by a set of discrete, coarsely spaced points. This process aims to capture the curvature of airfoil accurately and achieve a smooth enclosed final shape. This process aims to eliminate significant kinks along the surface caused by the coarse resolution. This leads to a more well resolved geometric representation of the investigated airfoil. In the second part of step 1, the thickness distribution and the camber line of the baseline airfoil is approximated by approximating the vertical distance between the upper and lower surfaces. This computation involves the discretization of both the upper and lower surfaces along the same set of x coordinates and the normalization of x and y coordinates with chord length c. Subsequently, the baseline camber is defined as the line passing through the midpoint of the computed thickness t.

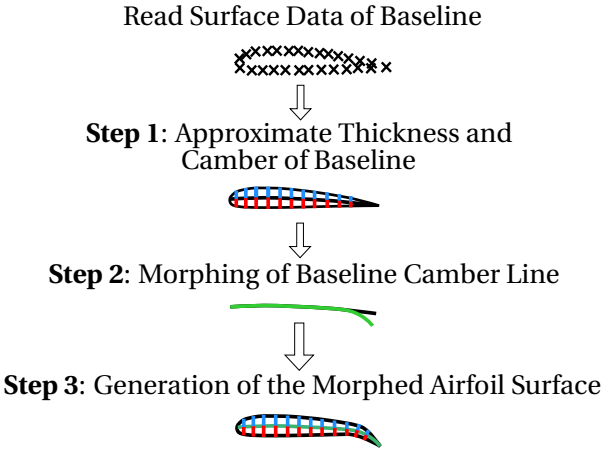

Figure 2.1.: Summary of the relevant steps to generate the morphed airfoils[5].

In step 2, the morphing of the baseline camber line is performed. The parabolic morphed camber of prescribed shapes is applied based on the Fish Bone Active Camber (FishBAC) concept introduced by Woods et al.[119]. Figure 2.2 illustrates the application of the parabolic camber to the baseline airfoil with the coordinates (x_b,z_b) along the morphing section between x_r and x_t. Here, x_r denotes the starting point of the camber morphing, and x_t represents its end point. For values of x_b in the range $[x_t, 1]$, the trailing edge of the baseline is assumed to be rigid. The mathematical representation of the applied parabolic camber is given by the equation presented in [5, 40]. The process of determining the coordinates x_{m_i} and z_{m_i} of the morphed camber involves discretizing the interval $[x_r, x_t]$ and defining x_{m_i} and z_{m_i} as follows:

$$x_{m_i} = x_{m_{i-1}} + (x_{bi} - x_{bi-1})\cos(\theta_{i-1}) \tag{2.6}$$

$$z_{m_i} = z_{b_i} + \tilde{z}_i \tag{2.7}$$

Here, the angle θ_{i-1} represents the slope of the polynomial at the point ($x_{m_{i-1}}$,$z_{m_{i-1}}$) in the $\tilde{x}, \tilde{z}$ baseline normalized coordinate system, as depicted in the close-up region of Fig. 2.2. The term $\tilde{z}_i$ denotes the incremental deflection in the z direction of the specific baseline point at $x_{b_i} \in [x_r, x_t]$ due to the parabolic camber morphing.

The reference coordinate system $\tilde{x}, \tilde{z}$ is defined across the morphing section, where $\tilde{z}_i$ corresponds to the deviation of a horizontal line bending into a third-order polynomial $\tilde{z}_i = k\tilde{x}_i^3$, representing the absolute difference between the baseline and the parabolically morphed camber. Conse-

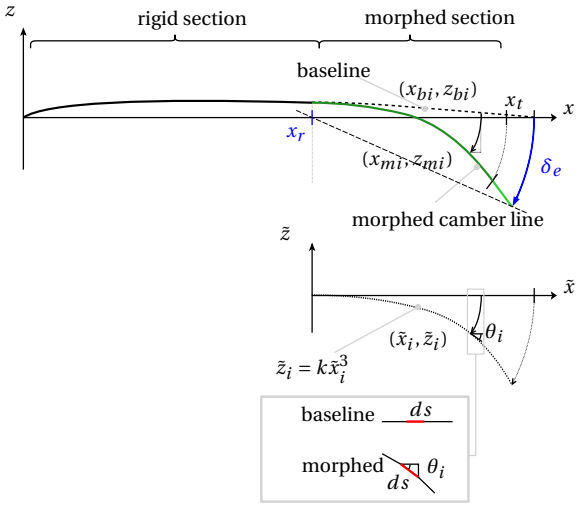

Figure 2.2.: Morphing of camber line based on the FishBAC concept. This figure is inspired from [5] and[40].

quently, the expression for z_{m_i} can be given as:

$$z_{m_i} = z_{b_i} + \tilde{z}_i \tag{2.8}$$

$$= z_{b_i} + k\tilde{x}_i^3$$

$$= z_{b_i} + k(x_{m_i} - x_r)^3 \tag{2.9}$$

In the coordinate system $\tilde{x}, \tilde{z}$, the slope angle θ_i is established by applying an infinitesimal increment in $\tilde{z}_i$ and $\tilde{x}_i$. The underlying concept of this approach involves adjusting the infinitesimal step size ds of the baseline in the x-direction using the cosine of the polynomial's slope angle θ_i as shown in Eq. 2.10 and Fig. 2.2. By using this approach, the stretching of the morphed camber in comparison to the baseline is avoided, ensuring that both maintain an equivalent length. The slope θ_i, which corresponds to the gradient at $(\tilde{x}_i, \tilde{z}_i)$ is progressively computed as:

$$\theta_i = \arctan(3k\tilde{x}_i^2) \tag{2.10}$$

$$= \arctan(3k(x_{mi} - x_r)^2) \tag{2.11}$$

From x_t onwards to the aft of the airfoil, the camber line is considered to be rigid and is calculated as a linear slope. Therefore, the computed morphed coordinates within this region are given by x_{m_i} and z_{m_i}:

$$x_{m_i} = x_{m_{i-1}} + (x_{b_i} - x_{b_{i-1}})\cos(\theta_t) \tag{2.12}$$

$$z_{m_i} = z_{m_{i-1}} + m_t \cdot (x_{m_i} - x_{m_{i-1}}) \tag{2.13}$$

where m_t is expressed as:

$$m_t = \frac{z_{m_t} - z_{m_{t-1}}}{x_{m_t} - x_{m_{t-1}}}, \tag{2.14}$$

and denotes the gradient of the linear segment that corresponds to the slope computed along the morphing interval $[x_r, x_t]$. Therefore, for each target deflection δ_e, the parabolic segment of morphed camber line in the interval $[x_r, x_t]$ is described through the equations 2.6 and 2.8. Over the range $[x_t, 1]$ the linear slope is defined using the equations 2.12 and 2.13. To solve the system of equations for each target deflection δ_e, the coefficient k is iteratively determined using a bisection algorithm. After determining the shape of the morphed camber line for a given δ_e, step 3 addresses the thickness distribution of the morphed airfoil. The thickness of the baseline is applied perpendicular to the camber line along the morphing section as shown in Fig. 2.3. Here, the half of the baseline thickness $t/2$, obtained from first step shown in Fig. 2.1, is used to generate the surface of the camber morphed airfoil. Thus, the upper and lower surfaces of the morphed airfoil is determined using the following equations:

$$\begin{aligned} x_{u_i} &= x_{m_i} - \frac{t_i}{2}\sin(\epsilon_i) \\ z_{u_i} &= z_{m_i} + \frac{t_i}{2}\cos(\epsilon_i), \end{aligned} \tag{2.15}$$

$$\begin{aligned} x_{l_i} &= x_{m_i} + \frac{t_i}{2}\sin(\epsilon_i), \\ z_{l_i} &= z_{m_i} - \frac{t_i}{2}\cos(\epsilon_i), \end{aligned} \tag{2.16}$$

where ϵ_i is the slope angle of the obtained morphed camber line, as suggested in [1].

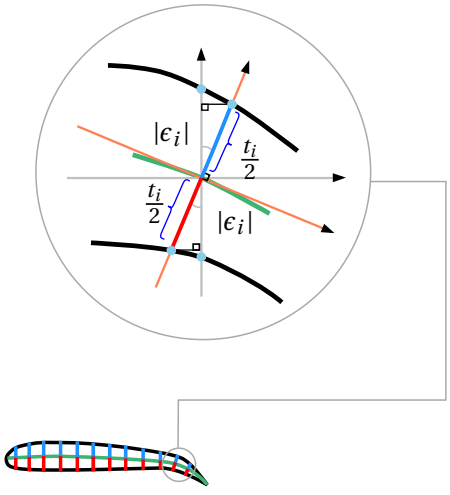

Figure 2.3.: Generation of the upper and lower surfaces of a camber morphed airfoil [5].

2.2.3. Grid Topology and Quality for 2D Airfoils

The resulting airfoil shapes are transferred to Pointwise [90] to generate a 2D structured O-grid with a radius equivalent to fifty times of the airfoil chord length ($50c$). To ensure the accuracy and reliability of the results, a consistent grid topology is adopted, and an automated process is implemented to generate the grids for both the baseline airfoil and the highly cambered airfoil. The height of the initial cell (1.2×10^{-6} m) is computed based on the free stream Mach number $M = 0.95$ and chord length $c = 0.27$ m to ensure that the dimensionless wall distance (y^+) is less than 1 up to $M = 0.95$. This approach allows for a fully resolved boundary layer over a wide range of simulations in the $0.2 \leq M \leq 0.9$ range. The leading edge radius is resolved with a fine cell length of approximately $7 \times 10^{-4}c$ in order to capture the high pressure gradient near to the stagnation point.

Same cell resolution is used for both the upper and lower surfaces with 143 points respectively and average spacing of $0.8 \times 10^{-3}c$ over each surface. The upper and lower sides of the tab are further refined respectively with 32 points, with an average cell length of $1.1 \times 10^{-3}c$. This transition region between the main airfoil and the tab is resolved with 14 uniformly spaced points with a spacing of approximately $1.5 \times 10^{-3}c$ for the upper and lower sides respectively. Finally, the trailing edge is modeled as half circle and 17 points with an average spacing of $5 \times 10^{-4}c$ to resolve its shape. The surfaces of the baseline and camber morphed airfoils are defined as viscous walls and are positioned in the center of the O-grid. The outer boundary of the O-grid is defined as the far field, as shown in Fig. 2.4. In order to generate a high-quality computational mesh, a hyperbolic grid solver is used in mesh generator Pointwise. The grid is designed with input constraints that aim to minimize the cell distortion, ensure a growth factor of 1.1 for the first cell layers, and maintain rectangular cell shapes whenever possible. Figures 2.5a and 2.5b show the obtained grids after applying the hyperbolic grid solver to the baseline and camber morphed airfoil with the deflection $\delta = 10$ deg. Furthermore, the cell growth factor of the meshes near the airfoil surfaces is depicted in Figs. 2.5c and 2.5b.

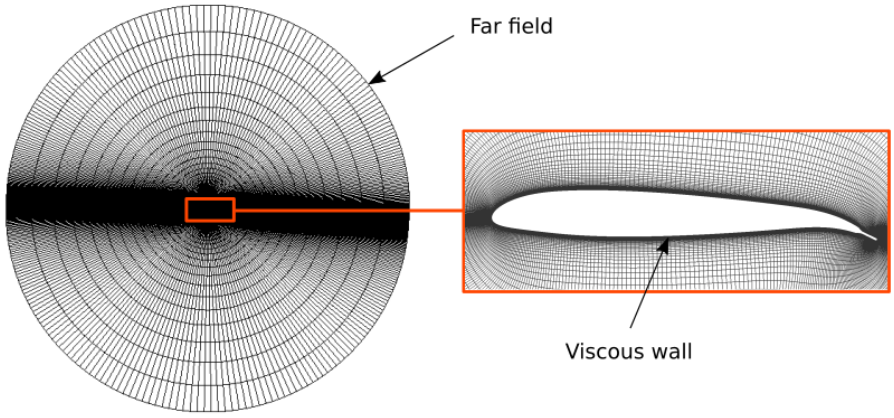

Figure 2.4.: The applied O-grid topology for the computational domain of camber airfoil with deflection $\delta = 10$ deg.

It is observed that the factor primarily varies between 1.1 and 1.2 near the surfaces. Even for the highly cambered airfoil (δ = 10 deg), the factor remains below 1.275 away from the lower surface. As shown in Figures 2.5e and 2.5f, the surface cells near the lower and upper surfaces of the airfoil exhibit angles ranging from 88 deg to 90 deg. This indicates that the cells are nearly orthogonal, allowing the grids for both the baseline and morphed airfoils to effectively calculate the numerical flux between two neighboring cells and resolve the boundary layer and accurately capture flow phenomena near the surfaces [81].

This study examines the aerodynamic performance of morphed camber airfoils derived from the BO105 helicopter airfoil with a chord length of c = 0.27 m. The morphed airfoil geometry, illustrated in Fig. 3.2, is generated using a third-order polynomial shape function to compute coordinates for the morphed mean camber line (details provided in subsection 2.2.2). The camber morphing is applied between $x = 75\%c$ and $x = 95\%c$ of the baseline airfoil. To investigate the effects of camber morphing direction and deflection magnitude, various cases are simulated. These cases include downward (positive) non-dimensional trailing-edge tip deflections for the morphed airfoils and two cases of upward (negative) deflection. Additionally, the impact of the deflection degree on the variation of 2D aerodynamic coefficients is explored, ranging from low deflection (δ = 1 deg) to extremely high deflection (δ = 10 deg).

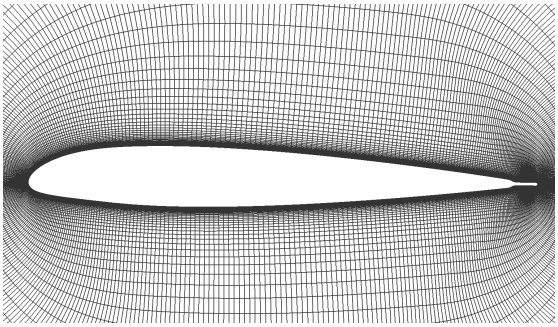

(a) Cell distribution around the baseline airfoil with δ=0 deg.

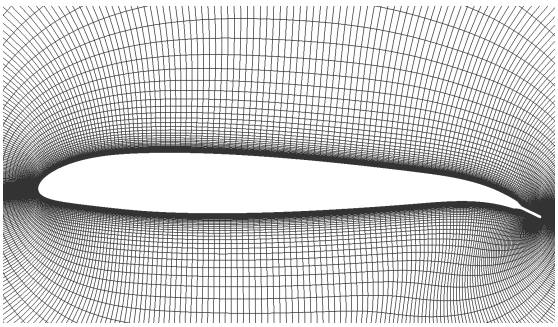

(b) Cell distribution around the morphed airfoil with δ=10 deg.

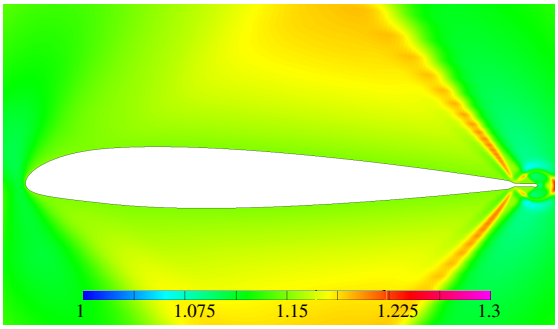

(c) Growth of the cell perpendicular to the baseline airfoil with δ=0 deg.

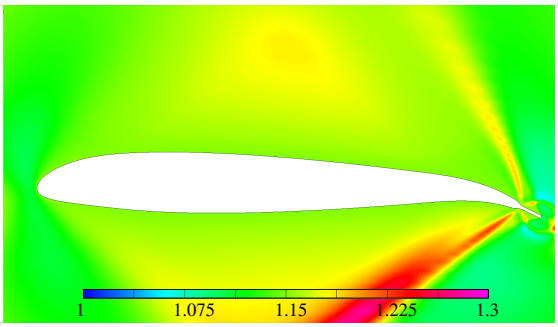

(d) Growth of the cell perpendicular to the camber morphed airfoil with δ=10 deg.

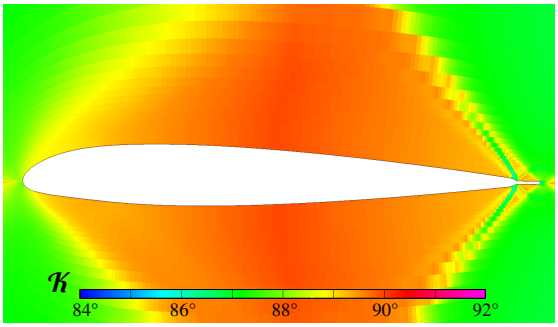

(e) Cell orthogonality κ around the baseline airfoil with δ=0 deg.

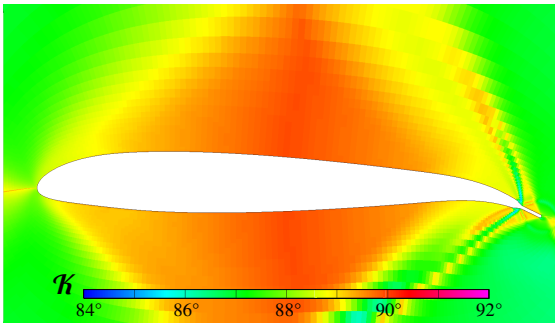

(f) Cell orthogonality κ around the camber morphed airfoil with δ=10 deg.

Figure 2.5.: Comparison of the CFD mesh growth rate and cell orthogonality κ around the basline and camber morphing airfoil with δ=10 deg.

2.3. Modeling Unsteady Aerodynamics of Camber Morphed Airfoils

2.3.1. Work flow of TAU Unsteady Simulations

A Python framework manages the unsteady TAU simulation workflow, as depicted in Figure 2.6. The time step size (Δt) for the unsteady simulation is computed as a fraction of the pitching period: $\Delta t = \frac{T_\theta}{\text{Number of time steps}}$. Both pitching and camber morphing are modeled by deforming the primary grid. The pitch angle and camber morphing deflection are specified at every time step using Fourier series:

$$\theta(t) = \theta_0 + \sum_{n=1}^{N} \theta_n \cos(2n\pi f_\theta t - \phi_{n\theta}) \tag{2.17}$$

$$\delta(t) = \delta_0 + \sum_{n=1}^{N} \delta_n \cos(2n\pi f_\delta t - \phi_{n\delta}) \tag{2.18}$$

The target deformed shape for each time step t is computed and saved within a scat file (scattered-data), as detailed in subsection 2.3.1.1. The simulation runs for a physical time of t_{end}, which is defined as a multiple of the pitch period: $t_{end} = N \cdot T_\theta$. To ensure consistency between the incoming flow conditions in CAMRAD II and the TAU unsteady simulation, the induced angle ϕ computed by CAMRAD II is applied in TAU as the angle between the free stream velocity U and the horizontal, as illustrated in Fig. 2.9b. Since the uniform inflow model is used, the induced angle ϕ remains constant along the blade radius and depends on the specified pitch and camber morphing schedule. The implicit Euler scheme is adopted for time discretization in this study due to its robust stability across varying time step sizes. For spatial discretization, a second-order Central differencing scheme is used. Additionally, fully turbulent flow over the airfoil surfaces is assumed, and the Spalart-Allmaras (SA) one-equation model is used for turbulence modeling.

2.3.1.1. Grid Deformation Applied for the 2D Airfoil

The grid surface is deformed to match the scheduled airfoil shape at each time step t. The reference grid (primary grid) used for this process is the 2D grid generated for the baseline airfoil (see Fig. 2.2.3). The grid deformation is performed using the RBF method implemented in TAU, as detailed in subsection 2.1.1.3. For the investigation presented in result section 3.2, both pitching and morphing are modeled through grid deformation. Figure 2.7 exemplifies the effectiveness of this method in capturing the deformed airfoil surface for combined pitch-morphing motions (θ = 4 deg and δ = 8 deg). The deformed airfoil surfaces (represented by red symbols) are compared to the target shapes (shown in black), demonstrating a close match between them. This confirms the ability of the RBF-based grid deformation method to accurately model the prescribed motions. The orthogonality of the deformed cells for the combined pitch-morphing case (θ = 4 deg and δ = 8 deg) is compared to the undeformed (primary) grid in Fig. 2.8. This comparison demonstrates the preservation of high-quality grid cells in the first layers and also in the surrounding

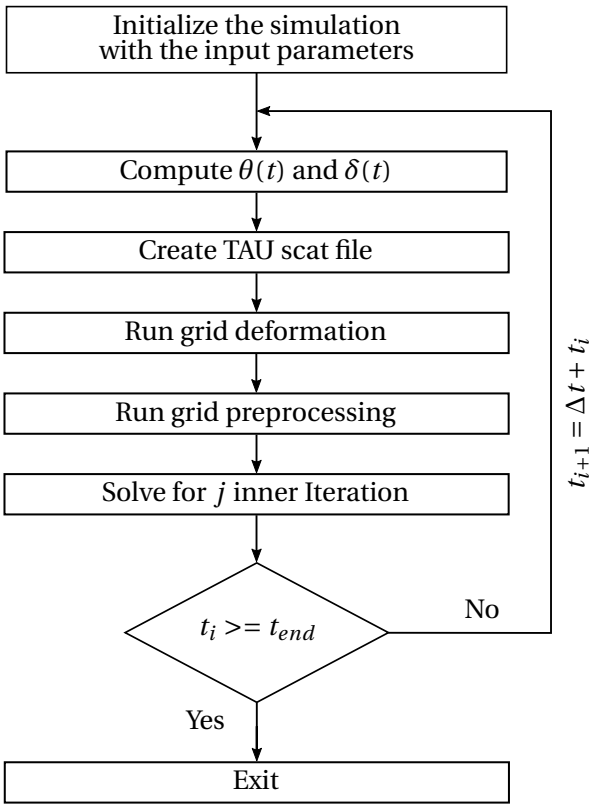

Figure 2.6.: Workflow of the 2D unsteady simulation in TAU.

airfoil region. Preserving high-quality grid cells in the first layers near the airfoil surface is particularly critical. These cells play a crucial role in accurately capturing the flow boundary layer. By maintaining the orthogonality of these cells, the RBF-based grid deformation method ensures a well-resolved boundary layer and more accurate flow simulations. The grid quality in the morphing section exhibits slight variations only at the trailing edge, where grid cell angles approach 70 deg. Despite this minimal deviation, this demonstrates the ability of the RBF-based grid deformation method to accurately model complex deformations of airfoils.

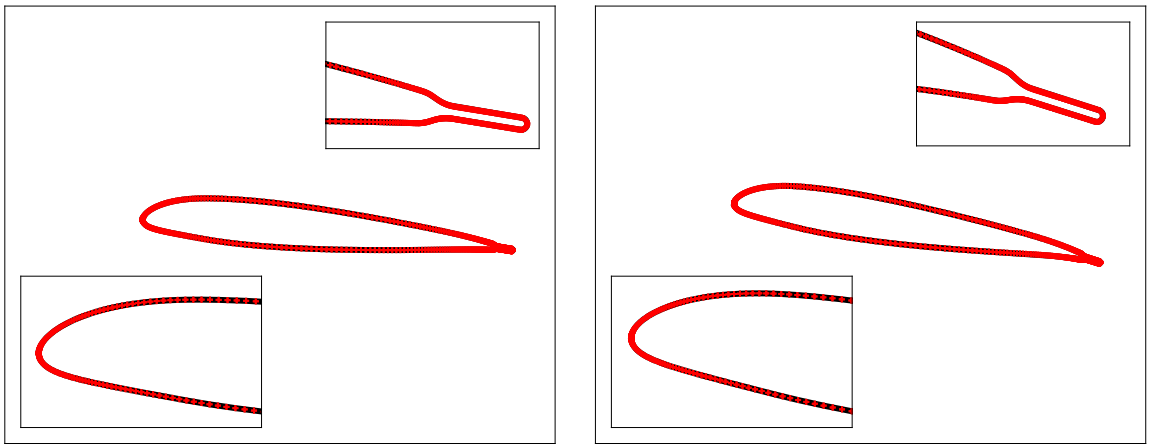

(a) Illustration of the target morphed shape in black with pitch angle $\theta = 4$ deg and morphing deflection $\delta = 2$ deg in comparison to the target camber morphed airfoil shape(red symbols).

(b) Illustration of the deformed grid surface(black line) with pitch angle $\theta = 8$ deg and morphing defelection $\delta = 4$ deg in comparison to the target camber morphed airfoil shape(red symbols).

Figure 2.7.: Comparison between the deformed grid surface shapes (black lines) and target camber morphed airfoils (red symbols) at different conditions.

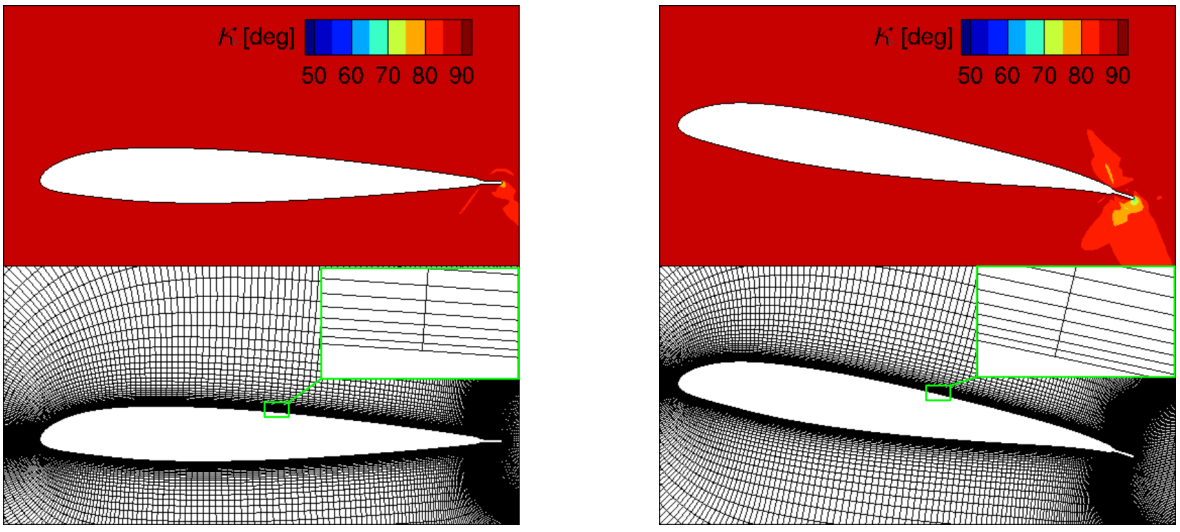

(a) Primary grid for the baseline airfoil.

(b) Deformed grid for the camber morphed airfoil.

Figure 2.8.: Comparison of cell orthogonality κ between the primary and deformed grids with pitch angle $\theta = 8$ deg and morphing deflection $\delta = 4$ deg.

2.3.2. CAMRAD Model for Unsteady Aerodynamic Test Case

In order to investigate mainly the unsteady effects caused by airfoil pitching and morphing, a single blade configuration is modeled in CAMRAD II for the hypothetical hovering case. Therefore, the complexities associated with blade wake interaction and flow asymmetry around the blade are not considered in this simplified model. This configuration aims to understand how CAMRAD II handles aerodynamic coefficients from the airfoil tables and their variation when applying an unsteady correction model, as discussed in result section 3.2. Moreover, the blade is modeled as rigid, non-twisted, and rectangular. It has a radius of $R = 4.912$ m, a tabbed NACA23012 airfoil with a chord length of $c = 0.27$ m, and is discretized using 26 panels (see Fig. 2.9a). The panel discretization is coarse near the blade root, gradually transitioning to a finer mesh towards the blade tip. Pitching motion is prescribed using a bearing positioned at $0.01R$ from the hub center. Flap and lead-lag motion are not considered. The blade is set to rotate at 420 RPM, corresponding to a frequency of 7 Hz, which is close to the actual rotation frequency of the Bo105 rotor (7.07 Hz). A uniform inflow model is used to guarantee consistent inflow conditions across the blade radius. The rotor is not trimmed, and the initial blade input is provided as follows:

Table 2.1.: Input parameter for the one bladed CAMRAD II model.

Collective [deg]	Lateral cyclic [deg]	Longitudinal cyclic [deg]
4.00	0	4.025

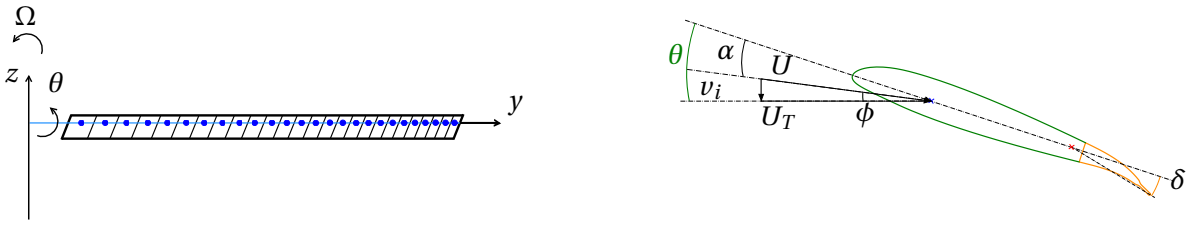

(a) Panel distribution along the blade span.

(b) Velocity vectors and relevant angles at the blade section.

Figure 2.9.: Illustration of the key parameter of the one bladed CAMRAD II model.

The camber morphing is continuously applied along the entire blade span, starting at $x = 0.75c$ and extending towards the trailing edge. The steady airfoil tables used for active camber morphing covered all aerodynamic coefficients for prescribed shapes ranging from -4 deg to 13 deg of

camber deflection. These tables are discretized with a spacing of 1 deg between each prescribed camber-morphed shape. The steady aerodynamic coefficients (C_l, C_d, and C_m) in the airfoil tables are computed using the numerical setup for the CFD steady simulations, as detailed in the method section 2.2. For morphed airfoil shapes not included in the airfoil tables, CAMRAD II interpolates linearly the steady aerodynamic coefficients. The interpolation is based on the coefficients of the nearest prescribed shapes in the table. In the result section 3.2, two CAMRAD II simulations are compared to assess the impact of unsteady aerodynamic effects on pitching and camber-morphing airfoils. The first simulation neglects flow unsteadiness and directly uses steady aerodynamic coefficients (C_l, C_d, and C_m) from the airfoil table to compute aerodynamic loads. In contrast, the second simulation activates the ONERA Edlin model (details of the model in [58]) to account for 2D aerodynamic unsteadiness not captured in the steady CFD simulations.

2.4. Modeling of the Active and Passive Rotors using CFD/CSD Coupling

This section details the models and methodologies used to compare the aerodynamic characteristics of the active and passive rotors presented in the results section 3.3. First, the CFD/CSD loose coupling is presented which is used for data exchange between TAU and CAMRAD II. Here, the aerodynamic loads (F_x, F_y and F_z) and their corresponding moments (M_x, M_y and M_z) are transferred from TAU to CAMRAD II and the resulting harmonic motion in CAMRAD II is then passed back to TAU. Second, the three-dimensional computational domain used in the TAU model is presented. This model is used to compute the aerodynamic loads and the complex flow dynamics surrounding both the passive and active rotor systems. Finally, the CAMRAD II model is also introduced. Using this model both passive and active rotors were trimmed.

2.4.1. Workflow of the Loose CFD/CSD Coupling

This section is extracted from the methodology section presented in the publication [4], which detailed the coupling of a passive and an active single-bladed rotor using CAMRAD II and TAU. This methodology is then applied to four-bladed passive and active rotors in result section 3.3. This thesis assumes that steady hovering and forward flight regimes can be modeled as periodic states. This enables the decoupling of the fluid-structure problem, allowing independent solutions for aerodynamics and structural dynamics using dedicated solvers with differing fidelities. This provides the flexibility to apply various software specialized for structural and aerodynamic analysis. Therefore, a loose coupling approach can be adopted in the workflow. Hence, the TAU solver is to model the aerodynamics of the passive and active rotors and CAMRAD II is used to model the motion of the blades based on the strucutral properties for the trimmed state. Therefore, the TAU solver is chosen to model the aerodynamics of both passive and active rotors, while CAMRAD II is used to model the motion of each blade for both rotors based on the blade structural properties for the trimmed state. For this purpose, a modular and extensible TAU-CAMRAD II coupling environment was developed using the preCICE coupling library [19]. The skeleton of this environment was created in collaboration with the preCICE developers [43]. This coupling environment comprises of three main components: a TAU adapter, a CAMRAD II adapter, and Python code. The Python code dictates the workflow, while preCICE manages data exchange between the two solvers and facilitates the application of different mapping schemes. For example, preCICE enables the mapping of three-dimensional loads from TAU onto the one-dimensional beam elements in CAMRAD II. The details of the implementation of the coupling can be found in [44].

The current work focuses on modeling a full-scale four bladed rotor neglecting blade elasticity. However, this same procedure can be applied to a rotor simulation with N blades and can also be extended to include elastic blade motion and various active morphing mechanisms. Within the adopted loose coupling approach the forces and moments passed from CFD to CSD was based on the delta air loads method, presented and explained in [87, 104, 91]. Figure 2.10 shows a simplified timeline of the CFD/CSD coupled simulations procedure and illustrate the workflow of the coupling procedure 2.11. Initially, for specific rotor trim and dynamics were computed in CAMRAD II

based on lifting line theory. Thereby, linear inflow was assumed to compute the induced velocity, and the blade aerodynamic forces ${L_{i-1}}^{LL}$ and moments ${M_{i-1}}^{LL}$ were predicted using lifting-line theory. This approach was based on two dimensional aerodynamic coefficients C_l, C_d and C_m which were separately computed using steady CFD simulations.

Once the comprehensive analysis is converged to the specified trim targets, the resulting blade displacements flap β, lag ζ, and pitch θ were transmitted to the coupling algorithm as Fourier coefficients to TAU via preCICE. The obtained displacements were given in the CAMRAD II reference system as translations $\Delta x(\psi)$, $\Delta z(\psi)$ which were normalized by the blade radius R and as the pitch angle $\theta(\psi)$ measured in the feathering axis, as shown in Fig. 2.12. This coordinate system is centered at the hub, with the z-axis aligned along the shaft, the y-axis along the quarter-chord of the reference blade, and the x-axis oriented towards the trailing edge. The reference coordinate system rotates with a user defined reference blade. Since within TAU the blade motion processed as Euler transformations around a defined virtual hinge, the flap and lag motion of the rotor blade are converted to angles using the approximations in Eqs. 2.19 and 2.19b.

$$\beta_0 \approx \tan^{-1}(\Delta x_0);\ \ \beta_{1C} \approx \tan^{-1}(\Delta x_{1C});\ \ \beta_{1S} \approx \tan^{-1}(\Delta x_{1S}) \tag{2.19a}$$

$$\zeta_0 \approx \tan^{-1}(\Delta z_0);\ \ \zeta_{1C} \approx \tan^{-1}(\Delta z_{1C});\ \ \zeta_{1S} \approx \tan^{-1}(\Delta z_{1S}) \tag{2.19b}$$

Subsequently, j rotor revolutions are simulated in TAU. Here, the URANS equations are solved for given number of inner iterations at time step t. The number of revolutions is adjustable from one coupling step to the next. In the first coupling iteration, it is necessary to solve the CFD simulation at least for two revolutions in order to avoid unphysical loads to CAMRAD II. In the case of active camber morphing, the dynamic actuation of the camber is modeled by deforming the grid using the RBF-based mesh deformation method implemented in TAU at every time step t. This was followed by preprocessing the grid before solving the URANS equations, as shown in Fig. 2.11.

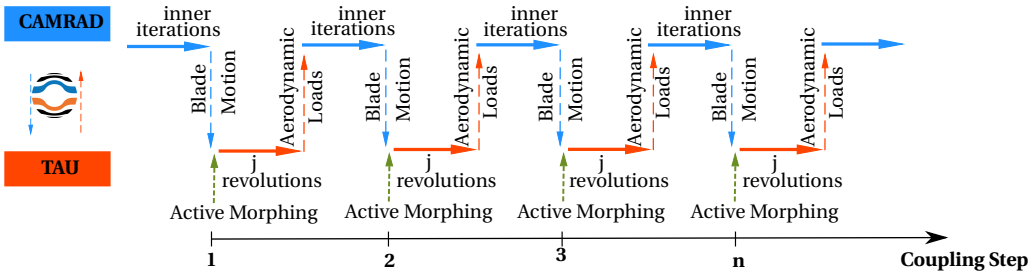

Figure 2.10.: Time line of the explicit loose coupling[4].

After simulating j rotor revolutions in TAU, the resulting aerodynamics were passed via delta air loads back to the CAMRAD II. For this purpose, a multi-scale mapping is applied to map the aerodynamic loads [43]. The aerodynamic loads are extracted from the last revolution computed in TAU with a step size of $\Delta\psi = 15$ deg as recommended in [30]. The aerodynamic loads are extracted in the aerodynamic frame in TAU and passed to the CSD solver CAMRAD II in the wing frame coordinate system. Both coordinate systems are tilted with the rotor shaft and rotate with the reference blade, positioned at an azimuth of 90 deg before the rotor starts rotating. As explained in [4], the aerodynamic forces and moments are mapped conservatively from the three-dimensional

CFD surface grid to an intermediate grid using a nearest-neighbor mapping scheme provided by preCICE [43]. The intermediate grid represents a two-dimensional fine discretization of the panel defined in the CSD solver along the rotor blade axis, see Fig. 2.12a. Then, the aerodynamic loads were integrated and assigned to the matching panel. Before restarting the CSD simulation for the next coupling step, the difference in forces and moments between the last CSD and CFD solutions are evaluated and multiplied by a relaxation factor λ ranging from zero to one. The resulting values are added to the previous values stored in the so-called delta tables, which were initially zero. These delta loads are then superimposed on the aerodynamic forces and moments calculated by the CSD solver. In the first coupling step, λ can be set to a value less than 1 since the forces and moments between the CSD and CFD computations can vary significantly in the first coupling step. This can potentially lead to the divergence of the CFD/CSD coupling process. From the second coupling step onward, λ can be set to 1. Both solvers use their most recent corresponding converged solutions as a restart solution during the coupling process in order to accelerate the convergence. The CSD/CFD coupling is considered to be converged when the absolute variation of integrated CFD rotor thrust and the collective, lateral, and cyclic blade pitch control does not exceed a user-defined tolerance.

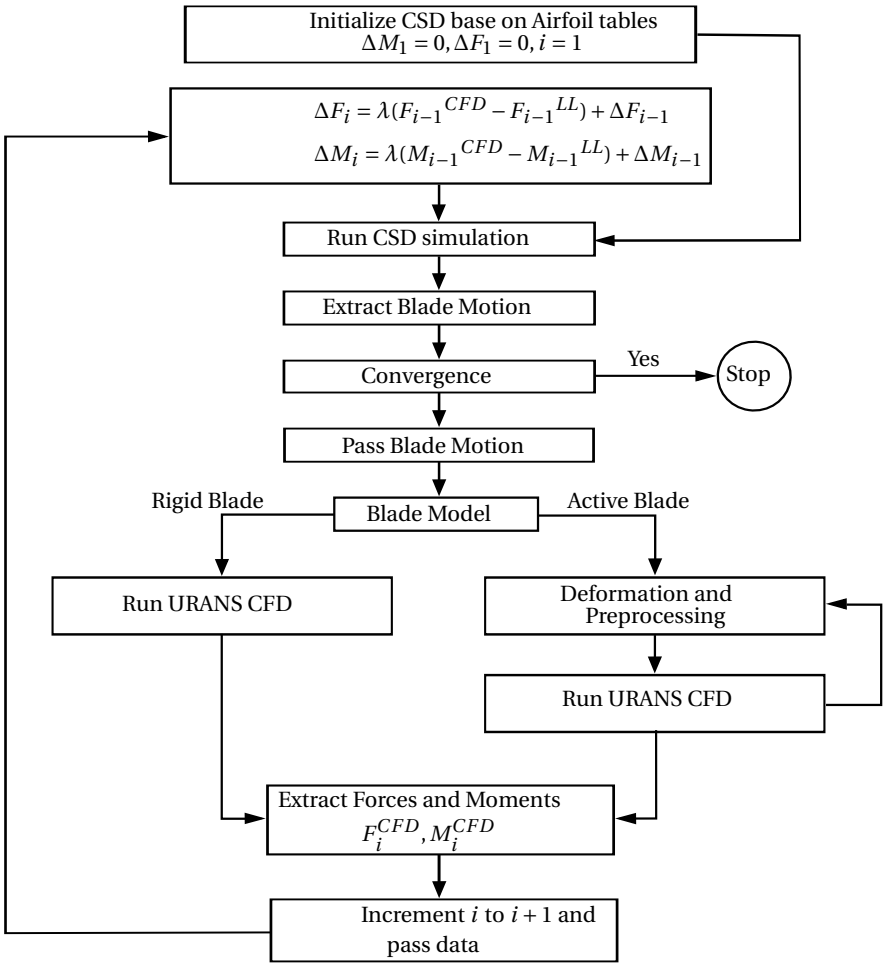

Figure 2.11.: Coupling workflow based on the delta loads method[4].

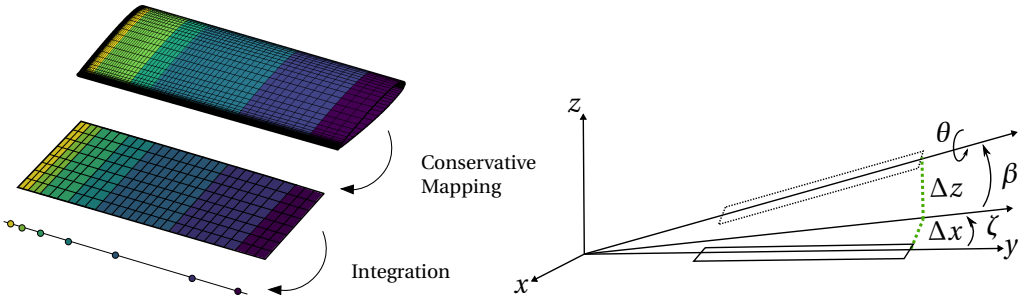

(a) Aerodynamic loads mapping from the CFD solution to beam in the CSD model.

(b) Calculation of motion angles from the reference coordinates system in CAMRAD II.

Figure 2.12.: Mapping strategies for aerodynamic loads and blade motion[4].

2.4.2. Grid Generation for the Rotor Blades in CFD Domain

A multi-block grid approach is used to capture the complex aerodynamics of rotating and articulating helicopter blades. The grid topology uses distinct grid blocks to discretize the computational domain, allowing the generation of a grid block for each blade. Hence, every blade block can be controlled individually to accommodate various blade motions such as rotation, pitching ,flapping, lead-lag, and morphing at every time step. This also allows the application of a fine grid resolution around the rotor blades while coarser grids are maintained in less critical areas. In this thesis, the computational domain is constituted of six overlapping grid blocks as illustrated in Fig. 2.13: four blade-specific blocks, a transfer block, and a background block. The following sections detail the generation of each block, the interpolation procedures between blocks, and the grid deformation technique implemented for active rotor modeling.

Table 2.2 provides an overview of the discretization for the different computational domain blocks. The entire domain is discretized using a total of 103.768.154 cells. Four identical blade blocks, spaced 90 deg apart, are used to model the rotor. These blade blocks primarily consist of structured cells, with each block containing 11.430.296 hexahedral cells. The transfer block uses a variety of cell types. To ensure accurate interpolation within the overlapping region between the blade and transfer blocks, 17.754.188 hexahedral cells are used. Throughout the remaining domain of the transfer block, 7.500.518 tetrahedral cells are used. For the overlapping region between the background block and the transfer block, 3.851.690 prism cells are used to facilitate accurate interpolation. The remaining background domain uses a combination of 163.202 pyramidal and 28.777.372 tetrahedral cells.

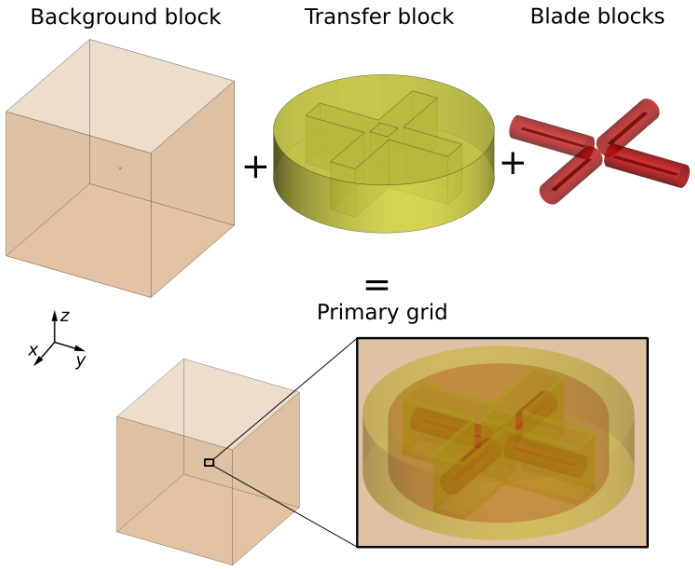

Figure 2.13.: Discretization of the computational domain using overlapping grids.

Table 2.2.: Grid resolution and cell types used for the different blocks of the computational domain.

Grid blocks	Block for every blade	Transfer block	Background block
No. of tetrahedra	0	0	28777372
No. of prisms	0	7500518	3851690
No. of pyramids	0	0	163202
No. of hexahedra	11430296	17754188	0

Discretization of the blade surface:
The geometry of the BO105 rotor blade was adopted to define the blade surface, which has a radius of $R = 4.912$ m. Along the span, the blade section is defined by a NACA2013 airfoil with a tab and a chord length of $c = 0.27$ m. Moreover, the blade exhibits a linear twist of -8 deg from the hub to the tip, consistent with assumptions made within the CAMRAD II model used for the CFD/CSD and described in section 2.4.5. Given that the primary focus is on the aerodynamic field generated by the isolated blades, the rotor hub is not modeled. Within the root region, the geometry is simplified to a rectangular form with a constant twist extending from $r/R = 0.2$ to $r/R = 0.22$, highlighted in red in Fig. 2.14. The helicopter blade surface is discretized using a structured grid with varying

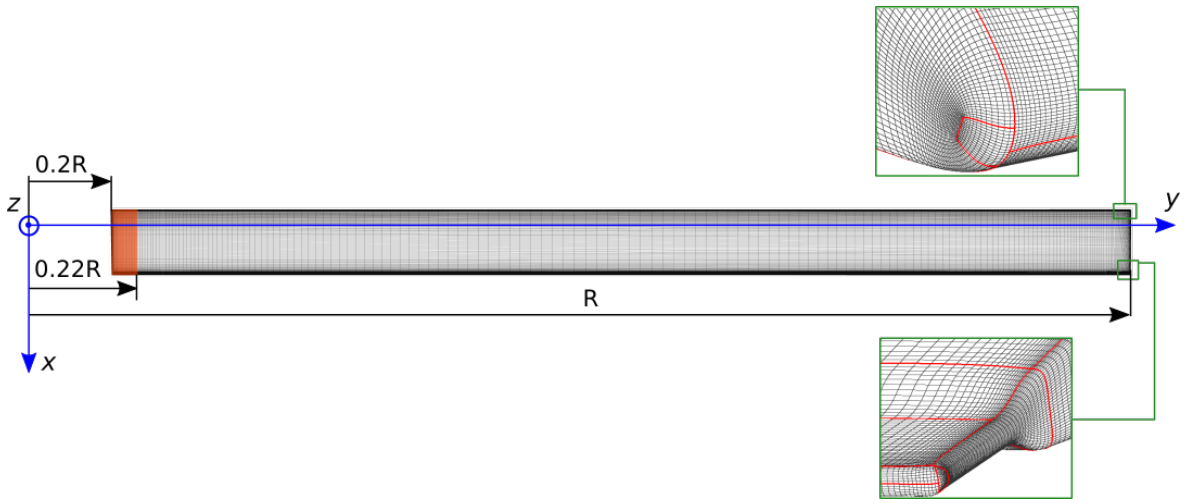

Figure 2.14.: Illustration of the modeled BO105 surface blade in the CFD domain.

resolution to effectively capture the complex flow behavior along the blade. The surface of root section, ranging from $r/R = 0.2$ to $r/R = 0.22$, is discretized with a resolution of 40 points along the span. The aerodynamic blade section, where the majority of lift is generated (from $r/R = 0.22$ to $r/R = 0.98$), uses a higher resolution of 145 points along the span. Finally, the blade tip region (from $r/R = 0.98$ to $r/R = 1$) is discretized with 45 points along the blade span. The grid refinement is applied near the blade tip and root due to the strong pressure gradients present along both the span and chord in these regions. This refinement is crucial to accurately capture the complex flow phenomena occurring at the blade extremities.

The blade surface was modeled as a viscous wall. The average length ratio across the blade surface remains approximately 1.05 along the blade chord and does not exceed 1.15, as shown in Fig. 2.15a. At each blade section, the leading edge radius is resolved with a cell length of approximately $7 \times 10^{-4} c$, enabling accurate representation of the high-pressure gradient. Both the upper and lower surfaces of the blade are discretized with the same resolution of 143 points, with an average spacing of $0.8 \times 10^{-3} c$. The transition between the main airfoil and the tab is smoothed using a Bezier spline (Fig. 2.15a). This transition region is resolved with 14 uniformly spaced points with a spacing of approximately $1.5 \times 10^{-3} c$. The tab itself is further discretized with 32 points, maintaining an average spacing of $1.1 \times 10^{-3} c$. Finally, the trailing edge is resolved with 17 points using an average spacing of $5 \times 10^{-4} c$.

Discretization of the blade block:
These blade blocks rotate with the rotor's frequency and undergo a predefined pitch, flap, and lead-lag motion, as well as a predefined grid deformation for the active rotor. A structured O-grid is extruded perpendicular to each blade section, extending from a radial location of $0.22R$ to $0.98R$, as depicted in Figure 2.15b. The center of the circle is located at the midpoint between the trailing and leading edges. Starting from the airfoil surface, 60 structured cells are used to capture pressure and velocity gradients. The first cell has a height of 1.2×10^{-6} m, equivalent to $4.5 \times 10^{-6}c$. This fine cell size is necessary to fulfill the $y^+ = 1$ requirement for a Mach number of $M = 0.95$ along the reference length of $c = 0.27$ m at standard atmospheric conditions.

A growth factor of 1.1 is used between successive cells to accurately approximate the pressure and velocity gradients in the boundary layer of the blade surface. An average skewness factor of 0.01 is achieved within the grid layer along the blade span, ensuring excellent grid quality. Subsequently, 45 structured cells are generated with a growth factor of 1.15 and an average skewness of 0.07. The outer boundary of these cells forms a circular arc with a radius of approximately $0.2R$. Perpendicular to this boundary, six identical equidistant cells are placed, highlighted in blue in Figure 2.15b, with a cell height of $9.5 \times 10^{-2}c$ and an average width of approximately $3.33 \times 10^{-2}c$.

To ensure orthogonality and prevent excessive length ratios between adjacent grid layers, the transitions between the different grid layers are smoothed using a multigrid solver implemented in Pointwise. The outer boundary of the equidistant cell layer, spaced approximately $0.098c$, forms a circle with a radius of approximately $0.26R$ and corresponds to the chimera block boundary, where the blade block begins to interpolate with the transfer block. To maximize the interpolation area of the chimera method, six cells are used. Within the region highlighted in blue, the cells are generated uniformly to simplify the grid topology of the interpolation zone in the transfer block and enhance the efficiency of the interpolation. Figure 2.16 depicts the grid layers perpendicular to the

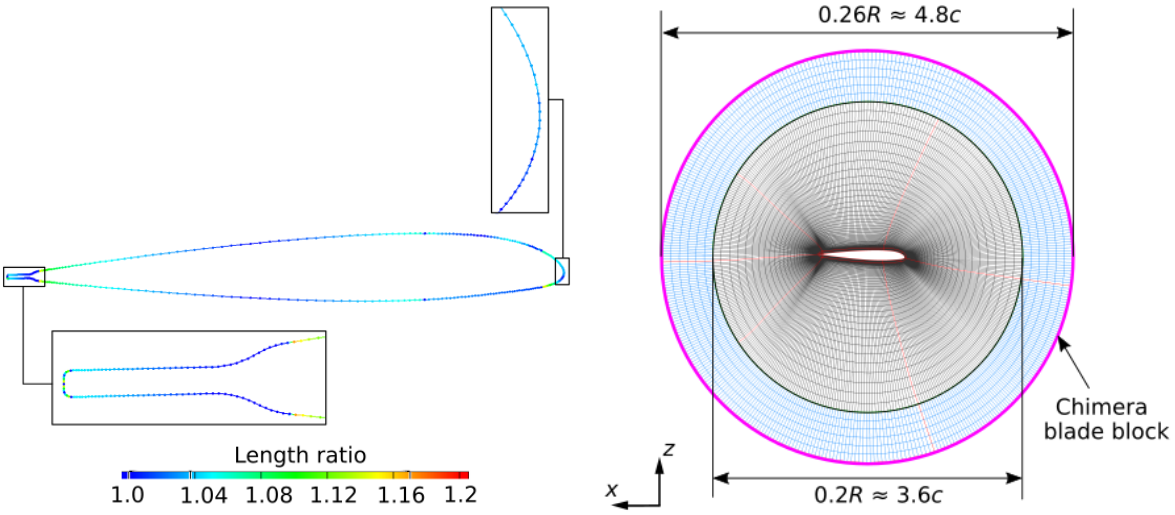

(a) Distribution of the length ratio over the blade section. **(b)** Slice from the blade block along the chord length.

Figure 2.15.: Illustration of the grid resolution along the chord length.

blade surface from radial location $0.22R$ to $0.98R$. The average cell angle is found to be 89.9 deg,

with a minimum cell width of $0.027c$ near the blade root and tip and a maximum cell width of $0.15c$ at $0.5R$. The average cell width is $0.096c$, and the growth factor between adjacent cells does not exceed 1.1 along the span. For the blade tip, an H-grid topology is used using structured blocks. The first cell width is also set to 1.2×10^{-6} m to comply with the $y^+ = 1$ requirement. The growth rate does not exceed 1.23 between successive cell layers, and the average cell width is $0.025c$, with a maximum cell width of $0.098c$. Two blocks originating from the trailing and leading edges of the blade tip, forming a 45 deg angle with the horizontal, are extruded to approximately $y = 1.2R$ outwards, as shown in the slice in Figure 2.16. From the $y = 1.2R$ level, six equidistant cells are extruded, highlighted in blue. This region, with a width of $0.013R$, forms part of the interpolation zone where the blade block interpolates with the transfer block. Similarly, for the blade root, a structured grid is used, extruded from the trailing and leading edges of the root to $y = 0.085R$. Here as well, the first cell width is 1.2×10^{-6} m, the growth rate is approximately 1.18 between two successive cell layers, the average cell width is $0.025c$, and the maximum cell width is $0.098c$. From $y = 0.085R$, the interpolation zone in the root region with a width of $0.009R$, consists of six equidistant cells with a width of approximately $0.03c$, highlighted in blue in Fig. 2.16.

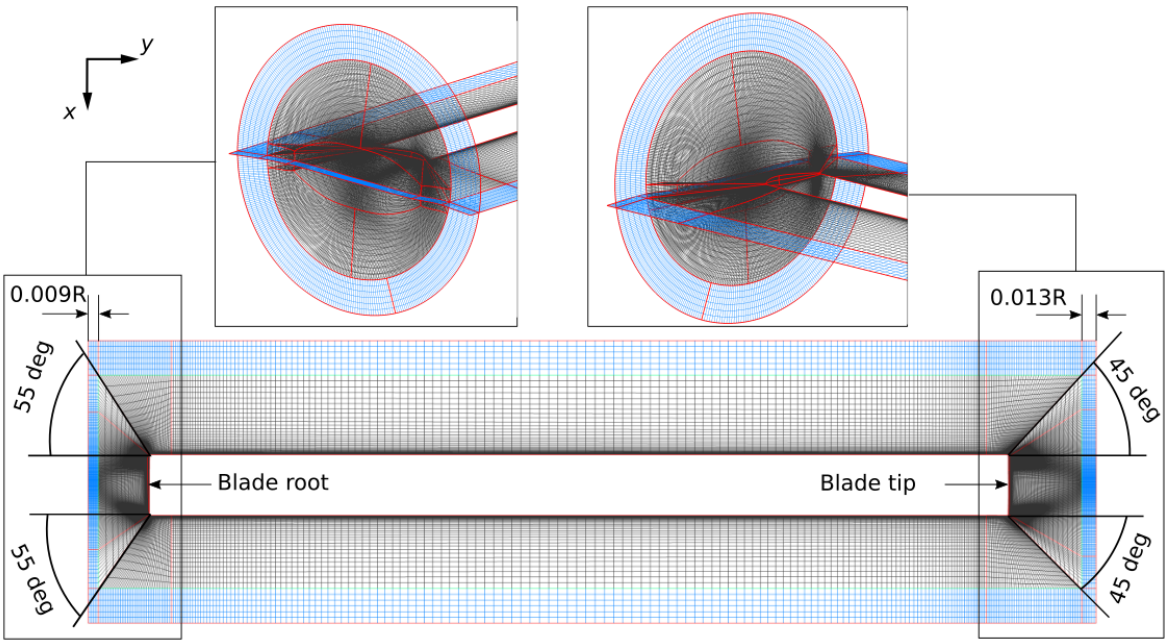

Figure 2.16.: Slice through the blade block along its span, illustrating the block's spanwise dimensions.

Discretization of the transfer block:
The transfer block rotates at the same frequency as the blades to facilitate efficient interpolation between the moving blade blocks and the stationary background grid. Two chimera interpolations occur within the transfer block: the first between the transfer grid and the blade blocks, and the second between the transfer grid and the background grid. The transfer block has a cylindrical shape with a radius of $1.5R$ and a height of $0.77R$, as shown in Fig. 2.17. This height ensures that even when a blade block experiences a 14 deg upward or downward flap motion when measured from the hub, the blade blocks remain within the transfer block's boundaries to guarantee the interpolation between the blade blocks and the transfer block. The transfer block consists of

four structured blocks within which the blade blocks can fit. Each structured block has the dimensions of $0.4R$ by $0.99R$ extruded along a height of $0.77R$ to accommodate the blade blocks. Along the span, each structured block is discretized using 192 cells, with a minimum cell width of approximately $0.037c$, a maximum cell width of approximately $0.21c$, and an average cell width of approximately $0.092c$. The growth factor between consecutive cells does not exceed 1.1 along the span. Fine resolution is used where the blade block is finely resolved, and coarser resolution is used where the blade block is coarsely resolved. Along the chord, 151 cells are uniformly distributed with a spacing of approximately $0.04c$.

To achieve a smooth transition between the structured and unstructured grids, finely distributed unstructured cells are used in regions where the structured grid is finely resolved. Beyond these regions, the unstructured cells are uniformly distributed with a spacing of approximately $0.48c$. Within the region encompassing $2.5R$ to $3R$, where interpolation occurs between the background and transfer grids, the spacing for uniform unstructured cells is increased to approximately $0.6c$. Along the height of the transfer block, using a total of 157 cells, different cell distributions are implemented. Within the region where the blade block intersects with the transfer block, a uniform distribution is used with a cell spacing of approximately $0.06c$ over a distance of approximately $0.28R$. Starting from this intersection region and extending towards the top and bottom of the cylinder, a growth factor of 1.04 is initially applied between successive cells, resulting in an average cell spacing of approximately $0.09c$ over a distance of approximately $0.15R$. Subsequently, a uniform spacing of approximately $0.11c$ is used until the top and bottom of the cylinder are reached, where the interpolation with the background grid occurs.

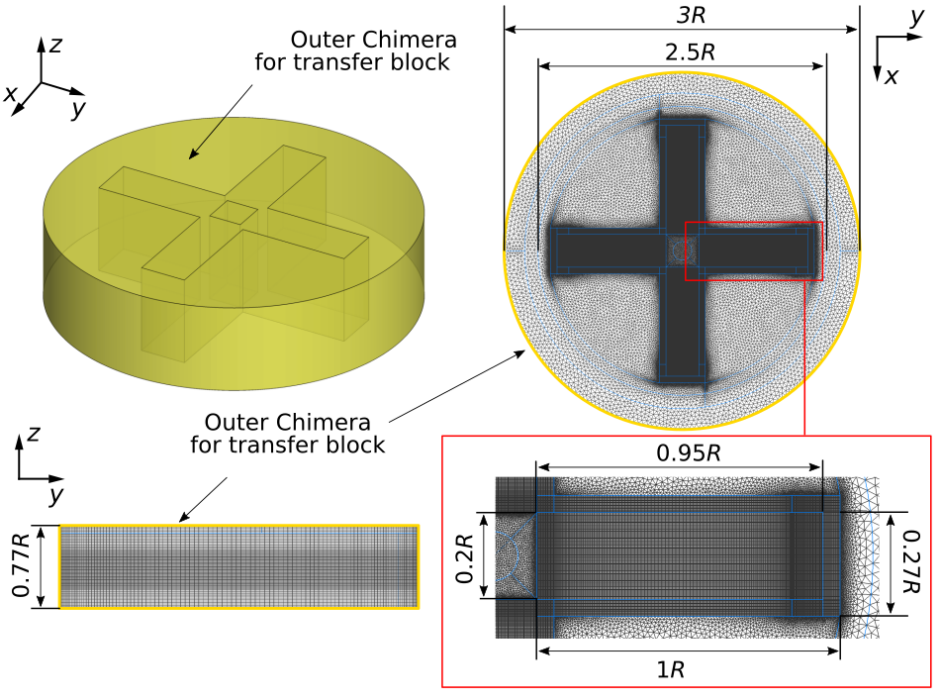

Figure 2.17.: Illustration of the dimensions of the transfer block and outer chimera boundary in yellow. The close-up of the grid section along a constant z value shows the overlapping region with a blade block.

Interpolation between rotating transfer block and rotating blade blocks:
The transfer block and the blade blocks rotate at the same speed, but the blade blocks exhibit additional motions due to flapping, lead-lag motion, and pitching. These motions depend on time, are specific to each blade, and vary across different coupling setups. This complexity makes it challenging to predefine a Chimera surface for interpolation between the rotating grids, needed to exchange the flow field data between the two blocks. To address this challenge, the Chimera hole cutting technique was used. This approach involves defining a 3D surface, treated as a "hole," which corresponds to the region where mesh elements are removed from the transfer block. The surface grid, where the mesh is removed, defines the chimera boundary. This boundary defines the interpolation zone between a specific blade block's predefined Chimera boundary and the transfer block, as shown in Figs. 2.18a and 2.18b .

By dynamically adjusting these Chimera boundaries in response to the blade blocks' motions, the technique ensures accurate and efficient interpolation, essential for capturing the complex dynamics of the system. Therefore, at every time step, new interpolation zones are determined between the transfer block and blade blocks, as highlighted in blue in Figs. 2.18b and 2.18b. The outer Chimera boundary of the transfer block is not used for the interpolation of the flow field data between the rotating transfer block and rotating blade blocks. It is mainly used to interpolate between the background block and the rotating transfer block.

Background grid Block:
The background block, located in the stationary portion of the computational domain, has a cubic shape with dimensions of $300R \times 300R \times 300R$, as shown in Fig. 2.20, and features a central cavity. The cavity boundary defines the inner boundary of the interpolation zone between the background and the transfer block, where data exchange occurs. The background block is a combination of a cylinder, a sphere, and an extruded cube. The cylinder, with a radius of $5.5R$ and a height of $2.6R$, forms the base of the background block and houses the cavity. The sphere, with a radius of $2.5R$, acts as a transition element between the cylinder and the cube. Finally, the cylinder extends from the sphere to complete the cubic shape. The volume starting from the cavity boundary (Chimera boundary) represents the interpolation zone between the stationary background block and the rotating transfer block. This volume is extruded from $2R$ to $3R$ in both the x and y directions so that it ensures an overlap of 11 cells along these axes, as shown in the close-up view of Fig. 2.20. Along both circles with radii $2R$ and $3R$, a total of 140 cells are distributed uniformly with equidistant cell lengths of $ds = 0.5c$ and $ds = 0.73c$, respectively. Additionally, the upper and lower cavity boundaries expand in the z-direction by $0.65R$, guaranteeing a 10 cell overlap with the transfer block along the z-axis. Within the interpolation volume, the grid discretization of both the stationary background block and the rotating transfer block is identical. This design ensures seamless and accurate interpolation of flowfield data across the boundary. The sides of the cube, as shown in Fig. 2.20, mimic the geometry of a wind tunnel. All sides of the cube are discretized using a uniform structure with a resolution of 150×150 cells distributed uniformly with an equiwall distance of $2R$. The upper and lower sides, corresponding to the roof and floor, are defined as Euler walls. This means no boundary layer is modeled. The front and back walls are designated as the inlet and outlet, respectively. The side walls are considered symmetry planes. The free stream velocity is defined in the TAU-grid coordinate system. It aligns with the positive x-axis and is perpendicular to the y-axis[28].

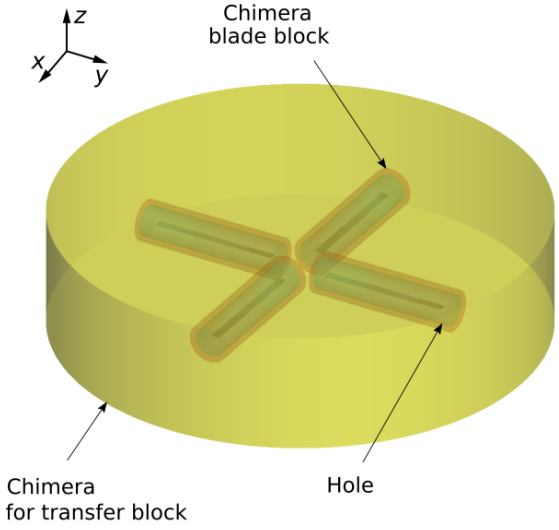

(a) Overview of the overlap between transfer block and blade blocks. The interpolation zone is located at every time step between the holes and Chimera boundary of the blade.

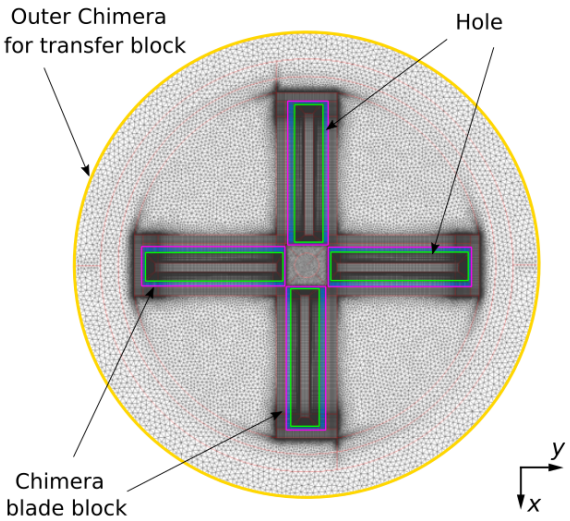

(b) Cross-sectional view of transfer and blade blocks overlap. Interpolation zones are between the holes and chimera blade blocks.

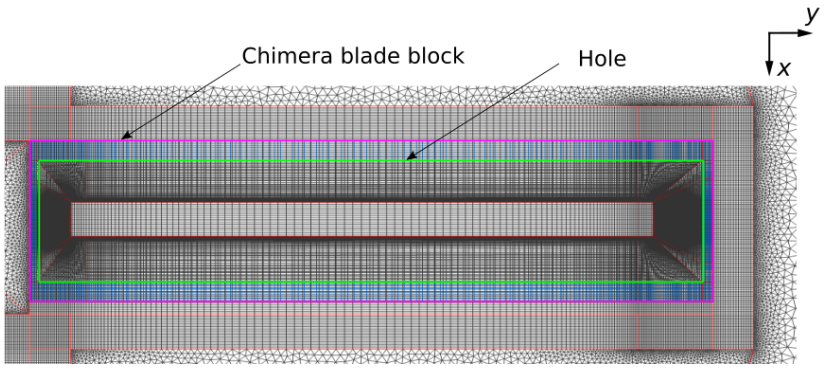

(c) Close-up view of the interpolation region between the transfer block and a blade block. The blue region represents the interpolation region.

Figure 2.18.: Illustration of the relevant boundary needed for the Chimera interpolations between the transfer block and blade blocks.

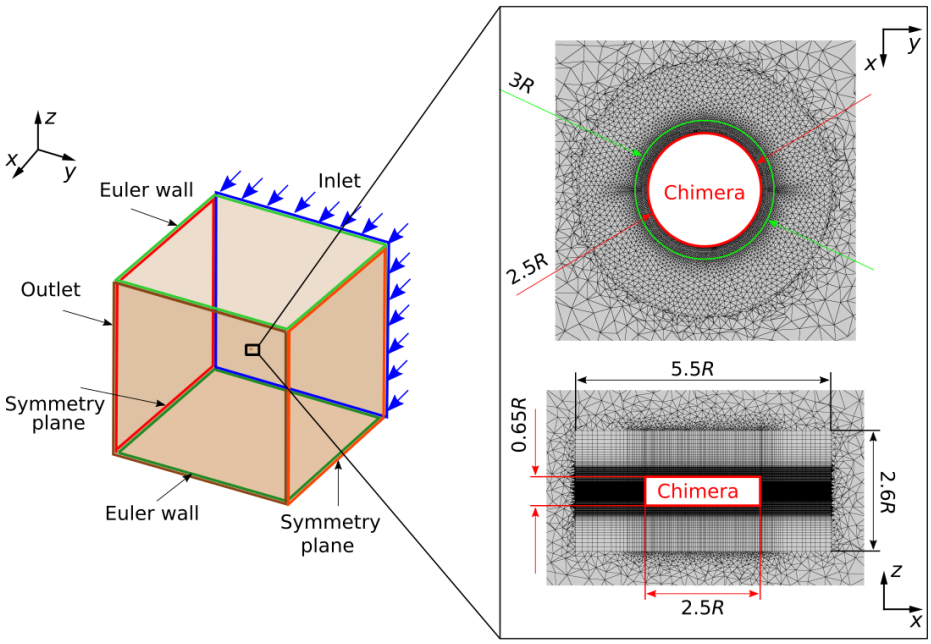

Figure 2.19.: Illustration of the shape of the background grid and relevant boundary conditions. The close-up view shows the Chimera boundary needed to exchange data with the rotating transfer block.

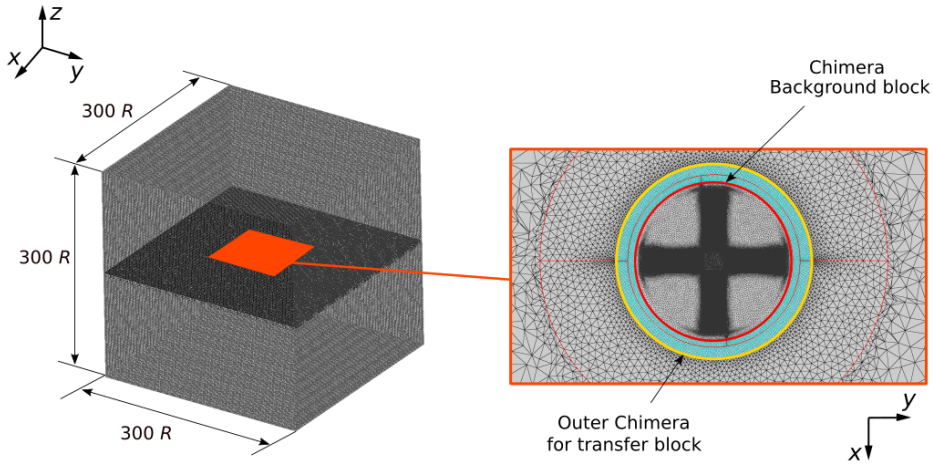

Figure 2.20.: Illustration of the dimensions of the background grid and the interpolation region. The interpolation zone between the background and the transfer block is highlighted turquoise.

Interpolation between background and transfer Block:
The interpolation zone between the stationary background block and the rotating transfer block is defined by the overlap region between the background block and the outer Chimera boundary of the transfer block. Since the transfer block rotates at a constant and predefined frequency over all coupling steps, no chimera hole cutting is required in this region. Figure 2.20 shows a close-up view of a cross-section. The highlighted turquoise region in the x-y plane represents the interpolation zone. Here, the grid discretization for both the background and the transfer blocks is identical to ensure accurate interpolation of flow field data.

2.4.3. Modeling of the Blade Motion in CFD Solver

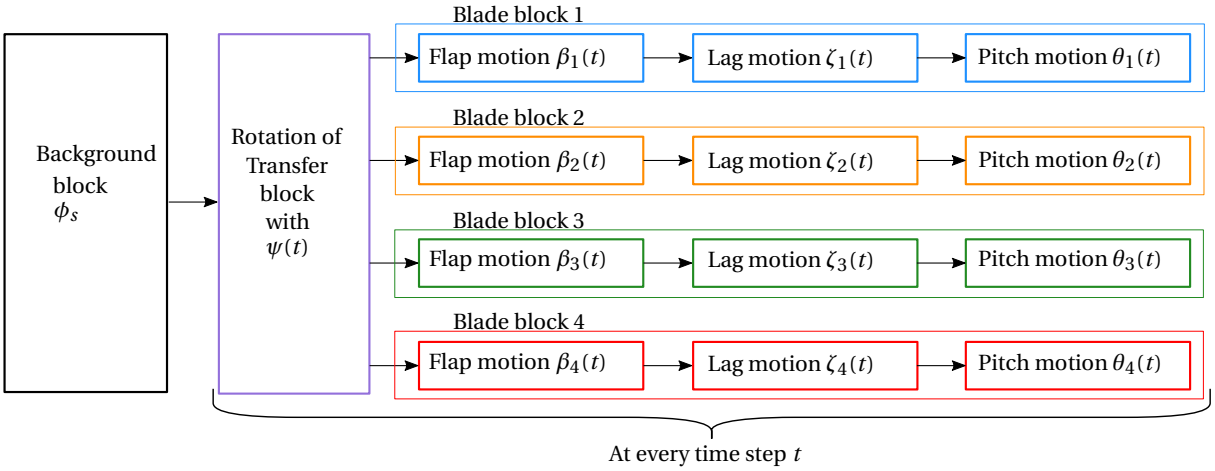

Figure 2.21.: Hierarchy of motion applied to grid blocks.

In the TAU simulation framework, the movement of distinct grid blocks can be effectively represented as a series of periodic rigid body motions. These motions can be defined through translation or rotation, relative to a user-defined coordinate system. These rigid motions are conveniently represented mathematically using either polynomial functions or Fourier series, enabling the modeling of a broad spectrum of complex motions. In the present study, rotation was used as the primary form of rigid body motion to accurately simulate the complex movements of the rotor system, including the pitch and roll of the rotor shaft and the flapping, pitching, and lagging motions of the rotor blades. The following Fourier series representation is implemented in TAU to compute, at every time step, the required angle of rotation:

$$\phi(t) = c_0 + \sum_{k=1}^{N_{FR}} \left(c_k \cos\left(k\omega_R t\right) + d_k \sin\left(k\omega_R t\right)\right), \tag{2.20}$$

where $\phi(t)$ denotes the angle of rotation at time t, c_0 is the constant term, c_k and d_k are the Fourier coefficients, N_{FR} is the number of Fourier terms, and ω_R represents the angular frequency. In order to achieve the desired end location of the blade and accurately model the behavior of the rotor system, a specific hierarchical order of motion must be followed when applying movements to the individual grid blocks. The specific hierarchical structure used in this work is depicted in Fig. 2.21. Within each time step t of the simulation, the rotor blades movements are systematically ex-

ecuted in a prescribed order. First, the corresponding pitch motion $\theta_i(t)$ was applied to different blade blocks, followed by the lead-lag $\zeta_i(t)$ and flap $\beta_i(t)$ motions in the specified sequence. Next, the grid assembly, consisting of all the blade blocks and the transfer block, undergoes the rotation $\psi(t)$ with a constant RMP. Finally, as the concluding step, the background, blade blocks, and transfer block are uniformly tilted with the constant shaft angle ϕ_s. The pitch motion, lead-lag motion, and flap motion are extracted from the CAMRAD II reference solution for the trimmed state. These motions are then applied to the corresponding blade in TAU, while the remaining blades receive the same motions with a corresponding phase shift. The Fourier coefficients used to represent the corresponding motions are determined by the mean value and the first harmonic.

2.4.4. Grid Deformation for the Active Blade Sections

In this work, the active blade section is fully integrated into the blade with no gaps in the spanwise or chordwise directions, since [54] showed that including gaps can deteriorate the lift-to-drag ratio. In order to model the actuation of the FishBAC mechanism, the CFD surface grid of the dynamically actuated BO105 rotor blade was divided into two regions: an undeformed part and an active section with width s. In between these two regions, linear transition regions of length t that connected to a fully active camber region. These two regions were connected by linear transition regions of length t. Figure 2.22a depicts how the camber morphing sections are applied to the active blades. Along the spanwise direction, the active camber is implemented between $0.35R$ and $0.85R$, including the transition region $t = 0.1R$ on the outboard and the inboard side of the blade. A constant morphing camber deflection of δ is applied along the spanwise range s from $r = 0.45R$ to $r = 0.75R$. This deflection transitions linearly from zero to the prescribed value δ, ensuring smooth blending between the passive and active sections. Notably, the camber morphing is applied to the corresponding blade section, starting at $0.75c$ and extending towards the trailing edge. The applied prescribed actuation schedule is shown in Fig. 2.22b and was extracted from the parametric study published by Komp et al. [65]. It yielded optimum rotor power savings related to camber morphing actuation at the advance ratio of $\mu = 0.15$ as the camber morphing was applied over a similar spanwise range. It shall also be noted, however, that this study was based on a comprehensive rotor analysis using the four-bladed BO105 rotor, including elastic rotor blade modeling. This actuation schedule is obtained from Eq. 2.21 using the values specified in Table 2.3. Here, the camber deflection δ is determined at every azimuth angle ψ using the mean value δ_{0P}, the first harmonic δ_{1P} and the second harmonic δ_{2P}. All four blades experience the same camber deflection δ at a given azimuth angle. The TAU utility grid deformation technique, detailed subsection 2.1.1.3, is used to achieve camber morphing of the blades. This technique deforms the grid around each morphing section on all four blades. The deformation extends outward from the blade surface, impacting cells within a circular region with a radius of 1.1 times the chord length ($1.1c$).

In order to apply the RBF method, as explained in 2.1.1.3, the reference undeformed surfaces have to be specified. While each blade has a highly detailed geometry defined by over 11.5 million points, using all of them for RBF deformation would be computationally expensive. To address this, only a strategically chosen subset of points is used to represent the blade surface during morphing. In this work, the number of base points required for the RBF interpolation method

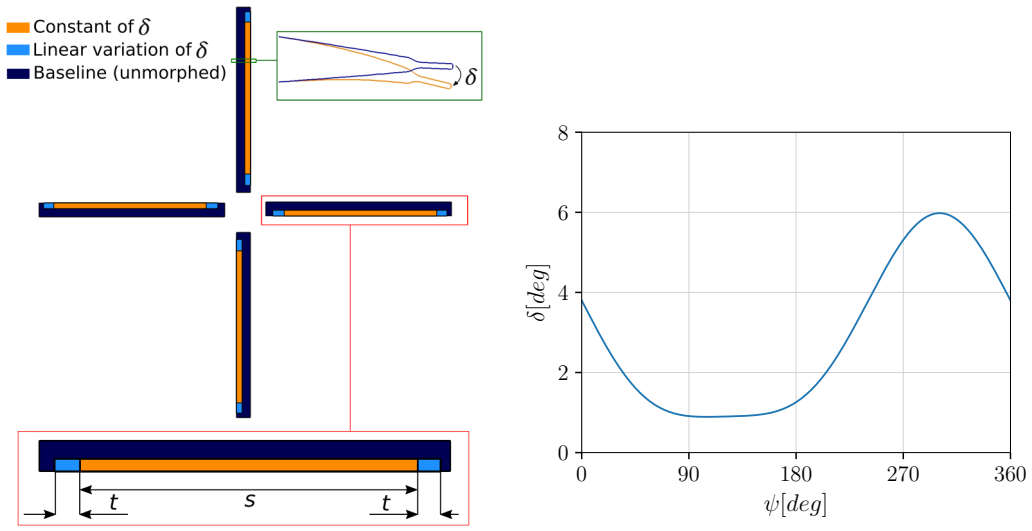

(a) Illustration of the active camber section along the blades.

(b) The applied schedule to camber morphed the blades over azimuth, extracted from [65].

Figure 2.22.: Definition of the active camber section and the actuation profile.

is reduced to 7,927 for every blade. These points are defined in separate scat files (scattered-data) specific to each blade. For each blade section experiencing camber morphing, every fifth point is chosen from the grid blade surface to define the grid deformation within the chordwise morphing zone ($0.75 < x/c < 0.99$). Additionally, to guarantee sufficient resolution for the trailing edge curvature, every third point is selected from the blade grid surface. Finally, to ensure good grid quality, a small portion of the unmorphed section is also included. This involves selecting every 30th point from the grid on the blade surface at the fourth blade section, as shown in Fig. 2.23.

Table 2.3.: Actuation inputs used to determine the camber morphing deflection over the azimuth ψ for the active blades.

Parameter	δ_{0P}	ϕ_{1P}	δ_{1P}	ϕ_{2P}	δ_{2P}
Actuation inputs	2.65°	299°	2.22°	249°	0.65°

$$\delta = \delta_{0P} + \sum_{n=1}^{2} \delta_{nP} \cdot cos(n\psi - \phi_{nP}) \tag{2.21}$$

Figure 2.23 serves as a representative example, comparing the target camber morphing with the actual deformed blade surface at a specific location ($r/R = 0.65$ and $\psi = 300$ deg) where the maximum of schedule deflection is achieved, as shown in Fig. 2.22b. The RBF-based grid deformation technique effectively captures the morphing of the blade at all time steps. Figure 2.24a demonstrates close match between the deformed surface grid and the target camber deflection throughout the entire morphing section for example at $r/R = 0.65$ and $\psi = 300$ deg, achieved using the RBF method. This agreement extends even to the trailing edge curvature of the deformed grid,

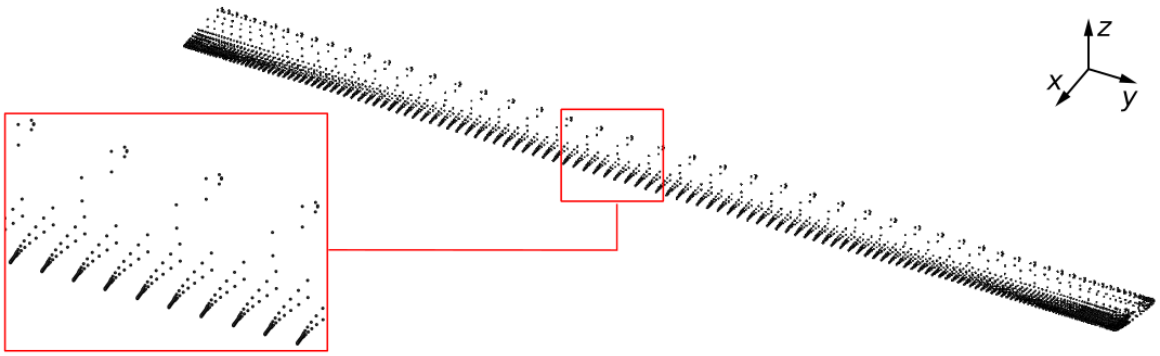

Figure 2.23.: Distribution of the scattered data which defines the target blade deformation.

as shown in Fig. 2.24b. Figure 2.25 compares the grid quality of the blade section at $r/R = 0.75$

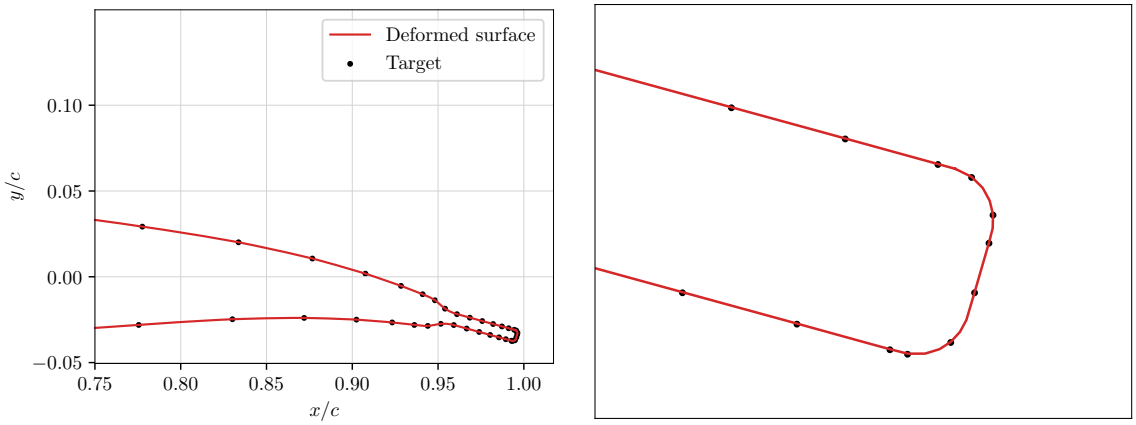

(a) Comparison between the deformed blade section at $r/R = 0.65$ and $\psi = 300$ deg and the target camber morphing.

(b) Close-up comparison between the deformed blade section and the target camber morphing at $r/R = 0.65$ and $\psi = 300$ deg.

Figure 2.24.: Illustration of the camber morphing section and the schedule applied over the azimuth ψ to morph the camber of the blades.

and $\psi = 270$ deg for both passive and active rotors, shown in 2.25a and 2.25b respectively. The orthogonality (measure of cell angle) of the grid cells near the blade surface remains consistent along the chord length untill $x/c = 0.95$, indicating minimal distortion in this crucial region. The most pronounced variation in grid quality occurs within the tab region, located below the lower surface. Despite the observed variation in grid quality within the tab region, the cell angles remain above 60 deg. This is still considered acceptable for accurate simulations, especially because this region is located below the trailing edge and has less influence on the overall aerodynamics.

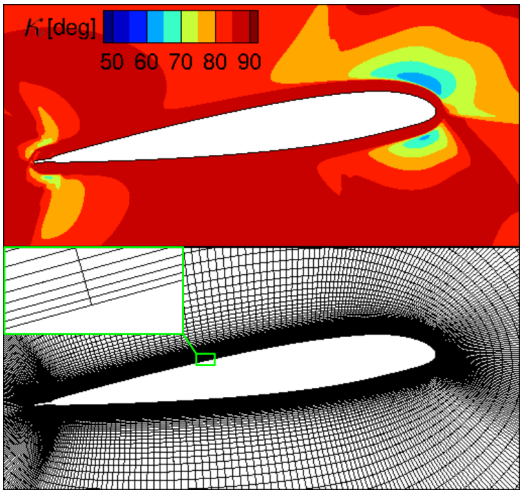

(a) Cell orthogonality κ of the passive blade at $r/R = 0.75$.

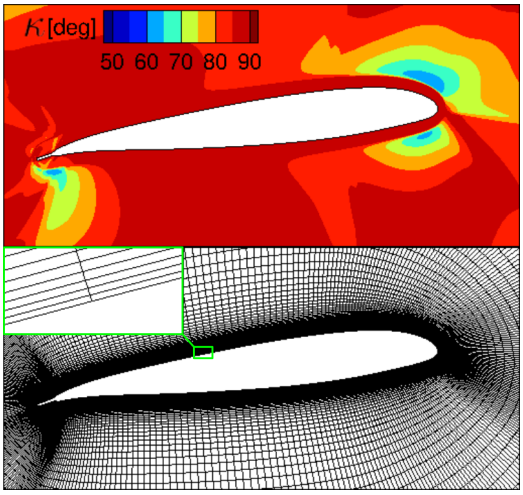

(b) Cell orthogonality κ of the active blade at $r/R = 0.75$.

Figure 2.25.: Comparison of cell orthogonality κ at $r/R = 0.75$ between the passive and active blade at pitch angle $\theta = 8$ deg and morphing deflection $\delta = 4$ deg. The shape of the active blade is obtained by means of grid deformation.

2.4.5. Modeling of the Rotor in the CSD Solver

The primary role of the CSD model in the CFD/CSD coupling is to determine the appropriate blade motion required to achieve the desired trim state. As mentioned earlier in Subsection 2.4.1, the aerodynamic loads calculated by the CFD solver refine the initial loads estimated by CAMRAD II. The iterative coupling between CFD and CSD ensures an accurate representation of rotor aerodynamic forces and moments distribution across the rotor disk. In this work, the rotor CSD model established in CAMRAD II, defines trim conditions by selecting three independent parameters from the integrated rotor forces and moments acting on the non rotating system. The trim conditions are defined to ensure that the rotor reaches equilibrium in aerodynamic forces and moments under the given flight conditions.

Both the passive and active rotor models feature rigid blades. The passive rotor model is derived from an existing equivalent rigid blade model for the four-bladed BO105 rotor which was published within the SABRE project by DLR [114]. The DLR equivalent model was developed to represent the fundamental blade flapping behavior of the hingeless BO105 rotor. In this reference model, the pitch bearing was located at $r_{PL} = 0.169$ m. Additionally, the flap and lead-lag hinges are positioned with an offset from the rotor hub, corresponding to $a_\beta = 0.746$ m and $a_\zeta = 0.817$ m, and with a spring constant equal to $k_\beta = -5849$ and $k_\zeta = 38814$ Nm, respectively. To simplify the transfer of blade motion from the CSD to the CFD model, as well as the interpolation between blade and transfer blocks in the CFD solver, the pitch bearing was positioned near the rotor hub at $r/R = 0.005$, while both the flap and lead-lag hinges were moved to $r/R = 0$ in the rotor model used for the CFD/CSD coupling. Additionally, the flapping and lagging spring constants are set to 50,000 Nm/rad to model the rotor as rigid and to ensure that under the same trim conditions both the thrust distribution across the rotor disk and the blade flapping behavior closely replicate those

of the equivalent BO105 rotor model. To highlight the differences between the equivalent BO105 rotor model from DLR and the rotor model used in the CFD/CSD coupling, Table 2.4 provides a summary of the key characteristics of both rotors. Additionally, Fig. 2.26 presents a qualitative comparison of the hinge locations for both rotor configurations.

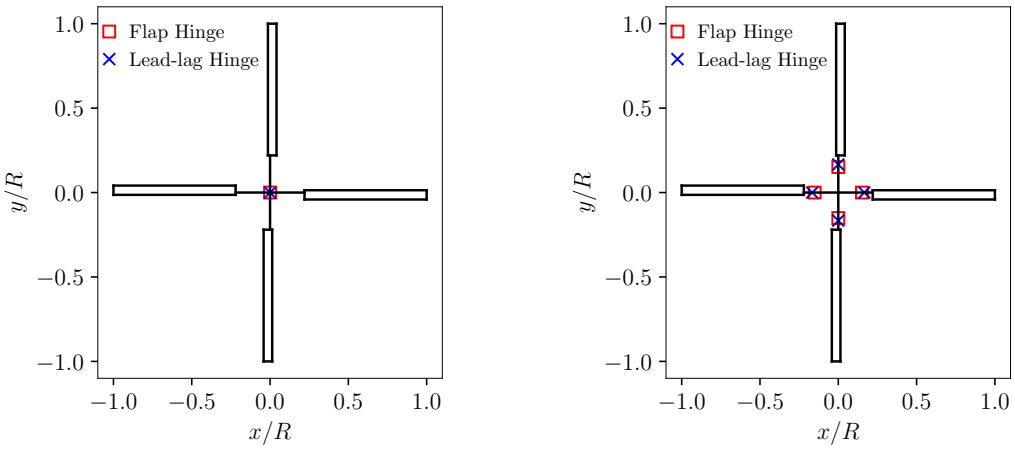

(a) Locations of flap and lead-lag hinges in the CAMRAD II model used in the CFD/CSD coupling.

(b) Locations of flap and lead-lag hinges in the CAMRAD II model used in the DLR BO105 equivalent model.

Figure 2.26.: Representation of the flap and lead-lag hinge locations in a CFD/CSD coupling model and a simplified BO105 equivalent model.

Rotor Blade Definition:
For both the equivalent DLR model and the rotor model used in the CFD/CSD coupling, each of the four blades is modeled as a rigid beam equipped with flapping and lead-lag hinges. For each blade, the original rectangular planform of the BO105 is adopted with a blade radius of 4.912 m and a blade chord of 0.27 m. Additionally, a linear blade twist of $\theta_{tw} = -8$ deg from hub to tip is applied. The twist distribution for each blade, adopted from [67], is illustrated in Fig. 2.27a. The blade mass and center of gravity distributions are defined at 41 radial positions as shown in Figs. 2.27b and 2.27c, respectively. Further details were also published in [67]. The root cutout region is assumed to extend to $r/R = 0.22$, where no aerodynamics are modeled.

For the active blade, the same properties as the passive blade are assumed also throughout the camber morphing region, with the structural dynamics of the morphing mechanism not considered in this study. No physical hinge was modeled for the start of camber morphing, as suggested in [65, 66, 67]. Instead, the camber morphing effect was modeled by reading the aerodynamic coefficients from the airfoil tables corresponding to the specific camber deflection. These simplifications are beyond the scope of the current work and are suggested for further investigation in future research.

Aerodynamic Modeling:
In the CFD/CSD coupling, the CAMRAD II model for both passive and active rotors uses a linear inflow model to calculate the initial aerodynamic forces and moments based on lifting-line theory. These forces are derived from the aerodynamic coefficients C_l, C_d, and C_m listed in the airfoil ta-

bles. The coefficients were computed using a steady TAU solver, as detailed in 2.2.1. Various angles of attack, within the range of $\alpha \in [-10, \alpha_{stall}]$, were considered with an increment of $\Delta\alpha = 0.5$ deg. The airfoil tables also cover a wide spectrum of Mach numbers M between 0.2 and 0.9, with an increment of $\Delta M = 0.1$. Additionally, the tables include the aerodynamic coefficients for the standard NACA23012 airfoil as well as for the camber morphed airfoils with deflections ranging from $\delta = -4$ deg to 14 deg, in increments of $\Delta\delta = 1$ deg. The resolution of the airfoil tables is improved by interpolating the aerodynamic coefficients for unconsidered camber morphed airfoils in the steady simulation. This is accomplished using radial basis function interpolation, with an increment of $\Delta\delta = 0.5$ deg to enable the inclusion of more aerodynamic coefficients across the range of prescribed camber-morphed airfoil configurations and ensure smooth transitions and numerical convergence across the deflection range, as suggested in [68]. A representative selection of the aerodynamic coefficients of morphed airfoils from the airfoil table is shown and discussed for $M = 0.4$ and $M = 0.6$ in the result section 3.1.

In CAMRAD II, the aerodynamic lifting line of the blade is discretized by 68 aerodynamic panels, which are distributed over the blade radius. The discretization of panels follows a pattern similar to the CFD grid resolution, with panel size progressively decreasing towards the rotor blade tip, as illustrated in Fig. 2.27d. Additionally, for both passive and active rotors models, the ONERA Edlin model, with it defaults setting, is used to account for unsteady effects not captured by the airfoil tables, as explained in 2.1.2. Furthermore, CAMRAD II does not provide the capability to model a smooth transition between unmorphed and morphed regions of the blade. For this reason, the active blade section is modeled from $r/R = 0.3$ to $r/R = 0.8$.

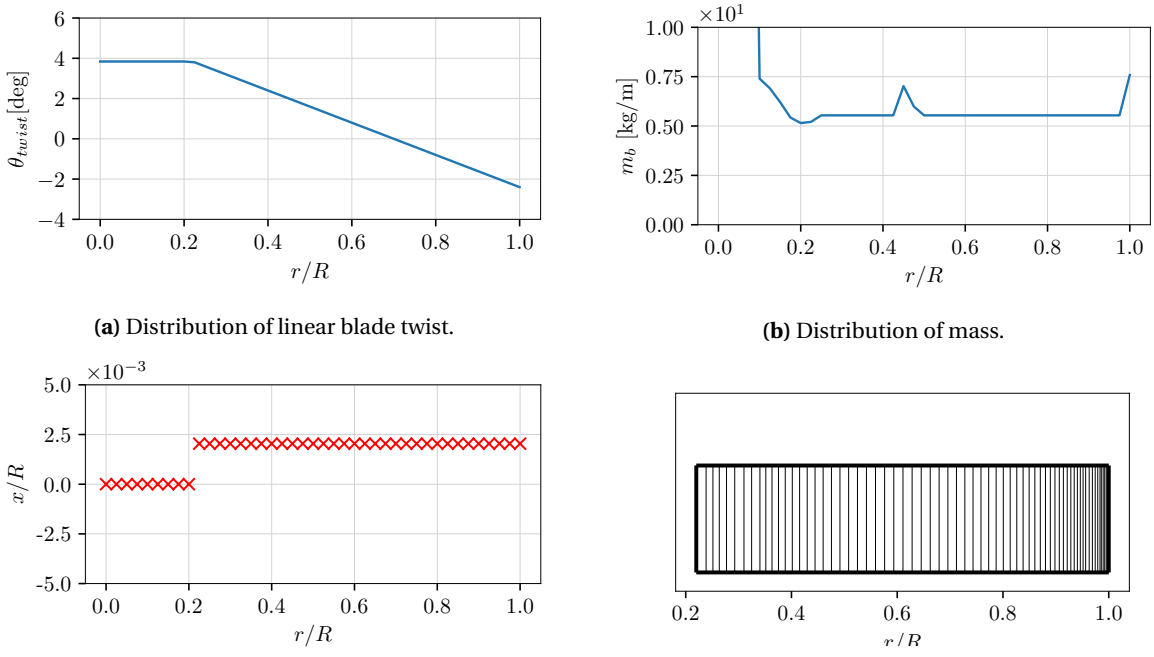

(a) Distribution of linear blade twist.

(b) Distribution of mass.

(c) Radial position of mass distribution.

(d) Distribution of the aerodynamic panels.

Figure 2.27.: Representation of the relative blade properties in CAMRAD II along the blade span.

Table 2.4.: Rotor geometry and test conditions for the CFD/CSD and the BO105 equivalent models.

Parameter	Symbol	Values for CFD/CSD model	Values for equivalent model	Units
Airfoil	-	NACA23012	NACA23012	-
	-	with tab	with tab	-
Blade chord	c	0.27	0.27	m
Blade twist	θ_{twist}	-8	-8	deg/R
Number of blades	N_b	4	4	-
Rotational speed	Ω	44.5(425)	44.5(425)	rad/s(RPM)
Rotor radius	R	4.912	4.912	m
Rotor shaft tilt (pos. aft)	α_S	-3	-3	deg
Zero pitch radial location	r_{ref}	0.70	0.70	-
Rotor solidity	σ_{MR}	0.07	0.07	-
Precon angle (pos. upward)	β_P	2.5	2.5	deg
Pitch bearing offset	r_{PL}	0.005	0.169	m
Flapping hinge offset	a_β	0.0	0.746	m
Lagging hinge offset	a_ζ	0.0	0.817	m
Flapping spring constant	k_β	-50000	-5849	Nm/rad
Lagging spring constant	k_ζ	50000	38814	Nm/rad

3. Results and Discussion

This chapter presents the results obtained from the investigation into the influence of camber morphing on the aerodynamics of helicopter rotor blades. As established in the introduction 1.3, the central research question of this thesis was decomposed into three key sub-questions. This chapter addresses these specific questions by presenting the findings obtained from the investigations. The first section of this chapter evaluates the aerodynamic characteristics of a 2D steady camber morphed airfoil. This analysis provides insights into the impact of camber morphing on key aerodynamic parameters such as lift and drag coefficients, under steady-state conditions. Building upon this knowledge, the second section investigates the differences between steady and unsteady aerodynamic effects. Here, the focus shifts to analyzing how conventional rotor comprehensive analysis tools can handle unsteady effects arising from camber morphing and pitching under pseudo-steady conditions. The final result section investigates the three-dimensional aerodynamics of active rotor blades compared to passive rotors. By means of a high-fidelity CFD/CSD coupling, this section explores the variations in thrust, blade surface pressure, and wake structure resulting from dynamic camber morphing. For a detailed description of the numerical methods, software tools, and the workflow used in these investigations, please refer to Chapter 2.

3.1. Evaluation of Steady Aerodynamics for 2D Steady Camber-Morphed Airfoils

3.1.1. Aim of the Study

In order to determine the aerodynamics of a rotor blade using comprehensive analysis tools such as CAMRAD II or Dymore, it is necessary to calculate the aerodynamic coefficient of the blade sections at various radial locations for different Mach numbers and angle of attack. Due to the rotation of the blades, every radial section experiences a different flow velocity U_r, depending on the operating conditions. During hovering flight condition, the Mach number varies only along the blade span, while it remains constant around the blade azimuth. In forward flight condition, the aerodynamic environment becomes asymmetric and the oncoming flow Mach number at the blade sections becomes a function of their radial location, rotor azimuth position, and the forward flight velocity [2]. Figure 3.1 illustrates the difference in the Mach number distribution between the hovering and forward flight conditions using the following simple equations 3.1 from blade element theory. The difference in Mach number distribution becomes more pronounced while the advance ratio μ increases, as shown in Figs. 3.1b and 3.1c.

$$M = \frac{U_r}{a} = \frac{U_{\text{tip}}}{a}(r + U_{\text{tip}} \cdot \mu \sin(\psi)), \tag{3.1}$$

where the speed of the sound is considered to be $a = 320$ m/s and the blade tip velocity $U_{\text{tip}} = 218$ m/s. For comprehensive rotorcraft analysis tools like CAMRAD II and Dymore, a wide range of Mach numbers, typically between 0.2 and 0.9 as shown in Fig. 3.1, is considered to compute aerodynamic blade loads. These tools rely on steady-state, two-dimensional aerodynamic coefficients (lift coefficient, C_l; drag coefficient, C_d; and moment coefficient, C_m) for the various airfoil sections of the rotor blade. These coefficients are determined across this broad Mach number range to account for different flight conditions. Additionally, a wide range of angles of attack at every Mach number are included, from negative values into stall to capture the variations in aerodynamic conditions across the rotor's azimuth and blade span.

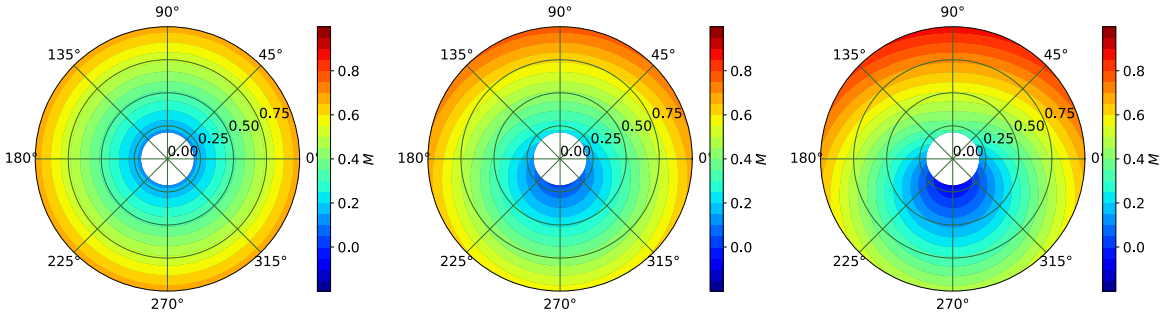

(a) $\mu = 0$ **(b)** $\mu = 0.15$ **(c)** $\mu = 0.3$

Figure 3.1.: Variation of Mach number over the rotor azimuth ψ for $U_{tip} = 218$ m/s.

The objective of this section is to analyze the aerodynamic coefficients of camber morphed blade sections in comparison to the NACA23012 baseline with a chord length of $c = 0.27$ m and a tab starting from $x = 0.957c$, specifically the 2D coefficients C_l, C_d, and C_m. This preliminary assessment can provide initial insights into the aerodynamics associated with the active rotor. It helps to develop an initial understanding of the rotor's aerodynamic behavior before diving into comprehensive rotor analysis studies. Figure 3.2 shows the prescribed camber morphing airfoil shapes considered in this investigations. An upward camber morphed shape with a deflection of $\delta = -4$ deg was chosen as a starting point. Subsequently, deflection angles were increased in increments of 2 deg until a maximum of $\delta = 10$ deg was reached. The camber morphing was applied from $x = 0.75c$ by means of the method explained in the subsection 2.2.2. Mach numbers 0.4 and 0.6 are commonly encountered across the rotor disk during hover, low speed ($\mu = 0.15$) or high speed ($\mu = 0.3$) flight regimes. These specific Mach numbers were chosen to evaluate the variation in aerodynamics resulting from camber morphing.

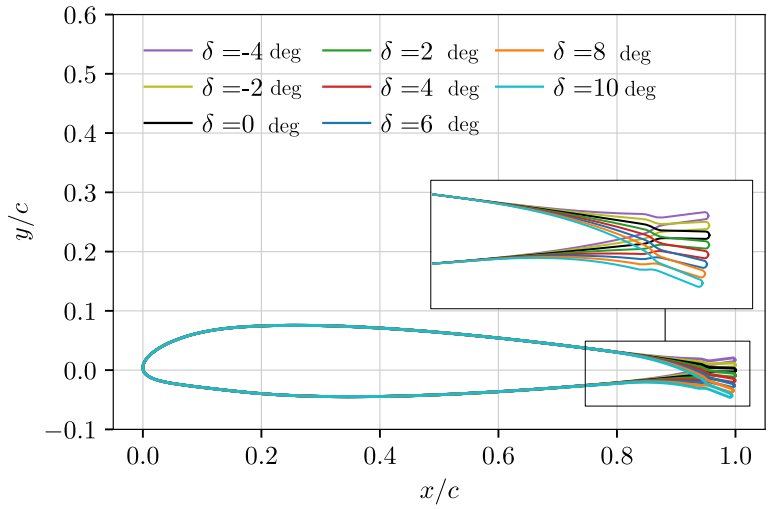

(a) Representation of the investigated prescribed camber morphed airfoils.

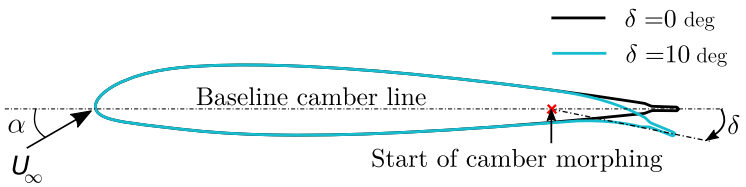

(b) Definition of angle of attack α and camber morphing deflection δ.

Figure 3.2.: Illustration of the investigated camber morphed airfoil and definition of angle of attack and camber morphing deflection.

3.1.2. Numerical Setup

In this study, TAU was used as a steady solver with the central scheme for spatial discretization and a second order backward Euler method was used for temporal discretization. Details of these discretization techniques are provided in 2.1.1.2. The Spalart-Allmaras turbulence model SA-neg was chosen, assuming the boundary layer to be fully turbulent. The turbulence modeling approach is explained in 2.1.1.1. The airfoils were simulated in a far field environment. The subsection 2.2.3 describes the grid topology used in the simulations and the overall workflow of the simulation process is outlined in subsection 2.2.1. The convergence criteria for the simulations were established at a density residual of 10^{-6}. To maintain consistency and minimize numerical errors, the same numerical setup was applied across both the baseline configuration and all variations involving camber morphing.

3.1.3. Verification Case

The numerical setup was first validated by reproducing the 2D polars of an experimental test on a tabbed NACA23012 airfoil with a chord length of 0.12 m (5.0 in) and span of 0.203 m (8.0 in), where the airfoil tab also started from $x = 0.957c$. The experimental study was conducted for different Mach numbers between 0.4 and 0.85. The tests were carried out in a two-dimensional cross section measuring 0.203 m (8.0 in) by 0.457 m (18 in) at the Aircraft Research Association (ARA) wind tunnel in Bedford [22]. In the CFD simulations, an O-grid block topology was used to model the computational domain, as explained in subsection 2.2.3. The grid resolution was chosen based on a convergence study in [2] conducted for an unmorphed and camber morphed NACA23013 airfoil without a tab and with a chord length of $c = 0.27$ m. In this study, the lower and upper surfaces were resolved using 150 points respectively and the entire domain consisted of approximately 80,000 cells.

The verification of the numerical setup was achieved by comparing the aerodynamic coefficients of a tabbed NACA23012 airfoil ($c = 0.12$ m) with the wind tunnel data at Mach numbers $M = 0.4$, 0.5, and 0.6. Figure 3.3 shows excellent agreement between steady CFD results and the experimental data for lift coefficient C_l versus angle of attack α across all Mach numbers. Minor discrepancies were noticeable near stall, but the overall trend aligns well. The comparison of the computed drag polars for various Mach numbers (see Fig. 3.4) also reveals a good correlation with wind tunnel data, particularly in the linear C_l regime. Notably, the CFD results capture drag behavior even at high Mach numbers $M = 0.6$. Finally, Figure. 3.5 demonstrates that for the considered Mach numbers the CFD simulations could replicate the variation of the measured pitching moment coefficient C_m over the angle of attack α with acceptable discrepancies near to the stall region. Therefore, this strong correlation between the CFD results and experimental data across different Mach numbers and angles of attack emphasizes the effectiveness of the numerical setup used in the 2D steady-state simulation for capturing the aerodynamic coefficients.

To ensure the credibility of the numerical setup, a verification process was conducted using an alternative steady compressible CFD solver, namely SU2. This verification was performed at a Mach number of $M = 0.4$ for both the baseline airfoil and the camber morphed airfoil with deflection

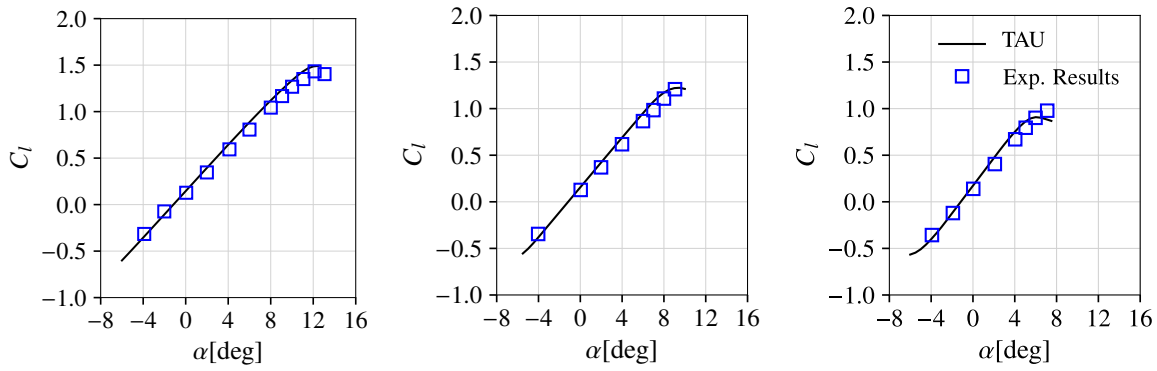

(a) $M = 0.4$ **(b)** $M = 0.5$ **(c)** $M = 0.6$

Figure 3.3.: Validation of the computed lift coefficient C_l with the experimental data from [22] for different Mach numbers.

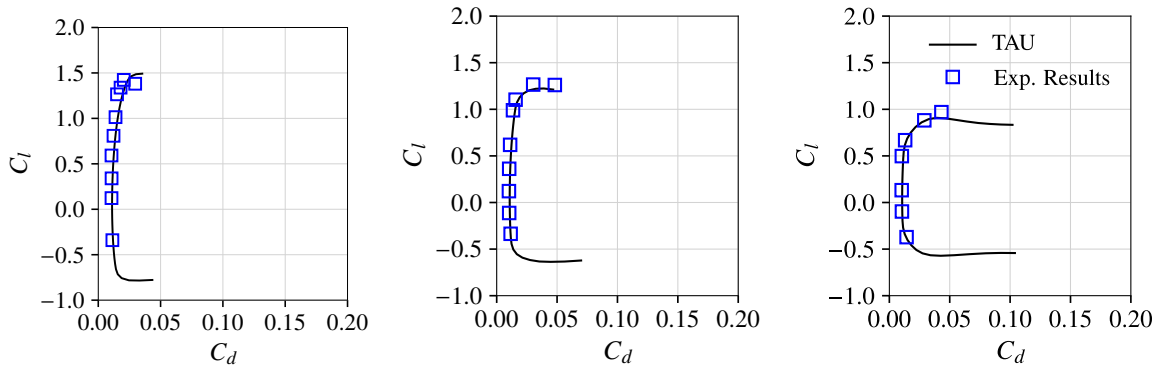

(a) $M = 0.4$ **(b)** $M = 0.5$ **(c)** $M = 0.6$

Figure 3.4.: Validation of the computed drag coefficient C_d with the experimental data from [22] for different Mach numbers.

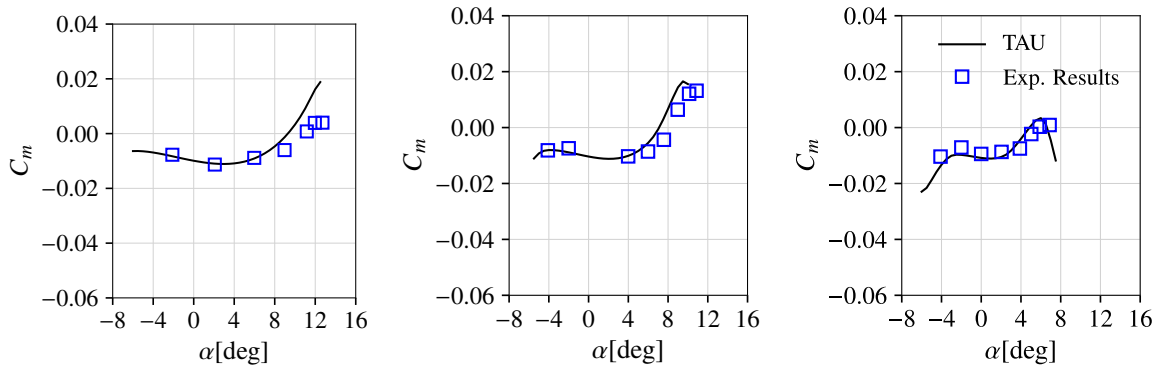

(a) $M = 0.4$ **(b)** $M = 0.5$ **(c)** $M = 0.6$

Figure 3.5.: Validation of the computed moment coefficient C_m with the experimental data from [22] for different Mach numbers.

angles of $\delta = 4$ deg (medium) and $\delta = 8$ deg (high). The same temporal and spatial discretizations were used in both TAU and SU2, and the identical computational mesh for the respective baseline or morphed airfoil was used in each solver to solve the RANS equations for the CFD domain. Figures 3.6, 3.7, and 3.8 compare the lift, moment, and drag coefficients computed with TAU against those obtained using SU2 for the baseline configuration, the camber morphed airfoil with a deflection angle of $\delta = 4$ deg, and the camber morphed airfoil with a deflection angle of $\delta = 8$ deg, respectively. Both solvers captured the same trends in the lift, moment, and drag coefficients across a wide range of angles of attack, from -8 deg to 8 deg. However, minor discrepancies were observed, primarily near the stall region from $\alpha = 9$ deg.

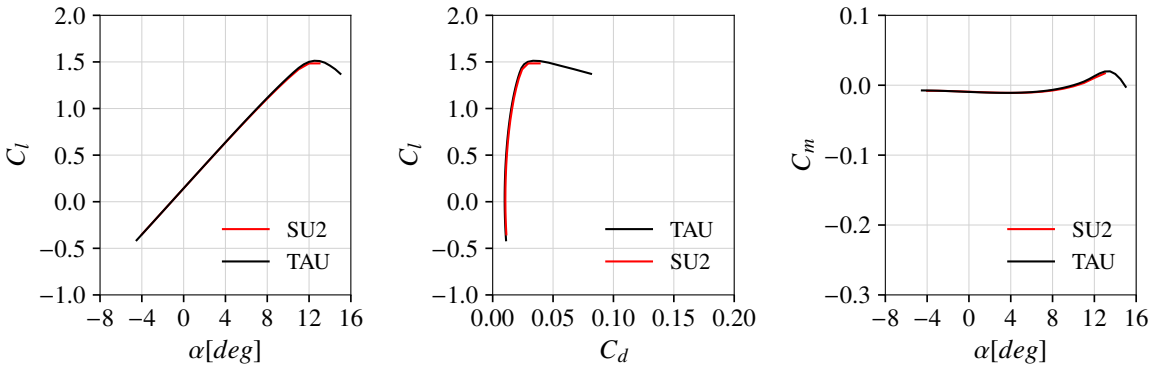

(a) Variation of C_l over α **(b)** Variation of C_l over C_d **(c)** Variation of C_m over α

Figure 3.6.: Comparison of aerodynamic coefficients computed by TAU against the coefficient obtained by SU2 at Mach 0.4 for the baseline airfoil.

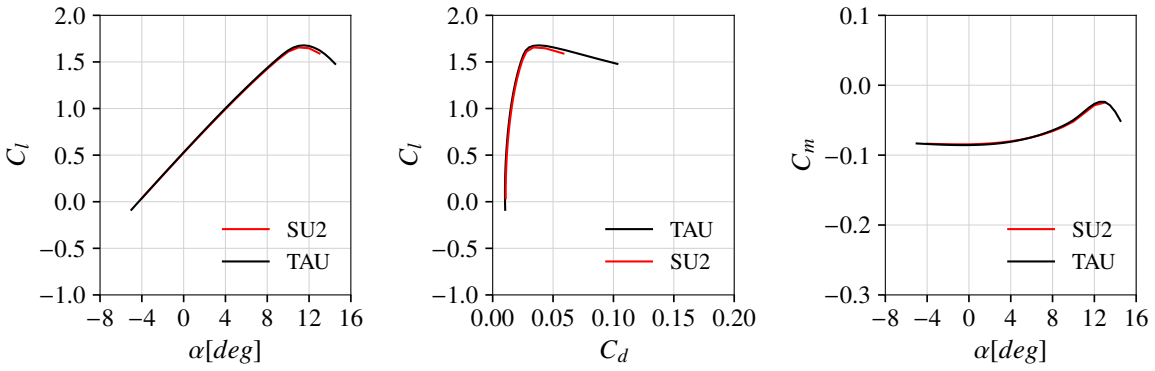

(a) Variation of C_l over α **(b)** Variation of C_l over C_d **(c)** Variation of C_m over α

Figure 3.7.: Comparison of aerodynamic coefficients computed by TAU against the coefficient obtained by SU2 at Mach 0.4 for the camber morphed airfoil with the deflection $\delta = 4$ deg.

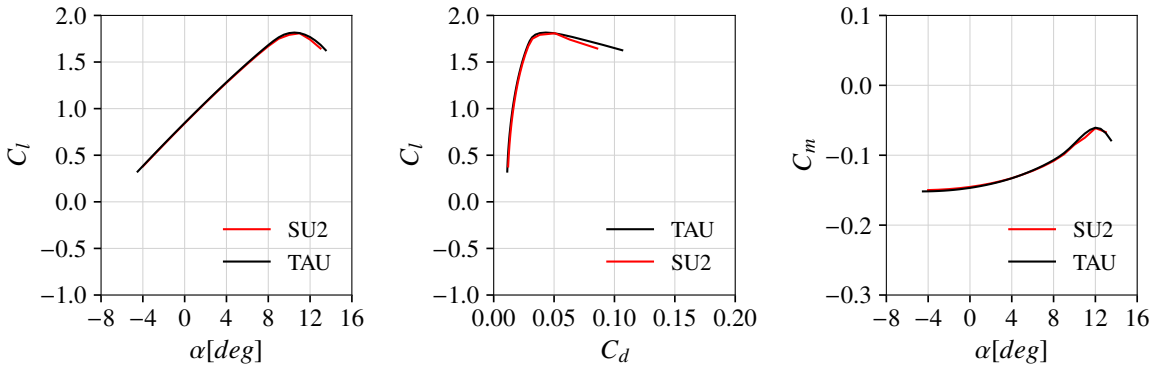

(a) Variation of C_l over α **(b)** Variation of C_l over C_d **(c)** Variation of C_m over α

Figure 3.8.: Comparison of aerodynamic coefficients computed by TAU against the coefficient obtained by SU2 at Mach 0.4 for the camber morphed airfoil with the deflection $\delta = 8$ deg.

3.1.4. Effect of Camber Morphing on Lift Coefficient

The impact of camber morphing on the lift coefficient was evaluated in comparison to the baseline across various angles of attack at Mach numbers 0.4 and 0.6, as shown in Figs. 3.9a and 3.9b, respectively. The investigated camber morphed airfoils are illustrated in Fig. 3.2, where the camber was morphed upwards by up to $\delta = -4$ deg and downwards by up to $\delta = 10$ deg.

Increasing camber morphing demonstrably decreases the zero lift angle of attack for both Mach 0.4 and 0.6, with the slope of the linear portion remaining relatively constant. This translates into a direct correlation – the greater the downward camber morph, the higher the lift curve lies in comparison to the baseline ($\delta = 0$ deg). Furthermore, Figs. 3.9a and 3.9b illustrate that the relative gain in lift coefficient dC_l from morphing is more pronounced for lower δ cases compared to cases with higher δ. For instance at $M = 0.4$, increasing the camber deflection from $\delta = 2$ deg to 4 at an angle of attack of $\alpha = 5$ deg yields a significant lift increase of $dC_l = 0.17$. This effect diminishes with higher camber airfoils, where morphing from 8 deg to 10 deg only results in a $dC_l = 0.10$ relative lift increase at the same angle of attack. It was also observed, that the downward camber morphing significantly improved the maximum lift capability compared to the baseline airfoil. This morphing technique enabled achieving the same maximum lift coefficient of the baseline airfoil $C_{l,max} = 1.51$ far from the stall region. This translates into increased operational safety under high lift conditions.

The greatest lift increase was achieved with downwards camber morphing deflection $\delta = 10$ deg. At Mach 0.4, this morphing technique yielded a remarkable 24% improvement in maximum lift coefficient $C_{l,max}$, from 1.51 to 1.87. This translates to a significant increase in blade lift generation capability without compromising stall characteristics. Similarly, at Mach 0.6, deflecting the camber by $\delta = 10$ deg led to a 50% increase in $C_{l,max}$ from 0.89 to 1.44. Thus, in scenarios where the mean lift coefficient of the rotor can be approximated as $\bar{C}_l \approx \bar{C}_L = 6(C_T/\sigma)$, as assumed in [74], the expansion of the lift envelope allows for greater thrust generation. This is particularly beneficial in challenging hover conditions, such as those encountered at high temperatures and

high altitudes, or when increasing lift on the retreating blade side is required during forward flight while minimizing the risk of stall [23]. This can also be relevant for heavy-lift operations, enabling the helicopter to carry a greater maximum takeoff weight. Additionally, morphing the camber upwards resulted in a noticeable decrease in lift compared to the baseline. For instance, deflecting the camber upwards with $\delta = -4$ deg or $\delta = -2$ deg produced a significant reduction in lift compared to the baseline configuration. For both Mach number 0.4 and 0.6, as the upwards morphing deflection δ of the camber increased, the lift coefficient C_l consistently decreased in comparison to the baseline.

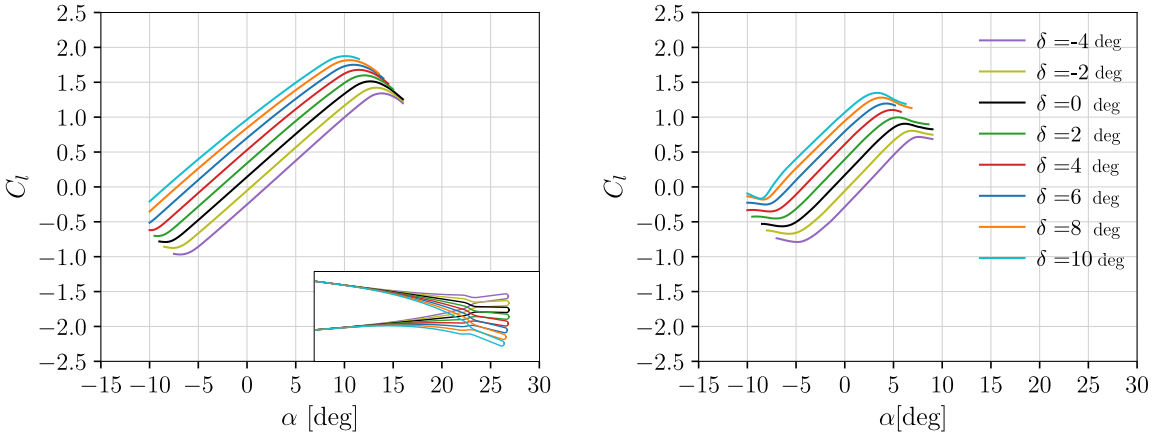

(a) Variation of C_l over α at $M = 0.4$.

(b) Variation of C_l over α at $M = 0.6$.

Figure 3.9.: Variation of the lift coefficient C_l of the morphed airfoils over the angle of attack α for the Mach numbers $M = 0.4$ and $M = 0.6$.

3.1.5. Effect of Camber Morphing on Drag Coefficient

The influence of camber morphing deflection on the drag polar, compared to the baseline airfoil at Mach numbers 0.4 and 0.6, is shown in Figs. 3.10a and 3.10b, respectively. Within the lift coefficient range (0 to 1.25) at $M = 0.4$, camber morphing downwards achieved the same lift as a baseline airfoil without incurring an additional drag penalty. The benefits of using camber morphing was pronounced mostly near stall conditions of the baseline airfoil. Here, downward camber morphing airfoils provided the same maximum lift coefficient of a baseline airfoil but with a significantly lower drag penalty. For example, at Mach 0.4, the baseline airfoil could achieve a maximum lift coefficient of $C_{l,max} = 1.51$, but at the cost of a high drag coefficient of $C_d = 0.035$. With camber morphing deflection $\delta = 8$ deg, the same lift was achieved with a much lower drag coefficient of $C_d = 0.024$.

At a Mach number $M = 0.6$, the range of lift coefficients for which the camber-morphed airfoils achieved the same lift as the baseline airfoil with minimal drag increase was narrowed to $0 < C_l < 0.65$. This is due to the lower stall angle of attack for the baseline at this higher Mach number. However, the benefits of camber morphing compared to the baseline became more significant as lift coefficient approached stall conditions for the baseline (around $C_l = 0.89$). For example,

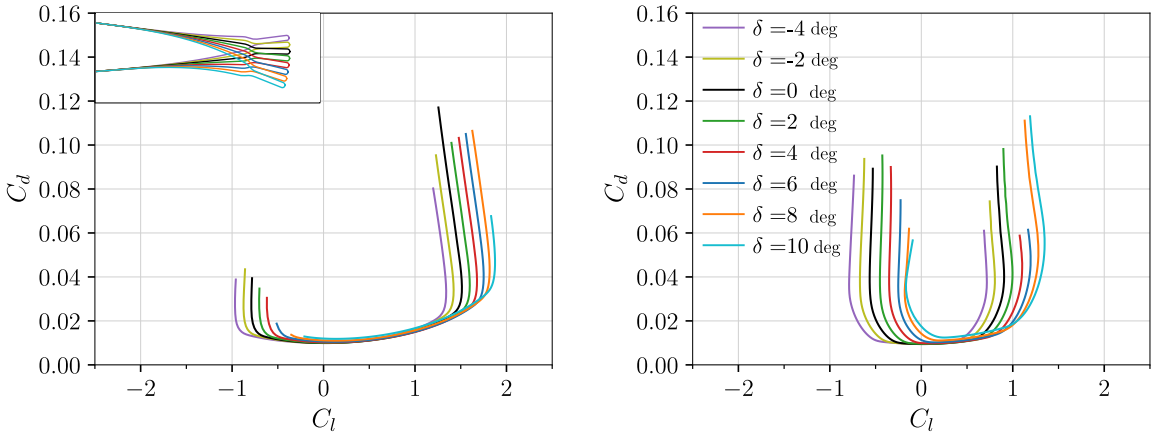

(a) Variation of C_l over C_d at $M = 0.4$.

(b) Variation of C_l over C_d at $M = 0.6$.

Figure 3.10.: Variation of the drag coefficient C_d of the morphed airfoils over the lift coefficient C_l for the Mach numbers $M = 0.4$ and $M = 0.6$.

the maximum lift coefficient $C_{l,max}$ of the baseline airfoil was achieved at the expense of a very high drag coefficient of $C_d = 0.04$. With a camber morphing deflection of $\delta = 8$ deg, the same lift coefficient can be achieved with a significantly lower drag coefficient of $C_d = 0.015$.

Furthermore, for both Mach numbers, the morphed airfoil achieved lift coefficients exceeding $C_{l,max}$ of the baseline without encountering significant increase in drag. For the linear range of C_l, the investigated upward camber morphed airfoil exhibited similar drag as the baseline. For C_l values near to stall, the investigated upward camber morphed airfoil exhibited an increase in drag at lower lift coefficients C_l compared to the baseline airfoil for both investigated Mach numbers. This behavior can be attributed to the lower maximum lift coefficient $C_{l,max}$ achieved by the morphed airfoil. For instance, at Mach $M = 0.4$, the drag increase for the upward morphed airfoil began at lift coefficients exceeding $C_l = 1.2$. This trend became even more pronounced at Mach number $M = 0.6$, where drag started to rise at a much lower lift coefficient $C_l = 0.55$. These findings suggest that upward camber morphed airfoils, at least in the configurations investigated, were not aerodynamically efficient for the investigated operating conditions. The upward camber morphed airfoil exhibited lower $C_{l,max}$ and higher drag compared to the baseline airfoil at the same high C_l values.

3.1.6. Effect of Camber Morphing on Aerodynamic Efficiency

The aerodynamic efficiency of camber morphed airfoils was compared to the baseline by analyzing the lift to drag ratio C_l/C_d across a range of lift coefficients C_l for both Mach 0.4 and 0.6, as shown in Figure 3.11. Within the C_l linear range of 0 to 0.75, corresponding to the baseline's lift range at Mach 0.4 (see Fig. 3.11a), and the C_l range of 0 to 0.6, corresponding to the baseline's lift range at Mach 0.6 (see Fig. 3.11b), both low ($\delta = 2$ deg and 4 deg) and medium ($\delta = 6$ deg and 8 deg) camber deflections exhibited similar C_l/C_d values compared to the baseline for a given C_l value.

In contrast, camber-morphed airfoils with high camber deflection angles $\delta = 10$ deg exhibited a significantly lower lift-to-drag ratio C_l/C_d compared to the baseline across the baseline's linear C_l range for considered both Mach numbers.

The improvement in the lift to drag ratio C_l/C_d relative to the baseline airfoil by means of the camber downwards camber morphing became more pronounced at lift coefficients C_l exceeding 0.8, which corresponds to the non-linear C_l region of the baseline airfoil, as shown in Fig. 3.9a. Over this range, the baseline airfoil experiences a rise in drag, primarily due to the increased pressure differences across its upper and lower surfaces preceding flow separation and stall [9]. Thus, C_l/C_d dropped, indicating a significant reduction in aerodynamic efficiency. As depicted in Fig. 3.10a, the C_l values achieved through downward camber morphing exceeded the $C_{l,max}$ of the baseline without a significant increase in drag. This resulted in a notable improvement in the lift to drag ratio C_l/C_d in comparison to the baseline. For example at $C_l = 1.51$, a 43.3% enhancement was observed with a camber morphing deflection of $\delta = 10$ deg, and the greatest improvement of 53% was achieved with a deflection of $\delta = 6$ deg. Furthermore, the most notable overall improvement was achieved using a deflection of $\delta = 4$deg, surpassing the $(C_l/C_d)_{max}$ of the baseline by 5%.

Figure 3.12a shows the maximum lift coefficient $C_{l,max}$ and maximum lift to drag ratio $(C_l/C_d)_{max}$ achieved for each camber-morphed airfoil at $M = 0.4$. Up to a deflection of $\delta = 4$ deg, both values exhibit a gradual increase, with the peak efficiency occurring at $\delta = 4$ deg for $M = 0.4$. This demonstrates the efficiency of camber morphing in boosting lift capablity and aerodynamic efficiency. For deflections of $\delta = 6$ deg and $\delta = 8$ deg, there was a gradual decline in $(C_l/C_d)_{\max}$, despite an increase in the maximum lift coefficient $C_{l,\max}$. For the highest camber morphing deflection $\delta = 10$ deg, although the highest $C_{l,\max}$ was achieved, the $(C_l/C_d)_{\max}$ dropped 4% compared to the baseline. This highlights the trade-off between maximizing lift and maintaining aerodynamic efficiency. The upward camber deflections, with angles of $\delta = -4$ deg and -2 deg, did not result in any improvement to either the lift coefficient (C_l) or the lift-to-drag ratio C_l/C_d compared to the baseline airfoil. This suggests that deflecting the camber upwards was less effective for enhancing lift capability and aerodynamic efficiency.

The enhanced aerodynamic efficiency and expanded lift capabilities of camber-morphed airfoils were further evaluated at Mach number of 0.6, as depicted in Figure 3.11b. Notably, in the non-linear range of the baseline lift coefficient, C_l, from 0.5 to 0.9, the improvement in the lift-to-drag ratio was more substantial compared to that at $M = 0.4$. At the higher Mach number $M = 0.6$, the lift-to-drag ratio, C_l/C_d, decreases more rapidly than at $M = 0.4$. The most significant enhancement in C_l/C_d relative to the baseline occurred at the maximum baseline lift coefficient of $C_{l,max} = 0.9$, achieving a remarkable 150% improvement through a medium camber morphing deflection of $\delta = 6$ deg. Using the maximum camber morphing deflection of $\delta = 10$ deg shifted the range of high lift to drag ratio C_l/C_d towards higher lift coefficients C_l, exceeding $C_{l,max}$ of the baseline. For instance, at $C_l = 1.1$, the C_l/C_d achieved with $\delta = 10$ deg matched the maximum $(C_l/C_d)_{max}$ of the baseline, which occurred at a much lower C_l of 0.6 in the baseline configuration. Figure 3.12b shows both the maximum lift and lift-to-drag ratio achieved by the baseline and camber-morphed airfoils. The highest lift-to-drag ratio was obtained by morphing the camber with a deflection of 6 deg, reaching maximum $(C_l/C_d)_{max}$ values of 59.4, which are 19% higher than the maximum $(C_l/C_d)_{max}$ values of the baseline. This enhancement was greater than the enhancement observed at $M = 0.4$. Furthermore, the increase in $(C_l/C_d)_{max}$ values showed a steeper

gradient compared to that at $M = 0.4$. Dadone identified in [23] critical design objectives for helicopter airfoils. One objective is achieving a high maximum lift coefficient $C_{l,max}$ of at least 1.5 at a Mach number of $M = 0.4$. This delays retreating blade stall and enhances helicopter performance. The morphed camber airfoils successfully met this requirement, demonstrating a significant lift improvement while maintaining high aerodynamic efficiency compared to the baseline. Additionally, Dadone emphasized the need for helicopter airfoils to generate a lift coefficient C_l of 0.6 at $M \approx 0.6$ without stalling, crucial for hover flight. The morphed airfoils achieved this objective as well, again exhibiting improved efficiency. Thus, downward camber morphing of helicopter airfoils unlocks remarkable capabilities by expanding the lift envelope and enabling operation across a broader range of conditions without sacrificing aerodynamic efficiency. This translates into improved helicopter performance and potentially increased payload capacity.

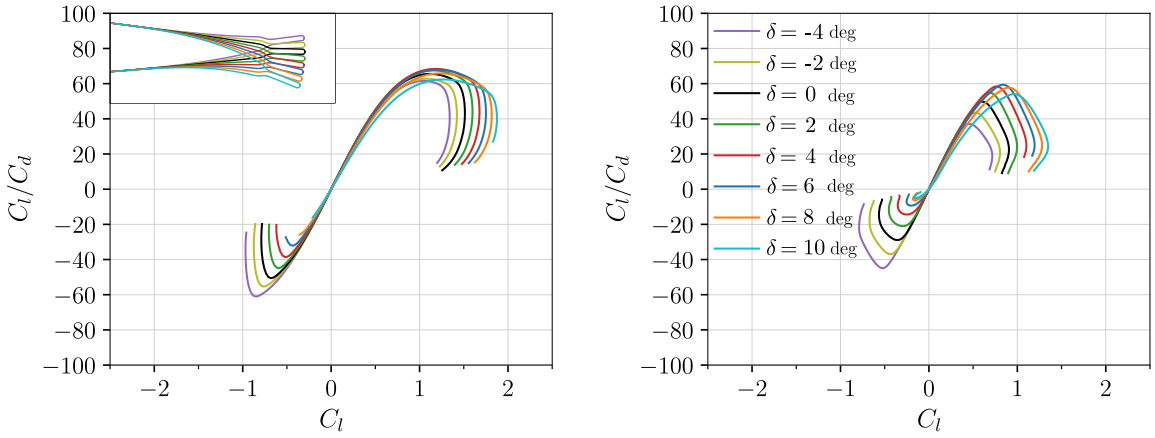

(a) Variation of C_l/C_d over C_l at $M = 0.4$.

(b) Variation of C_l/C_d over C_l at $M = 0.6$.

Figure 3.11.: Variation of C_l/C_d of the morphed airfoils over the lift coefficient C_l for the Mach number $M = 0.4$ and $M = 0.6$.

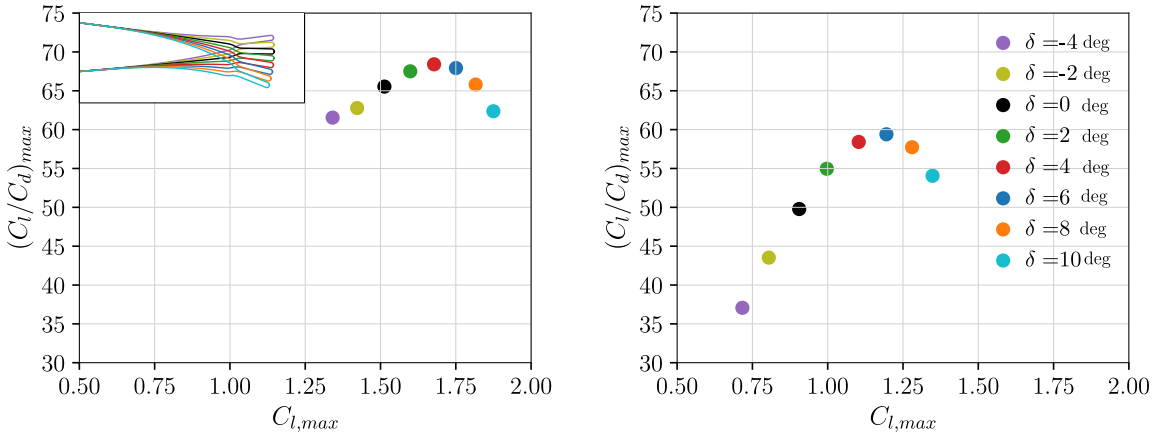

(a) Variation of $(C_l/C_d)_{max}$ over $C_{l,max}$ at $M = 0.4$.

(b) Variation of $(C_l/C_d)_{max}$ over $C_{l,max}$ at $M = 0.6$.

Figure 3.12.: Variation of $(C_l/C_d)_{max}$ of the morphed airfoils over $C_{l,max}$ for the Mach numbers $M = 0.4$ and $M = 0.6$.

3.1.7. Effect of Camber Morphing on Moment Coefficient

Figures 3.13a and 3.13b illustrate the impact of the camber morphing on the variation of pitching moment for a target C_l value at $M = 0.4$ and $M = 0.6$, respectively. For both Mach numbers, increasing the camber morphing led to more pronounced increase in the absolute value of C_m with respect to constant C_l. This becomes apparent when comparing the zero-lift pitching moment coefficient $C_{m,0}$ of the baseline airfoil with that of the airfoil featuring maximum morphing at $C_l = 0$, where the change in $C_{m,0}$, expressed $\Delta C_{m,0}$, increased by almost 0.2. Downward morphing of the airfoil generated a higher nose-down pitching moment, whereas upward morphing resulted in a positive moment coefficient. Moreover, while the pitching moment coefficient C_m of the baseline airfoil remained relatively constant across a broad range of lift coefficients C_l, the C_m variation with C_l became more non-linear as additional camber morphing was applied, even at the same Mach number. This aspect should be considered in the design of helicopters with active camber morphing, particularly during forward flight where lift changes along the azimuth at specific radial positions, since the increased magnitudes of C_m could affect the loads at the blade root, as noted in [52, 112]. For instance, a comprehensive study [67] on the active BO105 rotor used similar steady data to compute rotor aerodynamics. This study demonstrated significant variations in peak-to-peak pitch link loads and their magnitudes during forward flight. These variations were mainly induced by the dynamic morphing schedule applied over the blade azimuth, and the width and radial location of the morphing section. Moreover, this study concluded that optimizing these parameters through dynamic morphing could effectively reduce pitch link loads and decrease rotor power consumption.

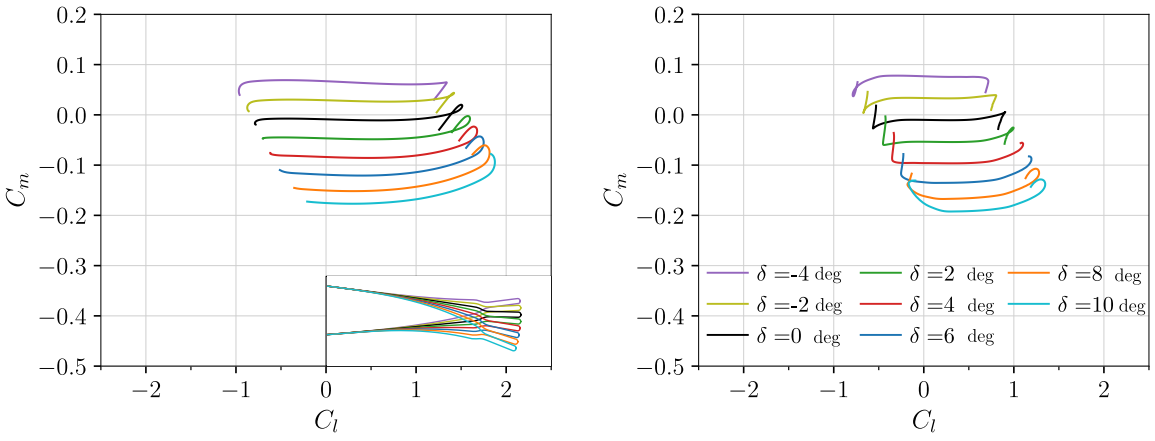

(a) Variation of C_m over C_l at $M = 0.4$.

(b) Variation of C_m over C_l at $M = 0.6$.

Figure 3.13.: Variation of the moment coefficient C_m of the morphed airfoils over the lift coefficient C_l for the Mach numbers $M = 0.4$ and $M = 0.6$.

3.1.8. Effect of Camber Morphing on Center of Pressure

The center of pressure x_{cp} is defined as the point around which the aerodynamic forces on an airfoil act [74]. The location of x_{cp} can be influenced by various factors, including the angle of attack, the shape of the airfoil, and the speed of the airflow [9, 74]. It is important to consider the location of x_{cp} while evaluating the aerodynamic characteristics of the wing or blade section because its location can affect the longitudinal stability of the rotor or fixed wing [21]. For this purpose, the location of x_{cp} for different camber morphed airfoils at Mach numbers $M = 0.4$ and $M = 0.6$ was determined using the following equation proposed in [74]:

$$x_{cp} = \frac{1}{4} - \frac{C_{m,1/4}}{C_n}, \text{ where } C_n = C_l \cos\alpha + C_d \sin\alpha. \tag{3.2}$$

For the baseline airfoil, x_{cp} was located slightly forward of the quarter-chord point, $x/c = 0.25$, due to the presence of a slight camber. This location remained relatively constant across different target lift coefficients. Moreover, increasing the Mach number from $M = 0.4$ to $M = 0.6$ had no significant effect on the location of the baseline x_{cp}, as shown in Figs. 3.14a and 3.14b. This indicates that the location of the baseline aerodynamic force was independent of the angle of attack α and incoming flow velocity. As the camber morphing deflection δ increased, the location of x_{cp} became more sensitive to the target C_l value. Increasing the camber morphing shifted the x_{cp} position towards the trailing edge for a given C_l value. As the camber was morphed upwards, the center of pressure moved towards the leading edge. This directly relates to the decrease in the effective aerodynamic upper surface, induced by upward camber morphing. This results in a lower pressure difference between the top and bottom of the airfoil [1, 9]. This translates into a decrease in the total lift generated and nose up pitching moment, as discussed in the subsections 3.1.4 and 3.1.7. It was also observed that as the C_l target was increased, the center of pressure x_{cp} moved closer to the $x/c = 0.25$ reference point for all investigated camber morphed airfoils. Additionally, the comparison between Fig. 3.14a and Fig. 3.14b reveals that the center of pressure location of the camber morphing airfoil depended on the incoming flow velocity. For the same camber morphed airfoil and C_l target, increasing the Mach number from $M = 0.4$ to $M = 0.6$ resulted in a slight shift of x_{cp} towards the trailing edge. For instance, as the Mach number was elevated from $M = 0.4$ to $M = 0.6$ while maintaining the same $C_l = 0.5$, the center of pressure x_{cp} of camber airfoil with deflection $\delta = 8$ deg experienced a minor shift from 0.32 to 0.33 respectively.

Moreover, since the center of pressure x_{cp} is defined as the point where aerodynamic forces act, the shift of x_{cp} significantly impacts the pitching moment calculated at the quarter chord point. Consequently, a greater shift of x_{cp} from the quarter chord point can lead to a higher pitching moment. These findings align with previous observations that an increase in downward camber morphing deflection results in a higher pitching moment. This has to be considered when designing an active rotor blade, since the shift of the center of pressure has a significant effect on longitudinal stability in aircraft, as explained in [122]. In the case of an active rotor, it can impact both longitudinal and lateral stability. This aspect is particularly critical when considering variations in the angle of attack and the dynamic morphing of the airfoil.

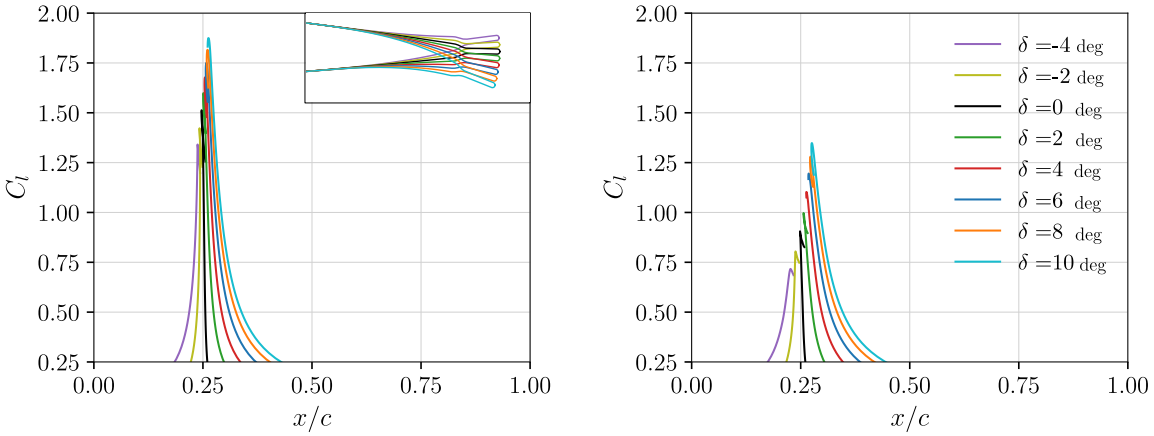

(a) Variation of x_{cp} over C_l at $M = 0.4$.

(b) Variation of x_{cp} over C_l at $M = 0.6$.

Figure 3.14.: Variation of the center of pressure of the morphed airfoils over the lift coefficient C_l for the Mach numbers $M = 0.4$ and $M = 0.6$

3.1.9. Effect of Camber Morphing on Pressure Distribution

This subsection examines the variation in pressure distribution with different downward camber morphing deflections at a Mach number of 0.4. It compares the pressure distributions between the camber morphed airfoil and the baseline airfoil for the same achieved lift coefficient. Additionally, this subsection explores how camber morphing can vary the pressure distribution at a constant angle of attack to achieve higher lift coefficients, as demonstrated in subsection 3.1.6.

Figure 3.15a compares the c_p distributions of different camber morphing airfoils with camber deflection $\delta = 4$ and 8 deg to the baseline, when the same target lift coefficient $C_l = 1.225$ was achieved. This comparison reveals that the same lift coefficient C_l can be achieved with less attenuated suction peaks and a higher pressure difference in the trailing edge section of the camber morphed airfoil compared to the baseline. As camber morphing deflection increased, the suction peak became less pronounced, while the pressure difference along the morphed section increased. Thus, higher camber deflections enabled achieving the same C_l at lower angles of attack. For instance, a lift coefficient of $C_l = 1.225$ was achieved with a camber morphing deflection of $\delta = 4$ deg at an angle of attack of $\alpha = 6$ deg. However, the same C_l value was attained at a lower angle of attack, $\alpha = 3.5$ deg, by increasing the camber deflection to $\delta = 8$ deg. Additionally, these variations in pressure distribution led to a downstream shift in the center of pressure, as previously illustrated in Fig. 3.14a. The differences in pressure distribution were not limited to the airfoil surface but also propagated into the surrounding flow field, as shown in Fig. 3.16.

Figure 3.15b illustrates the impact of camber morphing deflection on pressure distribution along the airfoil surface for a constant Mach number $M = 0.4$ and a constant angle of attack $\alpha = 2$ deg. With increasing camber morphing deflection (δ), a more pronounced pressure difference developed between the upper and lower surfaces along the morphing section ($x/c \geq 0.75$). This can be attributed to the enhanced curvature of the morphed section. The increase of curvature of the

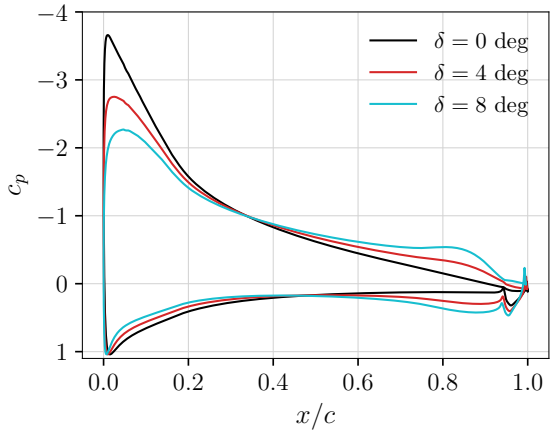

(a) Pressure coefficient c_p for constant lift coefficient(C_l = 1.225) of different morphed airfoils.

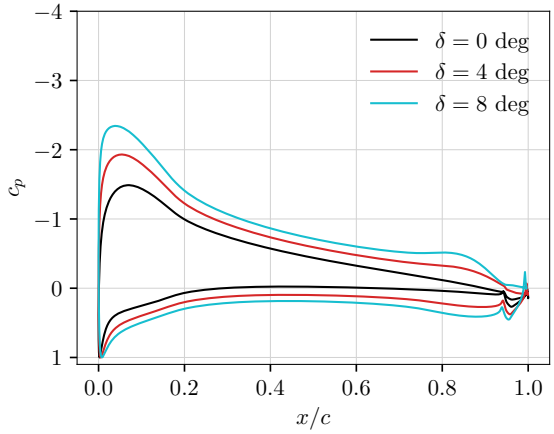

(b) Pressure coefficient c_p for same angle of attack α = 2 deg and at M = 0.4.

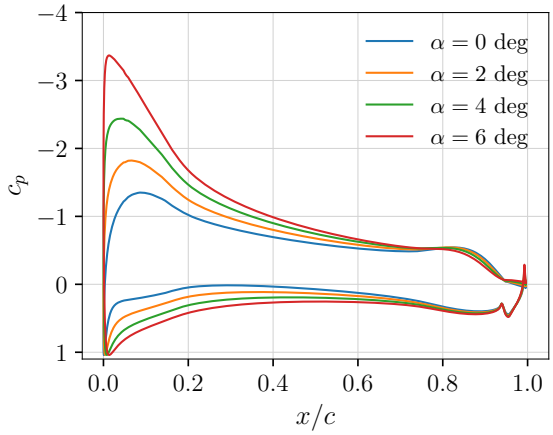

(c) Pressure coefficient c_p for different angle of attack of the morphed airfoil δ = 8 deg and at M = 0.4.

Figure 3.15.: Comparison of the pressure distribution c_p along the chord length at M = 0.4.

morphed section generated a greater pressure gradient that extended from the trailing edge towards the starting point of camber morphing. When this pressure gradient became excessively steep along the morphing section, it could trigger flow separation near the beginning of the camber morphing region [45]. The impact of the downward camber morphing propagated to the leading edge. Increasing camber deflection led to a steeper pressure gradient on the upper surface of the morphed airfoils. This resulted in a more pronounced suction peak, with the magnitude of the peak increasing with greater camber deflection. The lower surface c_p distribution showed a variation in comparison to the baseline. However, this c_p variation was less pronounced than for the upper surface. Thus, as the camber of the airfoil was increasingly morphed, the overall pressure difference between the upper and lower surfaces became more pronounced. This resulted in a significant increase in the lift coefficient C_l for the morphed airfoils compared to the baseline at the same angle of attack α, as shown in Subsection 3.1.4. For example, at $\alpha = 2$ deg, the baseline airfoil achieved a C_l of 0.39. By camber morphing with the deflections 4 deg and 8 deg, the C_l values increased to 0.76 and 1.08, respectively.

Figure 3.15c illustrates the pressure distribution variations for a camber morphing deflection $\delta = 8$ deg at increasing angles of attack α from 0 to 6 deg in 2 deg increments. The effects of increasing the angle of attack were most pronounced in the leading edge section on both the upper and lower surfaces, with diminishing influence toward the trailing edge. Additionally, variations in the pressure gradient along the morphing section $0.75 < x/c < 1$ were observed across the different angle of attack cases. These changes were less significant than those at the leading edge.

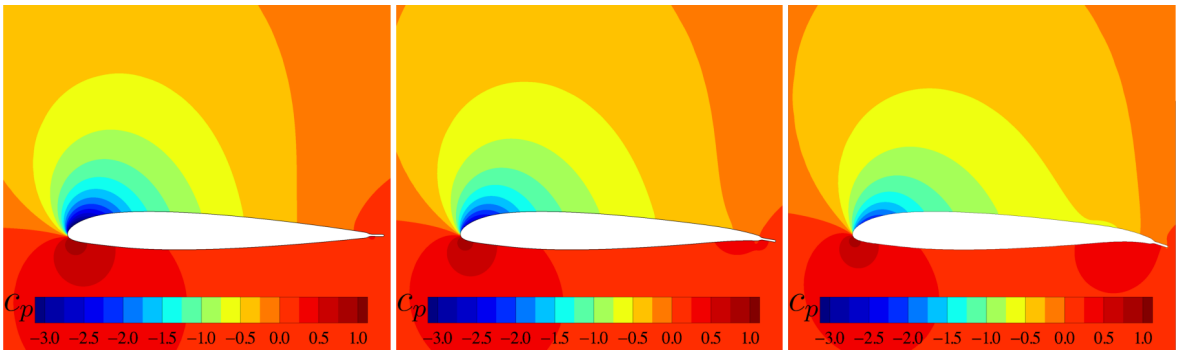

(a) $M = 0.4$, $\delta = 0$ deg, $\alpha = 9.00$ deg. **(b)** $M = 0.4$, $\delta = 4$ deg, $\alpha = 6.00$ deg. **(c)** $M = 0.4$, $\delta = 8$ deg, $\alpha = 3.50$ deg.

Figure 3.16.: Comparison of pressure contours for constant lift coefficient($C_l = 1.225$) of different morphed airfoils at $M = 0.4$.

3.1.10. Summary and Conclusions

Section 3.1 presents an evaluation of the aerodynamic performance of camber-morphed airfoils relative to a NACA23012 with tab baseline airfoil. The investigations were conducted using the TAU steady solver with the Spalart-Allmaras turbulence model. Key aerodynamic characteristics, including lift, drag, pitching moment coefficients, and pressure distribution, were evaluated at Mach numbers 0.4 and 0.6. The results provide fundamental insights into how these characteristics vary with the application of camber morphing upwards or downwards, particularly using smooth camber morphing similar to the FishBAC concept. These findings are essential for developing comprehensive rotorcraft analyses that incorporate active camber morphing mechanisms, enabling the identification of camber deflections that could minimize required power or achieve an optimal trade-off between high lift and an acceptable lift-to-drag ratio. The following conclusions were drawn from the lift evaluation conducted at Mach numbers 0.4 and 0.6 and different angles of attack for various prescribed camber-morphed airfoil shapes:

- The downward camber morphing significantly enhanced the maximum lift coefficient $C_{l,\max}$ compared to the baseline airfoil, expanding the operational lift envelope without reaching stall conditions. This enhancement can increase thrust capability, especially beneficial for hover, high-altitude, high-temperature conditions, and heavy-lift operations. Additionally, at Mach 0.6, the lift enhancement was more pronounced than at Mach 0.4. For instance, with the highest camber deflection of $\delta = 10$ deg, the lift capability was increased by up to 50% at Mach 0.6, while at Mach 0.4, the enhancement in lift was only 24% with the same camber morphing deflection.

- The downward camber morphing allowed achieving lift coefficient C_l values higher than the baseline $C_{l,\max}$ while maintaining a C_l/C_d close to the $(C_l/C_d)_{\max}$ of the baseline. Additionally, the C_l/C_d enhancement was observed across a wider range of lift coefficients C_l as the camber deflection increased. Moreover, the most notable enhancement in $(C_l/C_d)_{\max}$ were observed with moderate camber deflections $\delta = 4-6$ deg for both investigated Mach numbers, with further improvements at higher deflections after surpassing the baseline $C_{l,\max}$.

- While the baseline airfoil exhibited a constant and low pitching moment coefficient (C_m) across a wide range of lift coefficients C_l, camber morphing had a pronounced effect on both the magnitude and variation of C_m with respect to C_l. As camber deflection δ increased, C_m magnitude also increased, and the relationship between C_l and C_m became increasingly non-linear. Additionally, downward camber morphing produced a nose-down pitching moment, while the upward morphing resulted in a nose-up pitching moment.

- For the baseline airfoil, the position of the center of pressure x_{cp} remained stable near $x/c = 0.25$ as the Mach number increased from $M = 0.4$ to $M = 0.6$ and independent of the target lift coefficient C_l. In contrast, the downward camber morphing caused x_{cp} to shift slightly towards the trailing edge, while upward morphing shifted it towards the leading edge, with both shifts becoming more pronounced at higher Mach numbers and larger camber deflections. This underscores the importance of investigating how camber morphing can affect the longitudinal and lateral stability of an active rotor.

- The downstream shift of the center of pressure x_{cp} for a given lift coefficient C_l was attributed to the reduced attenuation of the suction peak and the increased pressure difference within the camber morphed section. The increase in the lift coefficient C_l, at a constant angle of attack achieved through the downward camber morphing, was driven by the enhanced suction peak and increased pressure difference across the morphed section.

3.2. Evaluation of Unsteady Aerodynamics for 2D Camber-Morphed Airfoils

3.2.1. Aim of the Study

This chapter primarily investigates the impact of periodically pitching and morphing camber on blade airfoil characteristics in unsteady aerodynamic conditions. The objective is to evaluate whether the unsteady aerodynamic effects caused by the simultaneous morphing and pitching of a blade section are adequately captured in rotor comprehensive analysis using CAMRAD II. For this purpose, the steady airfoil coefficients used to compute the aerodynamic loads in CAMRAD II, computed with steady TAU CFD solver, were compared to results computed with the CFD TAU unsteady solver at the same free stream Mach number and for the same simultaneous pitch and morphing motions.

Typically, unsteady correction models are used to adjust the steady airfoil coefficients in comprehensive analysis tools to account for unsteady aerodynamic effects. For instance, the ONERA Edlin model is used in CAMRAD II as a default unsteady correction model. In this study, the airfoil coefficients adjusted using the ONERA Edlin model were compared against the steady airfoil coefficients and unsteady CFD data. This evaluation aims to understand how effectively the airfoil coefficients corrected the unsteady effects arising from pitch and camber morphing motions using the default setting of the ONERA Edlin in CAMRAD II. For this purpose, different scenarios were investigated. Firstly, only standalone pitching motions were considered when comparing the unsteady coefficients, and raw and steady aerodynamic coefficients. The pitch frequency $f_\theta = 7$ Hz corresponds approximately to the angular velocity of reference BO105 rotor. Secondly, simulations involving simultaneous pitching and morphing motions were conducted. The camber morphing frequency was synchronized the pitch frequency, and was subsequently doubled. This analysis aims to understand how camber morphing frequency affects the variations in aerodynamic responses and how the differences between steady and unsteady aerodynamic coefficients change when camber morphing was applied. The investigated case are presented in Table 3.1, which outlines the different setups of the considered cases.

In order to isolate the unsteady effects primarily arising from the pitching motion and camber morphing, the Mach number $M = 0.4$ and pitch frequency 7 Hz were chosen for all the 2D airfoil simulations to ensure quasi-steady conditions with pitch reduced frequency $k = 0.0045$. The pitch angle was varied between 0 and 8 deg to ensure that the flow remained attached throughout the pitch time period, thereby avoiding flow separation. This approach was chosen to focus the analysis specifically on the unsteady effects arising from pitching motion and camber morphing, without evaluating additional complexity introduced by flow separation phenomean or dynamic stall. The cyclic pitching angle $\theta(t)$ was determined at every time step by means of the periodic equation 3.3, where the mean pitch angle $\theta_0 = 4$ deg, the first harmonic $\theta_{1C} = 4$ deg corresponds to the pitch amplitude, and a constant phase shift of 270 deg was applied, ensuring that the maximum deflection occurred at the azimuth of 270 deg. The impact of camber morphing frequency on discrepancies between steady state and unsteady aerodynamic response was further investigated through two cases. In the first case 1P, the camber morphing frequency f_δ was synchronized

with the pitch frequency $f_\theta = 7$ Hz. In the second case 2P, the camber morphing frequency f_δ was doubled to 14 Hz. The camber morphing was implemented using Eq. 3.4 for both cases and the morphing deflection varied between two values: $\delta = 0$ and $\delta = 4$ deg throughout the pitch cycle. The specific schedule for this variation is defined by the input parameters listed in Table 3.1.

Table 3.1.: Overview of the investigated cases.

Case	f_θ [Hz]	k_θ (reduced frequency)	θ_0 [deg]	θ_{1C} [deg]	$\phi_{1\theta}$ [deg]	f_δ [Hz]	δ_0 [deg]	δ_{1C} [deg]	$\phi_{1\delta}$ [deg]	δ_{2C} [deg]	$\phi_{2\delta}$ [deg]
Baseline	7	0.045	4	4	270	0	0	0	0	0	0
1P	7	0.045	4	4	270	7	2	270	0	0	0
2P	7	0.045	4	4	270	14	0	0	0	2	270

$$\theta(t) = \theta_0 + \sum_{n=1}^{\infty} \theta_{nC} \cos(2n\pi f_\theta t - \phi_{n\theta}) \tag{3.3}$$

$$\delta(t) = \delta_0 + \sum_{n=1}^{\infty} \delta_{nC} \cos(2n\pi f_\delta t - \phi_{n\delta}) \tag{3.4}$$

The discrepancies between unsteady CFD results and aerodynamic coefficients predicted by CAMRAD II, with and without the ONERA Edlin correction, were analyzed over the entire pitch cycle. This analysis aimed to assess the accuracy of steady CAMRAD II results and the effectiveness of the ONERA Edlin model in capturing unsteady aerodynamic effects. The discrepancies were quantified as percentage differences calculated over the entire cycle. Specifically, the analysis evaluated how well CAMRAD II, both with and without the correction, captured the variations in aerodynamic coefficients (e.g., lift, drag, moment) observed in unsteady CFD simulations for two scenarios: standalone pitching and combined dynamic camber morphing and pitching. The percentage difference in the lift, drag and moment coefficients were calculated over the entire pitch cycle using the Eqs. 3.5, 3.6, and 3.7 respectively. The unsteady CFD results served as the reference for calculating the relative difference at each time step. This relative difference was then normalized by the maximum value of the corresponding quantity coefficient from the unsteady CFD solver.

$$|\Delta C_l| = 100. \frac{|dC_l|}{max(|C_{l,\text{CFD,unsteady}})|} \quad \text{with} \quad dC_l = C_{l,\text{CFD,unsteady}} - C_l \tag{3.5}$$

$$|\Delta C_d| = 100. \frac{|dC_d|}{max(|C_{d,\text{CFD,unsteady}})|} \quad \text{with} \quad dC_d = C_{d,\text{CFD,unsteady}} - C_d \tag{3.6}$$

$$|\Delta C_m| = 100. \frac{|dC_m|}{max(|C_{m,\text{CFD,unsteady}})|} \quad \text{with} \quad dC_m = C_{m,\text{CFD,unsteady}} - C_m \tag{3.7}$$

Moreover, this study investigates how pitch and camber morphing history affects the pressure distribution and velocity profiles of an airfoil. To isolate unsteady effects not captured by traditional airfoil tables, pressure and velocity at the mean pitch angle θ_0 during upstroke and downstroke

were compared to steady state results. Steady simulations were conducted at the same angles of attack as those during the upstroke and downstroke at θ_0.

3.2.2. Numerical Setup

For the purpose of this study, the CFD simulations were configured to model the simultaneous pitching and camber morphing motion of a 2D airfoil at different frequencies. The work flow of the simulation is explained in subsection 2.3.1. Within this work flow, the URANS equations were solved at every time step to compute the flow field. The implicit backward Euler scheme was used for time discretization with dual time-stepping. Every case listed in 3.1 was simulated for a duration of six pitching periods, which corresponded to 0.8571 s in total. Each pitch period comprised of 720 time steps, corresponding to $\Delta t = 0.0013888$ s. Every time step included 150 inner iterations. The CFL number was set to 8 for the CFD simulations and the central scheme was used for the discretization space. The baseline 2D grid, known from subsection 2.2.3 and capable of maintaining wall distance y^+ less than 1 up to $M = 0.95$, was deformed at every time step to model either a standalone pitching motion or simultaneous pitching and camber morphing motion, as explained in the subsection 2.3.1.1. A two step deformation process was conducted at each time step. First, the pitching motion about the 25% chord location of the baseline airfoil. Thereafter, the camber morphed shape was obtained by applying morphing at the 75% chord location on the obtained pitched airfoil, as shown in Fig. 3.17a. The variations of pitching angle and camber morphing deflection over time for the investigated cases, ware listed in Table 3.1 and illustrated in Fig. 3.17. The pitch schedule was set up for these investigations such that the maximum pitch angle occurs at $\psi = 270$ deg in the CAMRAD II simulation, mimicking a forward flight scenario where the pitch angle is highest on the retreating side.

Figure 3.17b shows the stand alone pitching motion, and Figs. 3.17c and 3.17d show the schedule of the camber morphing applied simultaneously with pitching motion for the investigated cases 1P and 2P respectively. The convergence of the unsteady CFD simulations was monitored by tracking the residuals of density, lift, and drag. The convergence was considered to be achieved when the residuals of lift and drag was below 10^{-6}. In this study, the steady aerodynamic coefficients, originally listed in airfoil tables, were extracted from CAMRAD II at a specific radial station corresponding to a particular Mach number. The CAMRAD II model used for this study was described in the subsection 2.3.2. In order to evaluate the aerodynamic effects of pitch and camber morphing that are not included in the airfoil tables used in comprehensive analysis, two numerical setups were used:

- Firstly, a CAMRAD II setup featuring a single blade in a hypothetical hover condition was used, where the blade was allowed only pitch and camber morphing motions. The CAMRAD II model was initially operated without considering any unsteady correction. Then, the CAMRAD II model was executed with the ONERA Edlin model to account for unsteady aerodynamic effects.

- Secondly, a two-dimensional (2D) unsteady CFD model of a blade section which represents the modeled blade in CAMRAD II was used to compute the unsteady aerodynamics of the

given blade section. The unsteady CFD investigations were conducted at the same Mach number and applied pitch and camber morphing motions as the blade section in CAMRAD II.

These configurations enable the comparison of steady and unsteady coefficients C_l, C_d, and C_m for a 2D airfoil for same flow velocity and effective angle of attack and undergoing the same motions. Additionally, this comparison allows the evaluation of the ONEARA Edlin model's effectiveness to adjust the steady coefficients within comprehensive analysis with CAMRAD II, for example to account for the missing unsteady effects, especially when camber morphing is applied simultaneously with the pitch motion.

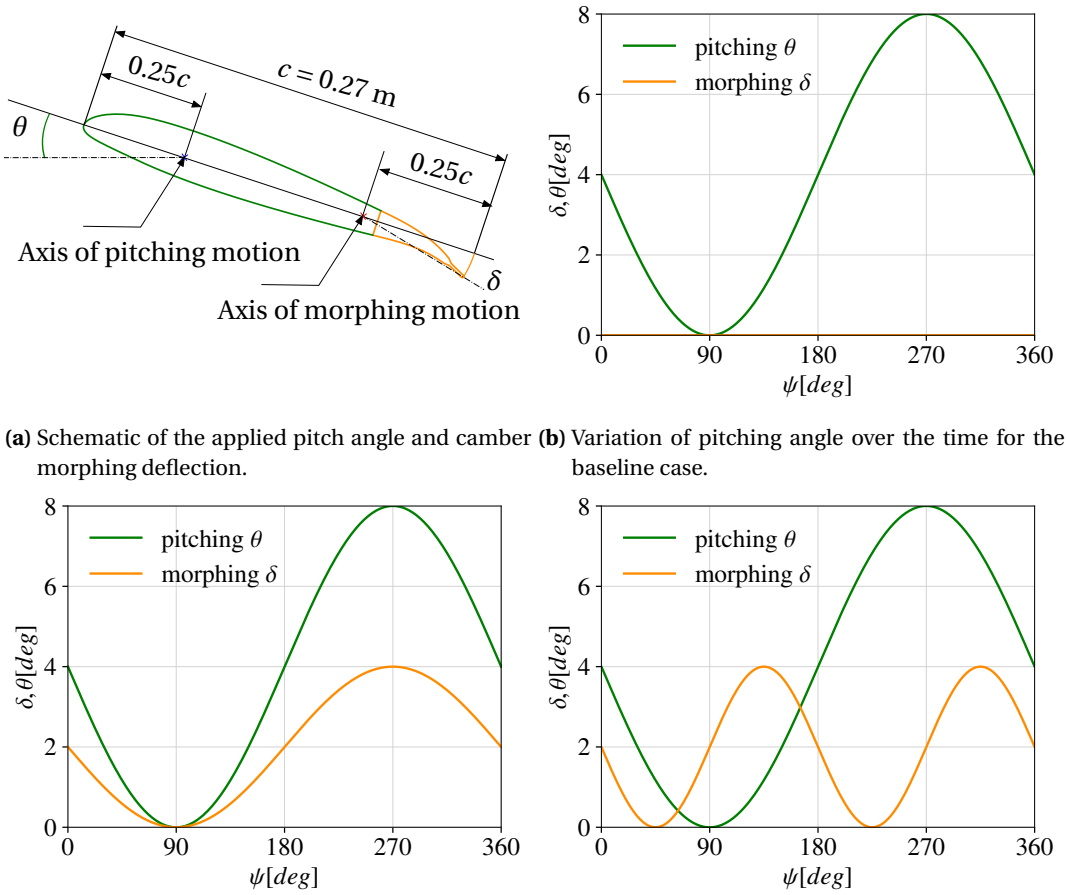

(a) Schematic of the applied pitch angle and camber morphing deflection.

(b) Variation of pitching angle over the time for the baseline case.

(c) Variation of pitching angle and camber morphing deflection over the time for the 1P case.

(d) Variation of pitching angle and camber morphing deflection over the time for the 2P case.

Figure 3.17.: Illustration of prescribed pitching motion combined with camber morphing actuation cycle of the insvetigated cases, Baseline, 1P and 2P listed in Table 3.1.

3.2.3. Verification Case

Description of the experimental Setup:

In the absence of experimental data for combined camber morphing and pitching of 2D airfoil, the published investigation by Krzysiak et al. [69]on a pitching NACA012 airfoil with an oscillating trailing edge flap provided a suitable verification case for the numerical workflow and settings. The pitch motion range investigated by Krzysiak et al. closely matched the range targeted for the baseline, 1P, and 2P cases at $M = 0.4$. Additionally, the actuation frequency of the trailing edge flap in Krzysiak's research (10 Hz) was found to be double the pitch frequency (5 Hz). This mirrored the 2P case where the camber morphing frequency was designed to be twice the pitching frequency. The verification study is designed to confirm that the workflow for the 2D unsteady simulations operates smoothly. Specifically, it focuses on the use of grid deformation to model changes in pitch and camber while ensuring that the grid resolution remains consistent. By successfully verifying the accuracy of the workflow and numerical simulations, a solid foundation was established for further investigations into the aerodynamic response of airfoils undergoing simultaneous pitch and camber morphing motion.

In the wind tunnel of the Institute of Aviation, Krzysiak et al. [69] investigated the aerodynamic coefficients of a NACA0012 airfoil with a chord length c of 0.18 m and a span of 0.6 m. The setup incorporated a trailing edge flap measuring 0.04069 m in length. A consistent gap of 0.0005 m was maintained between the flap and the airfoil. Both the airfoil and flap underwent pitching motion around hinge points positioned at 35% and 80% of the chord length, respectively, as illustrated in Figure 3.18b. This investigation was carried out within the 0.6 m x 0.6 m cross-section of the 1.58 m long test section at the Institute of Aviation wind tunnel [69, 75]. Further details on the experimental setup can be found in references [69].

The pitch motion of the main airfoil element was scheduled to follow the harmonic signals defined by Eq. 3.8. The trailing edge was set to oscillate according to the harmonic motion described by Eq. 3.9.

$$\theta(t) = \theta_0 + \Delta\theta \sin(\omega_\theta t), \quad \text{with} \quad \theta_0 = 4 \text{ deg}, \quad \Delta\theta = 6 \text{ deg}, \tag{3.8}$$

$$\delta(t) = \delta_0 + \Delta\delta \sin(\omega_\delta t + \varphi_\delta), \quad \text{with} \quad \delta_0 = 0 \text{ deg} \quad \Delta\delta = 5.4 \text{ deg}, \quad \varphi_\delta = 148 \ deg \tag{3.9}$$

After conducting the experiments, a discrepancy were reported between the measured pitch, $\theta(t)$, and trailing angle, $\delta(t)$, and the scheduled harmonic motions, as illustrated in Fig. 3.18a. To ensure consistency with the experimental results, the measured variations of pitch (represented by red symbols) and flap angle (represented by green symbols) were used as input functions for the unsteady CFD simulation. Figure 3.18a shows that inputs for the CFD simulation matched the measured pitch and flap angle variations over time. Other numerical studies [75, 78] used also the results published in [69] as reference to verify the applied numerical setup. In these numerical

studies, the measured variation of pitch and flap angles over time was also fed as an input for the CFD unsteady simulation.

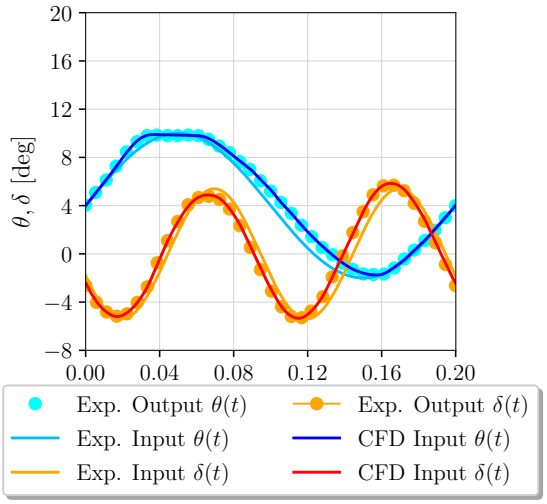

(a) Illustration of the scheduled and obtained the oscillation of NACA0012 airfoil and trailing edge in experimental in comparison to the input signal given for the unsteady CFD simulation.

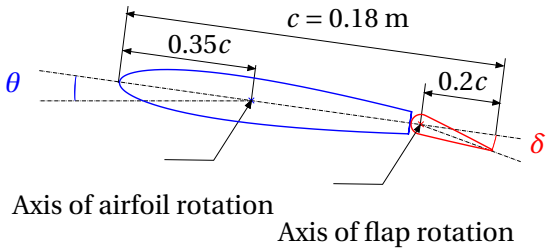

(b) Dimensions and geometric specifications of the NACA0012 Airfoil with Trailing-Edge Flap.

Figure 3.18.: Illustration of the dimensions of the investigated NACA0012 airfoil with trailing edge flap and the applied oscillation motion for main airfoil and the trailing edge. The experimental data are extracted from [69]

Description of the numerical setup of the verification case:

The computational domain used in the CFD simulation closely mirrored a section of the wind tunnel, as depicted in Fig. 3.19. With a length of 0.6 m and width of 0.6 m matching that of the wind tunnel cross section used for aerodynamic measurements of the pitching airfoil with oscillating trailing edge, the CFD domain provided an accurate representation of the cross section of the experiment. Within this domain, the airfoil and the flap were treated as viscous walls to properly capture boundary layer effects. The airfoil and the flap were positioned centrally within the cross section, as it was set in the experiment.

The airfoil and the flap surfaces were considered to be a viscous wall in order to solve effects related the boundary layer. The upper and lower surfaces of the airfoil were resolved using 213 points, while the leading edge radius was resolved using a finer mesh with a cell size of $dx_i/c = 0.0014\%$ and the maximum cell resolution did not exceed $dx_i/c = 1.25\%$. The upper and lower surfaces of the flap were resolved using 187 points. An O-grid had 6066 structured cells in the plane domain surrounding the airfoil, as shown in Fig. 3.20b. Figure 3.21 shows the distribution of cell growth rate AR perpendicular to the airfoil surface. The average growth rate is approximately 1.1, to ensure that the flow near the airfoil surface was resolved accurately. During the unsteady simulation, the first wall distance maximum y^+ was 1.1.

The side walls of the cross section were considered as symmetry planes, while the width of the wind tunnel was represented using a single structured cell. To prevent boundary condition reflections, the inlet was positioned 10c from the leading edge of the NACA0012 airfoil, and the outlet was located 20c from the leading edge. As the upper and lower walls were perforated in the experiments, they were modeled as euler walls in the CFD simulation. A structured grid resolved the inlet to the outlet, including the upper and lower walls. Meanwhile, the remainder of the computational domain, between the structured grids and the structured O-grid, was filled using an unstructured grid. The remaining space within the computational domain was filled with an unstructured grid, to connect the structured regions, extruded from the walls, inlet and outlet with the O-grid surrounding the airfoil, as shown in Fig. 3.20a.

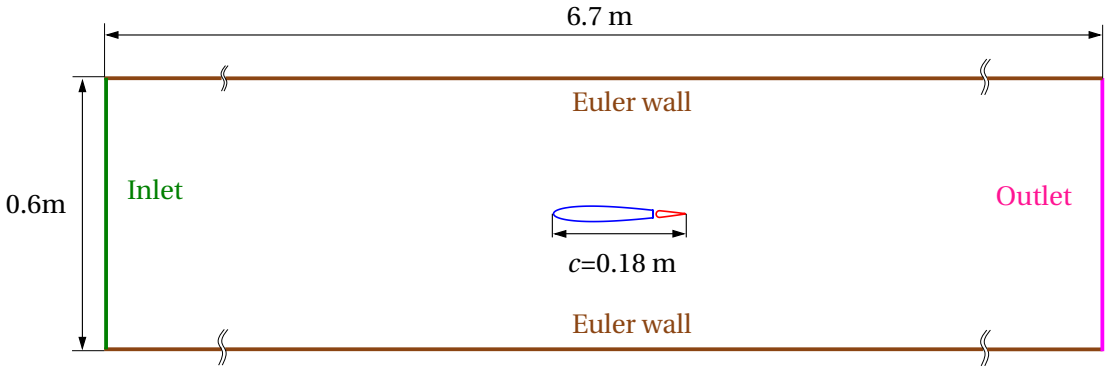

Figure 3.19.: Wind Tunnel boundary condition in the CFD simulation

The computed steady lift curve, without trailing-edge flap deflection, showed excellent agreement with the measured polar

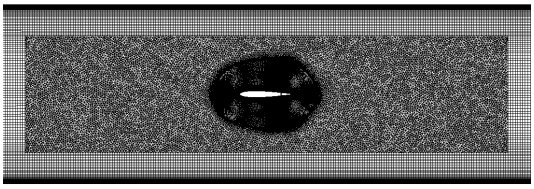

(a) Grid surrounding the NACA0012 airfoil with the trailing flap.

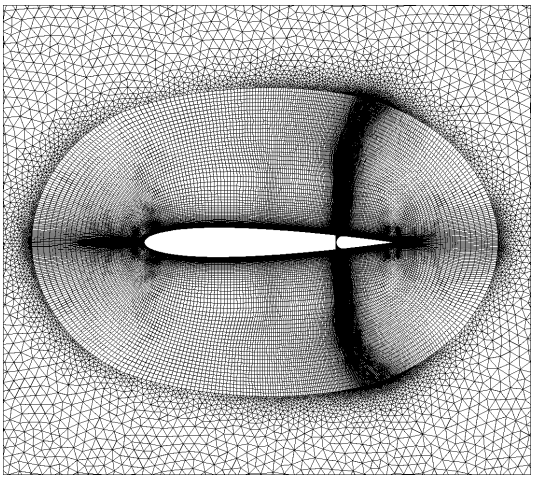

(b) Close look to grid surrounding the NACA0012 airfoil with the trailing flap.

Figure 3.20.: Illustration of the grid used to validate the numerical setup for the unsteady investigation.

The accuracy of grid deformation was verified under steady conditions by comparing computed lift and drag curves of a NACA0012 airfoil with a trailing edge to wind tunnel measurements published by Krzysiak et al. [69] from the Institute of Aeronautics (IoA), along with data from the Na-

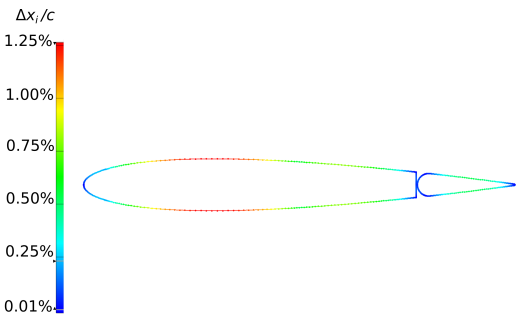

(a) Grid surrounding the NACA0012 airfoil with the trailing flap.

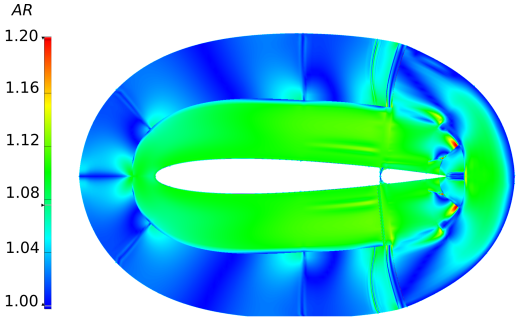

(b) Close look to grid surrounding the NACA0012 airfoil with the trailing flap.

Figure 3.21.: Illustration of the grid used to validate the numerical setup for the unsteady investigation.

tional Aeronautical Establishment, Canada (NAE), and the Aeronautical Research and Test Institute, Czech Republic (VZLU). The investigation, conducted at a constant free stream Mach number of $M = 0.5$, involved rotating both the airfoil and the O-grid surrounding it using grid deformation utilities to match angles of attack α considered in experimental investigations. No deflection of the trailing-edge flap was applied in this investigation. Figures 3.22a and 3.22b depict the computed steady CFD results compared to various wind tunnel measurements. The computed results exhibit excellent agreement with the measured lift curve and only minor deviations from the drag polars, affirming the maintenance of grid quality after applying the grid deformation.

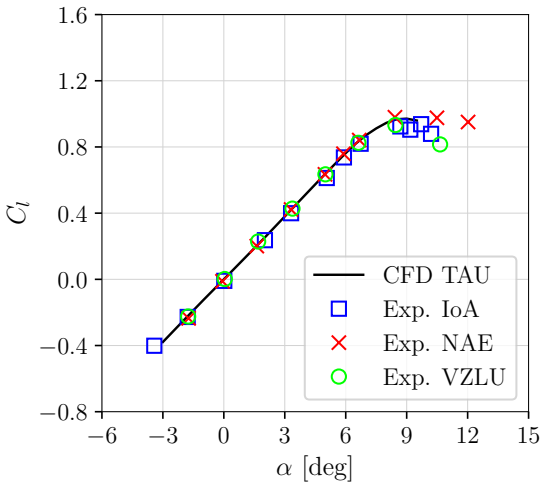

(a) Validation of the steady lift curve.

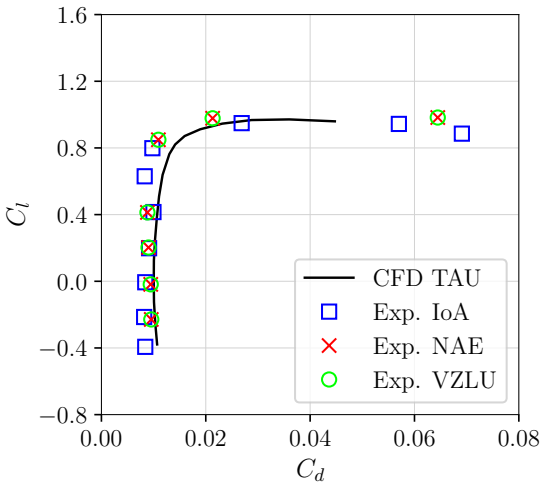

(b) Validation of the steady drag polar.

Figure 3.22.: Validation of grid and numerical setup of NACA0012 with trailing-edge flap by means of different wind tunnel measurements for $M = 0.5$, experimental data extracted from [69].

The 2D unsteady simulation workflow was verified using a similar experimental investigation to the current intended study for camber morphing simultaneously with the pitch motion, with a Mach number of $M = 0.4$ and comparable pitch motion. In this experimental investigation, conducted by Krzysiak et al. [69], involved pitching the airfoil at 5 Hz and the trailing edge at 10 Hz at $M = 0.4$, using the setup explained above. The oscillation schedule applied to the airfoil and flap

is depicted in Fig. 3.18a. Figures 3.23a and 3.23 shows a comparison between measured unsteady aerodynamic lift and moment coefficients, denoted by squared symbols, and those numerically computed using the TAU solver, following the workflow outlined in Subsection 2.3.1. Additionally, the investigation conducted by Krzysiak et al. served as a benchmark for validating the numerical setups applied by Nikki et al. [75] and Liu et al. [78], where used the OVERFLOW and CFD++ solvers, respectively. These comparisons were also shown in Figs. 3.23a and 3.23 and were also cross-checked against TAU results for further verification.

Figure 3.23a presents the numerical results for the lift coefficient over the pitch angle in comparison to experimental data. The results computed with the TAU solver capture the C_l hysteresis shape. Minor deviations in unsteady C_l were observed during the upstroke, particularly near θ_{min} and θ_{max}, when compared to the experimental results. The results reported by Nikki et al. [75], computed using OVERFLOW, demonstrated better agreement with the experimental data near θ_{max} but exhibited deviations near θ_{min}. The numerical results from Liu et al. [78] displayed an offset in comparison to the experimental results, with the lift coefficient being significantly overestimated during the upstroke for θ in [-2,10] deg, and during the downstroke for θ in [2,10] deg.

Figure 3.23 illustrates the computed variation of C_m with pitch angle θ in comparison to experimental data. The results computed with TAU, CFD++, and OVERFLOW solvers closely replicated the C_m hysteresis shape observed experimentally. The TAU and CFD++ solvers computed similar results, including an underestimation of the C_m values over the upstroke for θ in [4,10] deg and downstroke for θ in [-2,4] deg. Notably, the results by Nikki et al. [75], computed with OVERFLOW, displayed excellent agreement with the experimental data, especially concerning C_m. This high level of agreement is attributed to the use of a hybrid unsteady Reynolds-averaged Navier-Stokes/large eddy simulation approach, a 4th-order spatial scheme, and the $k-\omega$ turbulence model. In contrast, the TAU and CFD++ data, which was computed using the Spalart-Allmaras (SA) turbulence model and a 2nd-order spatial scheme, exhibited acceptable deviations. Despite minor discrepancies in C_l and acceptable deviations in C_m hysteresis, the TAU unsteady solver and the framework demonstrated reliable results, indicating their capability to capture unsteady loads in simulations involving pitching and morphing of 2D grids.

3.2.4. Evaluation of the Lift, Drag and Moment Coefficient

In the following section, the aerodynamic response of the cases outlined in Table 3.1 are presented and discussed. The focus of this section is to highlight the discrepancies between the unsteady CFD results and the steady aerodynamic coefficients used for a uniform inflow CAMRAD II model, first with, and then without the ONERA Edlin correction. This analysis reveals the unsteady effects not captured by steady airfoil tables and demonstrates how the ONERA Edlin model addresses these effects by separately adjusting the different aerodynamic coefficients. The strengths and limitations of this model are analysed by evaluating the effect that the ONERA Edlin correction has on the response of the CAMRAD II model in relation to the unsteady CFD results. It is noteworthy that the default parameters of the ONERA Edlin model were used in this study, as applied with a free wake model in the CAMRAD II comprehensive analysis for active rotors in [65, 66].

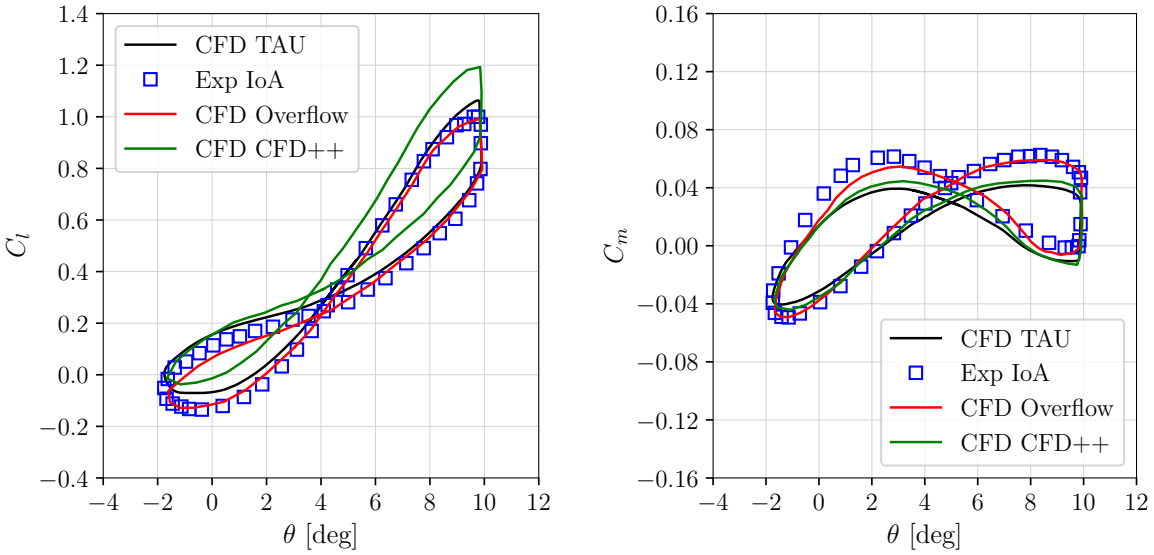

(a) Validation of lift coefficient hysteresis.

(b) Validation of moment coefficient hysteresis.

Figure 3.23.: Validation of the numerical setup for unsteady investigations using NACA0012 with trailing-edge: Exp IoA data extracted from [69], CFD Overflow data extracted from [75], CFD++ data extracted from [78].

The unsteady CFD results were compared to the steady aerodynamic coefficients obtained from the uniform inflow CAMRAD II model. This comparison focused on the lift coefficient C_l, moment coefficient C_m, and drag coefficient C_d. This study investigated how these discrepancies varied for both a standalone pitching airfoil and a pitching airfoil with simultaneously applied camber morphing. For this purpose three subplots were used to highlight the following: The variation of the coefficient over the azimuth for the unsteady CFD, the CAMRAD II with correction, and the CAMRAD II without correction; the magnitude of the percentage error between both of the CAMRAD II results and the unsteady CFD over the azimuth; and a graphical illustration of the blade pitch angle and active camber angle over the azimuth.

Evaluation of the Lift Coefficient:

First, the variations in lift coefficient C_l under standalone pitch motion were examined. The analysis involved comparing the results from the TAU unsteady solver to those obtained from CAMRAD II with and without the ONERA Edlin model correction. Figure 3.24 shows the comparison between the unsteady CFD results and each of the CAMRAD II results, depicting C_l variation for the baseline case over the pitch cycle, where no camber morphing was applied. The pitching frequency was the same as the rotor frequency in all of the models, and the pitch schedule, depicted by the green curve in the lower subplot of Fig. 3.24, was also consistent throughout all of the models.

The first observation in Fig. 3.24 reveals a negative phase shift in the TAU unsteady results relative to the prescribed pitch motion. This means that the lift response was delayed relative to the

pitch motion, highlighted by the minimum and maximum C_l values occurring after the minimum and maximum pitch respectively. This can be attributed to the TAU unsteady model which takes into account the resistance of the surrounding fluid due to the dynamic motion of the airfoil [74]. Hence, the inertia of the surrounding air delays the response of the C_l variation during pitch motion. The CAMRAD II results without the ONERA Edlin model showed no phase shift in relation to the pitch schedule, as the steady airfoil characteristics from the airfoil tables were computed using a TAU steady solver, making them inherently independent of prior history of airfoil pitching motion. The CAMRAD II results corrected with the ONERA Edlin model exhibited a minimal positive phase shift, reflecting the slight adjustments in C_l values from the steady airfoil tables. Since the ONERA Edlin model with the default settings induced a positive phase shift rather than negative, this led to shifting the C_l coefficient values further away from the unsteady CFD results. Previous research demonstrated that the ONERA Edlin model can accurately approximate unsteady airfoil coefficients. However, the accuracy can be enhanced by adjusting the parameter settings of the ONERA Edlin model. This accuracy relies on the selected parameter values of the ONERA Edlin model. These parameters are empirical and can vary based on the inflow model, as well as the investigated airfoil and the incoming flow velocity, as shown in [58, 80, 83, 94, 86]. Identifying optimal parameters of ONERA Edlin model to precisely align with higher fidelity simulations was not within the scope of this study and is recommended for future research.

The discrepancies between the TAU CFD unsteady results and the different CAMRAD II results over the pitch period are highlighted using the $|\Delta C_l|$ curves shown in the middle subplot of Fig. 3.24. These curves were derived by applying Eq. 3.5 throughout the pitch cycle. In general, the CAMRAD II model without correction displayed a smaller discrepancy to the unsteady CFD than the model with correction. The CAMRAD II results without the ONERA Edlin model showed less deviation compared to the TAU unsteady data. The maximum deviation in this case was $|\Delta C_l| = 8.73\%$. In contrast, the results computed using the ONERA Edlin model had a greater maximum deviation of $|\Delta C_l| = 11.42\%$. This difference in maximum deviations was attributed to the distinct phase shifts between the TAU unsteady results and both CAMRAD II results. The CAMRAD II results with ONERA Edlin correction showed a greater maximum deviation because it had a slightly larger phase shift relative to the TAU unsteady results. Moreover, both CAMRAD II models overpredicted the magnitude of the maximum lift coefficient $C_{l,max}$ in comparison to TAU, by $dC_l = 0.036$ and with the phase shift of $\phi = 7.2$ deg and underpredicted the minimum lift coefficient $C_{l,min}$ compared to the TAU unsteady CFD data, by $dC_l = 0.037$ with same phase shift of $\phi = 7.2$ deg. The CAMRAD II results overestimated $C_{l,max}$ and underestimated $C_{l,min}$ because these values were computed at maximum and minimum pitch angles, respectively. In contrast, the TAU unsteady simulation showed that $C_{l,max}$ and $C_{l,min}$ occurred with a negative phase shift to maximum and minimum pitch angles, due to additional inertia effects induced by the pitch motion, so that the airflow does not respond instantaneously to these changes. Instead, the flow near the airfoil surface exhibits a slight delay as the surrounding air adjusts to the new conditions imposed by the pitch motion. Consequently, the $C_{l,max}$ was computed in the TAU unsteady simulation at a lower effective angle of attack, and $C_{l,min}$ was reached after the minimum pitch angle, reflecting a higher effective angle of attack. Thus, the CAMRAD II models approximated a peak-to-peak $C_{l,PP} = 0.985$, which was slightly higher than the peak-to-peak value of $C_{l,PP} = 0.912$ calculated using the TAU unsteady CFD simulation.

Second, the impact of camber morphing on lift coefficient C_l variations throughout the pitch cycle

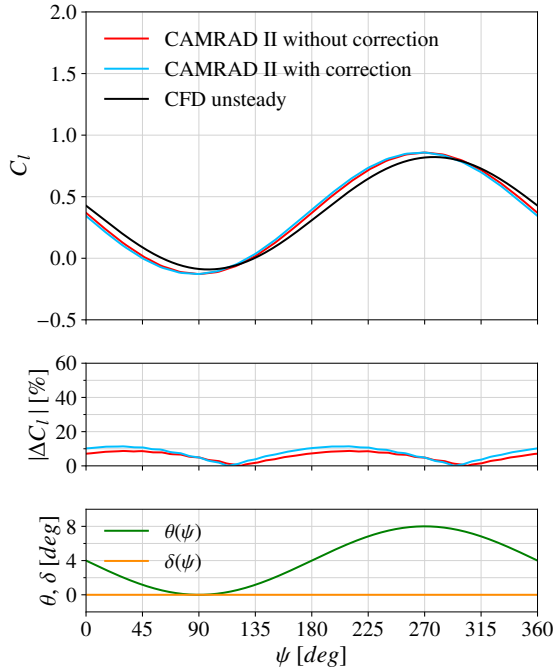

Figure 3.24.: Variation of C_l over pitching period for the baseline case at $M = 0.4$, with $f_\theta = 7$ Hz and $f_\delta = 0$ Hz.

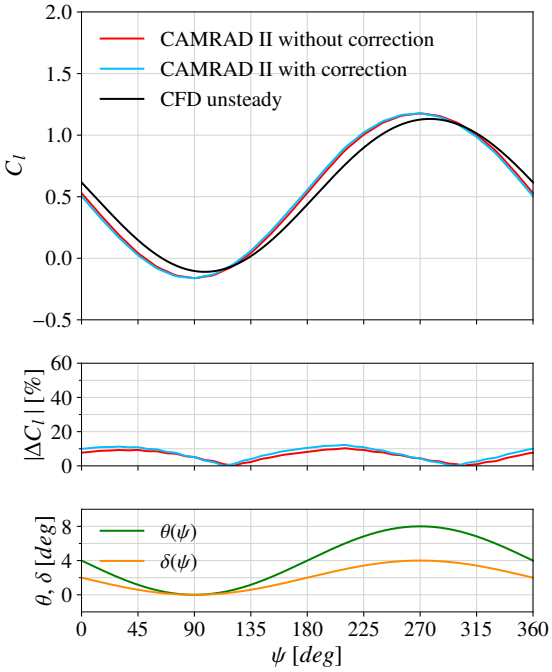

Figure 3.25.: Variation of C_l over pitching period for the 1P case at $M = 0.4$, with $f_\theta = 7$ Hz and $f_\delta = 7$ Hz.

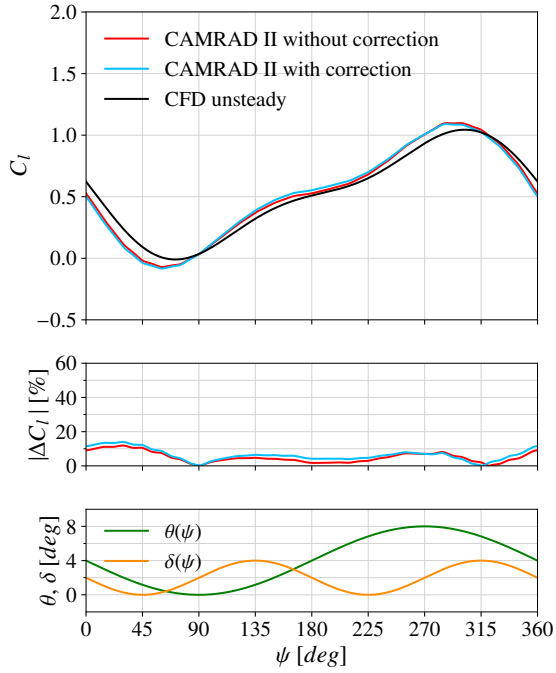

Figure 3.26.: Variation of C_l over pitching period for the 2P case at $M = 0.4$, with $f_\theta = 7$ Hz and $f_\delta = 14$ Hz.

was investigated. For this purpose, two scenarios were examined: In the first scenario, the camber morphing frequency was set to match the pitch motion frequency at $f_\delta = 7$ Hz (1P) and in the second scenario, the camber morphing frequency was doubled to $f_\delta = 14$ Hz (2P). Figures 3.25 and 3.26 depict the variations in lift coefficient C_l for these scenarios. The corresponding camber morphing schedules were depicted by the orange lines in the lower subplots, alongside the pitch schedule. In both camber morphing scenarios, both the CAMRAD II models– with or without the ONERA Edlin correction, captured the same trend in lift coefficient C_l variation over pitch cycle as the unsteady simulation. Furthermore, in both scenarios, the TAU unsteady results exhibited a negative phase shift relative to the schedule of the pitch motion, as also shown for the baseline case. When the camber morphing was synchronized with the pitch schedule, increasing the camber morphing effectively raised the angle of attack, while decreasing it lowered the effective angle of attack. Consequently for this scenario, the C_l variation over the pitch cycle exhibited a single harmonic variation. When the camber morphing frequency was doubled relative to the pitch schedule, the lift coefficient variation became a mix of different harmonics. Despite, the presence of these different harmonics, the variation in C_l was predominantly influenced by the single harmonic signal of the pitch motion.

Morphing the camber at a frequency of $f_\delta = 7$ Hz led to further increase of the phase shift in the TAU unsteady results relative to the prescribed pitch motion. Additionally, the camber morphing led also to an increase in the maximum lift coefficient $C_{l,max}$ of 0.31 in comparison the baseline case, as predicted by the unsteady CFD results. Both the uncorrected and corrected CAMRAD II results overestimated the maximum lift coefficient by approximately 0.045 when compared to the TAU unsteady CFD results. This overprediction was slightly greater than the difference observed in the baseline case, which was 0.036. Moreover, both unsteady CFD and CAMRAD II results approximated slightly lower $C_{l,min}$ values compared to the baseline. Here, the unsteady CFD results estimated a decrease in $C_{l,min}$ by $dC_l = 0.02$ in comparison to the baseline. Moreover, both CAMRAD II simulations, with and without the ONERA Edlin model underestimated, $C_{l,min}$ by $dC_l = 0.051$ and with the phase shift of $\phi = 7.7$ deg in comparison to the TAU unsteady results. Thus, the peak-to-peak value $C_{l,PP}$, as approximated by the CAMRAD models, was slightly higher with $C_{l,PP} = 1.337$ than the $C_{l,PP} = 1.241$ computed by the unsteady CFD for the camber morphing for the 1P scenario. Both peak-to-peak values were higher than the baseline case: $dC_{l,PP} = 0.352$ higher compared to the CAMRAD II models and $dC_{l,PP} = 0.329$ higher compared to the unsteady CFD model.

To highlight the differences between the TAU unsteady simulations and CAMRAD II simulations when camber morphing was synchronized with the pitch schedules, the magnitude of the lift coefficient difference $|\Delta C_l|$ is depicted in Fig. 3.25. The discrepancies between the TAU CFD unsteady results and each set of CAMRAD II results over the pitch period exhibited a similar trend to the baseline case. At the mean pitch angle $\theta_0 = 4$ deg during the downstroke at $\psi = 0$ deg and the upstroke at $\psi = 180$ deg, a camber morphing deflection of $\delta = 2$ deg was applied downwards and upwards, respectively. At these azimuth angles, where the same pitch angle was reached and the identical camber morphing deflection was applied, the deviations between the unsteady CFD and uncorrected CAMRAD II results were $|\Delta C_l| = 7.69\%$ and 8.18%, respectively. Using the ONERA Edlin model, these deviations increased to $|\Delta C_l| = 10\%$ and 10.7%, respectively. Thus, the deviations exhibited by both CAMRAD II models showed slightly higher magnitudes to those in the baseline case at the azimuth angles $\psi = 0$ deg and $\psi = 180$ deg, indicating that the introduction of

the camber morphing decreased the accuracy of the correction.

When the camber morphing frequency was increased to $f_\delta = 14$ Hz, the maximum lift coefficient $C_{l,max}$ and minimum lift coefficient $C_{l,min}$ were shifted relative to the minimum and maximum pitch angles, respectively. The minimum lift coefficient $C_{l,min}$ was shifted towards the minimum camber deflection, which occurred before the minimum pitch angle, while $C_{l,max}$ was shifted towards the camber deflection that occurred after the maximum pitch angle. The enhancement in $C_{l,max}$ was less pronounced compared to the morphing at $f_\delta = 7$ Hz.

The unsteady CFD results indicated an increase, denoted as $dC_l = 0.222$, relative to the baseline. Both CAMRAD II results, with and without the ONERA Edlin model, overpredicted $C_{l,max}$ by approximately $dC_l = 0.054$ compared to the TAU unsteady results. This overprediction was slightly larger than those observed in the baseline ($dC_l = 0.036$) and 1P ($dC_l = 0.045$) cases, due to slightly larger phase shift ϕ. Thus, both $C_{l,max}$ values computed with the CAMRAD II models exhibited a phase shift of $\phi = 10.7$ deg to the unsteady CFD results: greater than the values obtained for the baseline ($\phi = 7.2$ deg) and 1P ($\phi = 7.7$ deg) cases. Moreover, when the camber morphing frequency was increased to $f_\delta = 14$ Hz, the minimum lift coefficient $C_{l,min}$ obtained from the TAU unsteady results exhibited a pronounced increase compared to the baseline and 1P cases. These differences were quantified as $dC_l = 0.082$ and $dC_l = 0.104$ in comparison to $C_{l,min}$ of the baseline and 1P cases, respectively. The CAMRAD II results, both with and without the ONERA Edlin model, underestimated $C_{l,min}$ compared to the unsteady CFD results. The uncorrected CAMRAD II results showed an underestimation of $dC_l = 0.073$ while the corrected CAMRAD II results showed an underestimation of $dC_l = 0.061$. Thus, the unsteady CFD results for 2P case showed a peak-to-peak value of $C_{l,PP} = 1.05$, while the CAMRAD II models estimated a slightly higher peak-to-peak value of $C_{l,PP} = 1.169$ and $C_{l,PP} = 1.172$ without and with the ONERA Edlin correction, respectively. These differences between the peak-to-peak values, obtained with unsteady CFD and CAMRAD II simulations, were greater than those observed in the baseline and 1P cases, highlighting how the increase in camber morphing frequency can affect the reliability of the results. Furthermore, it is noteworthy that increasing the frequency to 14 Hz resulted in a lower rate of change in C_l over $90 < \psi < 180$ deg and significantly higher C_l values compared to the baseline and 1P cases. This can be attributed to the increased camber morphing of the airfoil, which consequently increased the effective angle, while the pitch rate was low before reaching the mean value of $\theta_0 = 4$ deg.

At the azimuth angles $\psi = 0$ deg and $\psi = 180$ deg, which corresponded to the mean pitch angles during the downstroke and upstroke respectively, the same camber morphing deflection of $\delta = 2$ deg was applied upwards. The deviation between the uncorrected CAMRAD II results and the unsteady CFD results was 9.09% and $|\Delta C_l| = 1.74\%$, at $\psi = 0$ deg and $\psi = 180$ deg respectively. The ONERA-Edlin model exhibited deviations of $|\Delta C_l| = 11.5\%$ at $\psi = 0$ deg and $|\Delta C_l| = 4.4\%$ at $\psi = 180$ deg compared to the unsteady CFD results. Here, the adjustment of the C_l coefficient using the ONERA Edlin model in CAMRAD II also did not account for the fluid inertia missing in the airfoil tables. The deviations of the CAMRAD II results at the azimuth angles $\psi = 0$ deg were larger than those observed in the 1P case, when the same camber morphing deflection δ =2 deg was also applied upwards. This suggests that increasing morphing frequencies, which led to a different morphing rate, can decrease the accuracy of the CAMRAD II compared to unsteady results. Moreover, at azimuth angle $\psi = 180$ deg, where the camber morphing deflection δ =2 deg was applied upwards, opposing the motion of the pitching movement, the differences between the

unsteady CFD and the CAMRAD II results were significantly lower than the differences obtained at $\psi = 0$ deg. This indicates that the phase between camber morphing and pitch motion can also affect the accuracy of the steady coefficient for approximating unsteady lift variation.

Evaluation of the Moment Coefficient:

The variation of the moment coefficient C_m was investigated for the baseline, when camber morphing was synchronized with the pitch schedule, and when the camber morphing frequency was doubled to $f_\delta = 14$ Hz. Additionally, the adjustment of the raw steady state data from the airfoil tables by the ONERA Edlin model is discussed.

The variation of the moment coefficient C_m for the baseline case, as illustrated in Fig. 3.27, shows that both the unsteady CFD and CAMRAD II results exhibited minimal changes in C_m throughout the pitch cycle. The uncorrected CAMRAD II data appeared relatively constant over time and the results obtained with ONERA Edlin model were closely aligning with the unsteady CFD results. Unlike the variation of the lift coefficient C_l, almost no phase shift was observed between the corrected results with the ONERA Edlin model and the unsteady CFD results. This indicates that the ONERA Edlin model successfully accounts for the impact of the inertia associated with the pitching motion of the airfoil on the moment coefficient C_m. The values of the deviation $|\Delta C_m|$ over the pitch period appear unusually high. However, this is primarily due to the fact that the absolute values of C_m were close to zero throughout the pitch cycle, hence increasing the percentage error. The deviation $|\Delta C_m|$ obtained when using the ONERA Edlin model in CAMRAD II were lower over the pitch cycle compared to the uncorrected data. This demonstrates that the ONERA Edlin model effectively adjusted the raw steady state data to align more closely with the unsteady CFD results. Figures 3.28 and 3.29 demonstrate that the magnitude of the moment coefficient C_m varied significantly compared to the baseline when the camber morphing was applied, with the frequencies $f_\delta = 7$ Hz and $f_\delta = 14$ Hz respectively. Notably, the variation of C_m closely mirrored the temporal changes in the camber morphing motion, rather than superposition of both the camber morphing and pitching schedules.

When the camber morphing frequency was $f_\delta = 7$ Hz, unlike the baseline case with low and relatively constant C_m values throughout the pitch cycle, a significant variation in C_m was induced across all models with a response which was dominated by the single harmonic frequency, as shown in Fig. 3.28. Given the nearly constant C_m response in the baseline case, the notable variation of C_m in the 1P case appears to be induced by the camber morphing. The unsteady CFD results ranged from a minimum $|C_{m,min}|$ of 0.0085 at $\psi = 90$ deg, corresponding to zero pitch and camber deflections and, to a maximum of $|C_{m,max}| = 0.081$ at $\psi = 270$ deg, corresponding to the peak of pitch angle and camber deflection. The $|C_{m,min}|$ was predicted accurately by both CAMRAD II models. However the $|C_{m,max}|$ was also overpredicted by both models, so that both CAMRAD II results undepredicted the $C_{m,PP}$. At the mean pitch angle during the downstroke ($\psi = 0$ deg) , a camber morphing deflection of $\delta = 2$ deg was applied downward. Similarly, at the mean pitch angle during the upstroke ($\psi = 180$ deg) , a camber morphing deflection of $\delta = 2$ deg was applied upward. At these azimuth angles the deviations $|\Delta C_m|$ between the unsteady CFD and uncorrected CAMRAD II results were 4.27% and 5.51% respectively. When the ONERA Edlin model was applied, these deviations was reduced to 2.29% and 0.89% respectively, improving the accuracy of the CAMRAD II results.

The uncorrected CAMRAD II model exhibited a negative phase shift in C_m variation when compared to unsteady CFD data, indicating that the predicted changes in C_m lagged behind those observed in the unsteady CFD simulations. In contrast, the C_l variation from the uncorrected CAMRAD II model showed a positive phase shift relative to the unsteady CFD, meaning that the changes in C_l occurred earlier in the CAMRAD II results than in the unsteady CFD data. When the ONERA Edlin model was applied to correct the CAMRAD II results, it induced a negative phase shift in both the C_m and C_l curves relative to the uncorrected CAMRAD II results. This adjustment effectively reduced the discrepancies only for the C_m variation. The positive phase shift introduced by the ONERA Edlin correction counteracted the initial negative phase shift of the uncorrected CAMRAD II model, resulting in a closer alignment of the corrected CAMRAD II results with the unsteady CFD data. This is demonstrated by the small deviations $|\Delta C_m|$ between the unsteady CFD and the CAMRAD II results after applying the ONERA Edlin model, as shown in Fig. 3.28, with the highest discrepancies occurring near θ_{max}, due to the limitations of the ONERA Edlin model at high angles of attack [58, 80]. As such, it could be said that the ONERA Edlin correction increases the accuracy of the C_m results of the CAMRAD II model in this instance.

When camber morphing frequency was doubled to $f_\delta = 14$ Hz, the variation of C_m also followed the camber morphing schedule, as shown in Fig. 3.29. This was inconsistent with the C_l response for the 2P case, where the variations in C_l resulted from a superposition of different harmonics over time, influenced by both pitch and camber morphing motions. In contrast to the 1P case, the minimum value of the moment coefficient $|C_{m,min}|$ did not occur at zero pitch angle. Instead, it was observed during the airfoil downstroke phase with zero camber morphing. Similarly, the maximum $|C_{m,max}|$ value was not achieved at the maximum pitch angle, as observed in the 1P case, but rather when the highest camber morphing was applied during the airfoil upstroke phase. The uncorrected CAMRAD II model underpredicted $|C_{m,max}|$ and overpredicted the $|C_{m,min}|$, leading to a underprediction of the peak-to-peak moment coefficient $C_{m,PP}$. The ONERA Edlin model, however, improved the C_m extreme values, closely matching the $C_{m,PP}$ calculated by the unsteady CFD. Notably, the only discrepancy observed with the ONERA Edlin model occurred at θ_{max}, where C_m did not match the unsteady results. This indicates that the ONERA Edlin model was effective in correcting the C_m steady data from the airfoil table and aligning it with the unsteady results, except at the high pitch angle θ_{max}, as also shown for the 1P case.

The effectiveness of the ONERA Edlin model at capturing time-dependent C_m variation is demonstrated at $\psi = 0$ deg and $\psi = 180$ deg, which corresponded to the mean pitch angles during the downstroke and upstroke, respectively. At these azimuth angles, the same camber morphing deflection of $\delta = 2$ deg was applied upwards. The deviation of the corrected results using the ONERA Edlin model relative to the unsteady TAU results was $|\Delta C_m| = 1.97\%$ at $\psi = 0$ deg and 1.10% at $\psi = 180$ deg. Moreover, throughout the entire pitch cycle, the deviations in the CAMRAD II results using the ONERA Edlin model did not exceed 3.14% when relative to unsteady results, except at θ_{max}, where the deviation $|\Delta C_m|$ was 4.45%.

The deviation $|\Delta C_m|$ of the CAMRAD II results without the ONERA Edlin model relative to the TAU CFD unsteady results were also considered to be low, although they showed higher deviations in comparison to the results obtained with the ONERA Edlin model. The deviation $|\Delta C_m|$ over the pitch cycle between CAMRAD II results without the ONERA Edlin model and unsteady CFD was also considered relatively low but exceeded those observed when the ONERA Edlin model was

applied. The largest deviation, $|\Delta C_m| = 6.18\%$, occurred after θ_{max}. This was due to the phase shift caused by the lack of consideration of inertia effects at θ_{max} in the steady C_m values from the airfoil tables. The phase shift observed in the CAMRAD II results without ONERA Edlin model relative to the unsteady CFD results varied inconsistently throughout the pitch cycle. Specifically, the phase shift was positive during the downstroke motion of the airfoil and shifted to varying positive and negative phases during the upstroke motion. However, the ONERA Edlin model adjusted the phase of the C_m curve to align more closely with the unsteady CFD results over the entire pitch cycle. This adjustment demonstrates that the ONERA Edlin model improved the accuracy of C_m predictions by dynamically responding to camber morphing frequencies higher than the pitch frequency, effectively accounting for inertial effects and reducing the error when compared to the unsteady CFD model.

Evaluation of the Drag Coefficient:

Alongside lift coefficient C_l and moment coefficient C_m, this study also investigated how the drag coefficient C_d varied when the stand-alone pitching motion was applied and also when camber morphing motion was introduced. Figure 3.30 shows the approximated drag variation under a stand-alone pitch motion, using the TAU unsteady solver and CAMRAD II, with and without the ONERA Edlin model.

The first significant observation from this study was that both CAMRAD II results overlapped. This is because the ONERA Edlin model in CAMRAD II did not include an unsteady correction for drag prediction. Additionally, unlike the lift coefficient C_l and moment coefficient C_m results, which showed similar trends and magnitudes between unsteady CFD and CAMRAD II results, the CAMRAD II model exhibited significant deviations in the drag coefficient C_d response to airfoil motion. Specifically, the CAMRAD II simulations approximated significantly lower gradients of drag coefficient C_d over the pitch cycle in comparison to the TAU unsteady results, particularly at pitch angles below the pitch mean value of 4 deg, corresponding to the range $0 < \psi < 180$ deg, the drag variation approximated with CAMRAD II models was almost constant with $C_d \approx 0.01$ for all investigated cases. In contrast, the unsteady CFD results captured a pronounced variation of drag throughout the pitch cycle in particular over the range between $180 < \psi < 360$, corresponding to the time interval with high pitch angles.

For the baseline case, the highest C_d value of $C_{d,max} = 0.021$ was obtained using the TAU unsteady simulation before reaching the maximum pitch angle, with a phase shift of $\phi = 32$ deg from θ_{max}. The minimum drag coefficient $C_{d,min}$ value, approximately 0.005, was obtained just at θ_0 during the downstroke phase. Since the CAMRAD II model did not take into account any time-dependent behaviour, $C_{d,min}$ and $C_{d,max}$ were approximated at the minimum pitch angle θ_{min} and θ_{max} respectively, not introducing any phase shift. The deviation between the unsteady CFD and CAMRAD II results, expressed as $|\Delta C_d|$, was computed using Eq. 3.6. The deviation was lowest within $45 < \psi < 135$ deg when the pitch angle was lowest. The largest discrepancy between the CAMRAD II and TAU unsteady results reached 38.17% and occurred at the point of maximum drag $C_{d,max}$ in the unsteady CFD results. This significant discrepancy indicates that the CAMRAD II model does not accurately approximate the maximum drag. At $\psi = 0$ deg and $\psi = 180$ deg, corresponding to θ_0 during the downstroke and upstroke, respectively, the drag coefficient C_d values from CAMRAD II remained unchanged and matched the values from the airfoil tables for the corresponding ef-

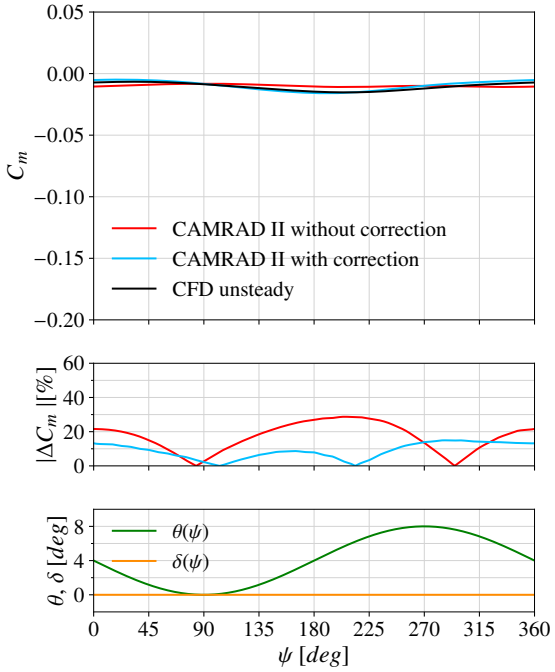

Figure 3.27.: Variation of C_m over pitching period for the baseline case at $M = 0.4$, with $f_\theta = 7$ Hz and $f_\delta = 0$ Hz.

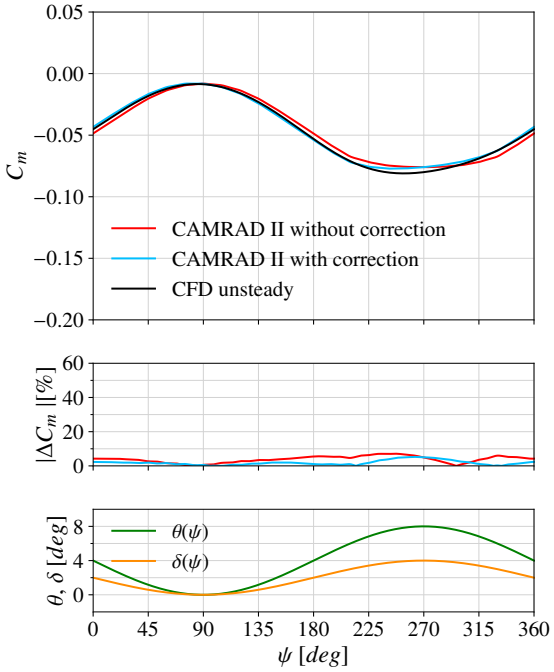

Figure 3.28.: Variation of C_m over pitching period for the 1P case at $M = 0.4$, with $f_\theta = 7$ Hz and $f_\delta = 7$ Hz.

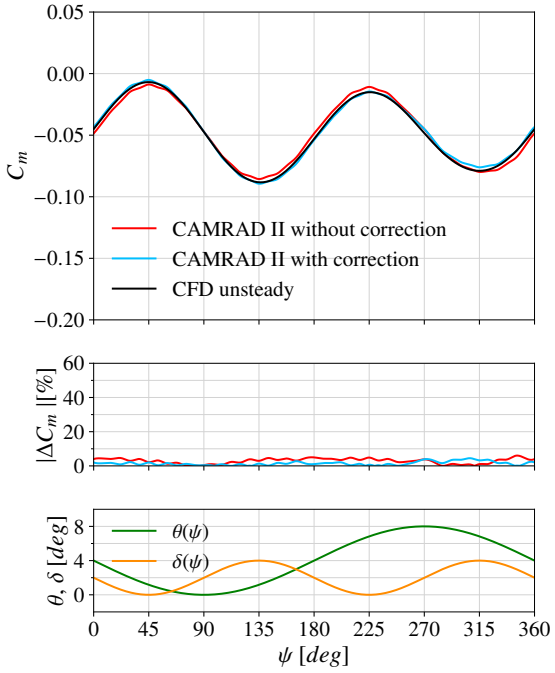

Figure 3.29.: Variation of C_m over pitching period for the 2P case at $M = 0.4$, with $f_\theta = 7$ Hz and $f_\delta = 14$ Hz.

fective angle of attack. In contrast, the TAU unsteady simulation accounted for the resistance of the surrounding fluid to the dynamic motion of the airfoil. Consequently, the CAMRAD II data underestimated C_d at $\psi = 0$ deg by 25.05% and overestimated C_d at $\psi = 180$ deg by 17.95%.

When the camber morphing was synchronized with the pitch motion, the TAU CFD unsteady results showed a larger variation in the drag coefficient C_d over the pitch cycle compared to the baseline case, as shown in Fig. 3.31. In contrast, the CAMRAD II models showed much lower drag variation than the TAU unsteady simulation. This led to a significant difference in approximating the maximum $C_{d,max}$ and minimum $C_{d,min}$ drag coefficients between the TAU and CAMRAD II results. Since synchronizing the camber morphing with the pitch motion led to a consistent increase in the effective angle of attack, the maximum drag coefficient $C_{d,max}$ of the baseline and 1P case occurred at the same pitch angle and the minimum drag coefficient also occurred at θ_0 during the downstroke phase, similar to the baseline case. The evaluation of the deviations $|\Delta C_d|$ for the 1P case in Fig. 3.31 reveals that the consistent increase in the effective angle of attack resulted in larger amplification of the deviations between the CAMRAD II and TAU CFD results, in comparison to the baseline case. At the azimuth angles $\psi = 0$ deg and $\psi = 180$ deg, which corresponded to the mean pitch angles during the downstroke and upstroke respectively, the same camber morphing deflection of $\delta = 2$ deg was applied upwards. At these azimuth angles, the deviations $|\Delta C_d|$ were 31.81% at $\psi = 0$ deg and 22.22% at $\psi = 180$ deg. The discrepancies were greater at these specific azimuth angles compared to the baseline case. Moreover, when camber morphing was applied in synchronization with pitch motion, the TAU unsteady results showed an overall maximum deviation of $|\Delta C_d| = 48.29\%$, which was considerably larger than the maximum deviation in the baseline case. Thus, the combined effects of pitch and camber morphing significantly amplify the inertia effects related to airfoil motion, leading to lower accuracy in drag predictions computed with airfoil tables.

Figure 3.32 shows the variation of the drag coefficient when camber morphing was applied at $f_\delta = 14$ Hz. The drag variation by the CAMRAD II results, similar to the 1P and baseline cases, exhibited lower gradients in the drag coefficient C_d over the pitch cycle compared to the unsteady CFD results. Additionally, $C_{d,\text{min}}$ and $C_{d,\text{max}}$ occurred at different azimuth angles. The unsteady results exhibited a more significant time dependence between 90 deg and 135 deg compared to the baseline and 1P cases, as the camber morphing was applied downward with a higher rate during this interval. Thus, the deviation between the CAMRAD II and TAU unsteady results was higher over this range in comparison to the baseline and 1P cases. The maximum drag coefficient $C_{d,max}$ computed with TAU unsteady was lower than in the 1P case because a lower camber morphing deflection was applied at θ_{max}, resulting in a lower angle of attack at the maximum pitch angle.

The maximum drag coefficient $C_{d,max}$ was not obtained at θ_{max} and was reached after $\psi = 270$ deg, so that $C_{d,max}$ was shifted towards the highest camber morphing deflection at $\psi = 315$ deg due to the inertial effects. The CAMRAD II models also approximated the maximum drag coefficient $C_{d,max}$ to be shifted negatively from the maximum pitch angle location, however, this was induced by the effect of the camber morphing rather than the inclusion of time-dependent effects. The effect of camber morphing frequency on unsteady drag became apparent when comparing the deviation $|\Delta C_d|$ at $\psi = 0$ deg and $\psi = 180$ deg, where the same mean pitch angle during downstroke and upstroke were applied, as well as the same mean camber deflection $\delta = 2$ deg upwards. At azimuth angle of $\psi = 0$ deg, the 2P case demonstrated a larger discrepancy, with $|\Delta C_d| = 41.03\%$,

between the unsteady drag predicted by TAU and the steady drag from the airfoil tables used in the CAMRAD II simulations. This difference was greater compared to the 1P case, despite both the 2P and 1P cases having the same mean pitch angle of $\theta_0 = 4$ deg and an upward camber deflection of $\delta = 2$ deg at that time point. This observation further underscores that the rate of camber morphing can significantly influence the unsteady drag variations caused by the combined pitch and morphing motion. At azimuth angle $\psi = 180$ deg, the deviation between the CAMRAD II models and the unsteady CFD was reduced to $|\Delta C_d| = 13.28\%$, since the pitch and camber morphing motion were out of phase. This demonstrates that the phase relationship between camber morphing and pitch motion can significantly affect the accuracy of the steady coefficient in approximating unsteady drag variation.

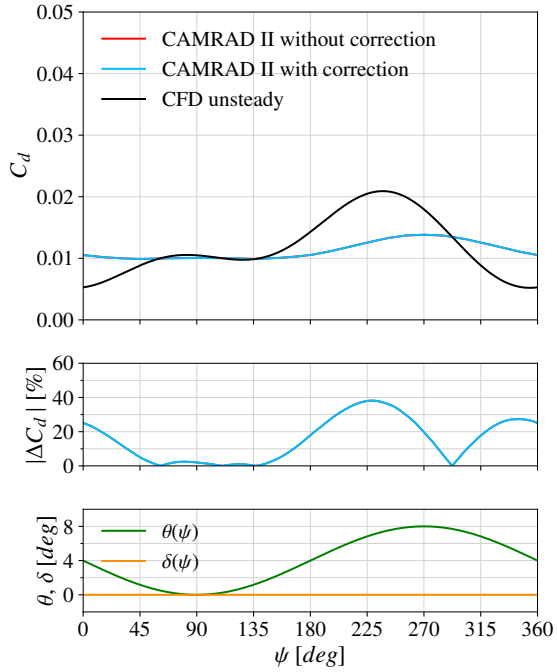

Figure 3.30.: Variation of C_d over pitching period for the baseline case at $M = 0.4$, with $f_\theta = 7$ Hz and $f_\delta = 0$ Hz.

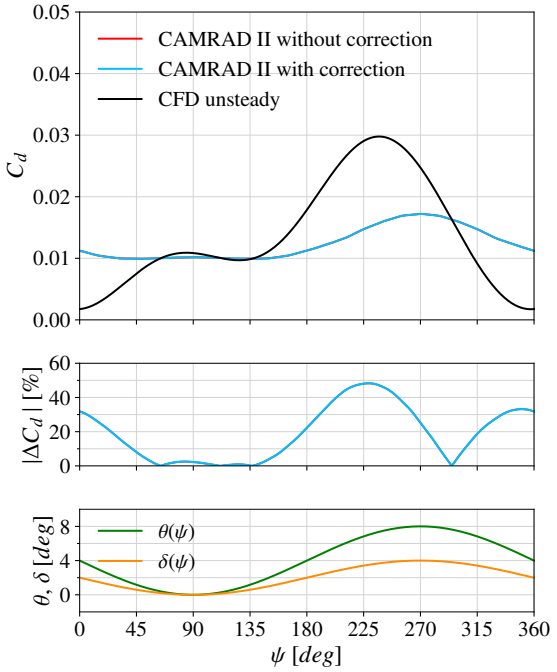

Figure 3.31.: Variation of C_d over pitching period for the 1P case at $M = 0.4$, with $f_\theta = 7$ Hz and $f_\delta = 7$ Hz.

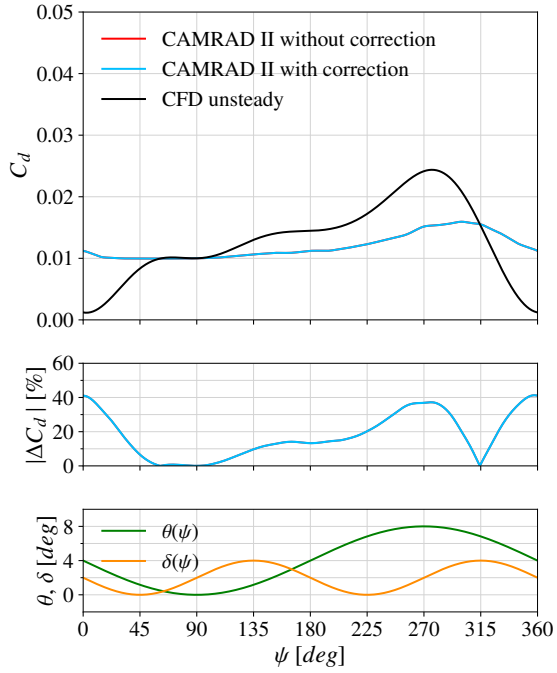

Figure 3.32.: Variation of C_d over pitching period for the 2P case at $M = 0.4$, with $f_\theta = 7$ Hz and $f_\delta = 14$ Hz.

3.2.5. Comparison of the Pressure Distribution and Velocity Profiles

This subsection focuses on demonstrating the impact of pitch and camber morphing history on pressure distribution and velocity profiles. To highlight the unsteady effects not captured in the airfoil tables used for comprehensive rotor analysis, the pressure and velocity at the mean pitch angle θ_0 during both upstroke and downstroke motions were compared to steady-state results at the same angles of attack. The mean pitch angle θ_0 was reached at$\psi = 0$ deg during the upstroke and at $\psi = 180$ deg during the downstroke, as explained in 3.2.4.

During the downstroke and upstroke motions, when the mean pitch angle θ_0 was reached, the camber-morphed airfoils had the same pitch angle as the baseline, with the same camber deflection applied for both the 1P and 2P cases. To highlight the impact of the time histories of the pitch and camber morphing motions, the pressure distribution along the chord length was extracted from the unsteady solution at θ_0 during the downstroke and upstroke, and compared to the steady-state result. Additionally, the local normalized velocity profiles U_x/U_∞ were extracted perpendicular to the upper and lower surfaces of the airfoil at two specific locations $x/c = 0.1$ and $x/c = 0.25$ along the lines A, B, C, and D, as shown in Fig. 3.33.

During the downstroke motion of the baseline airfoil, the section along $0 < x/c < 0.25$ was rotating in the upstream direction. This led to a significant increased in the velocity near the upper surface at probe location A and a slight decreased in the velocity near the lower surface compared to the steady state results at probe location C, as shown in 3.34b. The induced accelerated flow field over the leading section during the downstroke led to a favorable pressure gradient on the upper surface, characterized by an increased suction peak and a higher pressure difference $0 < x/c < 0.25$ in comparison to the steady state simulation, resulting in a higher lift coefficient C_l compared to the steady state results. In contrast, the unsteady results exhibited lower velocities over the upper leading section during the upstroke motion. These differences led to a reduction of the suction peak, a smaller pressure difference, and thus a lower lift coefficient C_l in comparison to the steady results. Starting from the location $x/c = 0.25$, the steady and unsteady results extracted during downstroke and upstroke motions showed almost no differences in the pressure distribution and velocity profiles, as shown by probe locations B and D. This indicates that the influence of the airfoil motion on flow velocity diminished progressively along the airfoil chord.

When the camber morphing was synchronized with pitch motion (1P case), the unsteady effects were more significant in comparison to the baseline case, since the discrepancy in the pressure distribution and velocity profiles between the steady and unsteady results at θ_0 became more pronounced, mainly over the upper surface of the section $0 < x/c < 0.25$, as shown in Fig. 3.35a and 3.35b. As a result, the discrepancy in computing C_l became greater for the steady state condition compared to the unsteady results during the downstroke and upstroke motions, as discussed in 3.2.4. The lack of phase shift between the pitch and camber morphing motions for both steady and unsteady state results led to a higher velocity along the probe line A compared to the baseline, thereby enhancing the favorable pressure gradient on the leading edge section of the upper surface, as shown in Fig. 3.35a. Thus, a higher suction peak and an increased pressure difference between the upper and lower surfaces were achieved, resulting in a higher C_l compared to the baseline. Furthermore, a higher pressure difference was observed due to camber morphing

in the airfoil section between $x/c = 0.75$ and 1.0 compared to the baseline. Notably, the pressure difference calculated from steady state and unsteady simulations exhibited minimal variation, indicating negligible unsteady effects on pressure along the morphing section.

When the morphing section of the airfoil was subjected to a 14 Hz frequency (2P case), the camber morphing was applied upward during the upstroke and the downstroke phases at θ_0. As shown in Figs. 3.36a and 3.36b, the unsteady results of the pressure and velocity profiles during the downstroke phase at θ_0 were nearly identical for both the 1P and 2P cases. This similarity can be attributed to the consistent camber morphing schedule during the downstroke in both cases at θ_0, with both experiencing a decreasing camber morphing and reaching the same camber deflection. However, during the upstroke phase, the pressure and velocity profiles for the 2P case deviated from those of the 1P case. These profiles more closely aligned with steady state results, suggesting that unsteady effects due to camber morphing were less pronounced at θ_0. This reduced impact of the unsteady effects can be attributed to the decreasing camber morphing deflection as the pitch angle increases during the upstroke motion. Thus, the lift coefficient C_l values at θ_0, computed with both unsteady CFD and steady methods, were close to each other during the upstroke, as shown in Fig. 3.26. This highlights the critical role of phase relationship between camber morphing and pitch motion in influencing the unsteady state pressure and velocity.

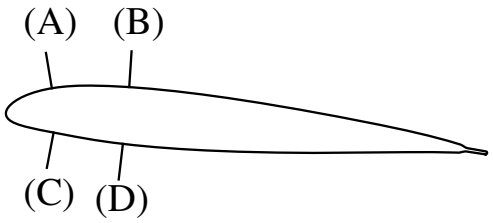

Figure 3.33.: Velocity profile extraction locations on the airfoil surface: Upper surface probe locations A and B were positioned at $x/c = 0.1$ and $x/c = 0.25$, respectively. Lower surface probe locations C and D were positioned at $x/c = 0.1$ and $x/c = 0.25$, respectively.

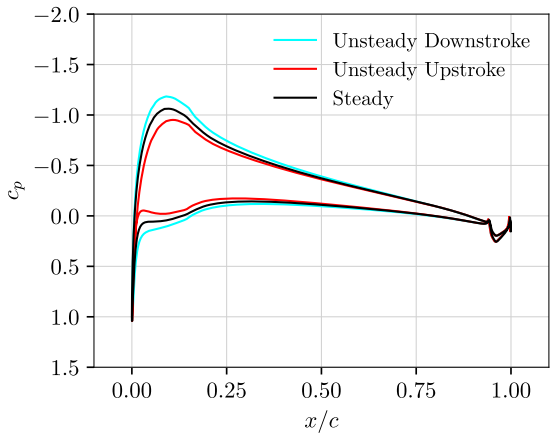

(a) Comparison of the pressure distribution c_p of the baseline case along the airfoil surface at $\theta_0 = 4$ deg.

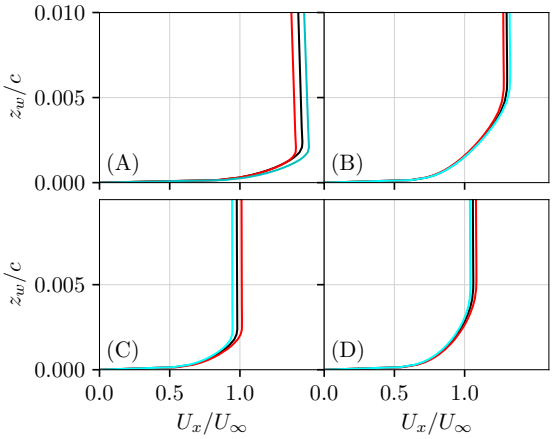

(b) Comparison of velocity profiles, extracted along the A, B, C, and D lines for the baseline case at $\theta_0 = 4$ deg.

Figure 3.34.: Comparison of the pressure distribution c_p and velocity profiles over the airfoil surface during the unsteady downstroke and upstroke, as well as in the steady state at $\theta_0 = 4$ deg, for the baseline case for the reduced frequency $k = 0.045$ and Mach number $M = 0.4$.

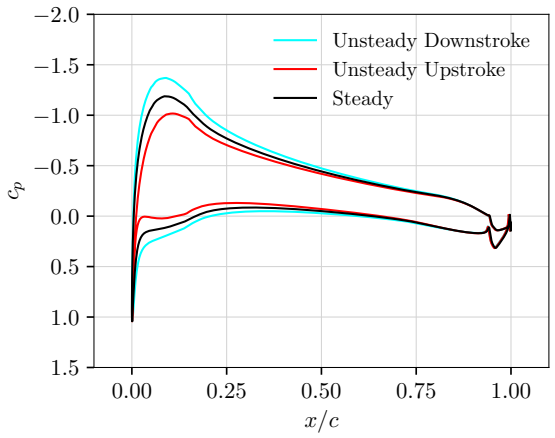

(a) Comparison of the pressure distribution c_p along the airfoil surface of the 1P case at $\theta_0 = 4$ deg.

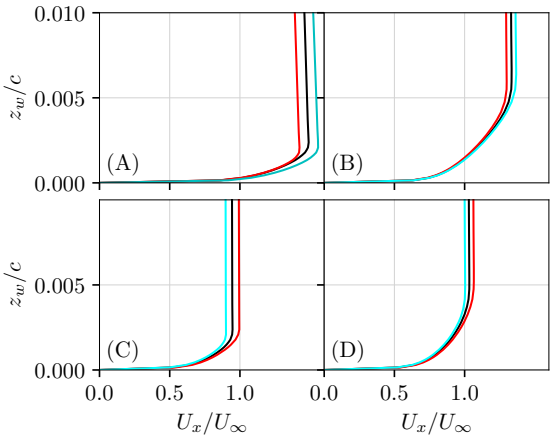

(b) Comparison of velocity profile, extracted along the A, B, C, and D lines for the 1P case at $\theta_0 = 4$ deg.

Figure 3.35.: Comparison of the pressure distribution c_p along the airfoil surface and velocity profiles during the unsteady downstroke and upstroke, as well as in the steady state at $\theta_0 = 4$ deg, when camber morphing with the frequency $f_\delta = 7$ Hz was synchronized with the pitch motion (1P case) for the reduced frequency $k = 0.045$ and Mach number $M = 0.4$.

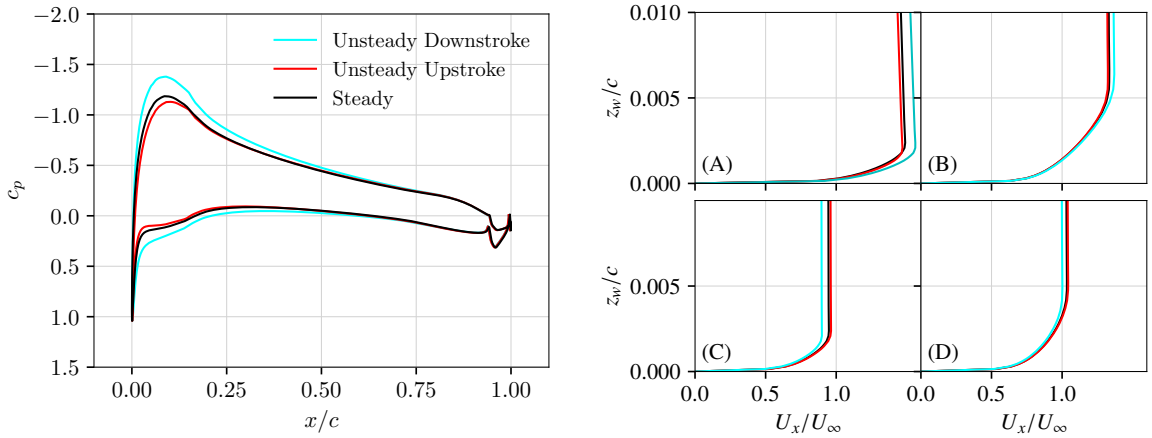

(a) Comparison of the pressure distribution c_p along the airfoil surface for the 2P case at $\theta_0 = 4$ deg.

(b) Comparison of velocity profile , extracted along the A, B, C, and D lines for the 2P case at $\theta_0 = 4$ deg.

Figure 3.36.: Comparison of the pressure distribution c_p along the airfoil surface and velocity profiles during the unsteady downstroke and upstroke, as well as in the steady state at $\theta_0 = 4$ deg, when camber morphing with the frequency $f_\delta = 14$ Hz was applied simultaneous to the pitch motion (2P case)for the reduced frequency $k = 0.045$ and Mach number $M = 0.4$.

3.2.6. Summary and Conclusions

Section 3.2 presents an evaluation of the discrepancies between unsteady CFD simulations and steady aerodynamic coefficients used within the CAMRAD II model under uniform inflow conditions. The primary objective is to identify unsteady effects not captured by conventional airfoil data and to assess the capability of the ONERA Edlin model with its default settings in addressing these discrepancies through independent adjustments to aerodynamic coefficients C_l, C_m, and C_d. To exclude the effect of the inflow model on the blade aerodynamics, a uniform inflow model was used in CAMRAD II. The pitch angle was restricted to a range between 0 and 8 deg ensuring attached flow conditions. The Mach number was set to 0.4 and the pitch frequency to 7 Hz, resulting in quasi-steady conditions with a reduced frequency of 0.0045. These parameters were selected to focus on unsteady effects primarily induced by pitching and camber morphing. The camber morphing was applied from $x/c = 0.75$ .The investigations included the 1P case, where the camber morphing frequency was synchronized with the 7 Hz pitch frequency, and the 2P case, in which the camber morphing frequency was doubled to 14 Hz.

The following conclusions were drawn from a comparison of the lift coefficient C_l, pitching moment coefficient C_m, and drag coefficient C_d computed using the TAU unsteady model against those obtained from the CAMRAD II model, both with and without using the ONERA Edlin model.

- The ONERA Edlin model introduced a positive phase shift for both the moment coefficient C_m and the lift coefficient C_l, improving the accuracy of C_m predictions by accounting for inertia effects during pitching and camber morphing motions. This adjustment effectively enhanced the prediction of the pitching moment by capturing the dynamic response more accurately. However, the ONERA Edlin model could not fully align C_m values with unsteady

CFD results when the airfoil was subjected to maximum pitch angles.

- The ONERA Edlin model could not capture fluid inertia effects in lift coefficient C_l results due to the positive phase shift, resulting in lift coefficient values being calculated at inaccurate effective angles of attack. This adjustment of the C_l from the airfoil tables resulted in further deviations from the unsteady CFD results.

- The ONERA Edlin model, with its default settings in CAMRAD II, did not adjust the C_d values from the airfoil tables. This limitation underscores the need for alternative modeling approaches to accurately represent drag behavior in dynamic conditions. As a result, the CAMRAD II results failed to capture the significant drag variations throughout the pitch cycle and the impact of camber morphing on drag, due to the absence of unsteady effects in the airfoil tables.

- The variation of the moment coefficient C_m was primarily driven by camber morphing. As a result, the camber morphing led to higher C_m magnitude values compared to the baseline. In contrast, the lift coefficient C_l variation was mainly driven by pitch motion, as changes in pitch angle directly affected the effective angle of attack and pressure distribution.

- When comparing the pressure and velocity profiles at the mean pitch angle, the most pronounced differences between unsteady downstroke and upstroke results compared to steady state were observed at the leading section $0 < x/c < 0.25$ of the airfoil induced by the pitching motion. Synchronizing camber morphing with pitch motion significantly amplified the differences in pressure distribution and suction peaks between the unsteady and steady results at the leading section, compared to the baseline. In contrast, when camber morphing was applied at double the pitching frequency, unsteady effects diminished as camber morphing gradually decreased during the upstroke phase, with pressure and velocity profiles similar to the steady state results. Thus, the phase relationship between camber morphing and pitch motion plays a crucial role in determining the extent of unsteady aerodynamic effects.

3.3. Evaluation of aerodynamic Characteristics for passive and active rotors using CFD/CSD coupling

3.3.1. Aim of the Study

In the previous Subsection 3.2, it was demonstrated that for a simple one-blade model under quasi-steady conditions with attached flow and uniform inflow, the lifting line method in CAMRAD II accurately captured the trends in lift and moment variation over the azimuth. The results showed acceptable accuracy when compared to more detailed unsteady simulations. However, using the uniform inflow failed to accurately predict the drag coefficient C_d, especially when camber morphing was synchronized with pitching motion. The accuracy of aerodynamic loads in CAMRAD II, based on lifting line theory, can be improved with a free wake model, providing better representation of rotor inflow non-linearities and rotor wake dynamics [76, 13, 88]. Moreover, the non-linear aerodynamic loads on rotor blades can be further refined by incorporating semi-empirical correction models that account for drag and dynamic stall, such as the Leishman-Beddoes model, the ONERA Edlin model for dynamic stall, or the Boeing model [58]. Both free wake and advanced semi-empirical correction models do not account for viscous and turbulent effects. Furthermore, the size and evolution of the blade tip vortex in free wake models depend on empirical parameters, making it challenging to accurately predict the formation, strength, and trajectory of tip vortices across different flight conditions [12, 120].

Previous studies [92, 79, 121, 6, 24, 8] demonstrated that coupling a high-fidelity CFD model with a CSD model overcomes the limitations of the free wake and lifting line methods when computing rotor aerodynamics. This is because the approach solves the non-linear, unsteady aerodynamics of the rotor flow field using the Navier-Stokes equations, while the CSD model is used to trim the rotor. As a result, it enables accurate modeling of complex phenomena, including cross-flow variations along the blade span, blade-vortex interactions, and unsteady, three-dimensional vortex dynamics. It can resolve the details of vortex roll-up and diffusion around the rotor, leading to better predictions of oscillatory pitch-link loads, torsion moments, and vibrations [15, 24, 121, 25]. Additionally, the CFD/CSD coupling approach offers a significantly more accurate approximation of blade-vortex interaction (BVI) and associated noise, when compared to free wake models [55, 92, 107, 113].

Encouraged by the positive outcomes demonstrated in previous studies, the development of a high-fidelity and extensible CFD/CSD loose coupling approach for both passive and active rotor blades was initiated in this work. This framework captures critical phenomena essential for understanding rotor performance, including compressibility effects, blade-vortex interactions (BVI), blade tip vortex roll-up, wake diffusion, and blade sectional pressure variations. Thus, in this section a loose CFD/CSD coupling is used to identify how camber morphing influences pressure distributions, rotor wake characteristics, and consequently, the resulting sectional thrust and drag in comparison to a passive blade. These findings with the CFD/CSD coupling can contribute to more accurate insights into rotor aerodynamics and blade motion, which are essential for determining the required power, vibration, and noise for passive and active rotors. Additionally, the results obtained with the CFD/CSD coupling approach for both passive and active rotor were compared with

standalone CAMRAD II comprehensive analysis results using free wake and linear inflow models, to highlight the differences in fidelity level between these investigation approaches.

3.3.2. Numerical Setup

This section presents the numerical setup used to demonstrate the capability of the CFD/CSD coupling approach for the passive and active four-bladed isolated rotor. The compressible unsteady TAU DLR code [28] was used as the CFD solver to compute the URANS equations at every time step to approximate the flow field surrounding the passive and active rotor. The blade surfaces were modeled as a fully turbulent viscous wall, and the one equation Negative Spalart–Allmaras turbulence model was used to solve the transport equation for the eddy viscosity. The central scheme was used for the convective RANS flux for the spatial discretization, while an implicit backward Euler scheme handled the time discretization. The details of the numerical schemes used in TAU are explained in Subsection 2.1.1.

The three-dimensional fluid domain was comprised of six blocks: four identical rotating blocks for the rotor blades, a stationary far field block to represent the rotor environment, and a rotating transfer block for interpolation between the blocks of the rotating blade and stationary far field. The blades were modeled as rigid surfaces with the BO105 rotor blade geometry, including its linear built-in twist and the NACA23012 airfoil with a tab, used also for the previous results shown in Sections 3.1 and 3.2. Details on how the different grid blocks in the three-dimensional domain are generated to solve the rotor field are provided in Subsection 2.4.2. Both the passive and active rotors adopted a rotation frequency of 44.5 rad/s (425 RPM), corresponding to the BO105 helicopter operating rotation frequency. The flow field of one rotor revolution was resolved using 720 time steps, which corresponds to a time step of $\Delta t = 0.000196$ s. Incoming flow velocity was set to $U_\infty = 32.404$ m/s at standard sea-level conditions with an air temperature $T_\infty = 15$ °C and an air density $\rho = 1.225\text{kg/m}^3$, resulting in an advance ratio of $\mu = 0.15$, as listed in Table 3.2. A CFL number of 8 and a two-stage multigrid cycle were used for all simulations. Convergence was monitored by targeting a density residual of 10^{-6} and tracking the residual of the resultant lift and drag for both passive and active blade simulations.

For the active blades, camber morphing was modeled using the TAU grid deformation utility. The active blades featured a linear transition region of length $t/R = 0.10$ between the fully active camber section s spanning from $r/R = 0.45$ to $r/R = 0.75$ and the unmorphed blade section at both ends. Subsection 2.4.4 provides a detailed description of the camber morphing blade section and the applied camber morphing schedule used throughout the blade rotation of the active rotor. At each time step, the blade surface and surrounding grid blocks were deformed according to the time varying camber morphing deflection schedule for each blade. This was followed by preprocessing the entire CFD domain and solving the fluid domain based on the previous time step. For both passive and active rotors, the flap and lead-lag hinges, and pitch bearings were positioned at the rotor hub center. For both passive and active rotor configuration, the shaft is tilted with $\alpha_S = 3$ deg towards the incoming flow. The order of the blade blocks' motion in the CFD simulations at each time step follows the hierarchy, outlined in Subsection 2.4.3.

Table 3.2.: Input flight condition in the TAU CFD and CAMRAD II CSD simulations.

Parameter	Symbol	Values	Units
Advance ratio	μ	0.15	-
Incoming flow velocity	U_∞	32.404	m/s
Air density	ρ	1.225	kg/m^3
Air temperature	T_∞	15	°C
Rotational speed	Ω	44.5(425)	rad/s(RPM)
Rotor shaft tilt (pos. aft)	α_S	-3	deg

The CAMRAD II rotor model was used within the CFD/CSD coupling framework to trim the rotor for the CFD simulations. Details of the passive and active rotor models, along with the blade properties in CAMRAD II, are provided in Subsection 2.4.5. The same advance ratio of $\mu = 0.15$, as used in the CFD simulation under the flight conditions listed in Table 3.2, was maintained to ensure moderately asymmetric flow conditions across the rotor disk. Additionally, the camber morphing actuation schedule was identical to that of the CFD simulation. Since a transition camber morphing region cannot be modeled in CAMRAD II, the full camber deflection δ was applied across the active section s spanning from $r/R = 0.4$ to $r/R = 0.8$. The trim target values were selected to prevent any potential strong blade vortex interaction or numerical instability. The rotor shaft, as also modeled in the CFD simulation, was tilted with $\alpha_S = 3$ deg towards the incoming flow. The trim targets were specified in terms of the roll moment M_x, the propulsive force X, and the lift force L, all defined in the CAMRAD II wind axis system, as explained in [57]. The specific trim values for both the passive and active rotors are presented in Table 3.3.

The CFD/CSD loose coupling approach was primarily used to correct the aerodynamic loads in CAMRAD II with those computed by the high-fidelity unsteady TAU solver, and to pass the motion of each blade to the CFD solver to trim the rotor. The framework of this loose CFD/CSD coupling, including the data exchange process between the CFD and CSD solvers, is detailed in Subsection 2.4.1. The CFD simulations were executed on the SuperMUC cluster at the LRZ, using a total of 960 CPUs, while the CAMRAD II simulations were run on a local single-core CPU. In the initial coupling step, the relaxation factor $\lambda = 0.75$ was applied to mitigate the significant discrepancies in forces and moments between the CFD and CSD simulations, ensuring stability and preventing divergence in the coupling process. Subsequently, λ was increased to 1.0 for the remaining iterations. This meant that the full values of the computed forces and moments over the span of the blades with TAU CFD solver were used to correct the aerodynamic forces and moments in CAMRAD II. Both solvers used their respective last converged solutions as restart points during the coupling process to expedite convergence. The CFD/CSD coupling convergence was established when variations in collective pitch control $\Delta\theta_0$, lateral control $\Delta\theta_{1c}$, and longitudinal control $\Delta\theta_{1s}$, as computed with CAMRAD II, was less than 0.02 deg between successive coupling iterations, and the change in total integrated thrust between consecutive TAU simulations remained under 2%.

Table 3.3.: Trim conditions in CAMRAD II for the model used in CFD/CSD and the BO105 equivalent model.

Parameter	Symbol	Values	Units
Roll moment (pos. left)	M_x	500	Nm
Rotor drag	$X/(0.5\rho U_\infty^2)$	-0.989	m^2
Rotor lift	L	22000	N

3.3.3. Verification of the CSD Model

The CAMRAD II structural rotor model used in the CFD/CSD coupling investigations was derived from an the DLR equivalent BO105 rotor model for rigid blades. Details and differences between both models are provided in 2.4.5. The purpose of this verification study is to show that the passive rotor model and the equivalent BO105 model from DLR exhibit equivalent aeromechanic behavior in terms of blade flapping and thrust distribution over the rotor disk. Both rotor models are compared, when considering the same wind tunnel trim condition listed in Table 3.3. These trim conditions fall within the range of those considered in [47, 48].

The blade tip displacement was decomposed into pitch, lead-lag, and flap angles, and evaluated over the rotor azimuth. A comparison of the pitch, lead-lag, and flap angles, obtained from both models is presented in Fig. 3.37. The flap blade variation of the CFD/CSD rotor model demonstrated a similar pattern to that of the DLR BO105 equivalent model, with only a slight phase shift, as shown in Fig. 3.37b. The pitch blade variation of the two rotor models also showed close agreement as shown in 3.37a, with minor differences in magnitude and a phase shift comparable to that observed when comparing the flap variation. The CFD/CSD rotor model maintained a nearly constant lead-lag angle of $\Delta\zeta \approx 1.7$ deg throughout the rotor azimuth. In contrast, the DLR BO105 equivalent model exhibited consistently lower lead-lag angles. As the magnitude of this difference remained nearly constant across the azimuth and no dynamic effect was initiated by this offset. Hence, this discrepancy was considered irrelevant for the present study.

Figure 3.38 shows a comparison of the thrust distribution between the DLR equivalent BO105 rotor and the rotor model used for the CFD/CSD coupling. The thrust distribution from the CFD/CSD rotor model closely matches that of the DLR BO105 equivalent model, with only minor differences observed at the rear (ψ = 0 deg) and front (ψ = 180 deg) sides. These differences can be attributed to the phase shift observed in the flap and pitch variation over the rotor azimuth. However, overall, the CAMRAD II rotor model used for the CFD/CSD coupling successfully captured the thrust characteristics similar to those of the DLR BO105 equivalent model over the azimuth range.
Moreover, Table 3.4 presents a comparison of aerodynamic forces and moments in the shaft axis computed with the rotor model used the CFD/CSD coupled rotor model against the equivalent BO105 rotor model after reaching trimmed state. As expected, both rotor models produced closely matched thrust and drag forces, as the roll moment was well-aligned, since they defined trim conditions. However, distinct differences in side force and pitching moment were observed. While similar thrust distribution were obtained, the CFD/CSD coupled rotor model generated approximately half the pitching moment compared to the BO105 equivalent. The pitching moment gen-

erated by the reference model was higher, whereas the pitching moment produced by the rotor model used for the CFD/CSD coupling was more realistic, falling within the range of pitching moments observed during BO105 flight tests under similar trim conditions, as published in [71]. The difference in pitching moment is attributed to the different flap stiffness and lever arm resulting from the hinge offset. Furthermore, this discrepancy in pitching moment is also linked to small variations in thrust distribution between the front and rear rotor sections. Additionally, both rotor models generated similar yaw moments due to the closely matched drag forces. The difference in side force can be interpreted as the blade tip plane tilting further to the side in the CFD/CSD rotor model, indicating lower stiffness compared to the DLR reference model. Nevertheless, the differences in side force and pitching moment are not significant for the purposes of this study, as the total power computed by both rotor models was nearly identical.

As expected, both rotor models produced nearly identical thrust and drag forces, as well as closely matched roll moments, since they were based on the same trim targets. In addition, both models produced comparable thrust distributions. However, significant differences were observed in side force and pitching moment. In this respect, the results of the CFD/CSD model are considered to be more realistic, since they were more consistent with experimental data from BO105 flight tests under similar trim conditions, as reported in [47, 48]. In addition, the difference in hinge offset and flap hinge stiffness led to small differences in thrust distribution between the front and rear rotor sections, which contributed to the difference in pitching moment. The difference in the side force can be explained by the fact that the blade tip plane is tilted further to the side in the CFD/CSD rotor model, indicating a lower stiffness compared to the DLR reference model. However, these variations in side force and pitching moment are not critical for this study, which is supported by the fact that both models are close in terms of yaw moment and therefore the power required to maintain this flight condition.
Overall, both the CFD/CSD coupling model and the DLR equivalent BO105 rotor exhibited comparable characteristics. The observed differences are not expected to affect the accuracy of a realistic scenario, despite the simplifications made regarding the flap and lead-lag hinge positions.

Table 3.4.: Comparison of both aerodynamic forces and moments obtained by means of the trimmed DLR equivalent BO105 rotor and the CAMRAD II rotor model used for the CFD/CSD coupling.

Force and moments generated by the rotors	CAMRAD II model for CFD/CSD coupling	CAMRAD II model for BO105 equivalent Model	Units
Thrust Force (trimmed condition)	21993.605	21999.207	N
Drag Force (trimmed condition)	499.804	500.021	N
Roll Moment (trimmed condition)	499.519	500.544	Nm
Side Force	-634.820	-454.847	N
Pitch Moment	1900.133	4104.123	Nm
Yaw Moment	-6077.573	-5981.479	Nm
Total power	270.460	270.235	kW

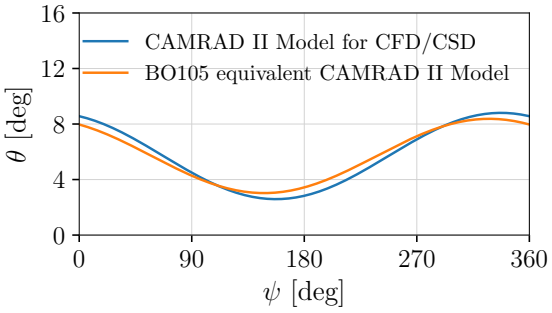

(a) Comparison of pitch angle θ over rotor azimuth ψ.

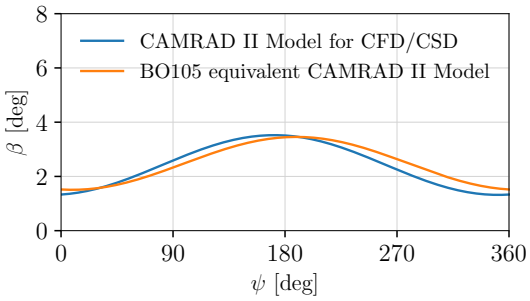

(b) Comparison of flap angle β over rotor azimuth ψ.

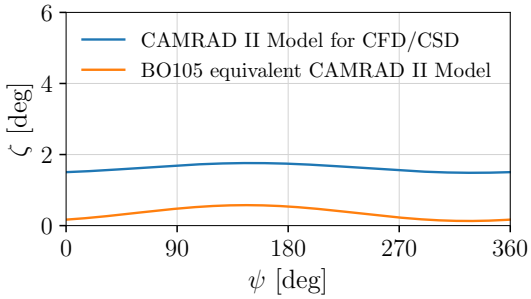

(c) Comparison of lead-lag angle over rotor azimuth ψ.

Figure 3.37.: Comparison of blade displacement computed by the rotor CFD/CSD coupling and the equivalent BO105 model rotor models using CAMRAD II at an advancing ratio of $\mu = 0.15$.

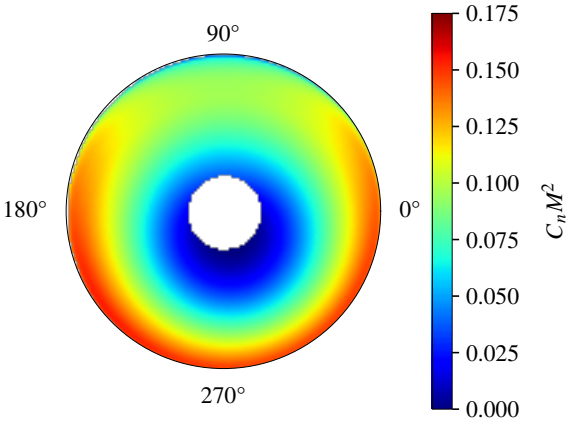

(a) Thrust distribution of the CFD/CSD coupling rotor CAMRAD II model.

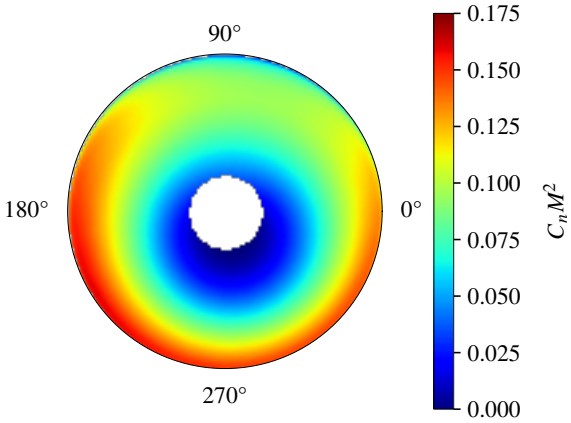

(b) Thrust distribution of the DLR BO105 equivalent rotor CAMRAD II model.

Figure 3.38.: Comparison between the thrust distribution computed by the rotor CFD/CSD coupling and the equivalent BO105 model rotor models using CAMRAD II at an advancing ratio of $\mu = 0.15$.

3.3.4. Convergence of the CFD/CSD Coupling

The convergence of the CFD/CSD coupling was evaluated by monitoring the evolution of integrated thrust over a revolution and the pitch angles between consecutive coupling steps for both passive and active blade simulations. The convergence criteria were satisfied when, for two successive coupling steps, the differences in collective pitch control $\Delta\theta_0$, lateral control $\Delta\theta_{1c}$, and longitudinal control $\Delta\theta_{1s}$ were below 0.02 degrees, and the difference between the integrated thrust calculated by CFD and the target thrust specified in CAMRAD II was less than 2%. The convergence of CFD/CSD coupling ensures that the delta loads and moments, which are applied to correct the lifting line method remain constant and do not vary from one coupling iteration to the next, as explained in Subsection 2.4.1. Figures 3.39, and 3.40 show the variation of integrated thrust over a revolution and the pitch angles between successive coupling steps for both passive and active blade simulations, respectively. In the first two coupling steps, the control angles and thrust varied significantly. Starting from the fourth coupling step, both passive and active CFD/CSD coupling simulations met the convergence criteria. This indicates that both passive and active high-fidelity CFD simulations were trimmed and achieved the same thrust trim target as the CAMRAD II models. Furthermore, the thrust generated by the rotor blades in the CFD simulations was monitored at each time step through the coupling, as shown in Fig. 3.41. In the initial phase of the passive rotor simulation, the thrust exhibited significant fluctuations as the simulation began from scratch. For the passive rotor, satisfactory results for the first coupling stage were acquired after three rotor revolutions. In contrast, the active rotor simulation was initiated from the converged CFD/CSD solution for the passive rotor, providing less pronounced thrust variation at the beginning of the CFD simulation and, thus, a more stable starting point.

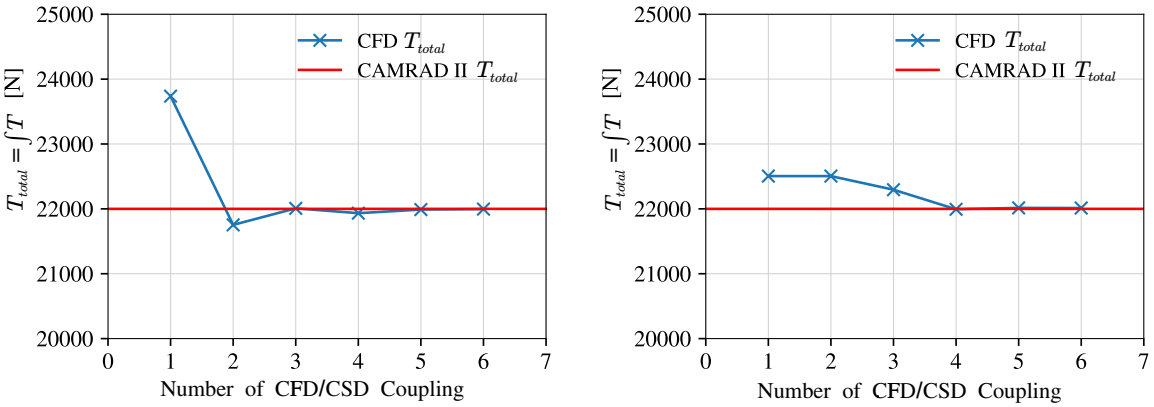

(a) Total rotor thrust T_{total} generated by the passive blades.

(b) ITotal rotor thrust T_{total} generated by the active blades.

Figure 3.39.: Comparison of target trim thrust against the CFD total rotor thrust T_{total} over simulated rotor revolutions for both passive and active rotors across coupling iterations at an advancing ratio of $\mu = 0.15$.

To further examine the convergence of CFD/CSD coupling simulations, the section force C_nM^2 was monitored over the blade span for passive and active rotors at azimuth $\psi = 90$ deg throughout the coupling steps. Figure 3.42 shows the variation of C_nM^2 between the CFD/CSD coupling steps

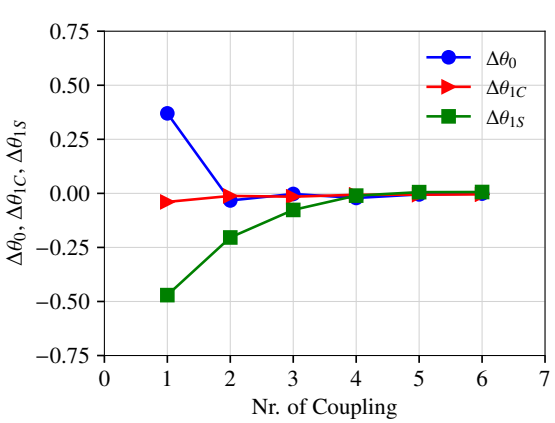

(a) Control angles of the passive blades.

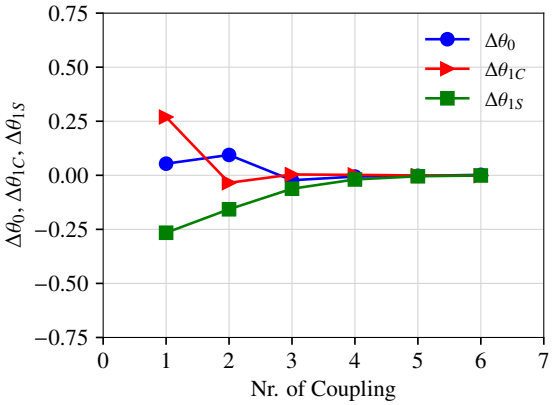

(b) Control angles of the passive blades.

Figure 3.40.: Variation in the absolute differences of collective pitch θ_0, lateral pitch θ_{1c}, and longitudinal pitch θ_{1s} for passive and active rotors across coupling iterations.

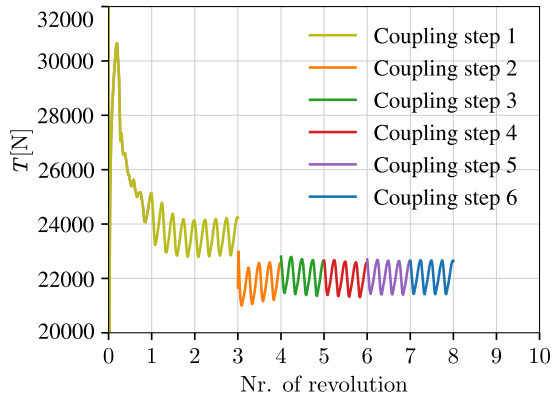

(a) Rotor thrust T variation per time step for the passive rotor.

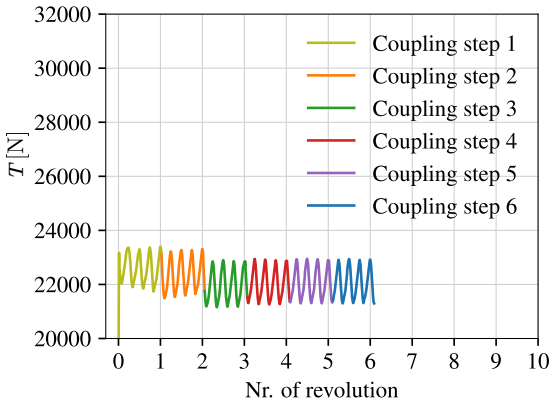

(b) Rotor thrust T variation per time step for the active rotor.

Figure 3.41.: Comparison of rotor thrust T (integrated thrust F_z variation) at time step for passive and active blades across rotor revolutions, with each color representing a different CFD/CSD coupling iteration at an advancing ratio of $\mu = 0.15$.

for the passive and active rotors at $\psi = 90$ deg after completing one coupling step. Before starting the CFD/CSD coupling (coupling 0), the section force was computed using the lifting line theory. In the first coupling step, the section was adjusted using high-fidelity CFD. By coupling steps 4 and 5, the section force $C_n M^2$ variation along the blade span at 90 degrees azimuth matched for both passive and active rotors, demonstrating that convergence in the section force $C_n M^2$ over the blade span had been achieved from coupling step 4 onward. Moreover, a comparison of the section force $C_n M^2$ along the blade span at further additional rotor azimuth angles, as presented in Appendix D.0.2, showed that the section force distribution remained unchanged from coupling step 4 for both rotors throughout the rotor azimuth.

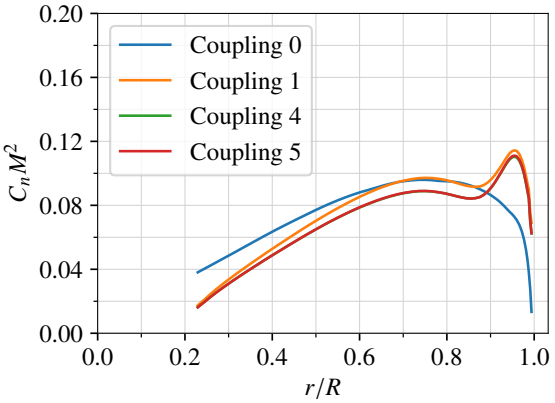

(a) Variation of $C_n M^2$ during the CFD/CSD coupling for the passive rotor.

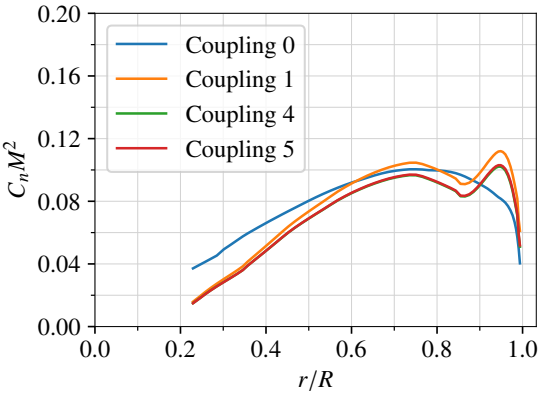

(b) Variation of $C_n M^2$ during the CFD/CSD coupling for the active rotor.

Figure 3.42.: Comparison of the section force $C_n M^2$ between the CFD/CSD coupling steps for the passive and active rotor at $\psi = 90$ deg at an advancing ratio of $\mu = 0.15$, with the green curve (Coupling 4) obscured by the red curve (Coupling 5).

3.3.5. Evaluation of the Blade Motion for the Passive and Active Blades

A comparison of the control angles for passive and active rotors after achieving convergence in the CFD/CSD coupling is presented in Fig. 3.43. To underscore the impact of active camber morphing on blade motion, when the prescribed schedule shown in Fig. 3.43d was applied, the blade motion was decomposed into pitch, flap, and lead-lag angles. When active camber morphing was introduced, the pitch motion of the rotor blade deviated significantly from that of a passive rotor, as shown in Fig. 3.43a. In contrast, the flap motion showed minimal variation over the rotor azimuth, with only a slight decrease being observed in the region where the highest camber morphing was applied, as shown in Fig. 3.43b. The lead-lag motion remained unchanged with the camber morphing over the rotor azimuth, as shown in Fig. 3.43c.

The active camber morphing allowed the rotor to maintain identical total thrust while significantly reducing pitch angle throughout the rotor azimuth. This was achieved by decreasing the collective pitch angle θ_0 from 5.37 deg to 4.12 deg and reducing the pitch half peak-to-peak value from 2.40 deg to 1.91 deg. These adjustments were accomplished through lateral control θ_{1c} and longitudinal control θ_{1s}, which were set to 2.10 deg and -1.11 deg, respectively, for the passive rotor, and 1.85 deg and -0.377 deg for the active rotor, as shown in Table 3.5. Thus, the maximum pitch value decreased from 7.8 deg to 6 deg. Additionally, the camber morphing caused a positive shift in the pitch motion, with the maximum pitch angle occurring at 348 deg azimuth, whereas the maximum pitch angle of the passive blade occurred at 333 deg.

Table 3.5.: Comparison of the passive and active blade motions: mean values and first harmonics of pitch, flap and lead-lag angles.

	θ_0	θ_{1c}	θ_{1s}	β_0	β_{1c}	β_{1s}	ζ_0	ζ_{1c}	ζ_{1s}
Passive	5.374	2.105	-1.114	2.419	-0.985	0.171	1.408	-0.075	0.042
Active	4.123	1.850	-0.377	2.347	-1.031	0.208	1.390	-0.076	0.0427

3.3.6. Evaluation of the Sectional Blade Thrust for the Passive and Active Rotor

Both passive and active rotors were trimmed to achieve identical overall total thrust. The impact of active camber morphing on the thrust distribution over the entire rotor disk is shown in Fig. 3.44, where C_nM^2 was evaluated in the reference coordinate system, which was tilted with the rotor shaft and rotated with the reference blade, positioned at an azimuth of 90 deg before the rotor started to rotate.

Figures 3.44a and 3.44b respectively show the thrust distribution over the rotor disk for the passive and active rotors. To highlight the rotor regions most affected by camber morphing, Figure 3.44c presents the difference in local thrust distribution between the passive and active rotor configurations. Additionally, Figure 3.44d illustrates the variation in camber morphing deflection δ across the rotor disk. While both rotors generated the same overall integrated thrust, their thrust distributions differed significantly. When comparing Figs. 3.44a and 3.44b, it can observed that

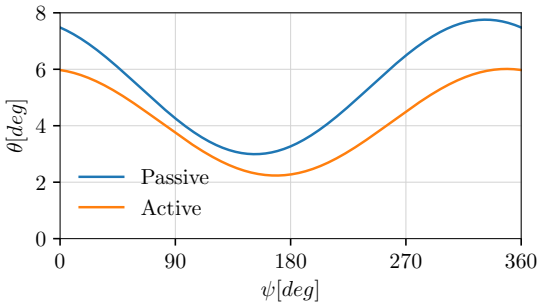

(a) Variation of pitch angle over the rotor azimuth.

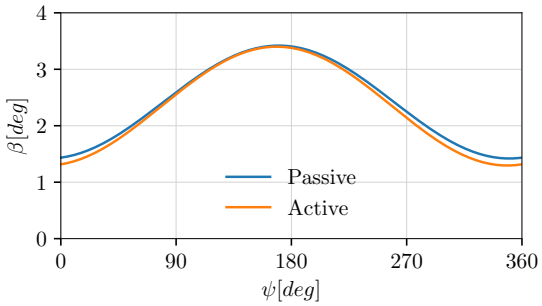

(b) Variation of flap angle over the rotor azimuth.

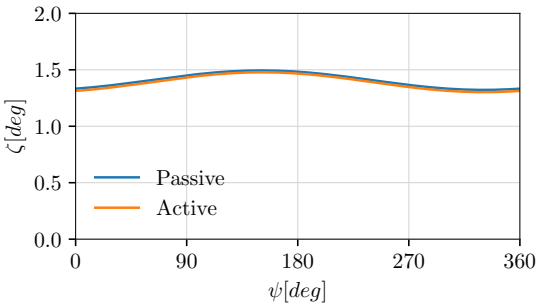

(c) Variation of lead lag angle over the rotor azimuth.

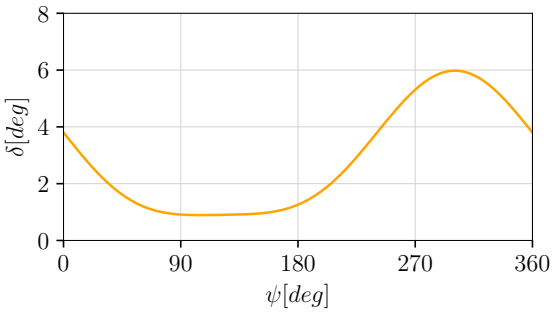

(d) Prescribed camber morphing schedule over the rotor azimuth.

Figure 3.43.: Comparison of blade motion between the passive and active rotors across the rotor azimuth ψ at an advancing ratio of $\mu = 0.15$.

the active camber morphing redistributed the thrust over the rotor disk. Notably, the active configuration exhibited a more uniform thrust distribution compared to the passive rotor, as also was shown in a previous investigation using harmonic actuation of a blade camber [65, 29].

Moreover, the comparison of Figs. 3.44a and 3.44b shows a significant thrust reduction due to the active camber morphing from $r/R = 0.95$ towards the blade tip across the entire rotor azimuth even though the blades were not morphed over this section. This reduction was especially pronounced in the rear rotor disk region, from 270 deg to 90 deg in the counterclockwise direction. Furthermore, the active camber morphing induced a noticeable thrust enhancement over the middle blade span over the region $0.4 < r/R < 0.85$. This enhancement was especially pronounced over the rotor azimuth range of $270 < \psi < 360$. It was also observed that the active camber morphing shifted the radial and azimuth location of the maximum thrust. For the passive rotor, the highest thrust occurred between the rotor azimuth 225 deg and 270 deg near to the blade tip region $0.80 < r/R < 0.95$, whereas for the active rotor, the highest thrust occurred over the blade mid-span region $0.5 < r/R < 0.8$ between the rotor azimuth 225 deg and 360 deg. As the thrust increased towards the mid-span due to the active camber morphing, a reduction in collective pitch was observed throughout the azimuth to maintain the same overall rotor thrust as the passive rotor, as already shown in Fig. 3.43a. Figures 3.45a and 3.45b compare the thrust enhancements at radial locations $r/R = 0.5$ and $r/R = 0.75$ achieved through active camber morphing. At $r/R = 0.5$, active camber morphing resulted in a thrust increase, with a harmonic variation similar to that of a passive rotor. However, at $r/R = 0.75$, the active blade induced higher thrust with less harmonic variation, leading to a nearly constant thrust variation between the rotor azimuth 90 and 225 deg.

In order to gain a closer understanding of the differences in thrust profiles between the passive and active rotors, the sectional thrust coefficient C_nM^2 was plotted along the aerodynamic blade section defined over the range $0.22 < r/R < 0.99$ at different azimuth angles, as shown in Fig. 3.46. At the blade root section $0.22 < r/R < 0.3$, insignificant differences were observed between the passive and active rotors. This indicated that the active camber morphing had a minimal impact on the aerodynamics near the root section. Within the morphing section $0.3 < r/R < 0.8$, the active rotor consistently exhibited a steeper slope of C_nM^2 over the blade span compared to the passive rotor. This was particularly noticeable in regions where the camber deflection was scheduled to be the highest, as shown in Fig. 3.46h. This increase in the C_nM^2 slope resulted in a shift of the peak of C_nM^2 towards the inboard region of the blade span for the active rotor. The impact of the camber morphing was also observed near the blade tip. Over the blade span region $0.9 < r/R < 0.99$, where camber morphing was not applied, the slope of C_nM^2 corresponding to the active blades exhibited a more rapid decline compared to the passive rotor. This resulted in a lower C_nM^2 value for the active rotor at the blades tips compared to the passive rotor. As a consequence, the active rotor demonstrated a reduced tip loading compared to the passive rotor. This lower tip loading can minimize the mechanical stress on the rotor blades, and thus extend the lifespan of the blades, as explained in [36, 18].
Remarkably, at the azimuth location $\psi = 90$ deg and within the radial station range $0.8 < r/R < 0.9$, the distribution of C_nM^2 exhibited a local minimum for both passive and active blades. However, at $\psi = 270$ deg, only the active blade showed a local minimum over the same radial station. This observed local minimum in the distribution of C_nM^2 corresponds to blade-vortex interaction, which is discussed in detail in Subsection 3.3.11.

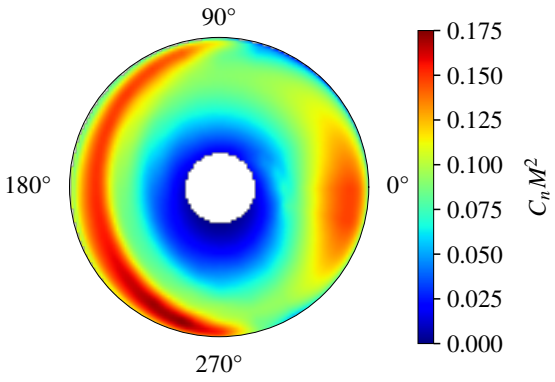

(a) Distribution of C_nM^2 for the passive rotor.

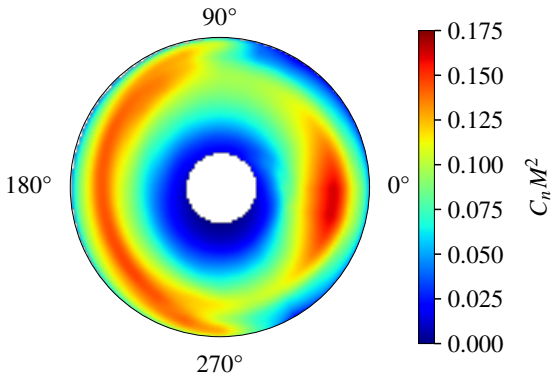

(b) Distribution of C_nM^2 for the active rotor.

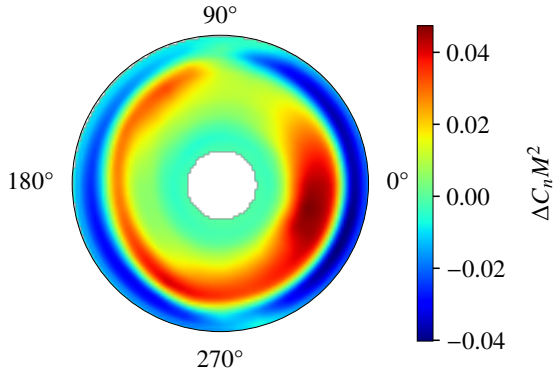

(c) Difference between the passive and active rotor (C_nM^2(active)-C_nM^2(passive)).

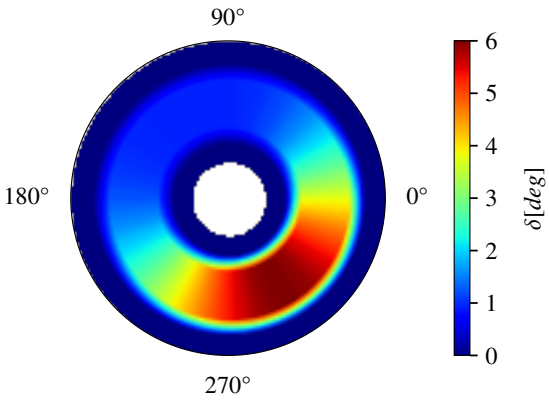

(d) Camber morphing deflection δ over the rotor azimuth.

Figure 3.44.: Distribution of the blade sectional thrust coefficient C_nM^2 over the passive and active rotor disk at an advancing ratio of $\mu = 0.15$.

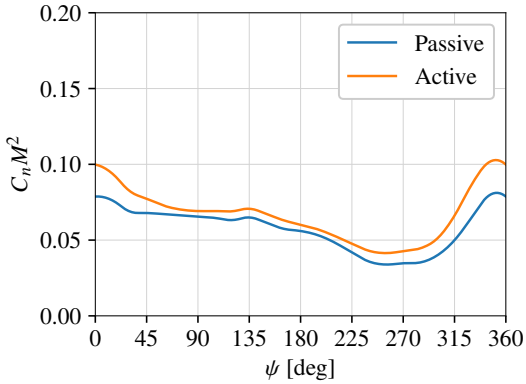

(a) Comparison of C_nM^2 at $r/R = 0.5$.

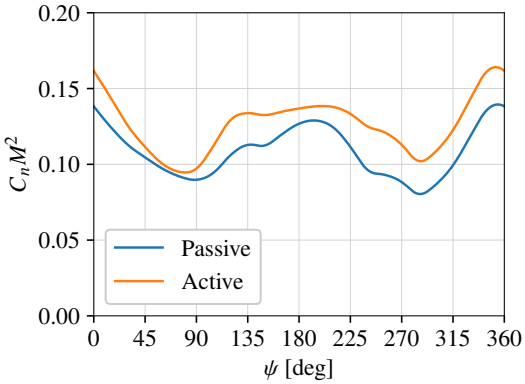

(b) Comparison of C_nM^2 at $r/R = 0.75$.

Figure 3.45.: Comparison of the sectional thrust coefficient C_nM^2 along azimuth ψ at $r/R = 0.5$ and $r/R = 0.75$.

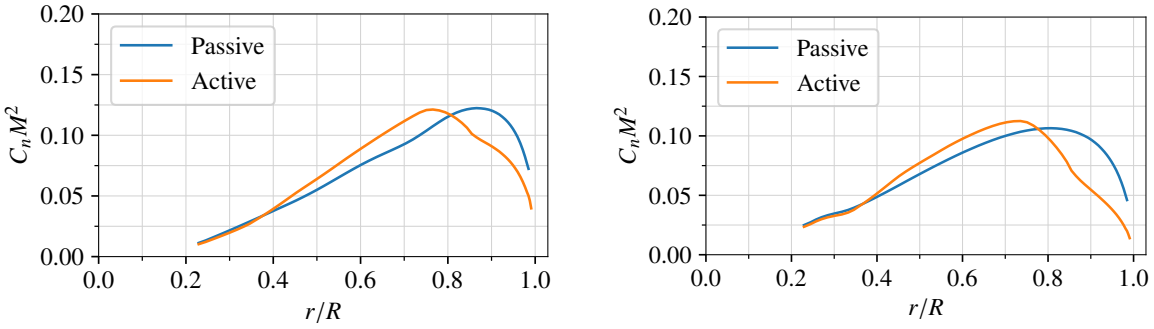

(a) $\psi = 0$ deg

(b) $\psi = 45$ deg

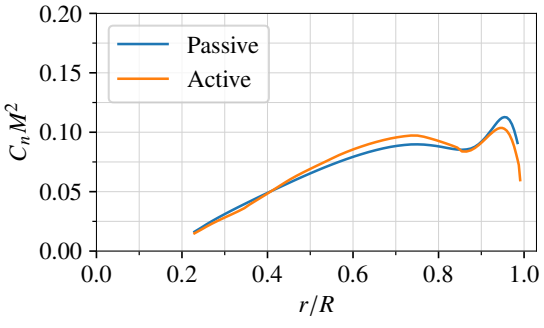

(c) $\psi = 90$ deg

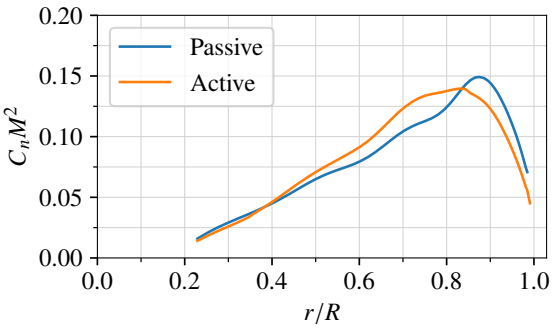

(d) $\psi = 135$ deg

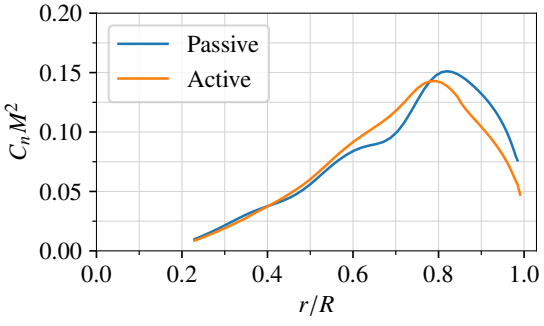

(e) $\psi = 180$ deg

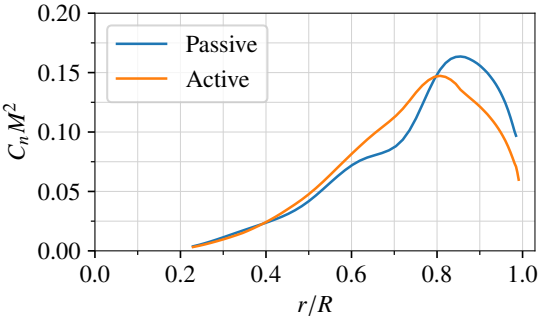

(f) $\psi = 225$ deg

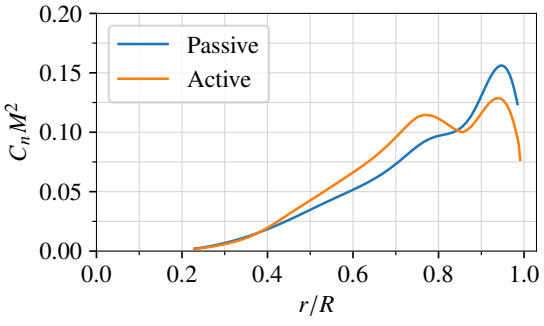

(g) $\psi = 270$ deg

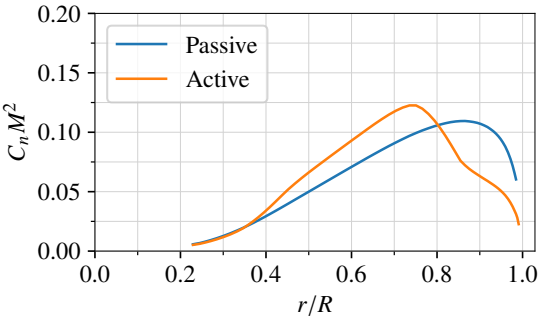

(h) $\psi = 315$ deg

Figure 3.46.: Variation sectional thrust coefficient C_nM^2 over the blade radius for passive and active rotor at different azimuth angles ψ.

3.3.7. Evaluation of the Sectional Drag Variation for the Passive and Active Blades

The chordwise force coefficient, C_xM^2, was evaluated in the same reference coordinate system as the thrust sectional force coefficient, C_nM^2. The coefficient C_xM^2 represents the blade section force component in the rotor disk plane, directed towards the trailing edge and perpendicular to the radial direction. This coefficient effectively denotes the sectional drag force within the rotor disk plane. Since chordwise force coefficient C_xM^2 was evaluated in the rotating blade frame, C_xM^2 represents a key parameter influencing the torque required to spin the rotor. Figures 3.47a and 3.47b show the distribution of the chordwise force coefficient C_xM^2 of the passive and active rotors respectively.

The comparison of both figures reveals that the sectional drag force was primarily redistributed using the active camber in the rear region of the rotor disk. Figure 3.47d shows the difference in sectional drag force between the passive and active rotors. This figure clearly demonstrates that active camber morphing increased sectional drag in the mid-span range $0.5 < r/R < 0.8$ and decreased it in the outboard section from $r/R > 0.85$ towards the blade tip, where no camber morphing was applied. Figures 3.48a and 3.48b show that the sectional drag increase was less pronounced in the front region of the rotor disk and was concentrated particularly where the highest camber deflection was scheduled and an increase in thrust was achieved, as demonstrated in a study of an active rotor using a normal trailing edge flap [54]. This increase in drag can be attributed to the increase in profile drag due to the higher camber of the blade section.

As already mentioned, C_xM^2 is representative of the torque required, which directly translates to the total required power for the rotor system. This means that the sectional drag force, indicated by C_xM^2, plays a crucial role in determining the overall power consumption of the rotor. While the inboard drag force increased and the outboard drag force decreased with the active camber morphing, the overall cumulative effect on power consumption was negligible. This was because the variations in drag distribution essentially balanced each other out in this present investigation at an advance ratio of $\mu = 0.15$ and with the specified camber morphing schedule. Specifically, the power consumption was 232.682 kW for the active rotor and 234.776 kW for the passive rotor, indicating only a minor difference. This negligible difference highlights that the implementation of active camber morphing did not significantly impact the total power required for the rotor at the advance ratio $\mu = 0.15$. Nevertheless, the active camber morphing mechanism can be convenient at this advance ratio to reduce hub vibrations or aeroacoustics, as demonstrated in [70].

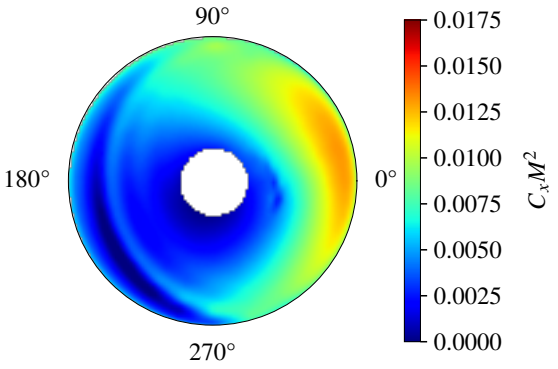

(a) Distribution of C_xM^2 for the passive rotor.

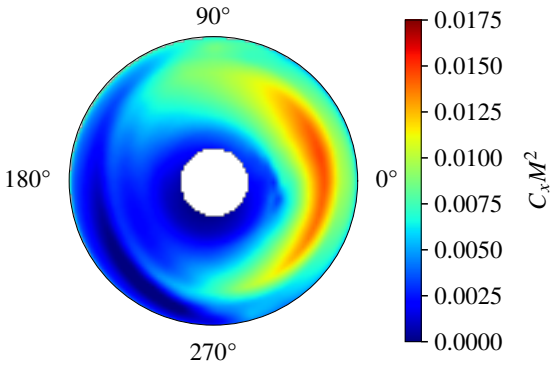

(b) Distribution of C_xM^2 for the passive rotor.

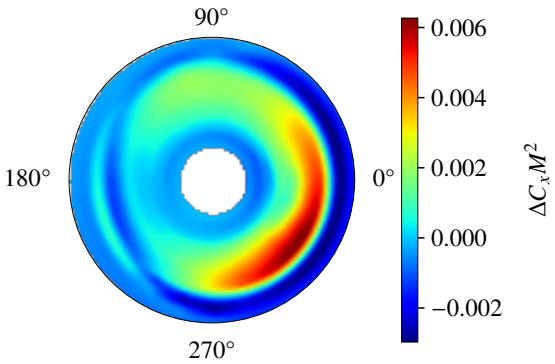

(c) Difference between the passive and active rotor (C_xM^2(active)-C_xM^2(passive)).

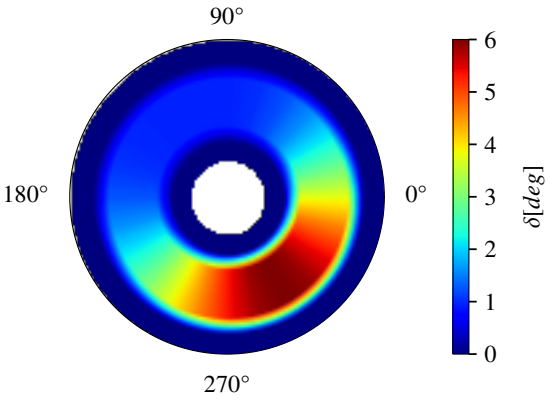

(d) Camber morphing deflection δ over the rotor azimuth.

Figure 3.47.: Distribution of the blade sectional drag coefficient C_xM^2 over the passive and active rotor disk at an advancing ratio of $\mu = 0.15$.

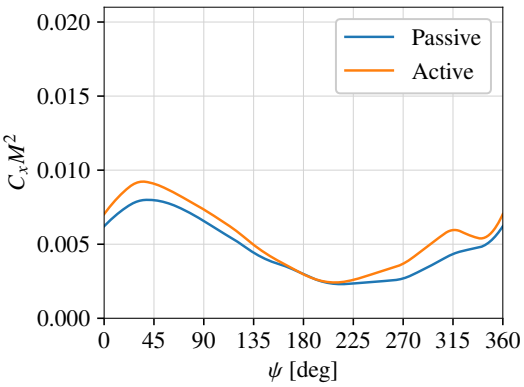

(a) $r/R = 0.5$

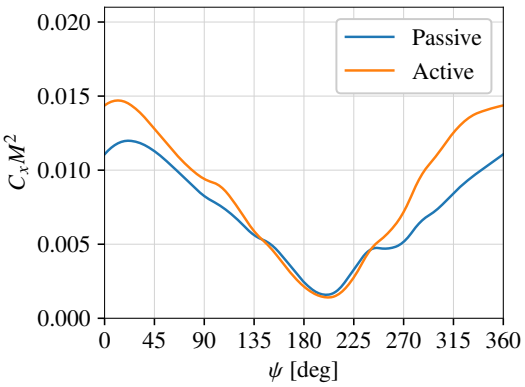

(b) $r/R = 0.75$

Figure 3.48.: Variation of the chordwise force coefficient C_xM^2 along azimuth ψ at the radial station $r/R = 0.5$ and $r/R = 0.75$.

3.3.8. Evaluation of the Pressure Variation for the Passive and Active Blades

This subsection aims to evaluate how active camber morphing affects the pressure distribution along the blade span. Figure 3.49 presents a comparison of the pressure contours over the upper surface of the passive and active blades at azimuth angles 0, 90, 180, and 270 deg. This comparison illustrates the impact of camber morphing on the pressure distribution across the upper surface of the blade. Both passive and active blades exhibited pressure gradients in the spanwise and chordwise directions. These gradients arise from the interactions of several factors within the complex flow field surrounding the rotor blades, including variations in velocity across the blade span, cross-flow effects, blade motion, and the unsteady nature of the flow. Over the aerodynamic section $0.22 < r/R < 0.5$, both blades exhibited similar pressure distributions, indicating that active camber morphing did not affect the pressure distribution in this section.

A significant variation in the pressure gradient between the passive and active blades was observed, particularly within the range of $0.8 < r/R < 1$ along the blade span. This variation was most pronounced near the leading edge, independent of the magnitude of the applied camber morphing deflection. Additionally, the influence of active camber morphing on the pressure distribution was noticeable along the chord section where the camber was morphed, starting from $x/c = 0.75$ towards the trailing edge. This effect became particularly pronounced when the camber deflection exceeded 3 deg, as observed at rotor azimuth angles $\psi = 270$ deg and $\psi = 0$ deg, where the camber morphing reached deflection angles of $\delta = 3.8$ deg and $\delta = 5.31$ deg, respectively.

Figure 3.50 presents a detailed analysis of the pressure distribution at the blade cross-section $r/R = 0.75$, a radial location where the active blade exhibited the maximum sectional thrust coefficient $C_n M^2$ across the blade span for the active rotor throughout the azimuth. This figure underscores the difference in pressure distribution between the passive and active rotors at azimuth angles of $\psi = 0, 90, 180$, and 270 deg. At the blade cross-section $r/R = 0.75$, the pressure differential near the leading edge between the active and passive blades was less pronounced compared to the region $0.8 < r/R < 1$, as shown in Fig. 3.49. The passive blade exhibited a slightly more pronounced suction peak due to its elevated pitch angle throughout the rotor azimuth in comparison to the active blade. The pressure distribution at the blade cross-section $r/R = 0.75$ exhibited significant differences between the passive and active blades, particularly within the chordwise morphing section $0.75 < x/c < 1$ of the active blade. The difference in pressure distribution between the blade configurations was more pronounced at higher camber morphing deflections, such as those observed at azimuth angles of $\psi = 0$ and 270 deg. This increase in the pressure difference along the section $0.75 < x/c < 1$ due to camber morphing, contributed to a higher $C_n M^2$ at $r/R = 0.75$ throughout the rotor azimuth, despite the lower pitch angle, as illustrated in Figure 3.46.

The pronounced differences in pressure distribution between the two blade configurations across the outer span region $0.8 < r/R < 1$ are illustrated in Fig. 3.50d. The chordwise pressure distributions of the passive and active blades at $r/R = 0.9$ were compared at azimuth angles of $\psi = 90$ deg and $\psi = 270$ deg, corresponding to the advancing and retreating sides, respectively. While the camber morphing was not applied at this radial section, the active blade still exhibited a decreased pressure difference compared to the passive blade. This is attributed to the fact that the

active blade had the same non-morphed airfoil shape but operated at a lower pitch angle. Consequently, this reduction in pressure difference resulted in lower thrust and drag coefficients for the active blade near the blade tip, as discussed based on the Figs. 3.44 and 3.47. Furthermore, the variation in pressure distribution near the blade tip between the passive and active configurations can influence the formation of blade tip vortices. The pressure difference near the tip drives the roll-up of the vortex, as noted by [106, 25]. The vortex formation itself originates at the leading edge near the blade tip, as demonstrated by [39]. Consequently, the pressure difference near the tip between the passive and active blades can significantly contribute to different development of the tip vortex, thereby affecting the distribution of vorticity in the blade wake.

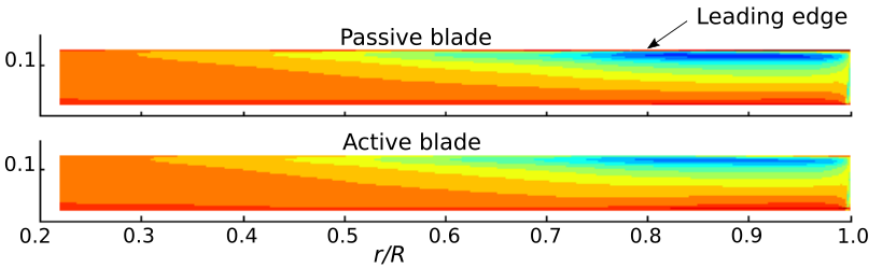

(a) $\psi = 0$ deg

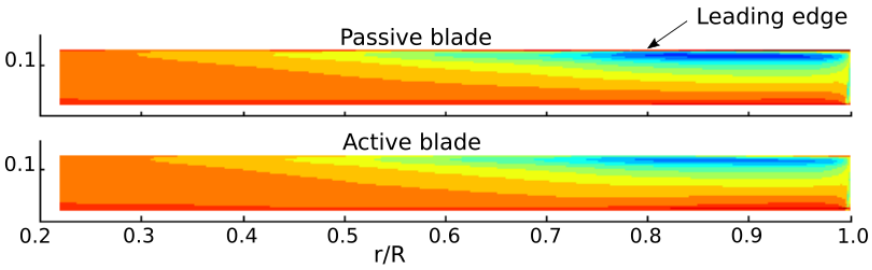

(b) $\psi = 90$ deg

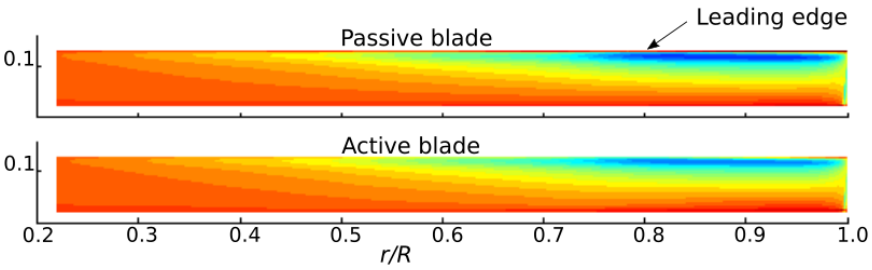

(c) $\psi = 180$ deg

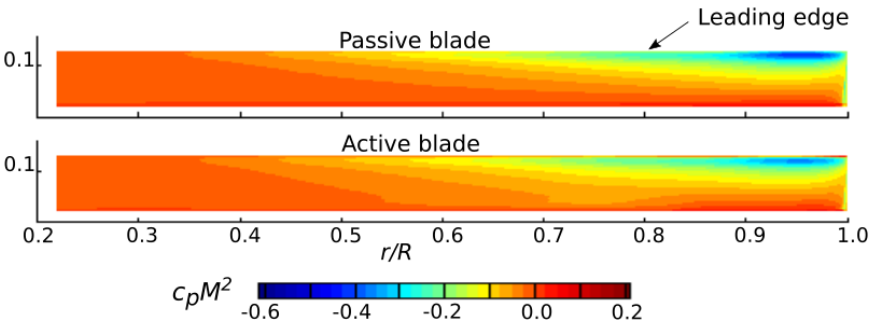

(d) $\psi = 270$ deg

Figure 3.49.: Comparison of the distribution of $c_p M^2$ over the upper surface for passive and active blades at different azimuth angles $\psi = 0, 90, 180$, and 270 deg.

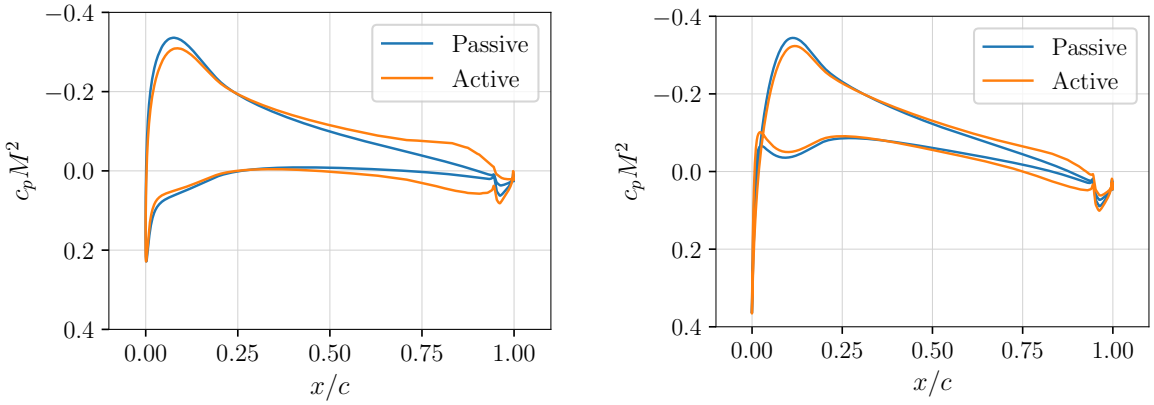

(a) $\psi = 0$ deg

(b) $\psi = 90$ deg

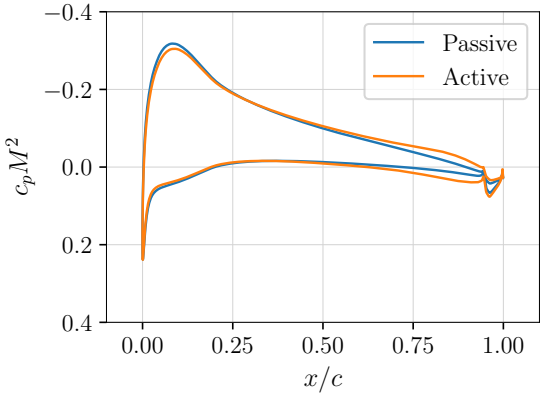

(c) $\psi = 180$ deg

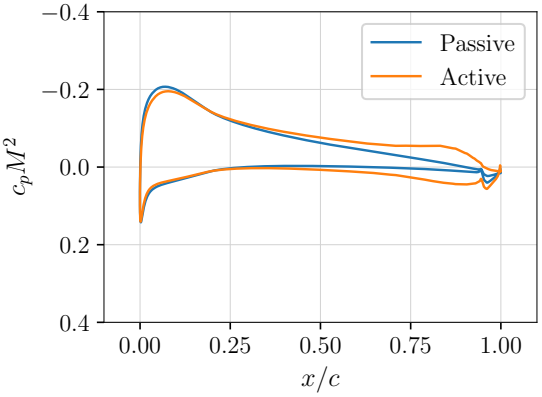

(d) $\psi = 270$ deg

Figure 3.50.: Comparison of the sectional pressure distribution c_pM^2 along the blade span at $r/R = 0.75$ for passive and active rotors at azimuth angles $\psi = 0, 90, 180$ deg and 270 deg.

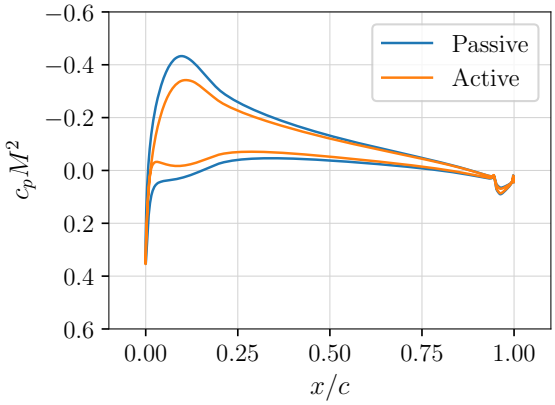

(a) $\psi = 90$ deg

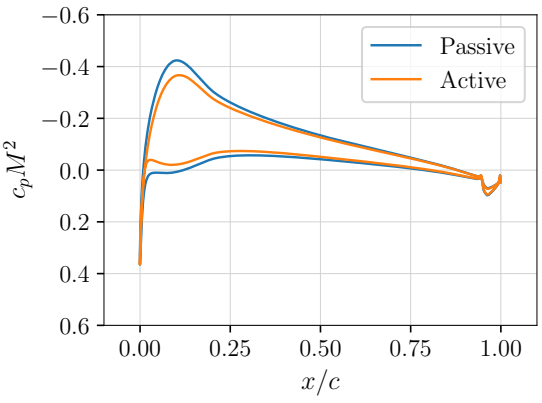

(b) $\psi = 270$ deg

Figure 3.51.: Comparison of the sectional pressure distribution c_pM^2 along the blade span at $r/R = 0.9$ for passive and active rotors at azimuth angles $\psi = 90$ and 180 deg.

3.3.9. Evaluation of the Wake for the Passive and Active Blades

The impact of the active camber morphing on blade wake characteristics was investigated using the λ_2 criterion, a well-established method for vortex core identification [31]. Figure 3.52 presents a comparative visualization of the wake structures generated by passive and active rotors at each quarter of the rotor revolution. For both passive and active rotors, two specific λ_2 values were chosen to generate isosurfaces within the computational domain around the blades. The isosurfaces were generated, starting from a radial position of $r/R = 0.3$ without considering the vortex structure near the rotor center. The values were selected to effectively highlight different vortex structure sizes. The lower λ_2 values, represented in blue and corresponding to $\lambda_2 = 50$, accentuated smaller vortex structures, while the higher λ_2 values, colored red and corresponding to $\lambda_2 = 150$, highlighted larger vortex structures. A close-up visualization near the blade tip region further emphasizes the differences between the passive and active rotors. When comparing the width of the $\lambda_2 = 150$ isosurfaces for the passive and active rotors, a significant reduction in vortex core width was observed, particularly tip the active blades. This suggests that active camber morphing effectively reduced the strength of the tip vortices. Furthermore, as the blade tip vortices roll up, two trailing vortices form behind the advancing and retreating blades [56, 38]. The width of the trailing vortices core, highlighted by the isosurfaces $\lambda_2 = 50$, was also reduced for the active rotor compared to the passive rotor. This implies that active camber morphing not only reduced the core width of the tip vortices but also influenced the overall wake structure. Moreover, the interaction between blade tip vortices and the overall wake structure exhibited significant differences between passive and active rotors. These differences were particularly noticeable when comparing the interaction between the trailing vortex on the retreating side and the blade tip vortex of the blade passing through the azimuth angle $\psi = 0$ deg.

To gain further insights into the rotor wake, Fig. 3.53 presents a comparison of vorticity isosurfaces with a magnitude of $\omega = 80$ 1/s for both passive and active rotors. The comparison between the isosurfaces of the vorticity of the passive rotor in Fig.3.53a and the active rotor in Fig.3.53b shows that active camber morphing resulted in a larger distortion of the tip vortex of the blades passing through the azimuth angles $\psi = 0$ deg and $\psi = 90$ deg. This led to a pronounced interaction with the trailing vortex on the retreating side and the blade tip vortex from the blade oriented towards the rear at the azimuth angle $\psi = 0$ deg. Figure 3.53b demonstrates how the trailing vortex interacted with the distorted blade tip vortex on the retreating side between planes A and B, causing the blade tip vortex to become deformed. This interaction underscores the significant impact of active camber morphing on the rotor wake geometry. Further insights into the effects of active camber morphing on the wake characteristics are presented in Subsection 3.3.10 by analyzing the vorticity at cross-sections A and B. Moreover, the comparison of the isosurfaces in Fig. 3.53 also highlights how tip vortices interacted with the preceding blade for the passive and active rotors at the azimuth angles 90, 180 and 270 deg. The tip vortex from the blade passing through the 0 deg azimuth angle was more distorted compared to the tip vortex of the passive blade. Consequently, the tip vortex originating from the active blade passing through the 0 deg azimuth impacted a larger area when it interacted with the blade passing through the 270 deg azimuth, compared to the passive blade. This blade vortex interaction is discussed further in Subsection 3.3.11, including its potential effects on the radial thrust distribution. In contrast, the active blade passing through $\psi = 270$ deg exhibited a smaller width of the blade tip vortex compared to the tip vortex origi-

nating from the passive blade at the same azimuth angle. This resulted in a reduced interaction area with the preceding vortex at $\psi = 180$ deg for the active blade, in comparison to the passive blade at the same azimuth angle. However, an elongation and further distortion of the vortex shedding due to active camber morphing were observed at $\psi = 270$ deg, particularly in the section $0.45 < r/R < 0.85$. When comparing the tip vortex from the blade passing through $\psi = 180$ deg for both passive and active rotors, both tip vortices interacted with the preceding blade passing through $\psi = 90$ deg. For the active rotor, this interaction occurred over a larger blade area at azimuth angle $\psi = 90$ deg compared to the passive rotor, due to the increased distortion of vortex shedding caused by the applied camber morphing. The impact of blade vortex interaction between the passive and active rotors at $\psi = 90$ deg is further analyzed and discussed in Subsection 3.3.11.
Near the blade root sections, the structure of the vorticity isosurfaces was similar for the passive and active blades, demonstrating that camber morphing has no significant impact on this blade root section.

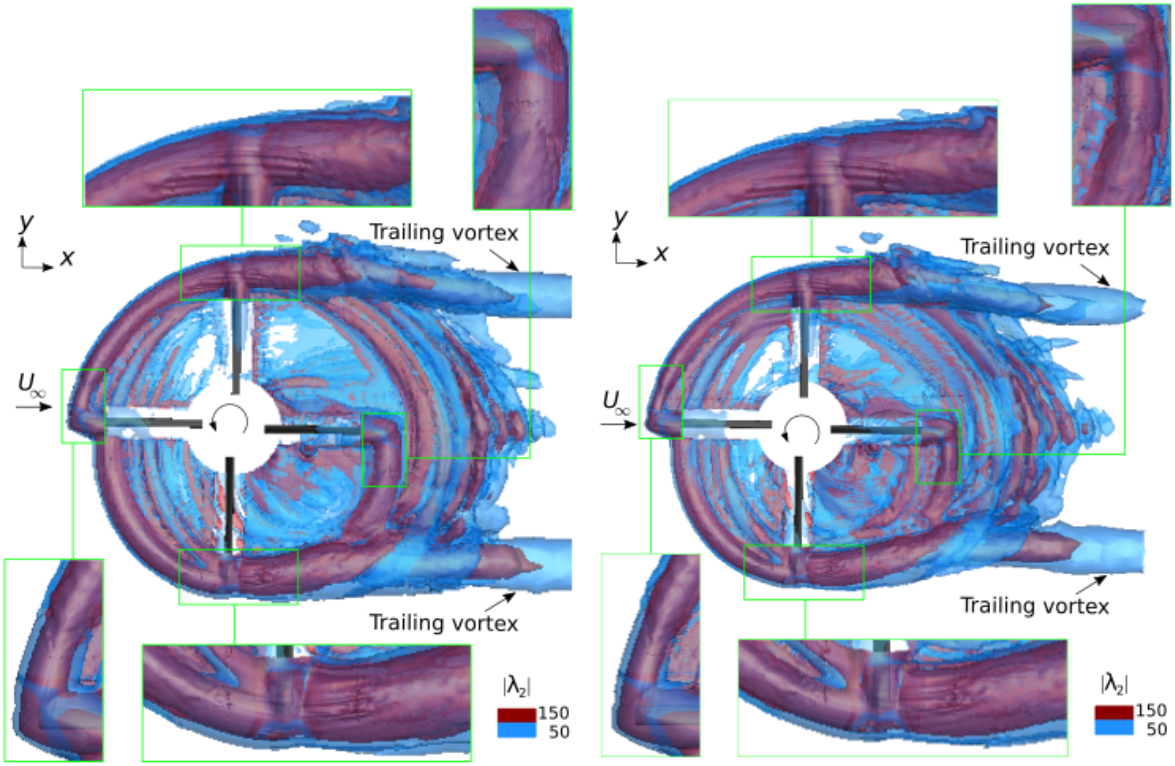

(a) Vortex structures of the passive rotor

(b) Vortex structures of the active rotor

Figure 3.52.: Comparison of the vortex structures near to the passive and active rotors by means of the λ_2 criteria.

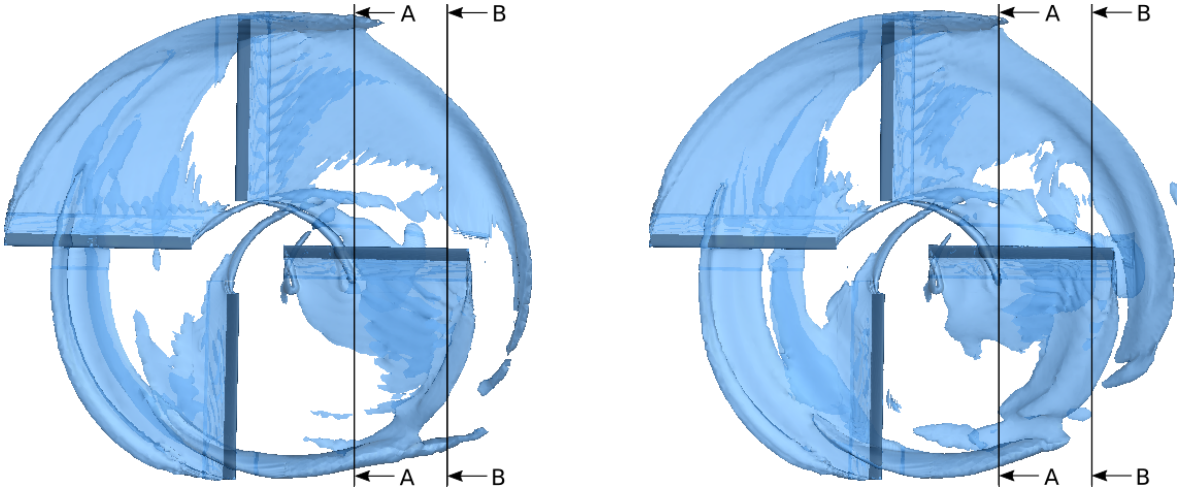

(a) Vorticity isosurfaces of the passive rotor

(b) Vorticity isosurfaces of the active rotor

Figure 3.53.: Comparison of active and passive rotor wake structures using the vorticity isosurfaces with $\omega = 80$ 1/s.

3.3.10. Evaluation of the Trailing Vortices

To highlight the influence of camber morphing on the development of trailing vortices, cross sectional slices A and B were extracted at radial locations $r/R = 0.5$ and $r/R = 0.9$ downstream of the rotor center, as depicted in Figs. 3.54 and 3.55, respectively.

Figure 3.54 illustrates that on the advancing side, active camber morphing resulted in a slightly lower vorticity magnitude in the vortex core in comparison to the passive rotor configuration. Additionally, on the advancing side, camber morphing induced a slight elevation of the tip vortex for the blade passing through at an azimuth angle of $\psi = 0$ deg compared to the passive blade. On the retreating side, the tip vortex of the active blade with camber morphing was significantly more elevated compared to the passive blade. The active camber morphing also caused the tip vortex to become distorted and slightly shifted inboard relative to the passive case. In the passive rotor configuration, the vorticity with a magnitude of $\omega = 100$ 1/s was distributed over a larger area, suggesting that camber morphing reduced the vortex strength. The effects of active camber morphing became more pronounced further downstream. This observation is highlighted in Fig. 3.55, which illustrates the differences in the vorticity field of the trailing vortices over the slice B, located at $r/R = 0.9$. On the advancing side, for both passive and active rotor configurations, the position of the trailing vortex remained consistent relative to the advancing blade at an azimuth angle of $\psi = 90$ deg. However, with active camber morphing, the trailing vortex exhibited a lower vorticity magnitude and was distributed over a smaller area. On the retreating side, the active camber morphing led to a significant reduction in both the size and strength of the trailing vortex as it moved downstream. For the passive rotor, the vorticity magnitude in the vortex core region reached up to 90 1/s, whereas for the active rotor configuration, the vorticity magnitude in the core region did not exceed 70 1/s. Additionally, in the active rotor configuration, the trailing vortex was notably more elevated and exhibited a pronounced inward shift compared to the passive blade configuration. This inward shift can be attributed to the interaction on the retreating side between the

trailing vortex and the distorted blade tip vortex, corresponding to the blade passing through the azimuth angle $\psi = 0$ deg, as discussed in section 3.3.9. These combined observations suggest that active camber morphing significantly impacted the trajectory and strength of the trailing vortices and hence had a measurable impact on the rotor wake, particularly behind the retreating side blade.

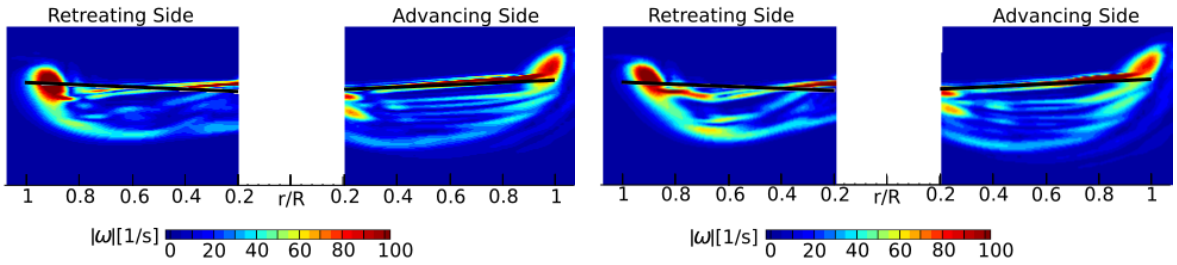

(a) Vorticity distribution in the wake of the passive rotor at slice A.

(b) Vorticity distribution in the wake of the active rotor at slice A.

Figure 3.54.: Comparison of vorticity distribution between passive and active rotors at slice A, extracted at $r/R = 0.5$.

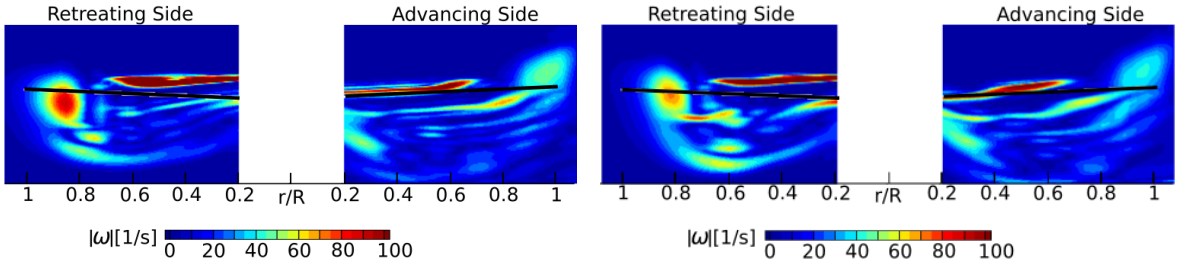

(a) Vorticity distribution in the wake of the passive rotor at slice B.

(b) Vorticity distribution in the wake of the active rotor at slice B.

Figure 3.55.: Comparison of vorticity distribution between passive and active rotors at slice B, extracted at $r/R = 0.9$.

3.3.11. Evaluation of the Vorticity at the Retreating and Advancing Blades

When comparing the vorticity isosurfaces with a magnitude of $\omega = 80$ 1/s for both passive and active rotors in Fig. 3.53, it was observed that the blades passing through 90, 180, and 270 deg were impacted by the tip vortex of the preceding blade. This subsection discusses only the differences in the interaction between tip and the advancing blade at 90 deg and the retreating blade at 270 deg for both passive and active rotor configurations.

Firstly, the effect of camber morphing on the size of the tip vortex associated with the blade preceding the advancing blade was assessed, and its influence on the interaction with the advancing blade was investigated. Figure 3.56 presents a detailed comparison of the interaction between the tip vortex of the preceding blade passing through $\psi = 180$ deg and the advancing blade at $\psi = 90$ deg for both passive and active rotors. To visualize this interaction, isosurfaces with two different magnitudes were used. The isosurfaces with vorticity magnitude $\omega = 80$ 1/s were used to capture the shape of the vortex and the isosurfaces with higher vorticity magnitude $\omega = 100$ 1/s were used to capture the core of the vortex. Multiple perspectives, including side, top, and isometric views, were used to highlight the differences in blade-vortex interactions between the passive and active rotors.

Figures 3.56a and 3.56b illustrate a comparative analysis of the vortex distribution along the z axis for passive and active rotors. The active rotor exhibits a slightly elongated vortex structure in the z direction, as indicated by the $\omega = 80$ 1/s isosurfaces. However, the vortex core, defined by the $\omega = 100$ 1/s isosurfaces, exhibits a slightly more compact distribution along the z-axis in the active configuration. In both rotor configurations, the blade passes through the center of the $\omega = 100$ 1/s isosurfaces. Additionally, the top views in Figs. 3.56c and 3.56d provide further insights into how the interaction area between the tip vortex and the advancing blade varied for both rotor configurations. A comparison of the top views shows that the isosurfaces with $\omega = 80$ had a similar distribution along the y direction for both rotor configurations. However, the vortex core, corresponding to the $\omega = 100$ 1/s isosurface, was more elongated in the y direction for the active rotor. This elongation occurred even before reaching the advancing blade and was attributed to the effect of camber morphing on the tip vortex of the preceding blade. As a result, the tip vortex of the active blade interacted with a larger area of the advancing blade in comparison to the passive configuration. The isometric views in Fig. 3.56e and 3.56f provide a three dimensional perspective on the blade-vortex interaction and confirm the observations made from the side and top views. Additionally, they reveal that the vortex in the active configuration is located slightly farther from the blade tip.

To further understand how active camber morphing impacts the interaction between the tip vortex and the advancing blade, slices from the vorticity field perpendicular to the blade at the quarter chord ($x/c = 0.25$) are shown in Figs. 3.56g and 3.56h. The region of interaction between the tip vortex and the advancing blade was identified as the distinct area where the vorticity exceeded the value $\omega = 50$ 1/s. This region spanned $0.87 < r/R < 0.99$ along the blade for the passive rotor, whereas for the active rotor, it extended over a broader range from $0.83 < r/R < 0.98$. Notably, it coincided with the blade span where the sectional thrust coefficient $C_n M^2$ exhibited a local minimum for both rotor configurations. This suggests that blade-vortex interaction on the ad-

vancing side contributed to this local minimum, as discussed in Subsection 3.3.6 and observed in Fig. 3.46c. Additionally, the comparison of the vorticity fields corresponding to the advancing blades of the passive and active rotor configurations revealed also high vorticity regions exceeding a threshold of $\omega = 100$ 1/s near the upper surface of the blades. For the passive blade, this region extended from $0.88 < r/R < 0.98$, while for the active blade, it spanned from $0.87 < r/R < 0.96$.

Figure 3.57 presents a detailed comparison of the interaction between the retreating blade at $\psi = 270$ deg and the tip vortex of the preceding blade passing through $\psi = 360$ deg for both rotor configurations from multiple perspectives. To ensure consistency, the same isosurface magnitudes used to analyze the blade vortex interaction with the advancing blade were applied to accurately capture the shape and core of the vortex at the retreating side.

The comparison of the side views 3.57a and 3.57b for the passive and active blades on the retreating side at $\psi = 270$ deg reveals distinct interaction patterns for both rotors. Both isosurface magnitudes $\omega = 80$ and $\omega = 100$ 1/s highlight that the passive blade passed through the upper third of the tip vortex, whereas the active blade intersected the vortex at mid-height. The isosurface with a vorticity magnitude of 80 1/s revealed that the tip vortex of the retreating active blade at $\psi = 270$ deg exhibited a less elongated shape in the z-direction. Furthermore, the vortex core, as defined by the isosurface with a vorticity magnitude of 100 1/s, showed a significantly more compact distribution along the z-axis in comparison to the passive configuration.

Figures 3.57c and 3.57d, depicting the top views of the passive and active blades, respectively, highlight further key differences in blade-vortex interaction on the retreating side. In both rotor configurations, the isosurface with a vorticity magnitude of $\omega = 100$ 1/s covered a similar area spanwise along the blade. However, in the active blade case, the isosurface was slightly shifted inboard. Additionally, when comparing the isosurface with a vorticity magnitude of $\omega = 80$ 1/s, the active rotor showed a significantly larger coverage spanwise compared to the passive rotor. This observation suggests that a larger region of interaction occurred between the blade and the vortex for the active case. Figures 3.57e and 3.57f present isometric views of the passive and active blades, reinforcing the observations from the top and side views. At $\psi = 270$, the vortex passing the active blade was more compact in the z-direction and more elongated in the spanwise direction. This observation suggests that in the active configuration, a larger region of interaction occurred between the blade and the vortex compared to the passive case.

The slices extracted at the quarter chord of the passive and active blades, as shown in Figs. 3.57g and 3.57h, provide deeper insights into the vorticity field surrounding the passive and active blades at $\psi = 270$ deg, respectively. For the passive blade, the core of the vortex exhibited a vorticity magnitude surpassing $\omega = 120$ 1/s, indicating a higher vortex core strength compared to the active case. This high-vorticity region primarily passed below the blade, suggesting a more localized interaction with the lower surface of the blade. For the active blade, the region of higher vorticity magnitude did not exceed $\omega = 120$ 1/s, indicating a weaker vortex core strength compared to the passive blade. The core of the vortex was concentrated on the upper surface of the blade. The region corresponding to the areas of interaction between the blade and the tip vortex, were identified by distinct zones with vorticity exceeding $\omega = 50$ 1/s for both passive and active rotors. For the passive blade, this vorticity region covered the blade span of $0.85 < r/R < 0.975$. For the active, this region was slightly shifted inboard, covering the blade span section $0.825 < r/R < 0.965$. Notably,

the region where vorticity exceeded $\omega = 50$ 1/s at $\psi = 270$ deg for the active blade coincided with the blade span section where the sectional thrust coefficient $C_n M^2$ distribution exhibited a local minimum, as shown in Fig. 3.46g. This can be attributed to the fact that the core of the vortex for the active blade was concentrated on the upper surface of the blade. For the passive blade, only slight gradient variation in $C_n M^2$ and no local minimum were observed over the blade span at $\psi = 270$ deg. This is likely to be because approximately two third of the vortex passed below the blade, with the region of vorticity magnitude higher than 120 1/s being primarily located below the blade. This suggests that the blade-vortex interaction affected mainly the lower surface of the passive blade.

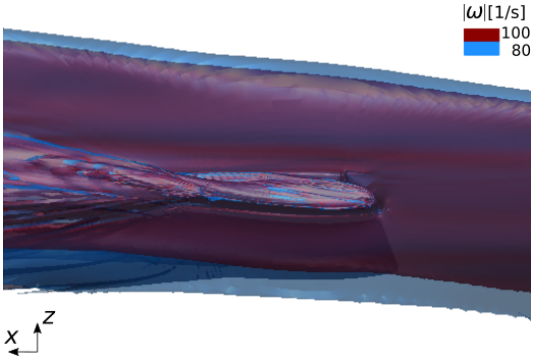

(a) Side view of the passive blade.

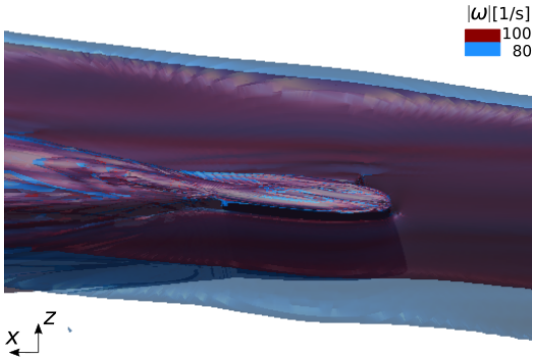

(b) Side view of the active blade.

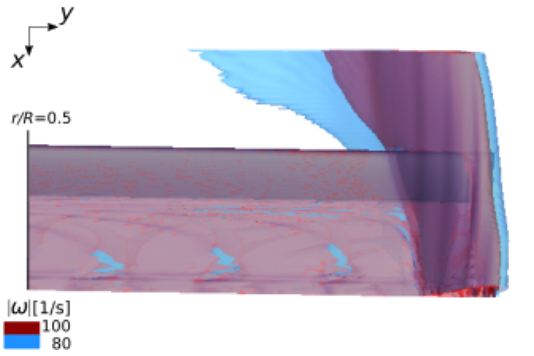

(c) Top view of the passive blade.

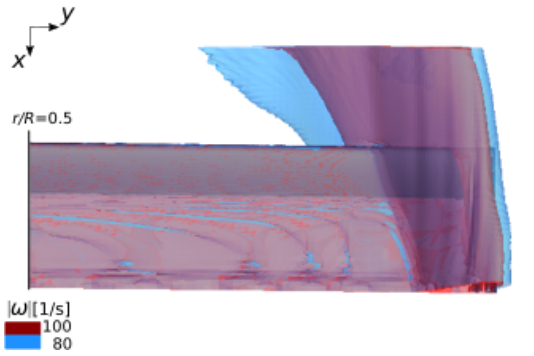

(d) Top view of the active blade.

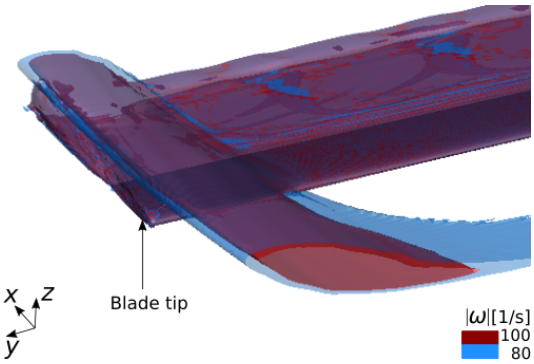

(e) Isometric view of the passive blade.

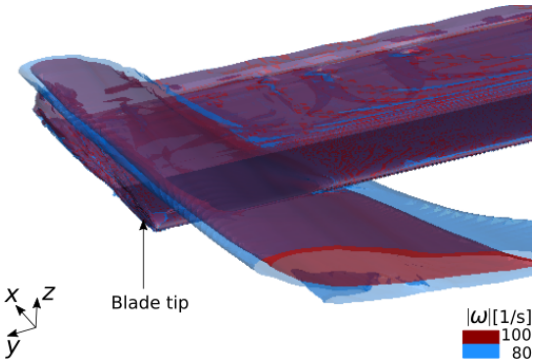

(f) Isometric view of the active blade.

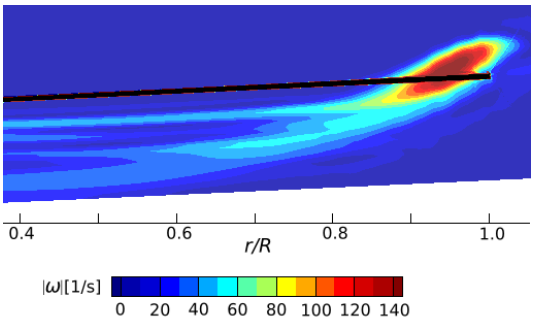

(g) Slice of vorticity field for the advancing passive blade at $x/c = 0.25$.

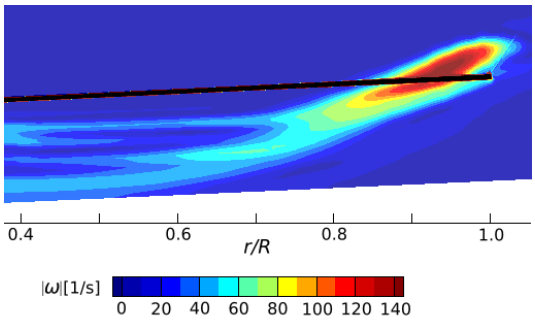

(h) Slice of vorticity field for the advancing active blade at $x/c = 0.25$.

Figure 3.56.: Comparison of the vortex structures passing near the vicinity of the advancing blade at $\psi = 90$ deg for the passive and active rotors by means of the magnitude of the vorticity.

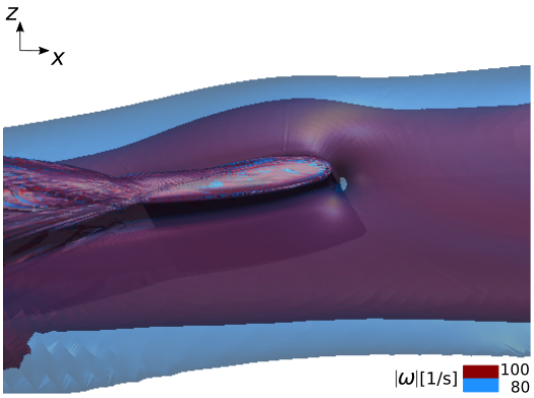

(a) Side view of the passive blade.

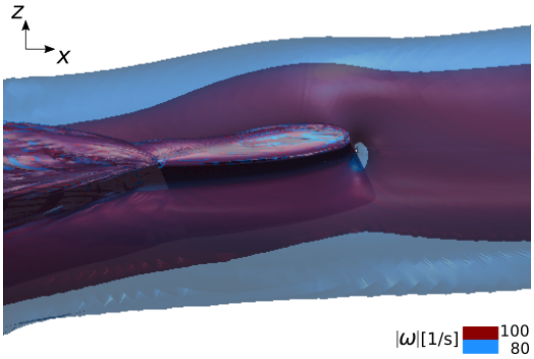

(b) Side view of the active blade.

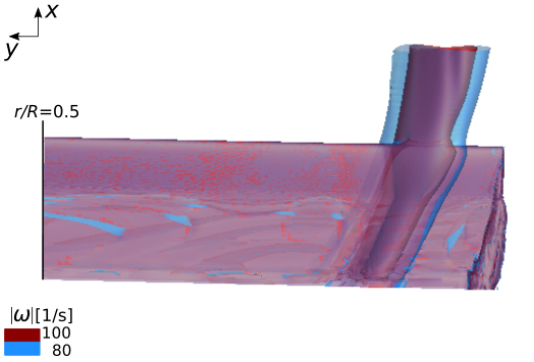

(c) Top view of the passive blade.

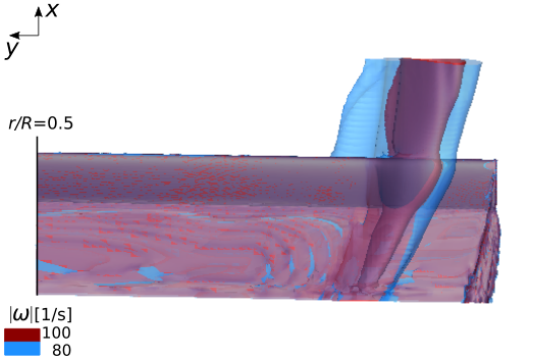

(d) Top view of the active blade.

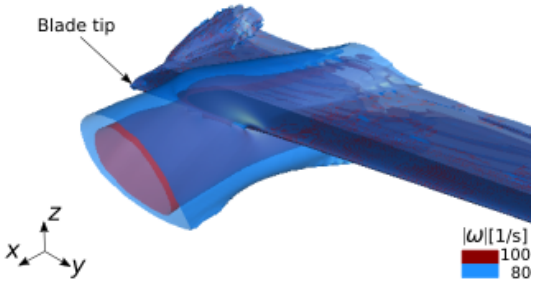

(e) Isometric view of the passive blade.

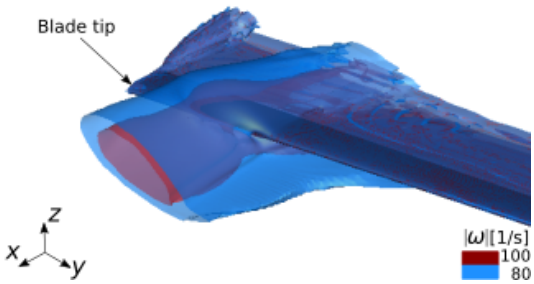

(f) Isometric view of the active blade.

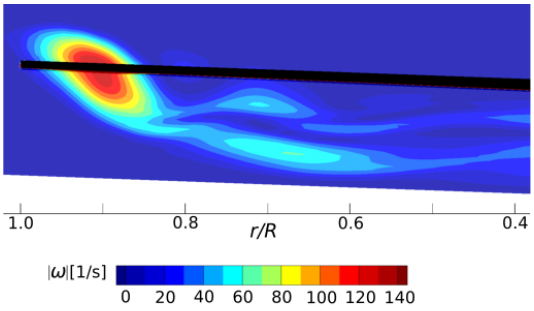

(g) Slice of vorticity field for the retreating passive blade at $x/c = 0.25$.

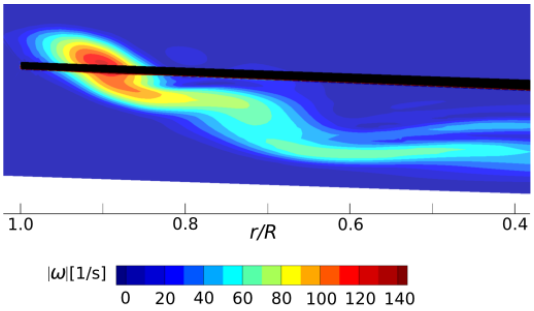

(h) Slice of vorticity field for the retreating active blade at $x/c = 0.25$.

Figure 3.57.: Comparison of the vortex structures passing near the vicinity of the retreating blade at $\psi = 270$ deg for the passive and active rotors by means of the magnitude of the vorticity.

3.3.12. Comparison of Computed Thrust and Drag using CFD/CSD Coupling Against Free Wake and Linear Inflow

The objective of this subsection is to discuss the influence of modelling fidelity on the accuracy of the approximations of thrust and drag for both passive and active rotor configurations. A detailed comparative analysis of thrust and drag predictions derived from CFD/CSD are compared with those obtained from the commonly used free wake and linear inflow methods in comprehensive rotor analysis. The approximations derived from linear inflow, free wake inflow, and CFD/CSD coupling provide the low-, mid- and high-fidelity analyses respectively. To enable the comparisons, the thrust and drag distributions over the azimuth angles were compared for each comprehensive rotor analysis method under identical trim conditions.

The linear inflow method, considered a low-fidelity approach, does not account for interactions between the wake and inflow. Standard linear inflow settings in CAMRAD II were used, incorporating the ONERA Edlin model with CAMRAD II standard settings to ensure unsteady effects were accounted for. The linear inflow results were derived from the initial CAMRAD II solution in the CFD/CSD coupling before correcting the aerodynamics with the TAU three-dimensional and unsteady solution.

The free wake solution was obtained using the standalone CAMRAD II model, which was also adopted in the CFD/CSD coupling. This was accomplished by replacing the linear inflow model in the CAMRAD II with a free wake inflow model. This approach captured the non-linear variation of inflow along the blade span and modeled the bounded vorticity to approximate the rotor wake and its impact on rotor inflow. Thus, more accurate rotor loads can be computed. The free wake CAMRAD II settings were adopted from previous investigations [65, 66, 67], where the CAMRAD II model for the baseline BO105 passive rotor was validated against experimental results. This validated model served as the baseline for comparison with the BO105 rotor equipped with active camber-morphing blades. As in previous studies, a trailing vortex was defined only at the blade tip ($r/R = 1$) for the passive rotor. In contrast, for the active camber-morphing blades, trailing vortices were introduced at $r/R = 0.5$ and $r/R = 0.9$ to reflect the altered aerodynamic characteristics and wake behavior resulting from the camber morphing, as in previous investigations.

Among the three modeling approaches, the CFD/CSD coupling is considered to provide the most accurate results. This is because the aerodynamics are modeled by solving the unsteady Navier–Stokes equations in a three-dimensional computational field using the compressible TAU solver. Additionally, this approach captures pressure variations along both the spanwise and chordwise directions, resolves vortex structures in the near and far wake, and incorporates inertial effects in the airflow.

Figure 3.58 presents the thrust distributions across the rotor disk for the passive rotor, using linear inflow, free wake inflow, and CFD/CSD methods. The CFD/CSD and free wake simulations exhibited close agreement when capturing the overall thrust distribution, with minor discrepancies primarily being observed in the outboard region of the retreating blade and near the azimuth of 0 deg. The free wake model also slightly underpredicted the magnitude of the thrust generated between 180 deg and 270 deg, however the general trend in thrust distribution was similar

to CFD/CSD coupled results. In contrast, the linear inflow model underpredicted thrust between 90 deg and 180 deg, and overpredicted thrust between 270 deg and 330 deg when compared to the CFD/CSD coupling and free wake simulations. Moreover, the linear inflow method overpredicted thrust on the advancing side between the rotor azimuth 0 and 180 deg in the inboard region spanning from $0.22R$ to $0.5R$. Thus, the low-fidelity linear inflow method was generally not able to accurately represent the trends or magnitudes of thrust computed using the CFD/CSD coupled approach, while the mid-fidelity free wake method captured similar thrust variation.

Figure 3.59 illustrates the thrust distribution approximated by each of the three methods for the active rotor. All three methods captured that the active camber morphing caused thrust redistribution over the rotor disk. However, similar to the observations made for the passive rotor, the linear inflow model very poorly matched the thrust distributions computed using both the free wake and the CFD/CSD coupled methods, which agreed closely with one another. The CFD/CSD simulations showed a localized thrust reduction between $r/R = 0.8$ and $r/R = 0.9$ on the retreating blade at $\psi = 270$ deg, attributed to blade-vortex interactions as previously discussed, which was not captured by the free wake model. Similar to the passive rotor case, the linear inflow model underpredicted thrust between 90 deg and 180 deg, and overpredicted thrust between 270 deg and 360 deg. As was shown for the passive rotor, the linear inflow method again overpredicted inboard thrust on the advancing side between 0 and 180 deg azimuth in the inboard region spanning from $r/R = 0.22$ to $r/R = 0.5$. Moreover, the linear inflow model could not compute the smooth thrust transition between the morphed and unmorphed sections, particularly at the transition region near the blade tip. A sharp thrust gradient variation was observed within the transition region at $r/R = 0.85$, particularly noticeable in the 180 to 360 deg range, where the camber morphing deflection δ was scheduled to increase, as shown in Fig. 3.43d. The free wake method was far better at modeling the smooth transition from morphed to unmorphed section, also displayed by the CFD/CSD coupled results. This can be attributed to the fact that trailer vortices were implemented at $r/R = 0.5$ and $r/R = 0.9$ as well as at the blade tip, which help to more accurately represent the inflow at the transition region. The linear inflow method does not allow the incorporation of vortex trailers along the blade span, explaining the harsh transition.

Figure 3.60a presents a closer comparison of the thrust distribution over the azimuth for the passive case, computed using the linear inflow, free wake, and CFD/CSD methods at $r/R = 0.75$. As previously mentioned, the free wake and CFD/CSD results exhibited similar trends over the azimuth, with slight discrepancies in $C_n M^2$ magnitude, particularly on the advancing side between 30 and 80 deg of azimuth. The linear inflow method failed to capture high-frequency load variations, as indicated by the unusually smooth curve. The comparison between free wake and linear inflow methods demonstrated the importance of considering the non-linear variation of the inflow and including the wake as well as vortex interactions to accurately compute load variations over the rotor disk.

Figure 3.60b provides a closer comparison of thrust distribution over azimuth for the active rotor at $r/R = 0.75$, calculated using linear inflow, free wake, and CFD/CSD methods. Similar to what is seen in the passive case, discrepancies between free wake and CFD/CSD simulations occurred between 30 deg and 80 deg azimuth, but the magnitude of the differences was amplified for the active rotor. Both CFD/CSD and free wake simulations exhibited increased thrust compared to the passive rotor between 90 deg and 360 deg, which can be attributed to the active camber morphing.

However, the free wake method generally underpredicted the active camber thrust enhancement to compared to CFD/CSD method within the 90 deg to 270 deg azimuthal range. The linear inflow method exhibited an almost linear thrust variation between 90 deg and 315 deg azimuth, lacking the high-frequency fluctuations. Notably, this absence of high-frequency fluctuations was even more pronounced than in the passive case, reducing the accuracy of the linear inflow model even further for the active rotor. This deficiency underlines the limitations of linear inflow for capturing dynamic load variations, essential, for example, for vibration analysis. Compared to both CFD/CSD and free wake simulations, the linear inflow method underpredicted thrust across the majority of the rotor azimuth. However, an overprediction of thrust was observed within the 270 to 315 deg azimuthal range.

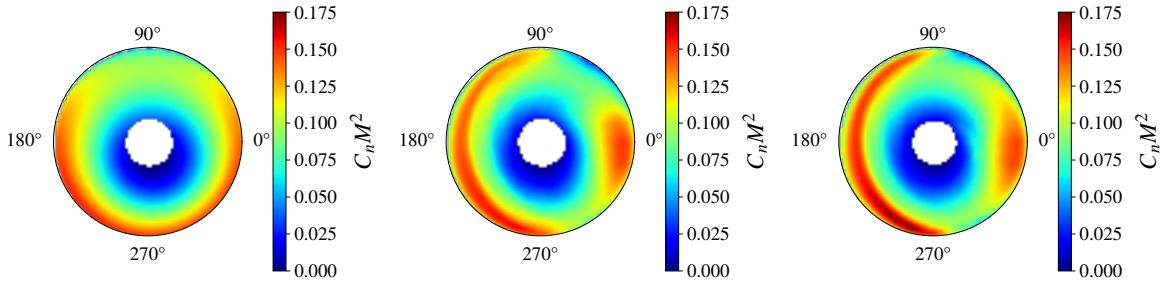

(a) Drag distribution using the linear inflow method. **(b)** Drag distribution using the free wake method. **(c)** Drag distribution using the CFD/CSD coupling method.

Figure 3.58.: Comparison of the blade sectional thrust coefficient C_nM^2 distribution over the passive rotor disk, obtained using linear inflow, free wake, and CFD/CSD methods at an advancing ratio of $\mu = 0.15$.

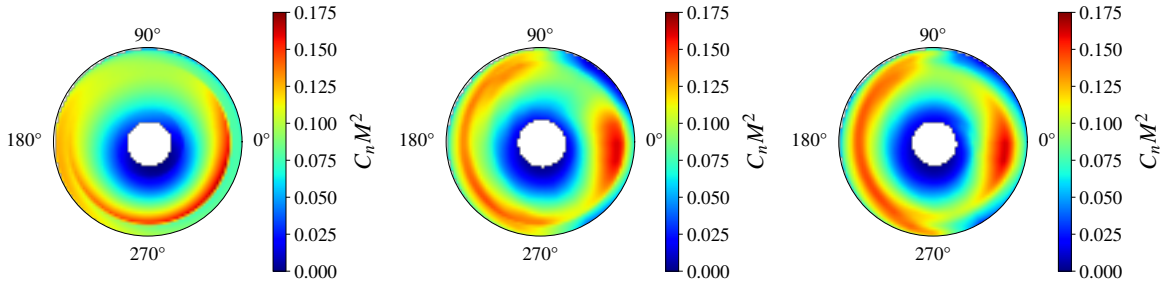

(a) Drag distribution using the linear inflow method. **(b)** Drag distribution using the free wake method. **(c)** Drag distribution using the CFD/CSD coupling method.

Figure 3.59.: Comparison of the blade sectional thrust coefficient C_nM^2 distribution over the active rotor disk, obtained using linear inflow, free wake, and CFD/CSD methods at an advancing ratio of $\mu = 0.15$.

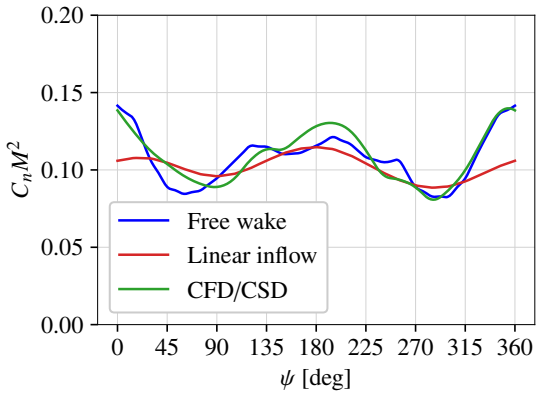

(a) Distribution of the blade sectional thrust coefficient C_nM^2 of the passive blade at $r/R = 0.75$.

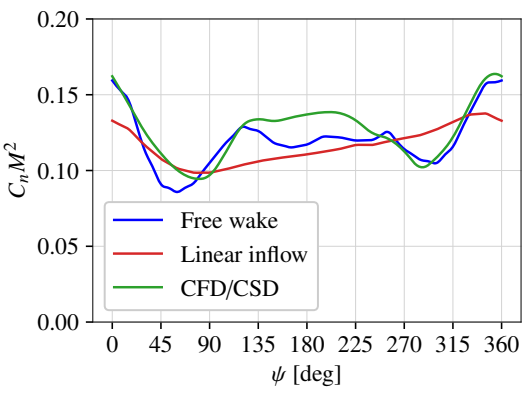

(b) Distribution of the blade sectional thrust coefficient C_nM^2 of the active blade at $r/R = 0.75$.

Figure 3.60.: Comparison of the blade sectional thrust coefficient C_nM^2 distribution at the blade section $r/R = 0.75$ over the rotor azimuth ψ, obtained using linear inflow, free wake, and CFD/CSD methods at an advancing ratio of $\mu = 0.15$.

Table 3.6.: Comparison of the total required power for passive versus active rotors, obtained using linear inflow, free wake, and CFD/CSD methods at an advancing ratio of $\mu = 0.15$.

Total required power	Linear inflow	Free wake	CFD/CSD
For passive rotor in kW	270.460	219.658	234.776
For active rotor in kW	273.087	217.870	232.684

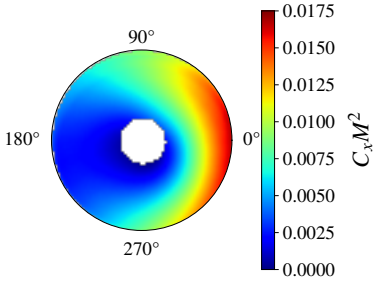

(a) Drag distribution using the linear inflow method.

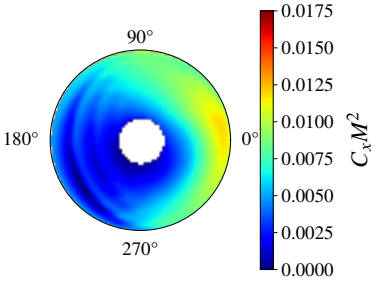

(b) Drag distribution using the free wake method.

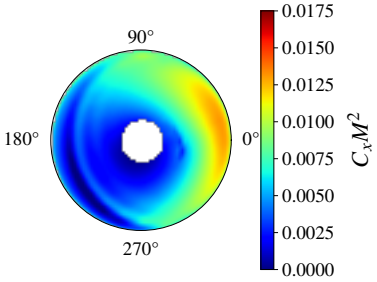

(c) Drag distribution using the CFD/CSD coupling method.

Figure 3.61.: Comparison of the blade sectional drag coefficient C_xM^2 distribution over the passive rotor disk, obtained using linear inflow, free wake, and CFD/CSD methods at an advancing ratio of $\mu = 0.15$.

Figures 3.61 and 3.62 present a comparative analysis of drag distribution for passive and active rotors using linear inflow, free wake, and CFD/CSD methods repectively. For the passive rotor model, the CFD/CSD and free wake results exhibited similar overall drag distributions, with minor discrepancies primarily in the outboard region of the rotor rear, between 315 deg and 45 deg where the free wake model underpredicted drag. Contrary to the thrust distribution, where the linear inflow model could not accurately compute the magnitude and the overall distribution of

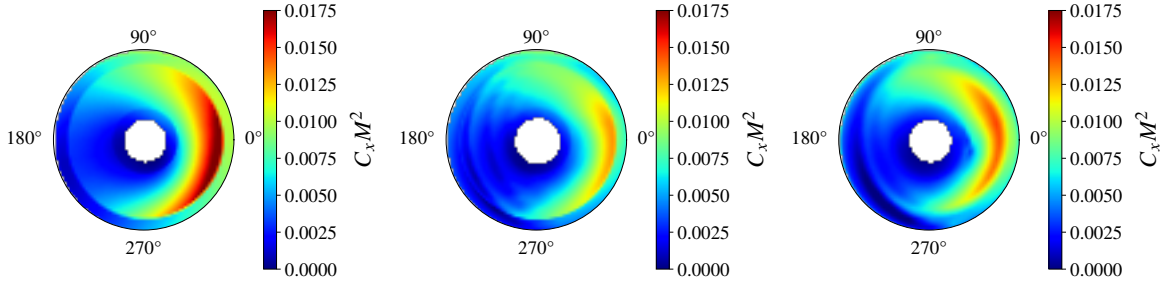

(a) Drag distribution using the linear inflow flow method.

(b) Drag distribution using the free wake method.

(c) Drag distribution using the CFD/CSD coupling method.

Figure 3.62.: Comparison of the blade sectional drag coefficient C_xM^2 distribution over the active rotor disk, obtained using linear inflow, free wake, and CFD/CSD methods at an advancing ratio of $\mu = 0.15$.

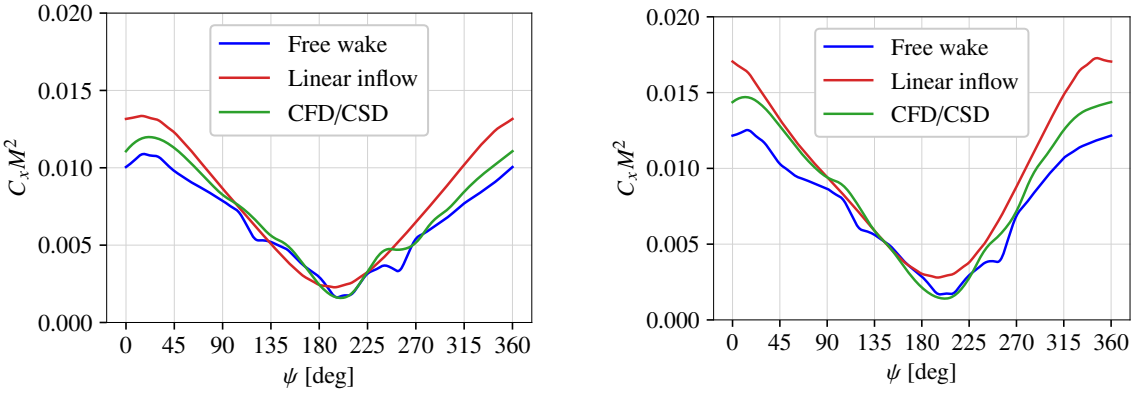

(a) Distribution of the blade sectional drag coefficient C_xM^2 of the passive blade at $r/R = 0.75$.

(b) Distribution of the blade sectional drag coefficient C_xM^2 of the active blade at $r/R = 0.75$.

Figure 3.63.: Comparison of the blade sectional drag coefficient C_xM^2 distribution at the blade section $r/R = 0.75$ over the rotor azimuth ψ, obtained using linear inflow, free wake, and CFD/CSD methods at an advancing ratio of $\mu = 0.15$.

the thrust accurately, the drag distribution calculated by the linear inflow model showed similar trends to those calculated by the free wake and CFD/CSD models. Nevertheless, the linear inflow model was not able to accurately calculate the magnitude of the drag, unlike the CFD/CSD coupled and free wake simulations. Notably, while the maximum thrust values across the rotor disk were underpredicted by the linear inflow model, the maximum drag values were drastically overpredicted by the linear inflow model, which was not the case with the free wake and CFD/CSD coupled models.

When active camber morphing was applied, as shown in Fig. 3.62, all models predicted drag reductions near the blade tip for $r/R > 0.85$ and increased drag in the morphing region $0.45 < r/R < 0.85$ over the 315 deg to 45 deg azimuth range. Similar to the passive case, the free wake model underpredicted drag in the rotor rear compared to CFD/CSD, while the linear inflow method exhibited the largest drag increase. The drag distribution computed with the linear inflow model for the active rotor showed pronounced sharp variations at the morphing transition at $r/R = 0.85$, similar to what is seen in the thrust distribution. As discussed before, this can be attributed to the lack of trailer vortices modelled at $r/R = 0.5$ and $r/R = 0.9$ and the blade tip. The absence of trailer vortices led to inaccurate modeling the induced velocity. In the free wake model, the definition of these trailer vortices led to a smoother transition of the drag variation between the unmorphed and morphed sections.

Figures 3.63a and 3.63b present a detailed comparison of drag distribution over the azimuth for the passive and active rotors respectively, at $r/R = 0.75$, calculated using linear inflow, free wake, and CFD/CSD methods. For the passive blade, all methods predicted similar drag magnitudes with only minor discrepancies between 90 and 270 deg azimuth. However, significant differences emerged on the advancing side from 0 to 90 deg and on the retreating side from 270 to 360 deg, where the linear inflow method computed the highest drag and the free wake method the lowest, aligning with the overall drag trends observed in Fig. 3.61. When applying active camber morphing, the differences in drag on the advancing side from rotor azimuth 0 to 90 deg and on the retreating side from 270 to 360 deg between the linear inflow, free wake, and CFD/CSD methods became more pronounced. The impact of active camber on drag variation being the least pronounced using the free wake method. In contrast, the linear inflow method exhibited the highest drag increase due to camber morphing at $r/R = 0.75$. Furthermore, similar in the thrust distribution over the azimuth, the linear inflow model was unable to capture the high frequency variations in drag present in the CFD/CSD coupled results, represented in Fig. 3.63b, so that the drag variation was smoothed over the rotor azimuth. When active camber was applied, similar to the observations made with thrust distribution, the linear inflow model also smoothed the drag. However, in contrast to thrust, the drag profile was not linearized.

The distinct drag distributions produced by the linear inflow, free wake, and CFD/CSD models had a direct influence on the calculated power requirements. Table 3.6 presents the total required power computed for each case considered. For the passive rotor, the free wake model calculated the lowest power requirement, at 6.4% lower than the CFD/CSD coupled model, whereas the linear inflow model calculated the highest required power, at 15.1% higher than the CFD/CSD coupled model. When active camber morphing was applied, the free wake model calculated a required power 6.4% lower than the CFD/CSD coupled model, while the linear inflow model calculated a 17.4% higher power than the CFD/CSD coupled model, which can be attributed to the high drag

predicted in the front and rear of the rotor using the linear inflow model. Moreover, comparing the passive to active rotor cases: when active camber was applied, the free wake and CFD/CSD models exhibited an approximate 0.9% power reduction, while the linear inflow model exhibited a 0.9% power increase. This change in power requirement arises mainly from the drag distribution shifting from the blade tip towards the inboard region, as well as a general increase in the magnitude of drag experienced across the rotor disk. The power consumption trend between passive and active rotors, as predicted by the linear inflow model, differed from that observed using free wake and CFD/CSD methods. This discrepancy can be attributed to the linear inflow model being unable to accurately represent the fluctuating drag distribution across the rotor disk and its tendency to overestimate drag at the rotor rear, compared to the more sophisticated free wake and CFD/CSD approaches.

3.3.13. Summary and Conclusions

Section 3.3 investigates the impact of camber morphing on sectional thrust and drag, as well as related pressure, vorticity distributions, and rotor wake characteristics, at an advance ratio of $\mu = 0.15$. This study aims to explore aerodynamic characteristics that are not fully captured by traditional comprehensive analysis tools. For this purpose, a high-fidelity CFD/CSD coupling framework was developed, combining the TAU CFD solver for detailed flow field resolution and CAMRAD II for rotor trimming. The investigation compared the aerodynamic characteristics of a four-bladed rotor with passive and active camber-morphing blades. The passive blade was modeled as a rigid surface based on the BO105 rotor blade geometry. For the active blade, full camber morphing deflection δ was applied based on a periodic and non-harmonic schedule over the rotor, specifically to the blade section from $r/R = 0.4$ to $r/R = 0.8$, with a linear transition between the fully camber-morphed region and the unmorphed region. The following conclusions were drawn from the investigation of passive and active rotors under identical trim conditions with an advance ratio of $\mu = 0.15$:

- While both passive and active rotors generated the same total thrust, active camber morphing redistributed the thrust more uniformly across the rotor disk, with thrust enhancements in the mid-span region and reductions near the blade tip. This shift of peak thrust inboard allowed for a reduction in collective pitch angle and pitch peak-to-peak variation, with minimal changes to flap and lead-lag blade motions.

- Active camber morphing redistributed the sectional drag force across the rotor disk. Drag increased in the mid-span region and decreased near the blade tip. Despite these changes, the overall impact on power consumption remained minimal at the advance ratio $\mu = 0.15$.

- Active camber morphing led to noticeable changes in pressure distribution in the morphing section along the chord from $x/c = 0.75$ to the trailing edge tip and in particular over the span region $0.5 < r/R < 0.8$. This effect was most pronounced when camber deflection exceeded 3 deg. The increased pressure difference over this span section shifted the maximum sectional thrust toward the blade mid-span. As a result, the active blade operated at lower pitch angles.

- Pronounced differences in pressure distribution were observed over the span region near the blade tip, where $r/R > 0.9$, and both the passive and active blades remained unmorphed. These differences were particularly notable near the leading edge. The variation in pressure distribution affected the formation and roll-up of blade tip vortices. This led to differences in the overall vorticity distribution and rotor wake.

- Active camber morphing significantly reduced the core width of both tip vortices and trailing vortices. This indicates that active camber morphing can effectively weaken the strength of the tip vortices. The wake structure generated by active camber morphing differs from that of passive rotors. This difference is especially clear in the size of trailing vortices and the interaction between tip vortices and trailing vortices.

- Active camber morphing reduced the vorticity magnitudes within the trailing vortex cores. It also caused significant distortion and shifting of the trailing vortices, particularly on the retreating side. The effects of camber morphing became more pronounced further downstream, underscoring the influence of the camber morphing on the far wake of the rotor.

- The shifting, elevation, and distortion of the tip vortices due to camber morphing on the retreating side resulted in intensified interactions between the distorted blade tip vortices and the trailing vortices in comparison to the passive rotor. This underscores the significant impact of camber morphing on the overall rotor wake.

- On the advancing side, active camber morphing caused the tip vortex to become more elongated in the spanwise direction, resulting in a larger interaction region between the vortex and the advancing blade. The elongated vortex core in the active rotor increased the interaction area compared to the passive rotor. In both configurations, the vortex core passed over the upper surface of the active blade, leading to a local minimum in the sectional thrust coefficient for both rotors.

- On the retreating side, the tip vortex in the active rotor exhibited a weaker core compared to the passive rotor. In the active configuration, the vortex core was concentrated on the upper surface of the blade, whereas in the passive configuration, the high-vorticity region primarily passed below the blade. The active blade intersected the vortex at mid-height, while the passive blade interacted with the upper third of the vortex. Additionally, the active rotor's vortex was more compact along the vertical z direction and more elongated in the spanwise direction. This difference in vortex position, size and strength, contributed to a local minimum in the sectional thrust coefficient for the active rotor, a feature not observed in the passive rotor.

- The sectional thrust and drag results of high-fidelity CFD/CSD coupling were compared to those of low-fidelity linear inflow and mid-fidelity free wake methods. The linear inflow model demonstrated significant limitations in accurately predicting thrust and drag distributions for both passive and active rotors, especially when compared to the free wake and CFD/CSD coupling methods. It failed to capture the smooth transition between unmorphed and morphed blade sections, as well as high harmonic load variations over the rotor disk. The thrust distribution generated by the linear inflow model was distinctly different from that produced by the CFD/CSD coupling and free wake simulations for both rotor configurations. Additionally, the linear inflow model overestimated drag in the rear rotor section. In contrast, the CFD/CSD coupling and free wake models generally agreed on thrust and drag distributions, with some differences noted on the retreating side and in the rotor rear.

- The CFD/CSD coupling and free wake simulations indicated that camber morphing could lead to a slight reduction in rotor power. However, the linear inflow model approximated an increase in power due to their limitations in computing the drag. This underscored the necessity for the high-fidelity models to accurately predict rotor aerodynamics.

4. Summary and Conclusion

This thesis presents a comprehensive analysis of the aerodynamic effects of active camber morphing on helicopter rotor blades, with a focus on morphing concepts similar to the Fishbone Active Camber (FishBAC). By combining 2D steady and unsteady CFD simulations with high-fidelity CFD/CSD simulations for both passive and active rotor blades, the study explores how camber morphing, applied from the 75% chord position to the trailing edge tip, influences not only the aerodynamic loads on the blade sections but also the overall rotor flow field.

A first investigation addressed the lack of published airfoil tables for camber-morphed blade sections, which are essential for comprehensive rotor analysis. Using 2D steady CFD simulations in TAU, the study evaluated how the steady-state aerodynamic coefficients C_l, C_d, and C_m change when camber morphing is applied, compared to the baseline NACA23012 airfoil with a tab, which represents the BO105 rotor blade section. Camber deflections of up to 10 degrees downward were assessed across a wide range of rotor-relevant angles of attack. The evaluation was conducted at Mach numbers $M = 0.4$ and $M = 0.6$. These Mach numbers were chosen because they occur in a large range of operating conditions such as hover, low-speed flight ($\mu = 0.15$), and high-speed flight ($\mu = 0.3$).

The 2D steady simulations from the first investigation showed that downward camber morphing significantly increased the maximum lift coefficient $C_{l,\max}$. This led to a broader lift envelope. At Mach 0.6, a 10-degree camber deflection increased lift by up to 50%. The increase in the lift coefficient C_l at a constant angle of attack was due to the amplified suction peak and larger pressure differences across the morphed section. Camber morphing also improved the lift-to-drag ratio C_l/C_d over a wider range of lift coefficients compared to the baseline airfoil. While the C_l/C_d of the baseline declined as it reached its maximum lift coefficient, camber-morphed airfoils with moderate deflections maintained higher C_l/C_d ratios at lift values equal to the $C_{l,\max}$ of the baseline. This demonstrates that camber morphing could increase aerodynamic efficiency while improving the lift generation capability of rotor blades. Such improvements are particularly beneficial for high-altitude and heavy-lift operations, where greater lift is required, as well as during hover and both low- and high-speed flight regimes, where the same required lift and thrust can be achieved with reduced drag. While the baseline airfoil exhibited a constant, low pitching moment coefficient C_m, camber morphing introduced significant changes in both the magnitude and variation of C_m relative to C_l. Camber morphing led to an increasingly non-linear relationship between C_l and C_m. Downward camber morphing, in particular, produced a pronounced nose-down pitching moment. Additionally, the center of pressure x_{cp} was shifted towards the trailing edge with increasing downward camber morphing. This shift became more pronounced at the higher Mach number $M = 0.6$. The downstream shift of x_{cp} was attributed to the reduced suction peak and increased pressure differences in the morphed section, which contributed to the lift increase at

a constant angle of attack compared to the baseline airfoil. This underscores the importance of examining the impact of dynamic camber morphing on rotor stability, as varying deflections can cause significant shift of the sectional aerodynamic forces throughout the rotor azimuth.

While the first investigation provided insights into how camber morphing affected the steady aerodynamic coefficients used in comprehensive rotorcraft analysis tools, a second investigation demonstrated that these coefficients do not take into account the unsteady effects caused by simultaneous pitching and camber morphing. This investigation compared unsteady CFD simulations in TAU with the steady aerodynamic coefficients used in CAMRAD II, aiming to identify the unsteady effects that are not captured in the airfoil tables. It also evaluated the effectiveness of the standard ONERA Edlin model in CAMRAD II in addressing these discrepancies. A uniform inflow model was used in CAMRAD II to focus specifically on the effects of pitching and camber morphing at a Mach number of 0.4. Two camber morphing frequencies were applied: the 1P case, where the camber morphing frequency was synchronized with the 7 Hz pitch frequency, and the 2P case, in which the camber morphing frequency was doubled to 14 Hz. The pitch angle was restricted to a range between 0 and 8 degrees to ensure attached flow conditions, allowing the analysis to concentrate on the unsteady effects induced by camber morphing.

The lift coefficient C_l varied over time mainly following the pitching schedule because C_l was directly affected by changes in the effective angle of attack. In contrast, the pitching moment coefficient C_m mainly followed the camber morphing schedule. Unsteady results for C_l consistently showed a negative phase shift compared to steady state results, for the unmorphed pitching case as well as when camber morphing was applied. This negative phase shift is due to fluid inertia associated with airfoil motion. For C_m, there was no clear or consistent phase shift between unsteady and steady state results. The unsteady drag coefficient C_d showed significant time variation compared to steady data, with C_d being notably underpredicted at high pitch angles. This discrepancy became even more pronounced when camber morphing was synchronized with pitch motion. This highlights that steady state models do not adequately take into account the fluid flow resistance during dynamic motions. The ONERA Edlin model improved the approximation of C_m by introducing a positive phase shift to take into account the inertia effects during pitching and camber morphing. However, the ONERA Edlin model could not fully capture C_m at maximum pitch angles. While this phase shift helped correct C_m, it caused inaccuracies in C_l, leading to further deviations from unsteady CFD results. This underscores the limitation of the model in approximating lift under dynamic conditions for this specific investigation. Furthermore, the standard ONERA Edlin model in CAMRAD II did not adjust the drag coefficient C_d. This proves the need for high-fidelity methods in rotor aerodynamic analysis to accurately compute drag, particularly when camber morphing is applied.

Moreover, the phase relationship between camber morphing and pitch motion significantly influences the unsteady effects, as demonstrated by comparing pressure distributions and velocity profiles from unsteady and steady state results at the same effective angle of attack. When camber morphing was synchronized with the pitch motion, unsteady effects were amplified, leading to significant differences in the pressure and velocity profiles, particularly near the leading edge. However, when the camber morphing frequency was doubled, the pressure distributions and velocity profiles more closely resembled those of the steady-state results as the camber morphing and pitch motion became out of phase. This demonstrates that having camber morphing and

pitch motion out of phase can reduce unsteady aerodynamic effects. The key finding of the second investigation shows that it is necessary to use advanced modeling approaches to accurately capture unsteady aerodynamic effects in rotor analysis. Using a high-fidelity modeling approach that solves the unsteady rotor field can address this need, in particular by taking into account the resistance of the flow to dynamic motion and its impact on drag and lift, whether or not there is a phase shift between pitch and camber morphing schedules.

In the third investigation, a high-fidelity CFD/CSD coupling framework was developed to resolve three-dimensional, unsteady, and non-linear effects not captured by lower-fidelity methods. This framework provided insights into how camber morphing influenced the flow field and wake structure of a four-bladed rotor. It integrated the TAU CFD solver for flow field resolution with CAMRAD II for rotor trimming. The study compared the aerodynamic characteristics of a four-bladed rotor with both passive and active camber-morphing blades. The passive blade was modeled as a rigid surface based on BO105 rotor geometry. The active blade featured full camber morphing deflection applied periodically in a non-harmonic schedule from $r/R = 0.4$ to $r/R = 0.8$, with a linear transition to the unmorphed region. Aerodynamic characteristics of both rotor configurations were evaluated under identical trim conditions at an advance ratio of $\mu = 0.15$.

A third and final investigation showed that active camber morphing significantly redistributed aerodynamic loads across the rotor disk and reshaped the rotor wake. Morphing the rotor blade led to a more uniform load distribution, reducing thrust and drag in the blade tip region while shifting the highest loads toward the midspan, thus reducing the need for large pitch angles. The influence of camber morphing extended into the unmorphed blade tip region ($r/R > 0.85$), where it lowered pressure differences near the leading edge compared to passive blades. This reduction affected the formation and roll-up of blade tip vortices, decreasing both their strength and core size. The tip vortices also became more elongated in the spanwise direction with active camber. These changes in vortex shape, strength, and trajectory had a notable impact on blade-vortex interactions. Compared to the passive rotor, the elongated tip vortices interacted over a larger area with the passing blades, but with reduced vortex strength, especially on the retreating side. Additionally, camber morphing reduced vorticity magnitudes in the trailing vortex cores, causing noticeable distortion and shifting of these vortices. These effects became more pronounced further downstream, impacting the interactions between trailing and tip vortices. This demonstrated how camber morphing could influence the far wake. These effects cannot be captured by standard comprehensive rotor analysis tools like CAMRAD II, which uses lower-fidelity wake models.

The comparison of high-fidelity CFD/CSD coupling, free wake, and linear inflow models revealed significant limitations in the linear inflow method for approximating thrust and drag in both passive and active rotors. The linear inflow model was unable to accurately capture the transitions between unmorphed and morphed sections, leading to an overestimation of rear rotor drag and neglecting high harmonic loads. In contrast, both the CFD/CSD and free wake models captured these transitions and demonstrated consistent accuracy in computing drag and thrust distribution across the rotor, albeit with acceptable discrepancies observed between these methods in the approximation of blade-vortex interaction effects on thrust on the retreating side. In comparison to the free wake results, the CFD/CSD simulation provided more detailed insights into the aerodynamic flow field, including the impact of camber morphing on the vorticity field and rotor wake. It offered a deeper understanding of how variations in pressure distribution and vorticity influence

sectional aerodynamic forces. Additionally, while both the CFD/CSD and free wake simulations showed that camber morphing could reduce rotor power, the linear inflow model inaccurately computed a power increase. This discrepancy underscores the limitations of low-fidelity models in capturing complex aerodynamic phenomena, which can lead to significant inaccuracies in approximating the overall rotor characteristics.

The framework developed in this thesis establishes a foundation for advancing research on the effects of camber morphing in elastic rotor blades. Future studies could explore how camber morphing influences the elastic behavior of rotor blades across a range of operating speeds, comparing the outcomes to wind tunnel experiments to validate the CFD/CSD coupling framework. A deeper understanding of the interaction between sectional blade loads and the elastic responses induced by camber morphing could be gained. These findings could lead to the optimization of camber morphing strategies that reduce hub vibrations and lower power consumption. Furthermore, the effects of active camber on the vorticity field and its influence on the rotor wake and the interactions between elastic blades and vortices in the rotor near field could be analyzed. Additionally, the aerodynamic loads obtained from the three-dimensional CFD flow field could be incorporated into aeroacoustic solvers to assess the impact of active camber on noise levels perceived by distant observers. This could help to identify camber morphing schedules that would reduce noise emissions.

A. List of Publications by the Author Relating to the Dissertation

Rauleder, J., van der Wall, B. G., Abdelmoula, A., Komp, D., Kumar, S., Ondra, V., Titurus, B., Woods, B. K. S.: "Aerodynamic Performance of Morphing Blades and Rotor Systems," American Helicopter Society 74th Annual Forum, Phoenix, AZ, 2018. American Helicopter Society 74th Annual Forum, Phoenix, AZ, 2018, [95] .

Abdelmoula, A., Rauleder, J.: "Aerodynamic Performance of Morphed Camber Rotor Airfoils," AIAA SciTech, San Diego, CA, USA, 2019, [2].

Komp, D., Kumar, S., Abdelmoula, A., Hajek, M., Rauleder, J: "Investigation of Active Rotor Design and Control for Performance Improvement," Vertical Flight Society 75th Annual Forum, Philadelphia, Pennsylvania, USA, 2019Vertical Flight Society 75th Annual Forum, Philadelphia, Pennsylvania, USA, 2019, [65].

Abdelmoula, A., Platzer, S., Hajek, M. and Rauleder, J.: "Numerical Investigation of the Effects of Dynamic Camber Variation on the Airfoil Characteristics of a Pitching Rotor Airfoil," AIAA Science and Technology Forum, Orlando, USA, January 2020.AIAA Science and Technology Forum, Orlando, USA, 2020, [3].

Huang Q., Abdelmoula A., Chourdakis G., Rauleder J., Uekermann B.: "CFD/CSD coupling for an isolated rotor using preCICE," 14th World Congress on Computational Mechanics (WCCM), February 202114th World Congress on Computational Mechanics (WCCM), 2021, [43].

Abdelmoula A.,Yurt M. K.,D Komp D., Hajek M-, Rauleder J.: "CFD/CSD Coupling for Camber Morphed Rotor Blades", AIAA AVIATION 2022 Forum June 27-July 1, 2022 Chicago, IL & Virtual AIAA AVIATION 2022 Forum June 27-July 1, 2022 Chicago, IL & Virtual, [4].

Abdelmoula A., Grimm, A., Yavrucuk, I., and Rauleder, J.: "Aerodynamic Analysis of Rotor Airfoils with Camber Morphing Mechanism versus Plain Flaps", 49th European Rotorcraft Forum, 2023, [5].

B. Appendix related to the subsection 3.1 Evaluation of Steady Aerodynamics for 2D Steady Camber-Morphed Airfoils

A convergence study was conducted for the grid of the baseline airfoil ($\delta = 0$ deg) and a camber-morphed airfoil with $\delta = 4$ deg camber deflection. Different grid resolutions were tested, including a coarse grid with 39,204 cells, a medium grid with 104,372 cells, and a fine grid with 158,004 cells, as shown in Table B.1. The number of cells varied primarily at the leading edge of the airfoil and in the direction perpendicular to the upper and lower surfaces. The results, which illustrate how lift coefficient C_l, drag coefficient C_d, and moment coefficient C_m varied with grid resolution, are presented in Fig. B.1. Both airfoils displayed similar trends: C_m showed little sensitivity to changes in grid resolution, while C_l and Cd were more affected. The variation in C_l decreased as the grid resolution increased, and the same was observed for C_d. Considering the trade-off between accuracy and computational time, particularly given the large sweep of simulations conducted to cover a wide range of angles of attack and Mach numbers, the medium grid was selected as the optimal choice for the study conducted in 3.1.

Table B.1.: Grid resolution used for the convergence study.

Resolution	Coarse	Medium	Fine
Number of cells	39204	104372	158004

Figure B.2 illustrates the pressure patterns, is an alternative representation of Fig. 3.15a over the baseline airfoil ($\delta = 0$ deg) compared to the camber-morphed airfoils with $\delta = 4$ deg and $\delta = 8$ deg camber deflections, all at the same lift coefficient $C_l = 1.225$. For the camber-morphed airfoils, less pronounced suction peaks were observed compared to the baseline airfoil. This indicates that at the same C_l, the camber-morphed airfoils achieve lift with a more moderate pressure gradient, leading to reduced suction effects on the surface of the airfoil.

Figure B.3 illustrates the pressure pattern variations for a camber morphing deflection of $\delta = 8$ deg at increasing angles of attack α from 0 to 6 degrees in 2 deg increments. This Figure is an alternative representation of Fig. 3.15c. The effects of increasing the angle of attack were most pronounced in the leading-edge section on both the upper and lower surfaces, while the influence diminished toward the trailing edge.

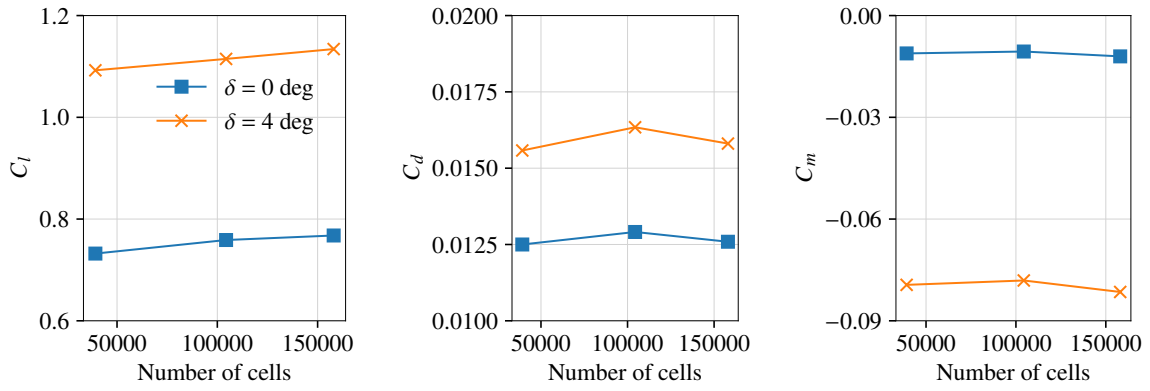

(a) Influence of grid resolution on C_l

(b) $M = 0.5$

(d) $M = 0.6$

(c) Influence of grid resolution on C_d

(e) Influence of grid resolution on C_m

Figure B.1.: Grid convergence study for the baseline airfoil and camber morphed airfoil with $\delta = 4$ deg, basedon the grid resolutions listed in B.1 .

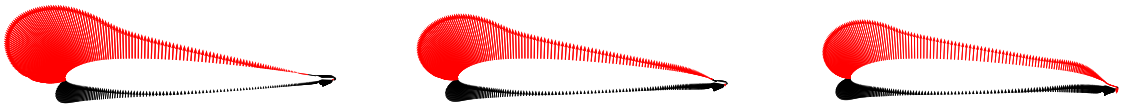

(a) $M = 0.4, \delta = 0, \alpha = 9.00$

(b) $M = 0.4, \delta = 4, \alpha = 6.00$

(c) $M = 0.4, \delta = 8, \alpha = 3.50$

Figure B.2.: Comparison of pressure patterns for constant lift coefficient($C_l = 1.225$) of different morphed airfoils.

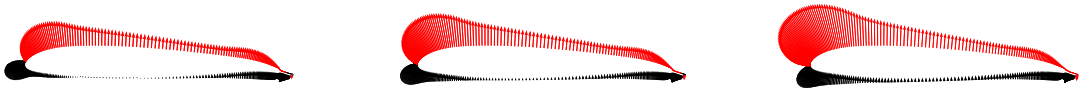

(a) $M = 0.4, \delta = 8, \alpha = 0.00$

(b) $M = 0.4, \delta = 8, \alpha = 2.00$

(c) $M = 0.4, \delta = 8, \alpha = 4.00$

Figure B.3.: Pressure patterns for different angle of attack of the morphed airfoil $\delta = 8°$.

C. Appendix related to the subsection 3.2 Evaluation of Unsteady Aerodynamics for 2D Camber-Morphed Airfoils

For the unsteady TAU simulations, temporal convergence study for the time step was conducted for the baseline airfoil. Here, the lift, moment and drag coefficient computed from investigations with different time steps $\Delta t_{fine} = T/720$, $\Delta t_{fine} = T/360$ and $\Delta t_{fine} = T/180$, were compared. This investigation showed that all time step provided similar results (not shown).

C.0.1. Evaluation of global difference

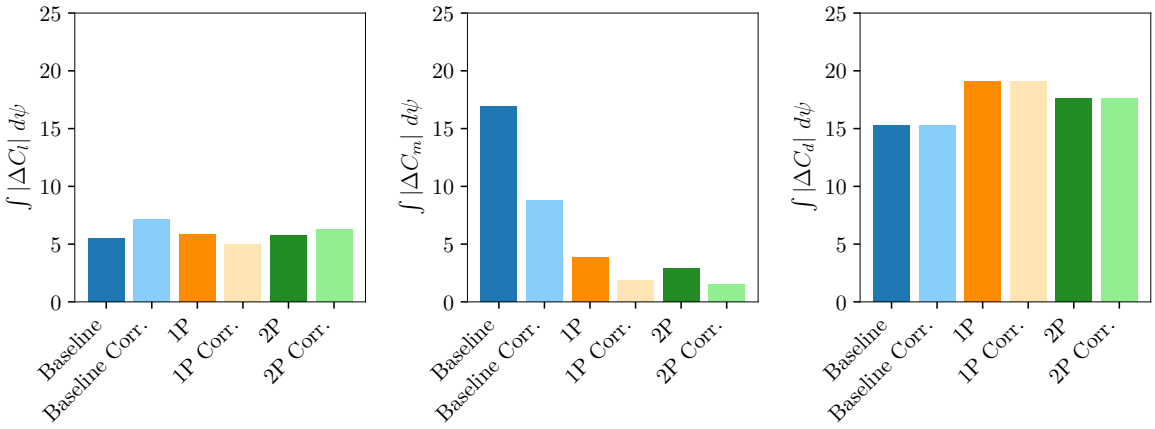

(a) Integrated difference in C_l. **(b)** Integrated difference in C_m. **(c)** Integrated difference in C_d.

Figure C.1.: Evaluation of global deviations between unsteady CFD and CAMRAD II results with and without ONERA Edlin corrections of the case listed in Table 3.1. Dark colors show the integrated deviation of raw steady results from unsteady results, while light colors show the deviation of ONERA Edlin-corrected steady results from unsteady results.

After evaluating the discrepancies between unsteady CFD results and the aerodynamic coefficients predicted by CAMRAD II throughout the pitch cycle, the overall deviations between these methods were quantified. This was achieved by integrating the absolute deviations $|\Delta C_l|$, $|\Delta C_d|$, $|\Delta C_l|$ of the raw steady and ONERA Edlin-corrected results from the unsteady CFD results over

the entire pitch period. This integrated approach provides a global measure of the residual deviations, thereby assessing the effectiveness of the ONERA Edlin model in adjusting steady results to account for unsteady effects not captured by the lookup tables. In Figures C.1a, C.1b and C.1c, which illustrate the global deviations, the dark colors indicate the integrated deviation of the raw steady results from the unsteady results, while the light colors indicate the integrated deviation of the ONERA Edlin-corrected steady results from the unsteady results.

Figure C.1a summarizes the global C_l deviations for the baseline, 1P, and 2P camber morphing cases. All cases exhibit a similar baseline discrepancy of approximately 5.6% when airfoil table data is used without adjustment. When using the ONERA Edlin model, a slight increase in deviation is observed for the baseline, as the ONERA Edlin model accounts for an incorrect phase shift. However, for the 1P and 2P cases with camber morphing, the deviations decreased nearly to the unadjusted level due to a reduced phase shift compared to the baseline. Overall, the maximum deviation remained below 10%, indicating acceptable accuracy for rotor pre-design using integral values, such as global thrust over disk loading. It is important to note that the ONERA Edlin model does not capture inertia effects, as shown in Figures 3.24, 3.25, and 3.26. This limitation can lead to an approximate shifted dynamic blade response over the rotor azimuth in CAMRAD II compared to the three-dimensional unsteady CFD simulations. On the other hand, Figure C.1b shows that the ONERA Edlin model was effective in correcting the steady data for C_m, particularly when dynamic camber morphing was applied simultaneously with the pitch motion. For the baseline case, the global deviation was high because the value of $\max(|C_{m,\text{CFD,unsteady}}|)$ used for normalization was near zero, resulting in a large relative $\Delta|C_m|$. For the morphed camber cases, the global deviation remained below 1.9% when the ONERA Edlin model was used. This indicates that the results obtained with the ONERA Edlin model can reliably approximate for example rotor key parameter linked with dynamic blade twist accurately, pitch link loads.

As shown in Figure C.1c, all evaluated scenarios exhibited notable deviations from the unsteady results, since the default ONERA Edlin implementation in CAMRAD II did not include drag corrections. Cases with morphed camber showed more pronounced deviations than the baseline, with the 1P camber morphed scenario showed the highest discrepancy, up to 19%. This discrepancy was caused by the combined effects of increased pitch and camber morphing deflection during the upstroke motion, particularly near θ_{max}. This study revealed limitations in using steady airfoil tables and the default ONERA Edlin model for predicting drag in dynamic scenarios, leading to potential inaccuracies in power calculations. Accurate drag prediction is essential for rotor power estimation, and the observed high discrepancies complicate assessments of power reduction through camber morphing. These inaccuracies can significantly impact rotorcraft performance and efficiency analyses.

The comparison of the flow around the airfoil for the baseline, 1P, and 2P cases at θ_{mean} during both upstroke and downstroke, as shown in the following Figs. C.2 C.3, and C.4, reveals that the differences in velocity were not limited to near region around the airfoil surface but propagate throughout the flow field surrounding the airfoil. This comparison is made against the steady simulation at the same effective angle of attack.

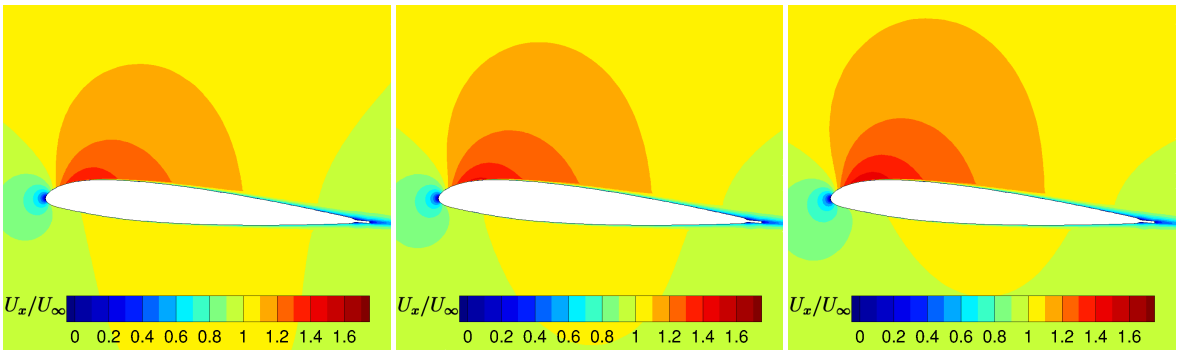

(a) Unsteady state results for baseline during upstroke motion.

(b) Steady state for the baseline.

(c) Unsteady state results for baseline during downstroke motion.

Figure C.2.: Comparison of the velocity contours for the baseline case at $M = 0.4$ and θ_{mean}.

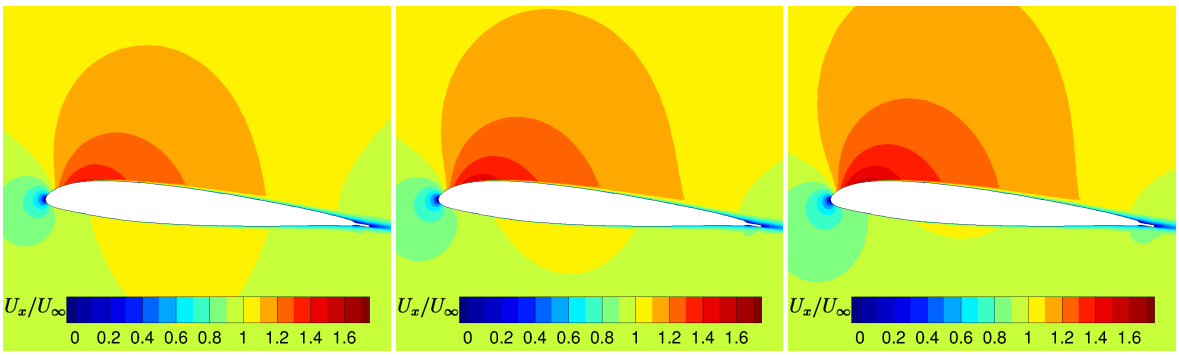

(a) Unsteady state results for the 1P case during upstroke motion.

(b) Steady state for the 1P case.

(c) Unsteady state results for the 1P case during downstroke motion.

Figure C.3.: Comparison of the velocity contours for 1P case at $M = 0.4$ and θ_{mean}.

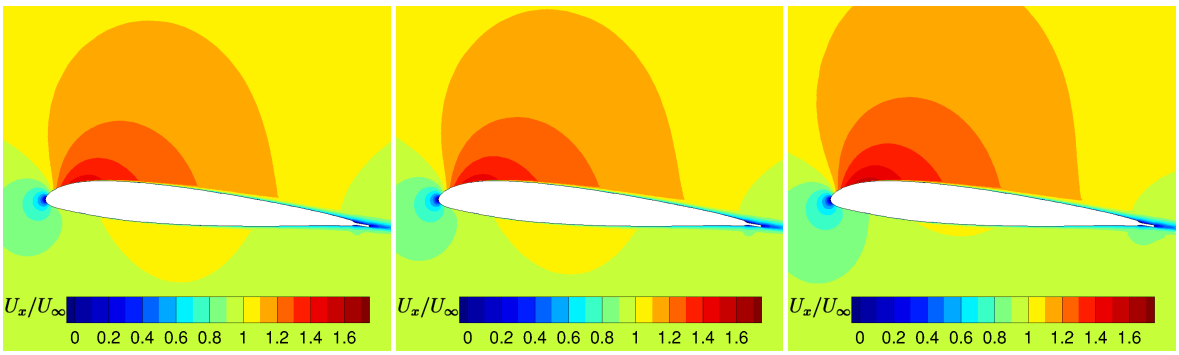

(a) Unsteady state results for the 2P case during upstroke motion.

(b) Steady state for the 2P case.

(c) Unsteady state results for the 2P case during downstroke motion.

Figure C.4.: Comparison of the velocity contours for 2P case at $M = 0.4$ and θ_{mean}.

D. Appendix related to the subsection 3.3 Evaluation of aerodynamic Characteristics for passive and active rotors using CFD/CSD coupling

D.0.1. Convergence of the grid deformation

Figure D.1 illustrates how the number of points selected from the scatter file,
given for the parameter `RBF maximum number of base points used` in the TAU input file, impacted the accuracy of the grid deformation process . This number corresponds to the points extracted from the scatter file to construct the matrix for Radial Basis Function (RBF) interpolation. The dark dots correspond to the prescribed grid deformation, while the different lines indicate that as the number of points given for `RBF maximum number of base points used` increased, the matching with the target improved. To compare the impact of resolution, the blade cross-section at $r/R = 0.65$ and $\psi = 300$ deg was evaluated for different deformed blades. The comparison revealed that 3,000 points were insufficient to accurately capture the curvature of the trailing edge tab. When using 6,000 points to construct the RBF matrix, a good match was achieved, but it did not fully align with the target shape. In contrast, using 7,927 points resulted in a strong alignment with both the target shape and the deformed blade section. For the grid deformation applied in this thesis, 7,927 points from each separate scatter file were used to compute the RBF interpolation matrix for the grid deformation schedule associated with each individual blade.

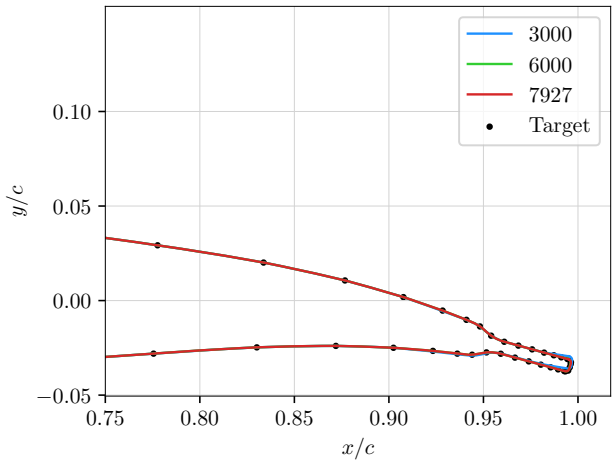

(a) Comparison of the deformed blade section at $r/R = 0.65$ and $\psi = 300$ deg depending on RBF base points.

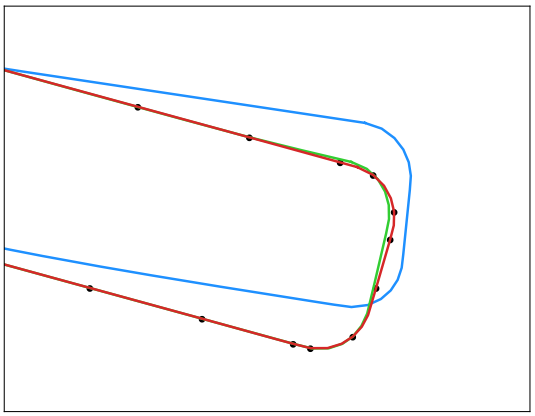

(b) Zoom of the comparison of the deformed blade section at $r/R = 0.65$ and $\psi = 300$ deg depending on RBF base points.

Figure D.1.: Influence of RBF Base Points on Blade Deformation

D.0.2. Convergence of the CFD/CSD coupling

Throughout the CFD/CSD coupling process, the residuals of the integrated lift and drag forces were closely monitored for both passive and active rotor configurations during the CFD simulations. These residuals ranged between 1×10^{-9} and 5.5×10^{-6}, indicating a highly refined and stable solution for lift and drag. Additionally, the density residuals of the CFD simulations fluctuated between 5×10^{-6} and 1×10^{-5} for both rotor configurations, demonstrating stable convergence as the iterations progressed. This consistent convergence behavior of lift, drag, and density residuals provides strong confidence in the accuracy of the results. The low magnitude and stability of these residuals confirm that numerical errors were minimized, ensuring that the aerodynamic loads and flow fields around the rotor blades were accurately captured.

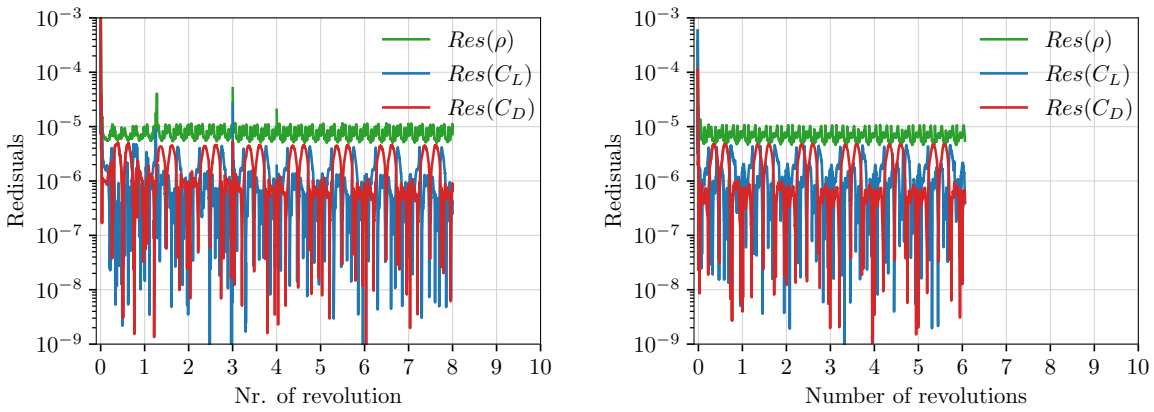

(a) Lift, drag, and density residuals for passive rotor.

(b) Lift, drag, and density residuals for active rotor.

Figure D.2.: Comparison of the lift, drag, and density residuals over the number of the revolutions for passive and active rotor.

Figure D.3 illustrates the variation of the sectional coefficients C_nM^2, C_xM^2, and C_yM^2 across coupling steps for both passive and active blades at an azimuth angle of $\psi = 90$ deg. These subfigures highlight the convergence behavior of these coefficients at each blade section along the span, as the coupling iterations progressed. Initially, at coupling step 0 (results computed with liner inflow model of CAMRAD II), the values of C_nM^2, C_xM^2, and C_yM^2 were significantly deviated from the final converged solution, indicating that the uncoupled results were not yet accurate. However, as the coupling iterations proceeded, the solutions began to converge, with noticeable improvements in each subsequent step. By coupling step 4 (green curve), the coefficients had converged, showing a strong agreement with the results at coupling step 5 (red curve). This demonstrates that by step 4, the solution had reached a stable state, as there were no significant differences between the results of step 4 and step 5.

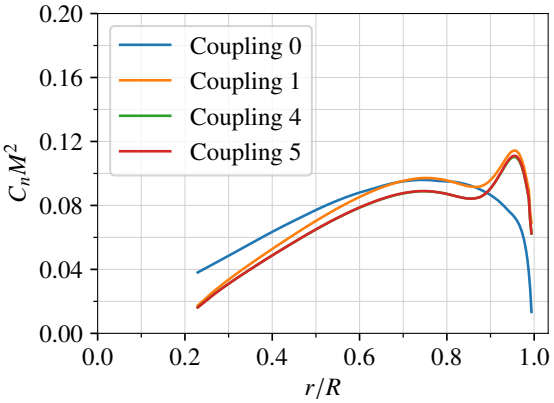

(a) Variation of C_nM^2 during the CFD/CSD coupling for the passive rotor

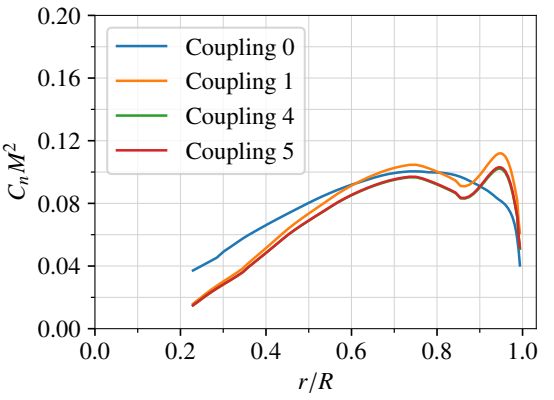

(b) Variation of C_nM^2 during the CFD/CSD coupling for the active rotor

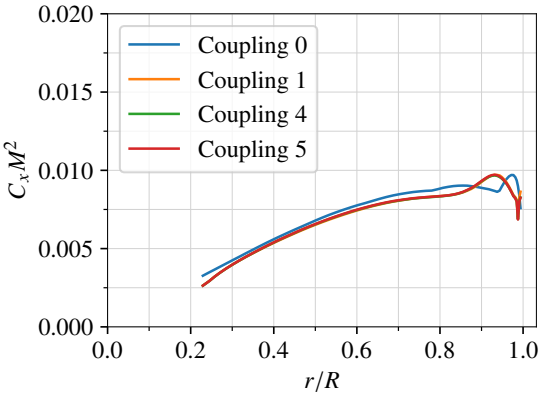

(c) Variation of C_xM^2 during the CFD/CSD coupling for the passive rotor

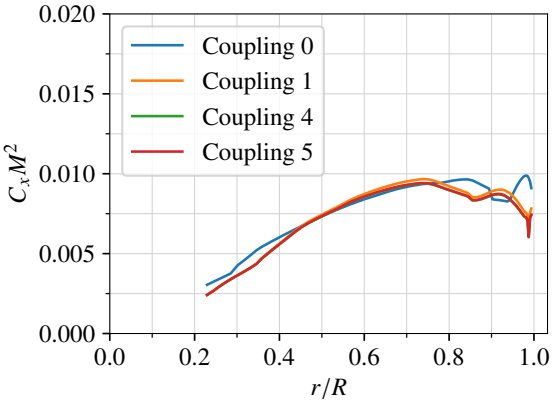

(d) Variation of C_xM^2 during the CFD/CSD coupling for the active rotor

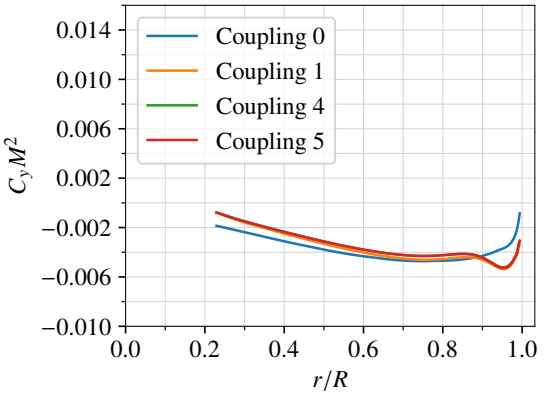

(e) Variation of C_yM^2 during the CFD/CSD coupling for the passive rotor

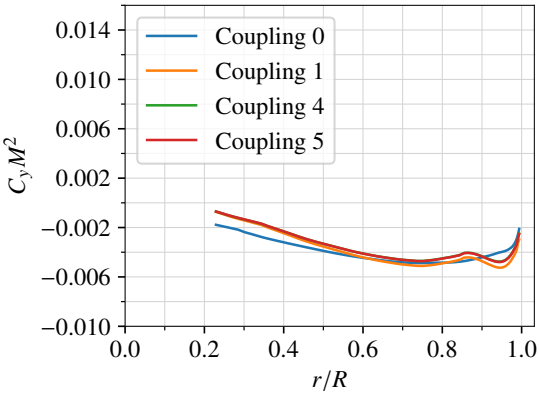

(f) Variation of C_yM^2 during the CFD/CSD coupling for the active rotor

Figure D.3.: Comparison of the C_nM^2, C_xM^2, and C_yM^2 between the CFD/CSD coupling steps for the passive and active rotor at $\psi = 90$ deg.

Bibliography

[1] Abbott, I. H. and Doenhoff, A. E. von. *Theory of Wing Sections*. New York: Dover, 1959.

[2] Abdelmoula, A. and Rauleder, J. "Aerodynamic Performance of Morphed Camber Rotor Airfoils". In: *AIAA Scitech Forum*. 2019.

[3] Abdelmoula, A., Platzer, S., Hajek, M., and Rauleder, J. "Numerical investigation of the effects of dynamic camber variation on the airfoil characteristics of a pitching rotor airfoil". In: *AIAA Scitech Forum*. 2020.

[4] Abdelmoula, A., Yurt, M. K., Komp, D., Hajek, M., and Rauleder, J. "CFD/CSD Coupling for Camber Morphed Rotor Blades". In: *AIAA AVIATION Forum*. 2022.

[5] Abdelmoula, A., Grimm, A., Yavrucuk, I., and Rauleder, J. "Aerodynamic Analysis of Rotor Airfoils with Camber Morphing Mechanism versus Plain Flaps". In: *49th European Rotorcraft Forum*. 2023.

[6] Ahmad, J. U. and Chaderjian, N. M. "High-Order Accurate CFD/CSD Simulation of the UH-60 Rotor in Forward Flight". In: 2011. URL: https://api.semanticscholar.org/CorpusID:18478963.

[7] Alcaraz Capsada, L. and Heinrich, R. "Development of the DLR TAU Code for Modelling of Control Surfaces". In: Deutsche Gesellschaft für Luft- und Raumfahrt - Lilienthal-Oberth e.V., 2019. URL: https://elib.dlr.de/126777/.

[8] Amiraux, M. "Numerical Simulation and Validation of Helicopter Blade-vortex Interaction using Coupled CFD/CSD and Three Levels of Aerodynamic Modeling". PhD thesis. University of Maryland, College Park, 2014.

[9] Anderson, J. *Fundamentals of Aerodynamics*. McGraw-Hill Education, 2010.

[10] Arnold, U. T. and Fürst, D. "Closed loop IBC Results from CH-53G flight Tests". In: *Aerospace Science and Technology* 9 (2005), pp. 421–435.

[11] Arnold, U. T. "Recent IBC Flight Test Results from the CH-53G Helicopter". In: *29th European Rotorcraft Forum*. 2003.

[12] Bhagwat, M. and Leishman, J. "Time-Accurate Modeling of Rotor Wakes Using a Free-Vortex Wake Method". In: *18th Applied aerodynamics conference*. 2000.

[13] Bhagwat, M. and Leishman, J. "Transient Rotor Inflow Using a Time-Accurate Free-Vortex Wake Model". In: *39th Aerospace Sciences Meeting and Exhibit*. 2001.

[14] Biedron, R. T. and Lee-Rausch, E. M. "Computation of UH-60A Airloads using CFD/CSD Coupling on Unstructured Meshes". In: *American Helicopter Society, 67th Annual Forum and Technology Display*. 2011.

[15] Bousman, W. G. *Putting the Aero Back into Aeroelasticity*. Tech. rep. 2000.

[16] Bousman, W. G. “Airfoil Design and Rotorcraft Performance”. In: *American Helicopter Society 58th Annual Forum*. 2002.

[17] Boyd Jr, D. D. “HART-II Acoustic Predictions using a Coupled CFD/CSD Method”. In: *American Helicopter Society, 65th Forum and Technology Display*. 2009.

[18] Brailsford, E. “The Aerodynamics of the Helicopter in Forward Flight”. In: *Journal of the Royal Aeronautical Society* 60 (1956), pp. 523–542.

[19] Bungartz, H.-J., Lindner, F., Gatzhammer, B., Mehl, M., Scheufele, K., Shukaev, A., and Uekermann, B. “preCICE–a Fully Parallel Library for Multi-Physics Surface Coupling”. In: *Computers & Fluids* 141 (2016), pp. 250–258.

[20] Cesnik, C. E. and Shin, S. “Design and testing of the NASA/Army/MIT active twist rotor prototype blade”. In: *American Helicopter Society 55th Annual Forum*. 1999.

[21] Clancy, L. *Aerodynamics*. Longman Scientific & Technical, 1986.

[22] Dadone, L. *US Army Helicopter Design DATCOM, Volume I-Airfoils*. Tech. rep. D210-11097. 1976. URL: https://apps.dtic.mil/sti/tr/pdf/ADA033425.pdf.

[23] Dadone, L. *Design and Analytical Study of a Rotor Airfoil*. Boeing Vertol Company, 1978.

[24] Datta, A., Sitaraman, J., Chopra, I., and Baeder, J. D. “CFD/CSD Prediction of Rotor Vibratory Loads in High-Speed Flight”. In: *Journal of aircraft* 43.6 (2006), pp. 1698–1709.

[25] Datta, A., Nixon, M., and Chopra, I. “Review of Rotor Loads Prediction with the Emergence of Rotorcraft CFD”. In: *Journal of the American Helicopter Society* 52.4 (2007), pp. 287–317.

[26] De Boer, A., Van der Schoot, M. S., and Bijl, H. “Mesh Deformation Based on Radial Basis Function Interpolation”. In: *Computers & structures* 85.11-14 (2007), pp. 784–795.

[27] Der Wall, B. G. van et al. “Smart Twisting Active Rotor (STAR)–Pre-Test Predictions”. In: *48th European Rotorcraft Forum*. 2022.

[28] Deutsches Zentrum für Luft- und Raumfahrt e.V. *Technical Documentation of the DLR TAU-Code Release 2020.1.0*. Tech. rep. 2020.

[29] Dietz, M., Krämer, E., Wagner, S., and Altmikus, A. “Active Rotor Performance Investigations Using CFD/CSD Weak Coupling”. In: *33th European Rotorcraft Forum*. 2007.

[30] Dietz, M. “Simulation der Aerodynamik von Hubschrauberkonfigurationen unter Berücksichtigung von Strömungs-Struktur-Kopplung und Trimmung”. PhD thesis. Ph. D. thesis University of Stuttgart, 2007.

[31] Du, H., Kong, W., Wang, Y., Liu, W., Huang, M., Zhang, W., and Tang, M. “Research on Rotorcraft Blade Tip Vortex Identification and Motion Characteristics in Hovering State”. In: *Symmetry* 12 (2020), p. 196.

[32] Enenkl, B., Klöppel, V., Preißler, D., and Jänker, P. “Full Scale Rotor with Piezoelectric Actuated Blade Flaps”. In: *28th European Rotorcraft Forum*. 2002.

[33] Friedmann, P. P. “On-blade Control of Rotor Vibration, Noise, and Performance: Just around the corner? The 33rd Alexander Nikolsky honorary lecture”. In: *Journal of the American Helicopter Society* 59.4 (2014), pp. 1–37.

[34] Furst, D. “Closed Loop IBC-system and Flight Test Results on the CH-53G Helicopter”. In: *American Helicopter Society, 60th Annual Forum*. 2004.

[35] Gardner, A., Richter, K., Mai, H., and Neuhaus, D. “Experimental Investigation of Air Jets for the Control of Compressible Dynamic Stall”. In: *Journal of The American Helicopter Society* (2013).

[36] Garipova, L., Batrakov, A., Kusyumov, A., Mikhaylov, S. A., and Barakos, G. “Aerodynamic and Acoustic Analysis of Helicopter Main Rotor Blade Tips in Hover”. In: *International Journal of Numerical Methods for Heat Fluid Flow* 26 (2016), pp. 2101–2118.

[37] Gerhold, T., Evans, J., and Galle, M. *Technical Documentation of the DLR T-Code*. Tech. rep. LIDO-Berichtsjahr=2020, 2020. URL: https://elib.dlr.de/13576/.

[38] Ghee, T. A. and Elliott, J. W. “The Wake of a Small-Scale Rotor in Forward Flight Using Flow Visualization”. In: *Journal of the American Helicopter Society* 40.3 (1995), pp. 52–65.

[39] Goerttler, A., Braukmann, J. N., Wolf, C. C., Gardner, A. D., and Raffel, M. “Blade Tip-Vortices of a Four-bladed Rotor with Axial Inflow”. In: *Journal of the American Helicopter Society* 65.4 (2020), pp. 1–13.

[40] Grimm, F. “Mesh Deformation of Camber Morphed Rotors”. Bachelor Thesis. Technische Universitaet Muenchen, 2021.

[41] Hagerty, B. and Kottapalli, S. *Boeing SMART Rotor Full-Scale Wind Tunnel Test Data Report*. Tech. rep. NASA Ames Research Center, 2012.

[42] Heinrich, R. *TAU Mesh Deformation Capability-TAU Training*. DLR.e.V.

[43] Huang, Q., Abdelmoula, A., Chourdakis, G., Rauleder, J., and Uekermann, B. “CFD/CSD Coupling for an Isolated Rotor using preCICE”. In: *14th World Congress on Computational Mechanics*. 2021.

[44] Huang, Q. “Loose Coupling of Isolated Rotorblade Rotorcraft CFD/CSD Simulations using preCICE”. MA thesis. Technische Universitaet Muenchen, 2019.

[45] Hunsaker, D. F., Reid, J. T., and Joo, J. J. “Geometric Definition and Ideal Aerodynamic Performance of Parabolic Trailing-Edge Flaps”. In: *International Journal of Astronautics and Aeronautical Engineering* 4.1 (2019), pp. 1–17.

[46] Jacklin, S. A., Haber, A., Simone, G. de, Norman, T. R., Kitaplioglu, C., and Shinoda, P. “Full-Scale Wind tunnel Test of an Individual Blade Control System for a UH-60 Helicopter”. In: *American Helicopter Society, 58th Annual Forum*. 2002.

[47] Jacklin, S. A. et al. *Investigation of a Helicopter Individual Blade Control (IBC) System in Two Full-Scale Wind Tunnel Tests: Volume I*. Tech. rep. NASA Ames Research Center, 2020.

[48] Jacklin, S. A. et al. *Investigation of a Helicopter Individual Blade Control (IBC) System in Two Full-Scale Wind Tunnel Tests: Volume II—Tabulated Data*. Tech. rep. NASA Ames Research Center, 2020.

[49] Jacklin, S. A., Blaas, A., Teves, D., Kube, R., and Warmbrodt, W. “Reduction of helicopter BVI Noise, Vibration, and Power Consumption through Individual Blade Control”. In: *American Helicopter Society,51th Annual Forum and Technology Display*. 1994.

[50] Jacklin, S. A., Blass, A., Swanson, S. M., and Teves, D. “Second Test of a Helicopter Individual Blade Control System in the NASA Ames 40-by 80-Foot Wind Tunnel”. In: *American Helicopter Society 2nd International Aeromechanics Specialists’ Conference*. 1995.

[51] Jacklin, S. A. “Full-scale Wind Tunnel Test of a Helicopter Individual Blade Control System”. In: *American Helicopter Society, 50th Annual Forum*. 1994.

[52] Jain, R., Yeo, H., and Chopra, I. “An Examination of Rotor Loads due to On-Blade Active Controls for Performance Enhancement using CFD/CSD Analysis”. In: *AHS Specialists' Conference on Aeromechanics*. 2010.

[53] Jain, R., Yeo, H., and Chopra, I. “Computational Fluid Dynamics-Computational Structural Dynamics Analysis of Active Control of Helicopter Rotor for Performance Improvement”. In: *Journal of the American Helicopter Society* 55.4 (2010), pp. 42004–42004.

[54] Jain, R., Yeo, H., and Chopra, I. “Investigation of Trailing-Edge Flap Gap Effects on Rotor Performance using High-Fidelity Analysis”. In: *Journal of aircraft* 50.1 (2013), pp. 140–151.

[55] Jia, Z. and Sinsay, J. “Comparison of Multi-Fidelity Approaches for the HART-II Rotor Noise Prediction Using CREATE TM -AV Helios”. In: *Vertical Flight Society, 78th Annual Forum*. 2022.

[56] Johnson, W. *Rotorcraft aeromechanics*. Cambridge University Press, 2013.

[57] Johnson, W. *CAMRAD II Manuals Volume I-VII*. Tech. rep. Release 4.10. Johnson Aeronautics, 2017.

[58] Johnson, W. “Rotorcraft Aerodynamics Models for a Comprehensive Analysis”. In: *American Helicopter Society, 54th Annual Forum*. 1998.

[59] Jung, S., You, Y., Kim, J., Sa, J., Park, J., and Park, S. H. “Correlation of Aeroelastic Response and Structural Loads for a Rotor in Descent”. In: *Journal of Aircraft* 49 (2012), pp. 398–406.

[60] Kaufmann, K., Costes, M., Richez, F., Gardner, A., and Pape, A. L. “Numerical Investigation of Three-Dimensional Static and Dynamic Stall on a Finite Wing”. In: *Journal of The American Helicopter Society* 60 (2015).

[61] Kaufmann, K., Gardner, A., and Costes, M. “Comparison Between Two-Dimensional and Three-Dimensional Dynamic Stall”. In: (2016), pp. 315–325.

[62] Kessler, C., Fuerst, D., and Arnold, U. “Open Loop Flight Test Results and Closed Loop Status of the IBC System on the CH-53G Helicopter”. In: *American Helicopter Society, 59th Annual Forum*. 2003.

[63] Keßler, C. “Active Rotor Control for Helicopters: Individual Blade Control and Swashplateless Rotor Designs”. In: *36th European Rotorcraft Forum*. 2010.

[64] Kloeppe, V. *Integration of Technologies in Support of a Passenger and Environmentally Friendly Helicopter (FRIENDCOPTER)*. Tech. rep. FRIENDCOPTER Consortium, 2009. URL: https://cordis.europa.eu/docs/results/502/502773/124772131-6_en.pdf.

[65] Komp, D., Kumar, S., Abdelmoula, A., Hajek, M., and Rauleder, J. “Investigation of Active Rotor Design and Control for Performance Improvement”. In: *Vertical Flight Society, 75th Annual Forum*. 2019.

[66] Komp, D., Hajek, D., and Rauleder, J. “Rotor Performance Enhancements with Spanwise Varying Active Camber Morphing”. In: *AIAA Scitech Forum*. 2021.

[67] Komp, D., Kumar, S., Hajek, M., and Rauleder, J. “Effect of active camber morphing on rotor performance and control loads”. In: *Aerospace Science and Technology* 108 (2021), p. 106311.

[68] Komp, D., Hajek, M., Yavrucuk, I., and Rauleder, J. “Rotor Power Savings and Pitch-Link Load Reductions with Spanwise-Varying Active Camber Morphing”. In: *Journal of Aircraft* 61.3 (2024), pp. 801–810. URL: https://doi.org/10.2514/1.C037505.

[69] Krzysiak, A. and Narkiewicz, J. “Aerodynamic Loads on Airfoil with Trailing-Edge Flap Pitching with Different Frequencies”. In: *Journal of aircraft* 43.2 (2006), pp. 407–418.

[70] Kumar, S., Komp, D., Hajek, M., and Rauleder, J. “Effect of Active Camber on Rotor Noise, Power and Hub Vibration”. In: *AIAA Scitech Forum*. 2021.

[71] Langer, H. J. and Traenapp, N. “BO105 Flight Test Data for a Wind Tunnel Test Program”. In: 1993.

[72] Lau, B. H., Straub, F., Anand, V., and Birchette, T. “SMART Rotor Development and Windtunnel Test”. In: *35th European Rotorcraft Forum*. 2009.

[73] Le Chuiton, F., D’Alascio, A., Barakos, G., Steijl, R., Schwamborn, D., and Lüdeke, H. “Computation of the Helicopter Fuselage Wake with the SST, SAS, DES and XLES Models”. In: *Advances in Hybrid RANS-LES Modelling: Symposium of Hybrid RANS-LES Methods*. Springer. 2007, pp. 117–124.

[74] Leishman, G. *Principles of Helicopter Aerodynamics with CD Extra*. Cambridge University Press, 2006.

[75] Liggett, N. and Smith, M. J. “The physics of modeling unsteady flaps with gaps”. In: *Journal of Fluids and Structures* 38 (2013), pp. 255–272.

[76] Lim, J. W., Potsdam, M., Strawn, R., Sim, B., and Nygaard, T. “Blade-Vortex Interaction Airloads Prediction Using Multidisciplinary Coupling”. In: 2006.

[77] Lim, J. and Strawn, R. “Prediction of HART II Rotor BVI Loading and Wake System using CFD/CSD Loose Coupling”. In: *45th AIAA Aerospace Sciences Meeting and Exhibit*. 2007.

[78] Liu, L., Padthe, A. K., Friedmann, P. P., Quon, E., and Smith, M. J. “Unsteady Aerodynamics of an Airfoil/Flap Combination on a Helicopter Rotor using Computational Fluid Dynamics and Approximate Methods”. In: *Journal of the American Helicopter Society* 56.3 (2011), pp. 1–13.

[79] Massey, S., Kreshock, A., and Sekula, M. “Coupled CFD/CSD Analysis of an Active-Twist Rotor in a Wind Tunnel with Experimental Validation”. In: *American Helicopter Society, 71th Annual Forum*. 2015.

[80] McAlister, K. W., Lambert, O., and Petot, D. *Application of the ONERA Model of Dynamic Stall*. Tech. rep. NASA Ames Research Center, 1984.

[81] Munz, C.-D. and Westermann, T. *Numerische Behandlung gewöhnlicher und partieller Differenzialgleichungen*. Springer, 2006.

[82] N., A. *Global Market for Military and Civil Helicopters - 2015-2024 - Market Dynamics, Competitive Landscape, OEM Strategies and Plans, Trends and Growth Opportunities, Strategic Outlook*. 2015. URL: https://marketpublishers.com/report/company_reports/global-market-4-military-civil-helicopters-2015-2024.html.

[83] Nguyen, K. and Johnson, W. “Evaluation of Dynamic Stall Models with UH-60A Airloads flight Test Data”. In: *American Helicopter Society, 54th Annual Forum*. 1998.

[84] Norman, T. R., Shinoda, P. M., Kitaplioglu, C., Jacklin, S., and Sheikman, A. “Low-Speed Wind Tunnel Investigation of a Full-Scale UH-60 Rotor System”. In: *American Helicopter Society, 58th Annual Forum*. 2002.

[85] Norman, T. R., Theodore, C., Shinoda, P., Fuerst, D., Arnold, U. T., Makinen, S., Lorber, P., and O’Neill, J. “Full-scale Wind Tunnel Test of a UH-60 Individual Blade Control System for Performance Improvement and Vibration, Loads, and Noise Control”. In: *American Helicopter Society, 65th Annual Forum*. 2009.

[86] Ōtomo, S., Henne, S., Mulleners, K., Ramesh, K., and Viola, I. M. “Unsteady Lift on a High-Amplitude Pitching Aerofoil”. In: *Experiments in Fluids* 62 (2021), pp. 1–18.

[87] Pahlke, K. and Wall, B. van der. “Calculation of Multibladed Rotors in High-Speed Forward Flight with Weak Fluid-Structure-Coupling”. In: *27th European Rotorcraft Forum*. 2001.

[88] Park, J. S., Jung, S., You, Y., Park, S., and Yu, Y. “Validation of Comprehensive Dynamics Analysis Predictions for a Rotor in Descending Flight”. In: *Aircraft Engineering and Aerospace Technology* 83 (2011), pp. 75–84.

[89] Platzer, S. “Aerodynamic Influences of Non-Parallel Ground Effect, Rotor-Rotor Interference, and Dynamic Actuation on Rotors in Hover”. PhD thesis. Technische Universität München, 2021.

[90] Pointwise. *Mesh Generation Software for CFD*. 2020. URL: https://www.pointwise.com.

[91] Potsdam, M., Yeo, H., and Johnson, W. “Rotor Airloads Prediction using Loose Aerodynamic/Structural Coupling”. In: *Journal of Aircraft* 43 (2006).

[92] Potsdam, M., Fulton, M., and Dimanlig, A. “Multidisciplinary CFD/CSD Analysis of the SMART Active Flap Rotor”. In: *American Helicopter Society, 66th Annual Forum*. 2010.

[93] Raichle, A. “Extension of the Unstructured TAU-Code for Rotating Flows”. In: *New Results in Numerical and Experimental Fluid Mechanics V: Contributions to the 14th STAB/DGLR Symposium*. 2006.

[94] Ramesh, K., Gopalarathnam, A., Edwards, J. R., Ol, M. V., and Granlund, K. “An unsteady airfoil theory applied to pitching motions validated against experiment and computation”. In: *Theoretical and Computational Fluid Dynamics* 27 (2013), pp. 843–864.

[95] Rauleder, J., Wall, B. G. van der, Abdelmoula, A., Komp, D., Kumar, S., Ondra, V., Titurus, B., and Woods, B. K. S. “Aerodynamic Performance of Morphing Blades and Rotor Systems”. In: *American Helicopter Society, 74th Annual Forum*. 2018.

[96] Ravichandran, K., Chopra, I., Wake, B. E., and Hein, B. “Trailing-Edge Flaps for Rotor Performance Enhancement and Vibration Reduction”. In: *Journal of the American Helicopter Society* 58 (2013).

[97] Richter, K., Pape, A. L., Knopp, T., Costes, M., Gleize, V., and Gardner, A. “Improved Two-Dimensional Dynamic Stall Prediction with Structured and Hybrid Numerical Methods”. In: *Journal of The American Helicopter Society* 56 (2011).

[98] Richter, P. and Blass, A. “Full Scale Wind tunnel Investigation of an Individual Blade Control System for the BO 105 Hingeless Rotor”. In: *19th European Rotorcraft Forum*. Sept. 1993.

[99] Rivero, A. E., Fournier, S., Weaver, P., Cooper, J., and Woods, B. K. S. “Manufacturing and Characterisation of a Composite FishBAC Morphing Wind Tunnel Model”. In: *29th International Conference on Adaptive Structures and Technologies*. 2018.

[100] Roth, D., Enenkl, B., and Dieterich, O. “Active Rotor Control by Flaps for Vibration Reduction-Full scale demonstrator and first flight test results”. In: *32th European Rotorcraft Forum*. 2006.

[101] Ruan, Y. “Numerical Investigation of Dynamic Stall on a Retreating Helicopter Blade”. PhD thesis. Technische Universität München, 2022.

[102] Rumsey, C. *The Spalart-Allmaras Turbulence Model*. URL: https://turbmodels.larc.nasa.gov/spalart.html.

[103] Schweikhard, R. “Actuator Disk for Helicopter Rotors in an Unstructured Flow Solver”. In: *Journal of The American Helicopter Society* 52 (2007), pp. 58–68.

[104] Servera, G., Beaumier, P., and Costes, M. “A Weak Coupling Method Between the Dynamics Code HOST and the 3D Unsteady Euler Code WAVES”. In: *Aerospace Science and technology* 5 (2001), pp. 397–408.

[105] Shin, S., Cesnik, C. E., and Hall, S. R. “Closed-Loop Control Test of the NASA/Army/MIT Active Twist Rotor for Vibration Reduction”. In: *Journal of the American Helicopter Society* 50 (2005).

[106] Shivananda, T., Mcmahon, H., and Gray, R. “Surface Pressure Measurements at The Tip of a Model Helicopter Rotor in Hover”. In: *Journal of Aircraft* 15 (1978), pp. 460–467.

[107] Smith, M. et al. “An Assessment of CFD/CSD Prediction State-of-the-Art using the HART II International Workshop Data”. In: *American Helicopter Society, 68th Annual Forum*. 2012.

[108] Stacey, S., Connolly, N., Court, P., Allen, J., Monteggia, C., and Oliveros, J. M. “Leonardo Helicopters Active Rotor Programmes to Improve Helicopter Comfort & Performance”. In: *American Helicopter Society, 74th Annual Forum Technology Display*. 2018.

[109] Straub, F. K., Anand, V. R., Lau, B. H., and Birchette, T. S. “Wind Tunnel Test of the SMART Active Flap Rotor”. In: *Journal of the American Helicopter Society* 63 (2018).

[110] Surrey, S., Wendisch, J.-H., and Wienke, F. “Coupled Fluid-Structure Simulations of a Trimmed Helicopter Rotor in Forward Flight”. In: *New Results in Numerical and Experimental Fluid Mechanics X: Contributions to the 19th STAB/DGLR Symposium*. 2016.

[111] Swanson, S., Jacklin, S., Blaas, A., Niesl, G., and Kube, R. “Acoustic Results from a Full-Scale Wind Tunnel Test Evaluating Individual Blade Control.” In: *American Helicopter Society,51th Annual Forum*. 1995.

[112] Thibert, J.-J. and Pouradier, J. *Design and test of an helicopter rotor blade with evolutive profile*. Office National d’Études et de Recherches Aérospatiales, 1980.

[113] Wall, B. G. van der, Lim, J. W., Smith, M. J., Jung, S. N., Bailly, J., Baeder, J. D., and Boyd, D. D. J. “The HART II International Workshop: An assessment of the State-of-the-Art in Comprehensive Code Prediction”. In: *CEAS Aeronautical Journal* 4 (2013).

[114] Wall, B. G. van der. “Deliverable D1.1 of the SABRE Project: Selection of the Baseline Rotor”. In: (2017).

[115] Wang, G., Mian, H., Ye, Z.-Y., and Lee, J. “An Improved Point Selection Method for Hybrid-Unstructured Mesh Deformation Using Radial Basis Functions”. In: 2013.

[116] Wilbur, M. L., Mirick, P. H., Yeager, W. T., Langston, C. W., Cesnik, C. E., and Shin, S. “Vibratory Loads Reduction Testing of the NASA/Army/MIT Active Twist Rotor”. In: *Journal of the American Helicopter Society* 47 (2002).

[117] Wilbur, M. L., Yeager Jr, W. T., and Sekula, M. K. “Further Examination of the Vibratory Loads Reduction Results from the NASA/Army/MIT Active Twist Rotor Test”. In: *American Helicopter Society, 58th Annual Forum*. 2002.

[118] Wilkie, W. K., Wilbur, M. L., Mirick, P. H., Cesnik, C. E., and Shin, S. “Aeroelastic analysis of the NASA/Army/MIT Active Twist Rotor”. In: *American Helicopter Society, 55th Annual Forum*. 1999.

[119] Woods, B. K. S. and Friswell, M. I. “Preliminary Investigation of a Fishbone Active Camber Concept”. In: *ASME 2012 Conference on Smart Materials, Adaptive Structures and Intelligent Systems*. 2012.

[120] Xu, B., Liu, B., Cai, X., Yuan, Y., Zhao, Z., and Wang, Y. “Accuracy of the Aerodynamic Performance of Wind Turbines using Vortex Core Models in the Free Vortex Wake Method”. In: *Journal of Renewable and Sustainable Energy* (2019).

[121] Yeo, H., Romander, E., and Norman, T. “Investigation of Rotor Performance and Loads of a UH-60A Individual Blade Control System”. In: *Journal of the American Helicopter Society* 56 (2011).

[122] Young, A. “Aerodynamics. By LJ CLANCY. Pitman”. In: *Journal of Fluid Mechanics* 77 (1976).

[123] Zaporozhets, O., Isaienko, V., and Synylo, K. “PARE Preliminary Analysis of ACARE Flight-Path 2050 Environmental Impact Goals”. In: *CEAS Aeronautical Journal* 12 (2021).